Development and Construction of a new Photoelectron Imaging Spectrometer for Studying the Spectroscopy and Ultrafast Dynamics of Molecular Anions

GARETH MICHAEL ROBERTS

Development and Construction of a new Photoelectron Imaging Spectrometer for Studying the Spectroscopy and Ultrafast Dynamics of Molecular Anions

Gareth Michael Roberts

Department of Chemistry
University of Durham

A thesis submitted in partial fulfilment of the requirements for the degree of *Doctor of Philosophy*

2010

"*Nothing in this world is to be feared, only understood*"
Marie Curie

This thesis is dedicated to the memory of

-

Sydney Fredrick Roberts
my loving grandfather

-

Frank Burley Johnson M.A.
a scientific inspiration

Declaration

The material contained within this thesis has not previously been submitted for a degree at the University of Durham or any other university. The research reported within this thesis has been conducted by the author unless indicated otherwise.

Acknowledgements

This thesis would not have been possible without the support and help of the following people:

First and foremost I thank my supervisor, Jan Verlet, without whom none of this would have been possible. Your guidance, advice, and patience (and I know that sometimes a lot of this was required!) have been invaluable to me over these last three years. You have helped me to develop into the scientist I have always aspired to be, and for this I am truly indebted to you.

Eckart Wrede, my second supervisor. I thank you for many stimulating scientific discussions, additional guidance, and for always providing me with an open door for extra advice.

I also thank David Tozer and Austin Dwyer for assistance with electronic structure calculations, and Paul Low for help with spectroelectrochemical analysis.

The many members of Team Verlet over the past three years: Steven Saville, Jonathan Nixon (the Labview genius!), Laurie King, Adam Chatterley, Simon Mihailovic, and Sagar Dodderi. I would like to especially acknowledge Julien Lecointre and Daniel Horke, who have helped to make my time in the group both scientifically productive and socially entertaining.

The Durham Laser Spectroscopy and Dynamics (LS&D) Group. All of you have been fantastic! There are too many to name, but I particularly want to thank Scott Sanders, Oliver Willis, Adrian Rowland, Hendrik Nahler, and David Carty. Oli, without you I would have been in limbo and finishing this thesis would have been far more difficult; thank you for the budget accommodation!

Importantly, a special mention needs to be given to the Vic and the delicious pints of Big Lamp bitter consumed on Friday evenings. I'm sure some of the best scientific ideas have been developed during conversations over a pint of ale in this pub. I will miss it dearly.

All of my friends, both at home and in Durham, especially Matthew McCoig-Lees, Nicholas Haywood, Bryn Hill, and Robert Shaw. I thank you all for constantly

reminding me that there is more to life than just work. Spending time with you all (particularly over the last three years) has allowed me to maintain the small amount of sanity that one can expect to retain at the end of a Ph.D.!

Finally, and most importantly, I thank my wonderful family: Mum, Dad, Daniel, Nan, and Grampy. I love you all dearly and without your love and support, none of this would have been possible.

Publications

This thesis is based on the following publications:

Chapter 3: G. M. Roberts, J. L. Nixon, J. Lecointre, E. Wrede, and J. R. R. Verlet, 'Toward Real-time Charged-particle Image Reconstruction using Polar Onion-peeling', *Rev. Sci. Instrum.*, **80**, 053104 (2009).

Chapter 4: G. M. Roberts, J. Lecointre, D. A. Horke, and J. R. R. Verlet, 'Spectroscopy and Dynamics of the 7,7,8,8-Tetracyanoquinodimethane Radical Anion', *Phys. Chem. Chem. Phys.*, **12**, 6226 (2010).

Chapter 5: J. Lecointre, G. M. Roberts, D. A. Horke, and J. R. R. Verlet, 'Ultrafast Relaxation Dynamics Observed through Time-resolved Photoelectron Angular Distributions', *J. Phys. Chem. A*, **114**, 11216 (2010).

Abstract

We present a detailed account of the development, construction, and commissioning of a new experiment for studying the spectroscopy and ultrafast dynamics of molecular anions in the gas phase. The new instrument incorporates: an electrospray ionisation source, which is capable of generating a vast class of molecular anions; a Wiley-McLaren time-of-flight mass spectrometer; and a compact photoelectron imaging arrangement for anions, which negates the use of pulsed high voltages. We use this instrument in conjunction with a femtosecond laser system to perform the first ultrafast time-resolved photoelectron imaging experiments on molecular anions generated through electrospray ionisation.

A method for reconstructing three dimensional charged particle distributions from their associated two dimensional projections on an imaging detector plane is described. This new method utilises: (1) onion-peeling in polar co-ordinates (POP) to perform the reconstruction; and (2) basis set concepts to significantly enhance the algorithms computational speed. We compare this new POP algorithm with other reconstruction algorithms, which shows that the method is as good as the benchmark pBASEX method in terms of accuracy. Importantly, we show that it is also computationally fast, allowing images to be reconstructed as they are acquired in a typical imaging experiment.

Original work is presented which investigates the spectroscopy and ultrafast excited dynamics of the 7,7,8,8-tetracyanoquinodimethane (TCNQ) radical anion. The photoelectron spectrum of $TCNQ^-$ is measured at 3.1 eV, which is used to gain insight into the electronic structure and geometries of both the anion and neutral states. Time-resolved photoelectron imaging experiments explore the relaxation dynamics of its first excited 1^2B_{3u} state, which we show undergoes internal conversion back to the $^2B_{2g}$ ground state on a timescale of 650 fs. Results also provide evidence of a wave packet motion on the excited state, which exhibits a characteristic frequency of 30 cm^{-1}.

Finally, we describe, for the first time, a formulism which allows ultrafast relaxation timescales to be extracted from the photoelectron angular distributions of isoenergetic photoelectron features. As an example, we use the time-resolved

photoelectron angular distributions of a nearly isoenergetic feature in the photoelectron images of $TCNQ^-$. From this model we extract a relaxation time for the 1^2B_{3u} state, which quantitatively agrees with those extracted from fits to the features in the photoelectron spectra derived from the images.

Contents

Chapter 1: Introduction

The topic of femtochemistry is introduced and we present an overview of this field's development and diversification over the last two decades. The fundamental concepts of gas phase spectroscopy experiments are then described, where we specifically focus on molecular beam methodologies, gas phase anion production, and introduce electrospray ionisation as a technique for generating large gas phase ion species. Femtosecond time-resolved photoelectron spectroscopy is discussed as an experimental tool for mapping the ultrafast dynamics of isolated gas phase molecules, with a specific emphasis on anions. We then follow on by presenting an overview of some of the most pertinent time-resolved photoelectron spectroscopy studies, which are of particular relevance to the work presented here. Finally, we close with an overview of this thesis.

1.1 Femtochemistry: Chemistry on an Atomic Timescale

The timescale on which atoms move in molecules is on the order of femtoseconds (10^{-15} s = 1 fs) and if we wish to gain a greater fundamental understanding of how atoms rearrange during chemical reactions, it becomes desirable to implement experimental methods that operate on comparable timescales to these atomic motions [1]. Such experimental methodologies were pioneered in the early 1980s, and culminated in Zewail being awarded the Nobel Prize for Chemistry in 1999 [2]. These ground breaking studies involved, for the first time, the development of state-of-the-art laser systems capable of producing laser light pulses lasting for a few hundred femtoseconds (commonly termed 'ultrashort' laser pulses). Such femtochemistry studies are generally performed in a time-resolved manner, whereby a first ultrashort 'pump' laser pulse excites the molecule of interest from its electronic ground state, $|g\rangle$, to some excited state, $|e\rangle$. As $|e\rangle$ evolves with time, *via* the various molecular relaxation pathways available to the molecule, a second ultrashort 'probe' laser pulse, interacting with the molecule at discrete time-delays after the initial pump pulse, is subsequently used to monitor the temporal evolution of $|e\rangle$. This process ultimately enables a time-resolved 'picture' of the chemical dynamics to be constructed.

Over the past two decades this pump-probe methodology, in combination with the development of commercially available ultrafast laser systems, has enabled the scientific community to break new ground in understanding a vast class of chemical reactions in intimate detail. Examples range from bond fission in simple homo- and hetero-nuclear diatomic molecules [3-6], to significantly more complex chemical dynamics in larger biomolecules [1].

In this thesis we aim to expand on these ideas and describe the development and construction of a new experiment designed to study the femtochemistry of large molecular systems, where we explicitly turn our attention towards understanding the ultrafast behaviour of negatively charged species pertinent to chemistry and biology. We begin by presenting a brief history of how femtochemistry has been diversified and developed over the last two decades.

Gas Phase Studies on NaI

Early seminal studies conducted by the Zewail group concerned the excited state dissociation dynamics of the alkali halide, NaI [5,6]. These studies, conducted in the collision-free environment of a vacuum chamber (gas phase), were performed by seeding the alkali halide species into a supersonic jet expansion (see Section 1.2.1). By isolating the species of interest from any surrounding molecules, which can potentially perturb the fundamental dissociation dynamics in question, Zewail and co-workers were able to obtain an intricate insight in the transient dynamics of the dissociation process.

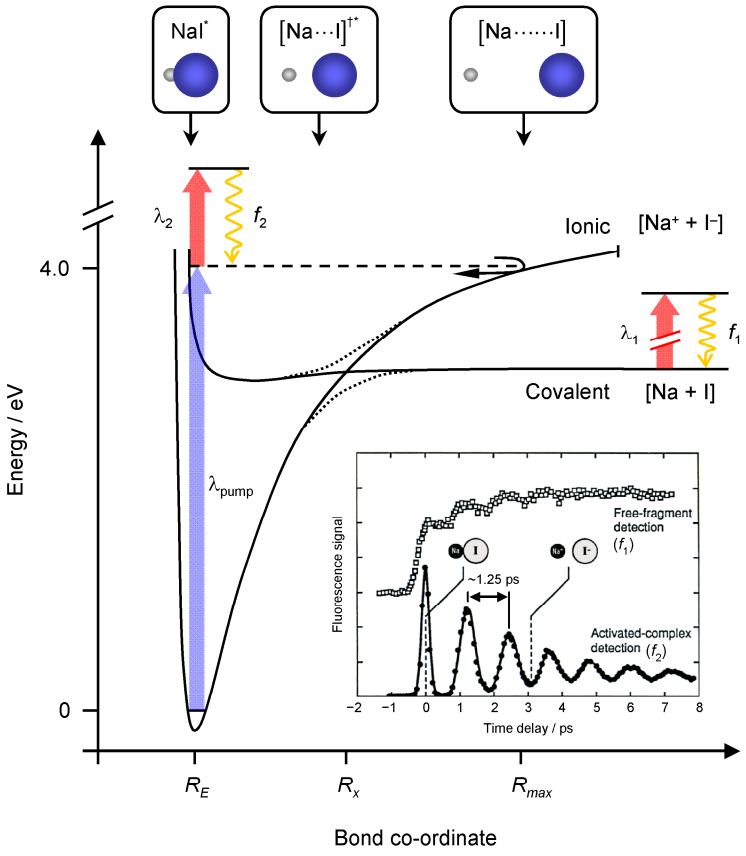

Figure 1.1: Schematic of the ground (ionic) and first excited (covalent) electronic potential energy surfaces of the NaI molecule. Solid black lines represent the diabatic surfaces and the dotted lines represent the adiabatic regions. R_x indicates the position of the avoided crossing between the two potentials (6.93 Å) and R_E is the equilibrium bond length of the ground state. A 4.0 eV (310 nm) pump pulse, λ_{pump}, excites the molecule to form NaI^*. The fluorescence of the free Na atom species or the NaI^* transient are subsequently monitored with time delayed probed pulses, λ_1 and λ_2, respectively. The trajectory of the excited state transient is shown by the dashed line as it evolves along the bond co-ordinate to the maximum elongation at R_{max} (transient configurations are shown above). Results of these studies as a function of pump-probe time delay are shown inset in the bottom right (results adapted with permission from reference [1]. Copyright 2000, American Chemical Society).

Alkali halides like NaI were seen as ideal candidates for studying bond dissociation in greater detail, as the ground and excited state potentials possess markedly different characteristics. The ground state is of a strongly bonded ionic character (Na^+I^-), while the excited state is only weakly bound and covalent in nature (Na–I). These potential energy surfaces, shown in Figure 1.1, become degenerate at an atomic separation of 6.93 Å (labelled R_x in Figure 1.1), leading to the formation of an avoided crossing between the two states. Upon excitation with an ultrashort pump pulse, λ_{pump}, the NaI molecule begins to dissociate along the bond co-ordinate, R. As the excited transient, $\left[Na\cdots I\right]^{\dagger *}$, approaches the avoided crossing, (1) some portion of the transient NaI species can dissociate along the covalent (diabatic) surface to form isolated Na and I products or, (2) the transient can remain on the ionic surface (adiabatic) and form loosely bound ionic products, Na^+ and I^-. Focusing on the latter, the loose ionic complex can then begin to contract again until it once again reaches the geometry at which it was excited, R_E. This oscillatory process proceeds, such that each time the bond length expands to R_x, more of the transient species can 'leak' out from the adiabatic surface onto the diabatic potential to form covalent products, continuing until all of the excited state transient population has dissociated into atomic Na and I species. This quasi-classical oscillatory behaviour of the excited state transient, known as a *wave packet oscillation* (see Section 1.3.1 for more detail), was observed for the first time by Zewail and co-workers using a time-delayed ultrashort probe pulse, λ_1, to monitor the fluorescence from the *D* line (589 nm, 2.1 eV) in the accumulating atomic Na products. The results, shown inset in Figure 1.1, show a 'step like' increase in the measured fluorescence signal every 1.25 ps. Similarly, the dynamics of the $\left[Na\cdots I\right]^{\dagger *}$ transient may also be observed through fluorescence from NaI using a second probe, λ_2. These results, also shown inset in Figure 1.1, show a sinusoidal functionality in the time-dependent signal, which is approximately out-of-phase with the periodic signal increases observed in the atomic Na products, elegantly reflecting the oscillatory behaviour of the excited state species. These results not only highlight the extremely fast timescales on which chemical dynamics can take place, but also emphasise the unprecedented level of detail attainable from femtochemistry experiments conducted in a gas phase environment.

Femtochemistry in the Condensed Phase

Most chemistry and virtually all biology naturally takes place in a condensed phase environment. In chemistry this is commonly in the medium of a solvent, such as water, and in biology the 'condensed phase environment' can for example be understood in terms of an extended protein manifold which may surround a bio-active chromophore. Hence, the elimination of this surrounding environment in gas phase experiments often provides an inappropriate model for nature, as many important solvent mediated processes become unobservable in the isolated gas phase species. It therefore appears more logical to study the chemical dynamics of such species *in situ* of the condensed phase environment.

In the years since the early gas phase experiments on NaI were performed, ultrafast pump-probe methodologies have been expanded to conduct experiments in the condensed phase. Early condensed phase studies commonly took the guises of transient absorption [7] and fluorescence up-conversion techniques [8,9], and over the years have provided invaluable insights into chemical and bio-dynamics occurring in their natural environment. Recently however, more complex multi-dimensional methodologies, such as ultrafast two-dimensional infra-red spectroscopy [10-12], and non-linear techniques [13], which possess added interfacial specificity [14,15], have emerged at the forefront of modern ultrafast experiments conducted in the condensed phase. However, ultrafast pump-probe experiments performed in solution regularly lead to complications when it comes to untangling the ultrafast dynamics. This often occurs as a result of the solvent manipulating the chemical or bio-dynamics being probed, such that it becomes non-trivial to distinguish between solvent mediated processes and those occurring in the isolated molecule of interest. As such, the gas phase still remains an attractive environment in which unperturbed ultrafast chemical phenomena can be studied.

Femtochemistry of Large Species and Biomolecules in the Gas Phase

Recent years have seen a drive to investigate larger molecular species in the gas phase, including large conjugated organic species [16-26], DNA bases [27-33] and other biomolecules [34,35] such as the chromophore of the photoactive yellow protein [36], although it can become non-trivial generating such species in the gas phase *via*

commonly used molecular beam methods. This issue primarily arises because larger species, which are often solids at room temperature, must first be vaporised into the gas phase *via* heating, regularly leading to their decomposition rather than the required sublimation. As such, it becomes desirable to find other methods which may be utilised to transport large molecules into the gas phase environment [37-42].

Here we present the motivations behind the development of a new instrument which will enable larger molecular species, specifically anions, to be readily interrogated in the collision free environment of the gas phase. This instrument, in conjunction with ultrafast pump-probe methodologies, aims to provide new insights into the intricate dynamics and chemical phenomena that occur in this wide ranging and diverse class of molecules.

Throughout the remainder of Chapter 1 an overview of gas phase spectroscopy and the techniques routinely used in this area of chemical physics is presented. Further to this, we introduce the reader to the fundamentals of femtosecond spectroscopy experiments, including a detailed overview of the photoelectron spectroscopy detection methodology which has been implemented in conjunction with the new instrument, described in detail in Chapter 2. We close this chapter by presenting a brief review of some of the most recent developments in the field of ultrafast gas phase spectroscopy, with a specific emphasis on large molecular systems and experiments which have attempted to provide insights into condensed phase behaviour from the perspective of the gas phase. Finally, an overview of the material covered in this thesis is presented.

1.2 Gas Phase Spectroscopy

1.2.1 Molecular Beam Methodologies

Generation and Properties of Molecular Beams

One of the most commonly used approaches for transferring molecules into the gas phase environment are supersonic jet expansions [43]. These methods are performed *via* the expansion of a gas through a small aperture into an evacuated vacuum chamber, as shown in Figure 1.2. This divergent free jet can subsequently be converted into a more directed flow of gas *via* the addition of a conical shaped skimmer, placed down stream

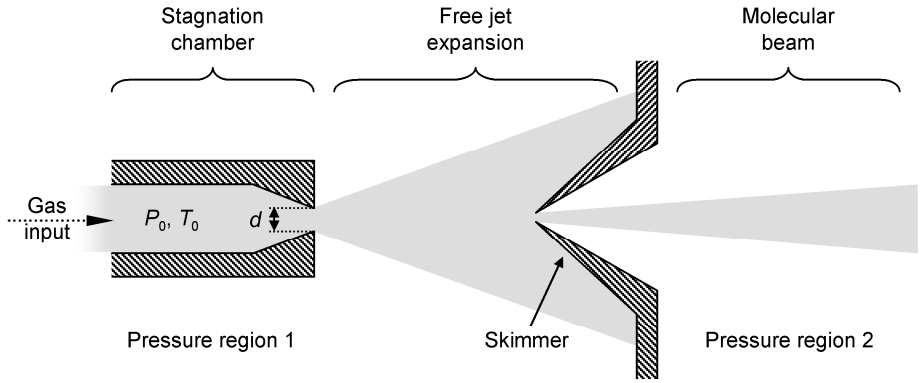

Figure 1.2: Schematic of a standard molecular beam arrangement. Gas molecules at a pressure and temperature of P_0 and T_0, respectively, are expanded from a stagnation chamber through a nozzle (with diameter, d) into a vacuum chamber (pressure region 1), leading to the formation of a free jet expansion. The supersonic jet is then passed through a small aperture in a conical shaped skimmer, into a second vacuum region of lower pressure (pressure region 2) producing a molecular beam.

from the exit aperture. The excess gas at the extremities of the free jet expansion is 'skimmed' off, resulting in the formation of the desired parallel flow of a molecular beam in the next differentially pumped vacuum chamber. This technique is particularly desirable for spectroscopic studies in the gas phase as it not only leads to the generation of internally cold species *via* molecular collisions, but also produces an appreciable density of molecules so that spectroscopy can feasibly be carried out.

For a jet expansion to enter into the supersonic regime, the pressure behind the nozzle, P_0, leading to the vacuum chamber must be increased to a point where the mean free path of the molecules in the stagnation chamber is less than the nozzle diameter, d. When these conditions are met, the flow of molecules immediately after the aperture increases considerably, enabling the speed of the molecules in the expansion to become much greater than the local speed of sound for molecules that are not contained within the beam (i.e. background gas molecules in the vacuum chamber). This leads to the Mach number, M, becoming $\gg 1$ ($M = 1$ corresponds to the molecules travelling at the local speed of sound) and hence, the term supersonic is applied to the jet expansion. This supersonic region of the jet expansion, commonly referred to as the 'zone of silence', arises from elastic collisions between molecules as they expand from the orifice into the vacuum, causing the conversion of random molecular motions into a directed flow. In this zone the velocities of the individual molecules tend toward the mean flow velocity leading to a reduction in the velocity distribution for the molecules

in the expansion, which defines their translational temperature. This phenomenon leads to molecular jet expansions commonly attaining translational distributions as low as 1 K [44]. Additionally, inelastic collisions also give rise to rotational and vibrational cooling *via* the direct conversion of internal energy into the kinetic energy of the bulk molecular flow, producing rotational and vibrational temperatures as low as 1-10 K and 50-100 K [44], respectively. In such temperature regimes, the number of internal states populated in the molecules is greatly reduced, which aids in simplifying the spectroscopic measurements one ultimately wishes to make.

As the translational temperature of the molecular expansion reduces, the mean velocity of the molecules also increases, until a point where they reach their terminal velocity, v_∞, defined by [43]:

$$v_\infty = \sqrt{\frac{2RT_0}{W}\left(\frac{\gamma}{\gamma-1}\right)}, \tag{1.1}$$

where R is the molar gas constant, T_0 is the temperature in the stagnation chamber, W is the molecular weight of the species in the expansion (in kg mol^{-1}) and γ is the ratio of the specific heat capacities of the gas at constant pressure, C_P, and volume, C_V, respectively. As an example, a free jet expansion of argon (a common gas used for the formation of molecular beams) can readily attain a v_∞ of ~550 m s^{-1}. For mixed gas expansions a similar approach can also be used to determine v_∞, by substituting the molar averages of W and γ into equation (1.1), determined by:

$$\begin{aligned} \bar{W} &= \sum_i X_i W_i \\ \bar{\gamma} &= \frac{\bar{C}_P}{\bar{C}_P - R} \end{aligned}, \tag{1.2}$$

where X_i is the molar fraction of molecules in the expansion and $\bar{C}_P = \sum_i X_i C_{Pi}$. Assuming that C_P is similar for both species, this gives rise to an important property of molecular beams; as v_∞ is inversely proportional to $\bar{W}$ this enables one to accelerate heavy molecular species to v_∞ by diluting them in a molecular beam of lighter atoms (e.g. argon), known as the 'carrier gas'. This process, called 'seeding', is a common method for transferring large molecules, such as conjugated organics, into the gas phase

by vaporising and seeding them into a molecular beam.

However, this methodology of introducing larger molecular species into the gas phase can be extremely restrictive as many of these species, which are solids at room temperature (e.g. DNA bases), fragment and degrade upon vaporisation [35]. This problem can become exacerbated when the species of interest is not only large, but also contains highly polar functional groups, such as nitro groups (NO_2), leading to strong chemical interactions in the solid [45]. Alternative methods for seeding larger species in molecular beams, which avoid direct heating of the seed species, have been developed in recent years and include laser desorption sources [37-40,42]. Unfortunately, these sources have the associated problem of producing significantly reduced number densities of seed molecules within the carrier gas expansion [38], often making it more difficult to perform spectroscopy with these sources.

Micro-solvation and Clustering in Molecular Beams

An extra feature of supersonic expansions is their ability, under the correct conditions, to form atomic and molecular clusters [46,47]. Clusters are isolated gas phase aggregates of individual atoms/molecules, and can contain anywhere from a few up to thousands of individual species. Over the years they have received wide-ranging attention from both an experimental [48-51] and theoretical [49,52-55] perspective. From an experimental view point, they present an interesting scenario whereby the sequential growth of these atomic/molecular aggregates potentially allows one to

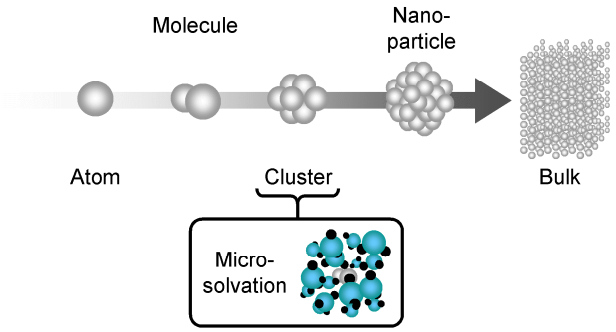

Figure 1.3: Schematic diagram of the size evolution of isolated atoms and molecules in the gas phase, through atomic/molecular clusters and nano-particles, into the bulk. Also shown is a pictorial representation of micro-solvation in the cluster regime, where a solute molecule in the gas phase is embedded in a cluster of solvent molecules, such as water.

investigate how the microscopic properties of isolated individual species extrapolate to behaviour observed in the bulk (condensed phase). Specifically, clusters appear to be ideal systems for investigating exactly how a solvent perturbs the chemical dynamics of a solute molecule, by the systematic *micro-solvation* of the solute, whilst also maintaining the benefits that gas phase studies offer [50,51,56-59]. As such, clusters have some times been somewhat sceptically heralded as a 'bridge' between the gas and condensed phase research areas.

The application of clusters has not only been restricted to the study of solvation dynamics, but has also aided in furthering a microscopic understanding of liquid structure [60-62], surface catalysis [63-68] and the electronic structure properties of metals [69-74]. The latter is exemplified by the size evolving properties of mercury cluster anions (Hg_n^-) [73,74], where small cluster sizes ($7 \le n \le 18$) display semiconductor-like properties and exhibit a band gap between the *s*- and *p*-bands, but as *n* increases the band gap reduces in energy until a transition to the electrically conducting behaviour observed in the bulk occurs.

The theory behind controlling the formation of clusters in molecular beam sources is not fully understood [47] however, from a simplified perspective, the experimental conditions for cluster formation generally depend on the product of the stagnation chamber pressure and the diameter of the nozzle aperture, $P_0 d$ (measured in Torr cm), where larger $P_0 d$ values increase the degree of clustering [75]. For monatomic beams, the onset of clustering generally occurs in the range $5 < P_0 d < 10$ when rare gases are used as carrier gases [76].[1] Hence, increasing P_0, generally leads to a rise in the number of clusters in the jet expansion, whilst simultaneously reducing their average internal temperature.

As increasing the amount of cluster formation relies on high source pressures (P_0 ≈ 200 bar), pulsed molecular beam sources are commonly used to reduce the gas load present in the vacuum chamber [46]. As an example, a continuous beam source with a nozzle diameter of d = 0.01 cm, a source pressure of 200 bar (1.5×10^5 Torr), and a chamber evacuated at 3000 l s^{-1}, will result in a chamber pressure of ~0.1 Torr, too high

[1] This $P_0 d$ regime does not hold when using helium as a carrier gas for cluster formation. This is due to the fact that the formation of the He dimer, required for subsequent cluster growth, is an unstable process. This results in a much greater $P_0 d$ onset of ~200 Torr cm.

for many diffusion and turbomolecular pumped vacuum systems. Whereas, a 10 Hz pulsed source producing 50 μs pulses reduces the background pressure in the chamber to ~10^{-5} Torr, well within the standard operating conditions of many vacuum pumps.

Pulsed beam sources are also particularly complementary in many modern laser spectroscopy experiments, where pulsed laser sources are commonly utilised, as they enable the beam source and the laser system to be synchronised, leading to an improved signal-to-noise ratio in spectroscopic measurements. In particular a femtosecond laser by definition cannot be continuous and typical systems operate at 1 kHz, requiring pulsed valves operating at this repetition rate [77].

1.2.2 Gas Phase Anions

Gas phase spectroscopy experiments over the years have not only been restricted to the study of neutral species, as discussed in the previous section, but have also covered considerable ground in investigating the chemical and physical properties of isolated negative ions [78-81]. In nature many anionic species are involved in chemically relevant processes, such as the well known SO_4^{2-} and PO_4^{3-} anions which play a vital role in the nucleation of ice crystals in atmospheric chemistry [82]. Bio-molecules also rely on the ultrafast dynamical processes of anionic chromophores, examples of which include proteo-rhodopsin [83] and the photoactive yellow protein [36,84], the former being responsible for the key trigger process of vision in the human eye.

Anions also have a stronger and generally more complex relationship with their surrounding environments than neutrals, arising because of their charge state, their high polarisability, and the diffuse nature of the excess electron [85,86]. In such cases, micro-solvation and cluster studies come into their own by enabling one to understand how the solvent, particularly polar species such as water, manipulate the electronic and physical processes taking place [48,51].

Experimentally, negative ions also present a number of additional benefits, not provided in neutral studies. The inherently charged nature of these species enables one to prepare and isolate anions *via* mass spectrometry and mass selection techniques, discussed in more detail in Chapter 2, enabling micro-solvated anions and clusters to be separated and probed according to their size.

Additionally, the electronic dynamics of anions are quite different from that of

neutrals. The interaction of the excess electron with the neutral 'core' species is much weaker than the Coulombic interaction of the electrons and the positive 'core' in uncharged molecules. As such, the energy required to remove an electron from a negative ion is typically significantly less than that needed for photoionisation of neutrals. This is particularly advantageous when implementing dynamical probing techniques such as photoelectron spectroscopy (see Section 1.3.3), as the low electron affinities simplifies not only the experiment but also the interpretation of the time-resolved results [51,81,87-89].

Many different methodologies currently exist for creating anions in the gas phase, each with their own pros and cons depending on the prerequisite aims of the experiments being performed. We present here a brief overview of a few of the most commonly used 'hard ionisation' methods for generating negative ions *in vacuo*.

Common Hard Ionisation Sources

Electron impact sources are routinely used to generate anions in the gas phase [90,91]. Such sources commonly consist of a pulsed free jet expansion, containing the analogous neutral species of interest, perpendicularly traversed by a continuously operating high energy electron beam (~1-2 keV). The electron beam is produced by passing a current through a metal filament possessing a low work-function (commonly tungsten or thoriated-iridium), leading to the thermionic emission of electrons which are then accelerated towards the expanding gas pulse, using an anode with an applied high voltage (~ –1 kV). Upon passing through the gas pulse, these primary high energy electrons collide with the neutral species in the molecular beam, leading to their subsequent ionisation and the concomitant generation of secondary low energy electrons (<10 eV) [90]:

$$M + e^-(1\ \text{keV}) \rightarrow M^+ + e^-(< 10\ \text{eV}) + e^-(\sim 990\ \text{eV}).$$

This process leads to the formation of a plasma containing cations and low energy electrons, in which the low energy electrons may go on to attach to the remaining neutral molecules in the molecular beam pulse. If the energy of the attached electrons is

sufficiently low that fragmentation of the molecule is not induced, then the anions of interest are generated. The excess energy the anion gains from the additional electron can in turn be dissipated into the bulk kinetic energy flow of the molecular beam pulse, leading to cold gas phase anions.

The generation of negative ions *via* electron impact techniques has been particularly fruitful in its application to negative cluster ion formation such as Ar_n^- [57,59,92], $(CO_2)_n^-$ [56,58,59,93-96], and in particular $(H_2O)_n^-$ [87-89,97-101] which often contain chromophore molecules of interest. However, due to the high electron beam energies used in this technique, large amounts of molecular fragmentation are often observed, in conjunction with the fact that one must still combat the primary difficulties associated with seeding larger molecular species into molecular beam pulses.

Alternative hard ionisation methodologies for the production of gas phase anions also exist [78]. Common examples include sputtering [102-105] and electric discharge sources [106-110]. The former utilises a beam of high energy alkali metal cations (commonly Cs^+ at ~2 keV), which is then focused onto a sputter target of interest. Target samples are often transition metals, metal oxides or inorganic semi-conductors such as GeAs (see Figure 1.4). Negative ions formed during the sputtering process are

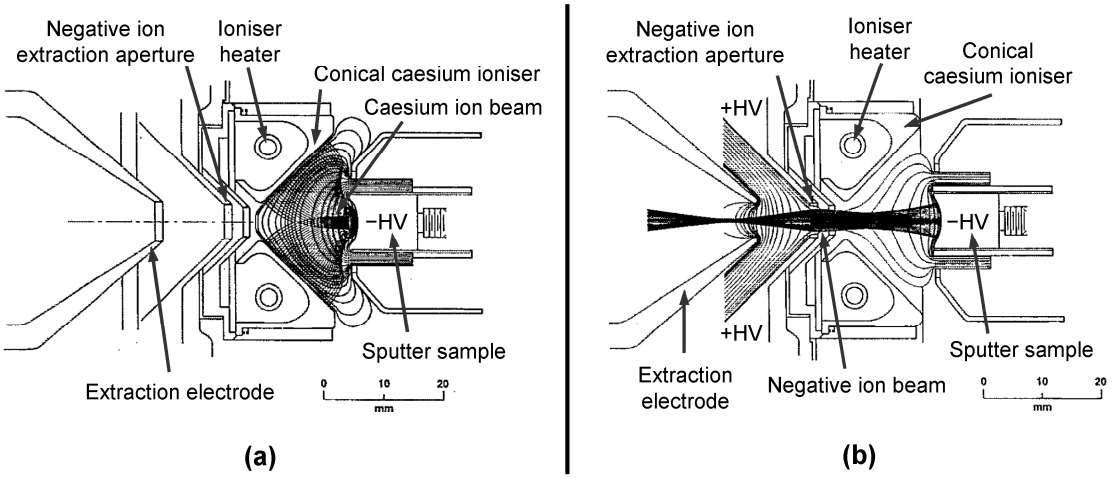

Figure 1.4: Schematic of a sputtering source for the production of negative ions. (a) Trajectories of the high energy Cs^+ beam, produced from the ionisation of Cs atoms at the heated ioniser, which are accelerated towards the sputter sample by applying a high negative voltage to it (–HV). (b) Trajectory of the anion beam produced from the sputter sample, which has been accelerated away from the target and towards the extractor electrodes and apertures which have high positive voltages applied (+HV). Reprinted with permission from reference [105], Copyright 1994, American Institute of Physics.

then accelerated away from the sputter target with a high negative potential, through a series of extraction optics and apertures held at high positive voltages (Figure 1.4b), producing anion beams with currents on the order of mA and associated beam energies of ~20 keV [104,105]. However, these sources are generally more applicable to the study of atomic and small molecular anions. Similarly, electric discharge sources have also proved to be useful for the generation of small molecular anions [106-110]. In these sources, a fine needle and a counter electrode containing the solid sample, have a high potential difference applied between them (~4 kV), leading to the production of a corona discharge, which subsequently vaporises and ionises the solid sample [106]. Unfortunately, anion beam intensities produced using this method are known to be in the nA regime [78], significantly less than alternative sputtering sources, although more modern discharge sources have begun to improve on this [109].

In general however, it becomes non-trivial to generate large molecular anions *via* hard ionisation processes, due to the large amounts of excess internal energy imparted to the molecule during ionisation. As a result a large portion of parent anions undergo rapid fragmentation, while those that are successfully formed often possess vibrational temperatures on the order of ~10^3 K [78], which significantly complicates spectroscopic measurements. In order to avoid the latter scenario one must consider the addition of cryogenic buffer gas cooling systems [111].

1.2.3 Electrospray Ionisation: A Solution for the Gas Phase

An alternative approach to forming large gas phase anions is to consider the application of 'soft ionisation' techniques [91]. Such techniques are generally defined as methods which induce minimal parent ion fragmentation and generally involve the transmission of anions directly from the condensed phased into a vacuum environment. This class of ionisation methods include techniques such as matrix-assisted laser desorption ionisation (MALDI) [112-115], where an organic matrix containing the anions of interest is irradiated by a laser tuned to the matrix absorption wavelength, causing the subsequent desorption of parent anions.

One of the most widely used soft ionisation techniques to date is electrospray ionisation (ESI) [116] and was first proposed as a viable source for gas phase ions in 1968 by Dole and co-workers [117]. However, the true potential of ESI was not realised

until a number of years later in 1984 by Fenn and co-workers, when they demonstrated its application to studying the electron detachment dynamics of negative ion species through mass spectrometry [118,119]. From this study he aptly concludes that,

"*…we plan to pursue what we think are very exciting opportunities for studying the photodetachment of electrons bound to complex molecules. Many other possibilities will doubtless occur to investigators interested in the chemistry and physics of negative ions.*"

Since these provisional studies into the ESI technique were performed, Fenn and co-workers have developed ESI into an invaluable tool for studying a vast class of large molecular ions, where it has proved to be particularly prevalent for mass spectrometry studies of proteins and biomolecules. For developing and furthering the ESI methodology, Fenn was subsequently awarded a share of the Chemistry Nobel Prize in 2002, where he gave a Nobel lecture entitled, "*Electrospray Wings for Molecular Elephants*" [120], truly emphasising it as the ideal approach for producing a wide range of large molecular anions in the gas phase.

ESI not only has the benefit of producing large gas phase anions in a soft manner but it also has a number of additional advantages. The method allows one to freely generate multiply charged anion species, provided they are stable as isolated species, a feat unachievable with hard ionisation techniques due to the Coulombic repulsion experienced during multiple electron attachment. It is this versatility which has made ESI sources so widely used in the discipline of mass spectrometry. Secondly, as anions are inherently derived from a solution phase environment, ESI also leads to the production of micro-solvated species [121-123].

General Principles of Electrospray Ionisation

A general schematic for an ESI source is represented in Figure 1.5a. A solution containing the molecular anions of interest, usually with a concentration in the range of 10^{-3} – 10^{-6} M, is flowed through a fine metal capillary with a high negative voltage applied to it, V_{ESI}. As a consequence of the high negative voltage being applied to the small capillary, a large electric field, E_{ESI}, is induced at the capillary exit, the magnitude of which can be quantified using [124,125]

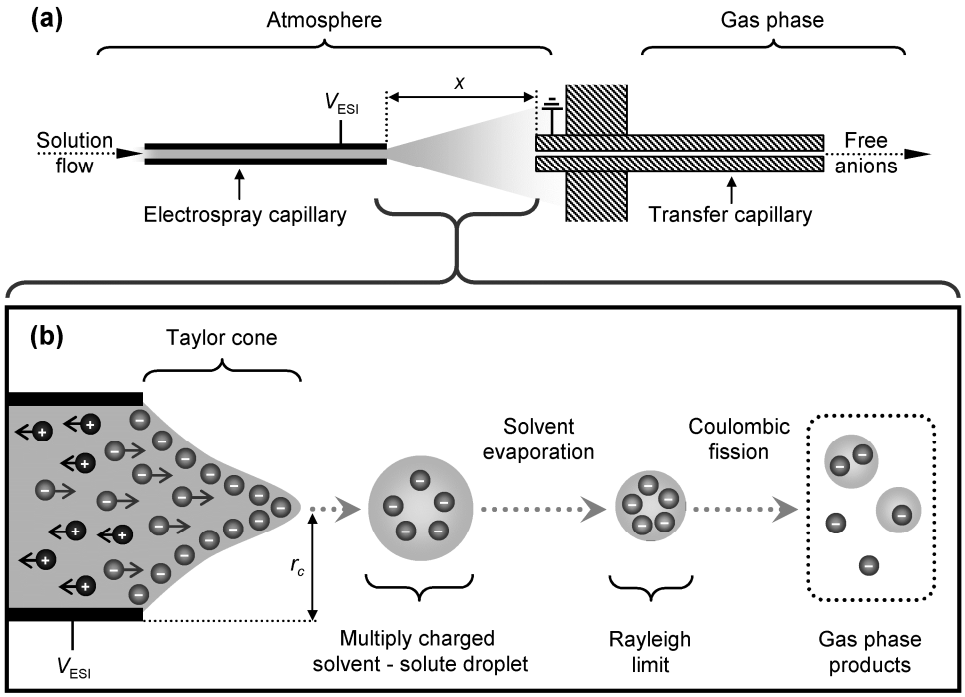

Figure 1.5: (a) Schematic of an electrospray ionisation (ESI) source. A solution of solute anions is followed through a fine electrospray needle placed at a negative high voltage (V_{ESI}) producing a spray of highly charged droplets. These flow towards the electrically grounded inlet of a metal transfer capillary, place at a distance x away from the electrospray tip, which acts as the interface to the gas phase. (b) Primary processes occurring in electrospray droplet evolution. r_c is the outer radius of the ESI capillary.

$$E_{ESI} = \frac{2V_{ESI}}{r_c \ln\left(4x/r_c\right)}, \tag{1.3}$$

where r_c is the outer radius of the electrospray capillary and x is the distance from the capillary tip to the entrance of the transfer capillary. This electric field in turn produces a dipolar layer at the meniscus of the solution [125-128], the origins of which can be understood more clearly when one considers the electrospray arrangement as a special type of electrolytic cell [129], which gives rise to an excess of negative ions at the solvent-air interface through an electrolysis process at the capillary aperture, whilst simultaneously removing cations. These excess negative ions lead to a distortion of the solution surface, producing a Taylor cone shown schematically in Figure 1.5b [130]. When E_{ESI} is large enough the repulsive space-charge effects between the surface anions becomes greater than the surface tension, yielding a jet of highly charged liquid droplets, containing the solute anions. This onset field, E_{on}, can be calculated using the

relationship [126]

$$E_{\text{on}} = \sqrt{\frac{2\gamma_{\text{s}} \cos\theta}{\varepsilon_0 r_{\text{c}}}}\,, \tag{1.4}$$

where γ_{s} is the surface tension of the solvent (in N m^{-1}), θ is the half-angle of the Taylor cone ($\theta = 49.3^{\text{o}}$ from [130]) and ε_0 is the permittivity of free space (ε_0 = 8.8 × 10^{-12} J^{-1} C^2 m^{-1}). One can in turn determine the potential required for electrospray onset, V_{on}, by combining equations (1.3) and (1.4) to arrive at the relationship

$$V_{\text{on}} = \ln\left(\frac{4x}{r_{\text{c}}}\right)\sqrt{\frac{r_{\text{c}}\gamma_{\text{s}} \cos\theta}{2\varepsilon_0}}\,, \tag{1.5}$$

which indicates that the minimum V_{ESI} required for electrospray is proportional to the surface tension of the solvent utilised. Common solvents used in electrospray experiments are methanol and acetonitrile, which have γ_{s} values of 2.3 × 10^{-2} and 3.0 × 10^{-2} N m^{-1}, respectively. Assuming values of r_{c} = 1 × 10^{-4} m and x = 4 × 10^{-2} m, V_{on} values of –2.2 and –2.5 kV are obtained for methanol and acetonitrile, respectively. It is important to note that, solvents with comparatively large γ_{s} values, such as water, are inadequate for electrospray, as V_{on} becomes large enough that undesired electric discharges occur before a stable spray can be produced ($V_{\text{on}}\left(\text{H}_2\text{O}\right)$ ≈ –4 kV for the conditions described above). However, recent methods have begun to be developed to alleviate this problem [131].

The aerosol of charged droplets produced from the ESI source generally produces ion currents, I_{ESI}, on the order of μAs at atmosphere [132,133]. To a first approximation, I_{ESI} tends to increase as the conductivity, κ, and the flow rate of the solution through the electrospray capillary, ρ, increase, such that [125,128]

$$I_{\text{ESI}} \propto \left(\rho\kappa\right)^n, \tag{1.6}$$

where n < 0.5 and κ is directly proportional to the concentration of the solution, C, in the limit of low concentration (C < 0.1 M); $\kappa \propto C$. However, the observed current of

anions transmitted into the gas phase through the transfer capillary is not inherently related to I_{ESI}, but instead bears a dependence on the size of the charged droplets formed from the electrospray source [116,132]. Smaller droplets, which are generated at lower values of ρ, tend to produce more isolated molecular anions is the gas phase.

Electrospray Droplet Evolution

As the multiply charged solvent-solute droplets migrate towards the transfer capillary, shown in Figure 1.5b, solvent evaporation begins to occur as a result of frictional heating from the surrounding air molecules [134]. Evaporation continues until the droplet size becomes sufficiently small that the repulsive forces between the anions become comparable to the force resulting from the surface tension of the droplet, a process which usually occurs over ~10^2 μs [135]. This stage of the droplet evolution is known as the Rayleigh limit and is formally defined by [136]

$$q_{Ry} = 8\pi\sqrt{\varepsilon_0 \gamma_s R^3}\,, \tag{1.7}$$

where q_{Ry} is the total charge of the droplet and R is its radius. When droplet sizes approach the Rayleigh limit, they undergo Coulombic fission, producing daughter droplets. Such fission processes tend to produce a number of small daughter droplets (~20) an order magnitude smaller in radius than those of the parent. Theories proposed by Dole and Röllgen [117] suggest that this process of solvent evaporation from the parent and daughter droplets continues in a sequential manner until it ultimately leads to the production of isolated anions. Contrary to this, an early rival theory of 'ion evaporation' put forward by Iribarne and Thomson [137] proposes that for droplets where R < 10 nm, produced following solvent evaporation, direct emission of anions from droplets occurs. However, mass spectrometric measurements indicate that either of these processes is plausible and the debate between them remains ongoing.

The final gas phase anions produced from droplet evolution include isolated molecular anions, small molecular clusters and micro-solvated species, with their product distributions ultimately depending on a wide range of experimental parameters. With careful instrument design and the implementation of ion focusing devices, one can

obtain ion currents on the order of pA's for performing laser spectroscopy [133,138], which is significantly lower than the number densities attainable in many neutral molecular beam experiments. These aspects of ESI instruments are considered in greater detail in Chapter 2. ESI sources do however have the benefit of generating molecular anions with a well defined internal temperature of 298 K, achieved *via* thermal equilibration with surrounding air molecules during droplet evolution. Although this internal temperature is relatively high compared to molecular beam techniques, this can be readily reduced using buffer gas cooling techniques in ion traps. This has most recently been demonstrated by the Wang group [139], who have successfully coupled their ESI source and cryogenically cooled ion trap (10 K) to a photoelectron analyser for performing photoelectron spectroscopy, evidencing that ESI techniques can readily be used as a source for studying the spectroscopy of large molecular anions in the gas phase.

1.3 Femtosecond Time-resolved Photoelectron Spectroscopy

Having discussed the methodologies utilised in gas phase spectroscopy, and more specifically ESI as an ideal method for the generation of isolated gas phase anions, we now move on to explore the concepts of femtosecond spectroscopy as a method for monitoring the ultrafast chemical dynamics of molecular anions in the gas phase. We begin by discussing the principles of forming excited states with ultrashort laser pulses and then progress to discuss how the excited state dynamics are probed using time-resolved photoelectron spectroscopy (TRPES).

1.3.1 Principles of Excitation with Femtosecond Laser Pulses

In Section 1.1 we briefly described how femtosecond spectroscopy utilises a pump-probe methodology, where the first key step is the interaction of an ultrashort pump laser pulse with the system of interest, resulting in the preparation of an excited state. To understand the behaviour of the prepared excited state in greater detail, we first consider the general principles of excitation with femtosecond laser pulses.

Wave Packets: Formation and General Principles

Due to the ultrashort temporal nature of femtosecond laser pulses, their associated energetic bandwidth becomes notably broad. For a transform limited ultrashort pulse, with a Gaussian temporal profile, the angular frequency bandwidth (in rads s^{-1}) at its full width at half maximum (FWHM), Ω, can be defined as [140]

$$\Omega = \frac{2\pi \cdot 0.44}{\Delta t}, \tag{1.8}$$

where Δt is the temporal width of the laser pulse in seconds. This characteristic of femtosecond pulses means that one tends not to excite a signal state but rather a coherent superposition of multiple eigenstates, $\left|\varphi_n^{\mathrm{e}}\right\rangle$, which defines the total time-dependent excited state wavefunction, $\Psi(Q,t)$, as schematically shown in Figure 1.6. The superposition of states, known as a *wave packet*, can be expressed as:

$$\Psi(Q,t) = \sum_n a_n \left|\varphi_n^{\mathrm{e}}\right\rangle \exp(-i\omega_n t), \tag{1.9}$$

where n are the eigenstates indexes for a sum which runs over all states, t is time and the angular frequencies of the excitation transitions, ω_n (in rads s^{-1}), are related to the frequency, ν, by $\omega = 2\pi\nu$. The co-efficients a_n describe the amplitudes and phases

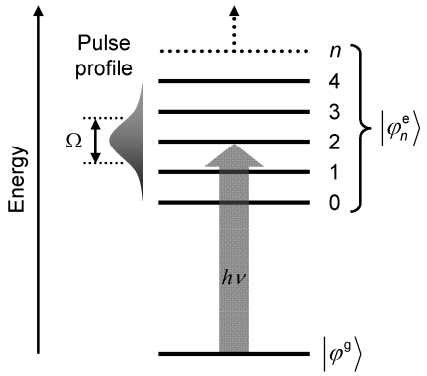

Figure 1.6: Schematic of an excitation process using an ultrashort femtosecond laser pulse, $h\nu$, with an associated angular frequency bandwidth, Ω. Excitation from the ground state, $\left|\varphi^{\mathrm{g}}\right\rangle$, leads to the production of an excited state wave packet, consisting of a superposition of n excited eigenstates, $\left|\varphi_n^{\mathrm{e}}\right\rangle$.

imparted to each $\left|\varphi_n^{\mathrm{e}}\right\rangle$ by the excitation laser pulse and can be written as

$$a_n = \left\langle \varphi_n^{\mathrm{e}} \left| \vec{\mu} \cdot \vec{E}_{\mathrm{pu}} \right| \varphi^{\mathrm{g}} \right\rangle, \tag{1.10}$$

where $\vec{\mu}$ is the transition dipole moment operator, $\vec{E}_{\mathrm{pu}}$ is the electric field vector of the pump laser pulse, and $\left|\varphi^{\mathrm{g}}\right\rangle$ is the ground eigenstate. One can then factor out the Gaussian envelope 'shape function', $g(\omega)$, associated within $\vec{E}_{\mathrm{pu}}$ so that equation (1.10) becomes

$$a_n = g(\omega) \left\langle \varphi_n^{\mathrm{e}} \left| \vec{\mu} \cdot \vec{E}_{\omega} \right| \varphi^{\mathrm{g}} \right\rangle, \tag{1.11}$$

where $\vec{E}_{\omega}$ is the remaining angular frequency component of the electric field vector and $g(\omega)$ is defined as

$$g(\omega) = \frac{1}{\sigma\sqrt{2\pi}} \exp\left(-\frac{\left[\omega - \omega_0\right]^2}{2\sigma^2} \right). \tag{1.12}$$

In equation (1.12) ω_0 is the centre angular frequency of the pump laser pulse and σ is related to Ω by $\Omega = 2\sqrt{2\ln 2}\,\sigma$.

The second term in equation (1.11) also defines the initial amplitudes of the individual $\left|\varphi_n^{\mathrm{e}}\right\rangle$ within the excited state superposition. For vibrational states, this can be understood in terms of the Franck-Condon principle, which describes the spatial overlap between the ground and excited state wavefunctions. By invoking the Born-Oppenheimer approximation the electronic and vibrational components in equation (1.11) can be separated to arrive at a formal definition of the Franck-Condon overlap:

$$f_n = \left\langle \varphi_n^{\mathrm{e}} \left| \varphi^{\mathrm{g}} \right\rangle, \tag{1.13}$$

where f_n are the Frank-Condon overlap factors for excited state vibrational states, $\left|\varphi_n^{\mathrm{e}}\right\rangle$, with the ground state vibrational state, $\left|\varphi^{\mathrm{g}}\right\rangle$.

Temporal Evolution of Vibrational Wave Packets

As the excited superposition of vibrational eigenstates is also time-dependent, the initially excited wave packet, $\Psi(Q,t=0)$, evolves along the spatial co-ordinate Q with time as a result of the different vibrational periods, T_n^{vib}, associated with each of the vibrational states:

$$T_n^{\text{vib}} = \frac{2\pi}{\omega_n}. \tag{1.14}$$

The exact nature of the wave packets temporal evolution can be understood in terms of a transformed variation of equation (1.9):

$$\Psi(Q,t) = \sum_n a_n \left|\varphi_n^{\text{e}}\right\rangle \left[\cos(\omega_n t) - i\sin(\omega_n t)\right], \tag{1.15}$$

where equation (1.15) has been arrived at using Euler's formula $e^{-i\theta} = \cos\theta - i\sin\theta$. By using further trigonometric identities, the sum of the cosine terms can be expressed in terms of difference frequencies, $\Delta\omega_n$, defined as $\Delta\omega_n = \omega_{n+1} - \omega_n$. The observable,

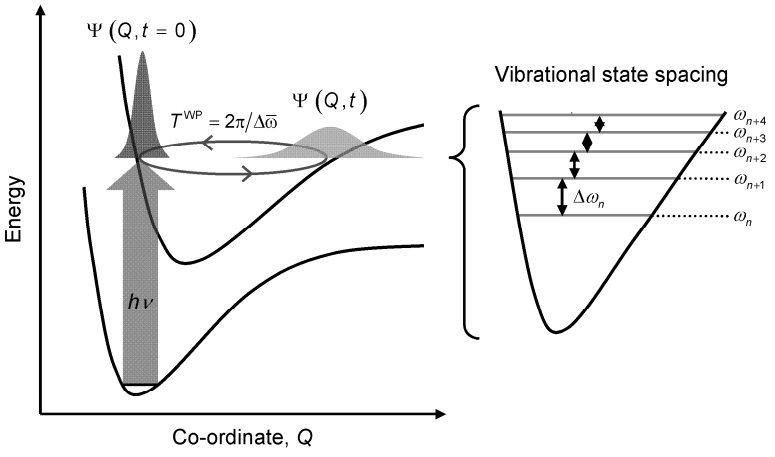

Figure 1.7: Temporal evolution of a vibrational wave packet formed on an excited electronic state potential. The initially excited wave packet, $\Psi(Q,t=0)$, evolves away from the classical inner turning point towards the outer turning point after a time *t*. The quasi-classical oscillation period of the wave packet is defined by T^{WP}. With time the wave packet, $\Psi(Q,t)$, spreads along the co-ordinate, *Q*. Also shown are the converging spacings, $\Delta\omega_n$, between the vibrational states due to anharmonicity, which results in the spatial spreading of the wave packet.

$\left|\Psi(Q,t)\right|^2$, which is the probability distribution of the wave packet at a given time, *t*, can be approximated as:

$$\left|\Psi(Q,t)\right|^2 \propto \cos(\Delta\bar{\omega}t), \tag{1.16}$$

where $\Delta\bar{\omega}$ is the average energy spacing between adjacent vibrational levels over the bandwidth of the laser pulse. Equation (1.16) shows that the wave packet oscillates on the excited electronic state potential in a quasi-classical manner, represented in Figure 1.7, with a characteristic frequency $\Delta\bar{\omega}$, or a period $T^{\mathrm{WP}} = 2\pi/\Delta\bar{\omega}$.

In equation (1.16) however, we have neglected higher order terms which arise from the anharmonicity in states across the excitation bandwidth. As different $\Delta\omega_n$ pairs beat at different frequencies, the wave packet will disperse along the co-ordinate *Q* and interfere with itself. Ultimately, with reference to Figure 1.7, the larger $\Delta\omega_n$ frequency differences (low *n*) will possess a shorter vibrational period, T_n^{vib}, than those with higher *n*. As time evolves, the larger $\Delta\omega_n$ pairs will therefore form the head of the wave packet and reach the classical outer turning point more rapidly than the smaller $\Delta\omega_n$, which form the wave packet tail. This results in the spatial smearing of the wave packet along the co-ordinate *Q*, and is a purely quantum mechanical effect with no inherent classical analogue.

1.3.2 Probing Excited State Wave Packets

Projection of Wave Packets onto Final States

Following the preparation of the excited state wave packet with an ultrashort pump pulse, a second ultrashort probe pulse interacting with the excited state at discrete time delays after this initial excitation process projects the temporally evolving wave packet, $\Psi(Q,t)$, onto final states, $\left|\varphi_n^{\mathrm{f}}\right\rangle$, which are accessible within the probe bandwidth. Probing the wave packet in this manner enables one to monitor its associated dynamics through the measurable signal, $S_n(t)$, obtained from pump-probe experiments, where each $S_n(t)$ is associated with projection onto an individual final state. When considering the projection of $\Psi(Q,t)$ onto a single final state, $\left|\varphi^{\mathrm{f}}\right\rangle$, we may write

$$S_n(t) = \left| \left\langle \varphi^{\mathrm{f}} \left| \vec{\mu} \cdot \vec{E}_{\mathrm{pr}} \right| \Psi(Q,t) \right\rangle \right|^2, \tag{1.17}$$

where $\vec{E}_{\mathrm{pr}}$ is the electric field vector of the probe pulse. With reference to equation (1.17) and recalling from equation (1.16) that $\left|\Psi(Q,t)\right|^2 \propto \cos(\Delta\bar{\omega}t)$, we may expect that as a function of time, *t*, the observed signal $S_n(t)$ will exhibit an oscillation with a characteristic frequency $\Delta\bar{\omega}$. Experimentally, $\Delta\bar{\omega}$ may present itself as a modulation in the signal amplitudes of the complete time domain spectrum, as exemplified by the gas phase experiments on NaI (Section 1.1) [1,5,6]. It is these modulations which ultimately provide the detailed information regarding the excited state wave packet dynamics, as well as the temporal evolution of the system under interrogation.

Choice of Final States and Detection Methods

The choice of final states onto which to the probe projects the wave packet is particularly important, as different final states possess differing overlaps with the excited state wave packet. Choosing an appropriate final set of states often helps to accentuate the dynamics one wishes to observe. However, as the probe pulse is also broad in energy, generally a number of $\left|\varphi_n^{\mathrm{f}}\right\rangle$ are accessible within the probe laser bandwidth. It is therefore important that one not only gives consideration to the final states, but also the methodology used to probe the wave packet dynamics. These can be classified into two categories: *integral* methods and *differential* methods. The former, which includes methods such as ion yield measurements, are inappropriate for observing the wave packet oscillations as the signal measured during the experiment is $S(t) = \sum S_n(t)$, and the dynamical information about $\Psi(Q,t)$ is lost by monitoring all $S_n(t)$ simultaneously because of the varying overlap of the probe pulse with individual $\left|\varphi_n^{\mathrm{f}}\right\rangle$. Differential methods generate a measurable signal described by equation (1.17) and include techniques such as photoelectron spectroscopy (PES). These methods are required for the detection of wave packet dynamics as they monitor the overlap of $\Psi(Q,t)$ with *individual* final states.

The differences between these two methods is elegantly exemplified by the excited state dynamics of the Na dimer [142], shown in Figure 1.8, where a vibrational wave packet is prepared on the $2^1\Pi_{\mathrm{g}}$ state and its subsequent dynamics are probed

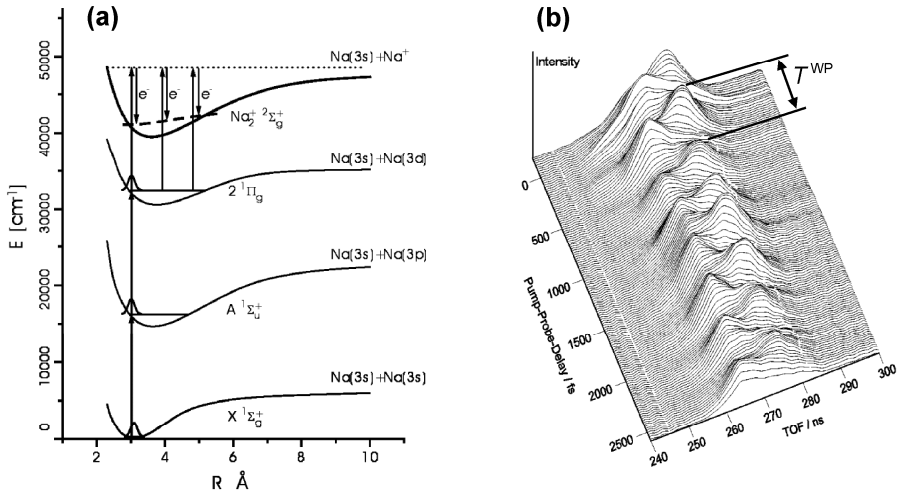

Figure 1.8: (a) Electronic state potentials of the neutral Na dimer and its associated cation state. The neutral is pumped to the $2\,^1\Pi_g$ state with two photons each at 618 nm. The excited state wave packet is subsequently probed using a time delayed ultrashort probe pulse (618 nm) to generate $Na_2^+\left(^2\Sigma_g^+\right)$ and a free photoelectron. (b) Time-resolved photoelectron spectra obtained from these experiments, which clearly indicates the wave packet oscillation period, T^{WP}, *via* the modulation in measured photoelectron kinetic energy, *eKE*, ($TOF \propto 1/\sqrt{eKE}$). Reprinted with permission from reference [142]. Copyright 1996, American Physical Society.

using PES. Here the final states are defined as $\left|\varphi_n^f\right\rangle = Na_2^+\left(^2\Sigma_g^+\left(v=n\right)\right)+e_n^-$, where n corresponds to pairs of cation vibrational states and electron kinetic energies. Integral based ion yield measurements of the cation products cannot resolve individual $Na_2^+\left(^2\Sigma_g^+\left(v=n\right)\right)$ as all Na_2^+ products are measured simultaneously, resulting in a constant ion signal measurement and a loss of information regarding the wave packet motion. Conversely, PES measurements readily resolve the different e_n^- as a function of their kinetic energies, and the modulations shown in the measured photoelectron energy spectra as a function of pump-probe delay (Figure 1.8b) intricately reflect the oscillation period of the wave packet dynamics, due to the time varying Franck-Condon overlap between different $\left|\varphi_n^f\right\rangle$ and $\Psi\left(Q,t\right)$.

1.3.3 Time-resolved Photoelectron Spectroscopy

General Principles of Photoelectron Spectroscopy

PES is one the most versatile methodologies used to probe the ultrafast chemical dynamics in pump-probe experiments [141,143-146], and is a direct extension of the

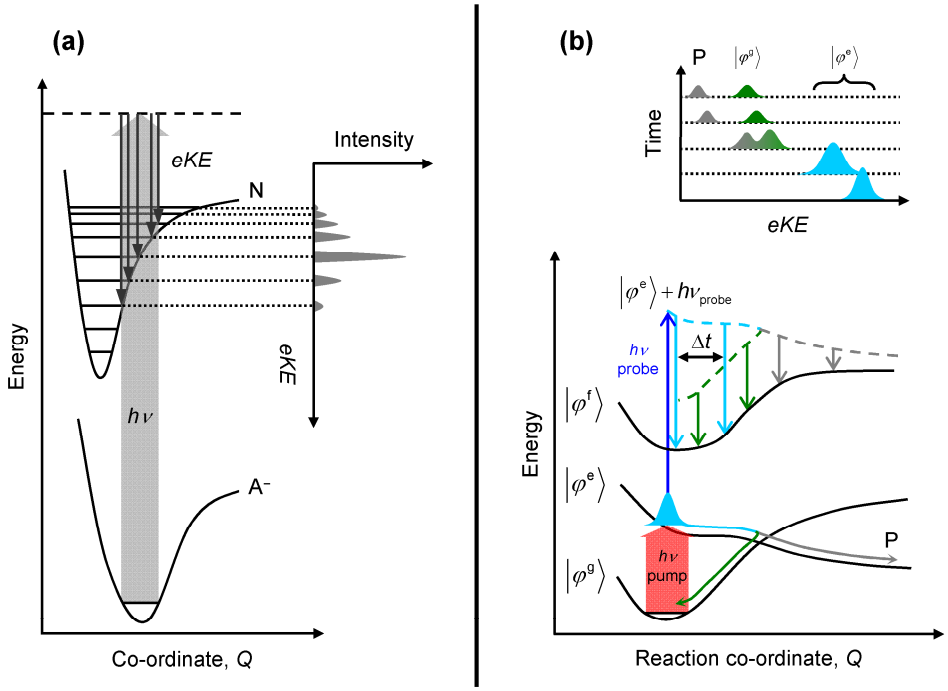

Figure 1.9: (a) Schematic of one-colour electron photodetachment from an anionic species, A^-, to form the associated neutral species, N, and photoelectrons with kinetic energies, *eKE*. Shown inset is the associated photoelectron spectrum generated from this process. (b) Schematic of a TRPES experiment. A pump pulse transfers population from the ground state, $|\varphi^g\rangle$, to form a wave packet on the excited state, $|\varphi^e\rangle$, at $t = 0$. A probe pulse subsequently detaches electrons from the system at discrete time delays after excitation, Δt, and their associated *eKE*s are measured (downward arrows). The time-resolved photoelectron spectra (shown above) correlate to the evolution of the excited state wave packet along the reaction co-ordinate, Q, where it can either evolve to form products, P (grey arrow and signals), or internally covert back to the ground state (green arrow and signals).

photoelectric effect, a theory for which Einstein was awarded the Physics Nobel prize in 1921. The theory states that if a sample absorbs a photon of light, $h\nu$, with sufficient energy then the sample will emit an electron. Conservation of energy defines that the kinetic energy of the ejected photoelectron, *eKE*, must be equivalent to the difference between the energy of the absorbed photon and the binding energy of the electron to the sample, E_{BE}:

$$eKE = h\nu - E_{BE}\,. \tag{1.18}$$

In PES it is this *eKE* which is measured using an appropriate detection arrangement, ultimately producing a desired photoelectron spectrum, where the signal intensities are governed by Franck-Condon overlaps and the photodetachment cross-sections. This is

schematically shown in Figure 1.9a for electron photodetachment from an anion. In the case of molecular species this relationship enables one to translate measured *eKE*s into vertical binding energies, E_{VBE}, which are defined as the energy differences between the final states, E^{f}, and the initial state, E^{i}, at the geometry of the initial state, Q^{i}:

$$E_{\mathrm{VBE}} = E^{\mathrm{f}}\left(Q^{\mathrm{i}}\right) - E^{\mathrm{i}}\left(Q^{\mathrm{i}}\right). \tag{1.19}$$

In its time-resolved variant, TRPES, the ultrashort probe pulse projects a temporally evolving excited state wave packet onto final states. Repeating the pump-probe process at a number of different time delays, Δt, leads to the generation of a series of time-evolving photoelectron spectra, where the temporal changes in *eKE* signals reflect the ultrafast dynamics of the wave packet on the excited and ground state potentials (see Figure 1.9b).

PES has a number of additional benefits over other detection methodologies. In particular, it has relaxed selection rules relative to optical detection techniques such as laser induced fluorescence, enabling both 'bright' and 'dark' states to be probed. As ionisation/electron detachment is uninhibited by Frank-Condon restrictions (provided the ionising/detachment photon has sufficient energy) and spin conservation, PES is able to probe the entirety of the reaction co-ordinate, provided the dynamics go to completion within the temporal limits of the experiment (commonly on the order of nanoseconds). This is particularly pertinent for studies conducted on anions, as the excess electron is bound by a sufficiently low energy that a single probe photon in the ultraviolet (UV) energy regime can be used to probe the dynamics occurring on both the ground and excited states simultaneously [51,87-89], as schematically shown in Figure 1.9b. However this is not the case for neutrals, as single UV photons are not sufficient to ionise neutral species from their ground states and so one loses track of the dynamics as the system relaxes. Analogous one photon probing methods are however beginning to be developed for TRPES studies on neutral species, using high harmonic generation (HHG) methods to produce photon energies in the vacuum and extreme UV (VUV and EUV, respectively) energy regimes [147,148], capable of ionising neutrals with a single photon.

Selection Rules: Koopmans' Correlations

Although PES has comparatively relaxed selection rules, the final states generated following photodetachment must be accessible within Koopmans' theorem [149], which states that the electronic configuration of the final state must remain unaltered from the initial state configuration with the photodetached electron removed. The rule originates from the fact that the ionisation/photodetachment process is fast relative to the time it takes for any of the remaining 'core' electrons to rearrange, hence, the final electronic configuration is fixed during photodetachment. This is shown schematically in Figure 1.10, where excitation from $\left|\varphi^{g}\right\rangle$ to $\left|\varphi^{e}\right\rangle$ is induced by an ultrashort pump pulse promoting an electron into the highest occupied molecular orbital (HOMO) from the HOMO–1 orbital. Photodetachment subsequently occurs from the HOMO in $\left|\varphi^{e}\right\rangle$ to form the excited final state $\left|\varphi_2^{f}\right\rangle$. However, the final state $\left|\varphi_1^{f}\right\rangle$ is not accessible within Koopmans' picture and so only eKE_2 is observed in the resultant photoelectron spectrum.

This correlation between initial states and final states, known as Koopmans' correlations, has in recent years proved to be particularly insightful in discerning the timescales of ultrafast dynamics [141,144,145], as these correlations can have the effect of producing dramatic changes in the measured *eKE*s in the time-evolving photoelectron spectra. Such correlations were first proposed as a probe for monitoring the ultrafast dynamics between excited states by Domcke [150,151]. Later, Stolow and co-workers,

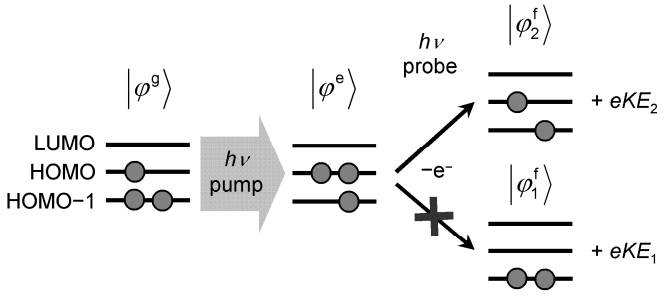

Figure 1.10: Schematic representation of Type I Koopmans' correlations. An initial pump pulse excites the system from its ground state, $\left|\varphi^{g}\right\rangle$, to an excited state, $\left|\varphi^{e}\right\rangle$. A second probe pulse subsequently detaches an electron from $\left|\varphi^{e}\right\rangle$ to form either $\left|\varphi_1^{f}\right\rangle$ or $\left|\varphi_2^{f}\right\rangle$, which are both accessible within the probe photon energy. However, detachment of an electron from the HOMO of $\left|\varphi^{e}\right\rangle$, can only lead to the formation of the final state $\left|\varphi_2^{f}\right\rangle$ in Koopmans' picture and so only eKE_2 will be observed in the resultant photoelectron spectrum.

for the first time, elegantly demonstrated the use of such correlations experimentally, by studying the ultrafast non-adiabatic dynamics occurring between the excited states of the neutral *all-trans*-decatetraene system and is discussed in greater detail in Section 1.4.1 [152].

Similar correlations for untangling dynamics can also be made *via* the vibronic overlap of the excited and final states, formally defined by the Franck-Condon factors and the photodetachment cross-sections. Such correlations are referred to as Koopmans' Type II, whereas the former described above are classed as Type I. Stolow and co-workers have also demonstrated the use of these Type II correlations to extract timescales for ultrafast internal conversion dynamics [17], although the general applicability of Type II correlations for extracting such timescales can be restricted for many systems due to the broad envelope of final states accessible within the energy bandwidth of the probe.

Symmetry Considerations: Origins of Photoelectron Angular Distributions

To fully characterise the photodetachment/photoionisation events which occur in PES, one must also give consideration to the symmetries of the individual components involved in process [146,153,154]. Specifically taking the case of photodetachment from molecular anions, the final symmetry of the photodetachment event must be conserved such that the cross product $(\otimes)$ of each of the individual symmetry components (defined by molecular group theory) involved in the process must contain the totally symmetric irreducible representation, Γ_{TS}, of the point group to which the system belongs. This symmetry conservation can be formally expressed as:

$$\Gamma\left(\varphi^{e}\right)\otimes\Gamma\left(\mu_{i}\right)\otimes\Gamma\left(\varphi^{f}\right)\otimes\Gamma\left(e^{-}\right)\supseteq\Gamma_{TS}, \tag{1.20}$$

where $\Gamma\left(\varphi^{e}\right)$, $\Gamma\left(\mu_{i}\right)$ and $\Gamma\left(\varphi^{f}\right)$ are the symmetries of the excited anion state, transition dipole moment and final neutral state, respectively. In the photodetachment process, photoelectrons are ejected on the surface of a radial expanding sphere with some distribution as a function of the angle relative to the laser polarisation vector, relating to the photoelectron wave function. The final symmetry term in equation (1.20),

$\Gamma(e^-)$, corresponds to the symmetry of the outgoing photoelectron wave, and experimentally this will define the photoelectron angular distributions (PADs). Provided one utilises a detection methodology that preserves this angular distribution [146], PADs can be used to provide an additional level of information from PES experiments, enabling one to extrapolate information regarding the orbitals from which detachment occurs in the case of small molecular species [81,146,153-155]. From the perspective of TRPES experiments on larger molecular species, if $\Gamma(\varphi^e)$ changes during the course of the wave packet evolution, then the resultant $\Gamma(e^-)$ can potentially alter leading to a change in the observed PADs as a function of time [156-158]. Such time-resolved PADs have begun to be used to greater effect in recent years and have most recently been used to directly extract timescales for non-adiabatic processes in molecular anions [159], which is described in Chapter 5 of this thesis.

1.4 Applications of Time-resolved Photoelectron Spectroscopy

Having covered the fundamental principles surrounding femtosecond TRPES experiments we now move on to discuss the applications of this experimental methodology. TRPES experiments have been applied to the study of ultrafast dynamics in a wide range of molecular systems and a number of comprehensive reviews have been published on the topic [141,143-145]. Here we focus on presenting a brief overview of some of some the most significant of these studies as well as those which bear particular relevance to the work presented in this thesis.

1.4.1 Discerning Ultrafast Non-adiabatic Dynamics

TRPES experiments have been particularly prominent in furthering the understanding of ultrafast non-adiabatic dynamics [160], which occur as a result of a break down of the Born-Oppenheimer approximation near electronic state crossing, enabling a coupling of vibrational modes with the electronic motions. When this occurs, rapid internal conversion (IC) between electronic potential surfaces is often observed. Such processes can play a particularly pivotal role in the ultrafast excited state dynamics of larger molecular systems where electronic and vibrational degrees of freedom can become rapidly entangled [161,162]. Of particular significance is the role non-adiabatic

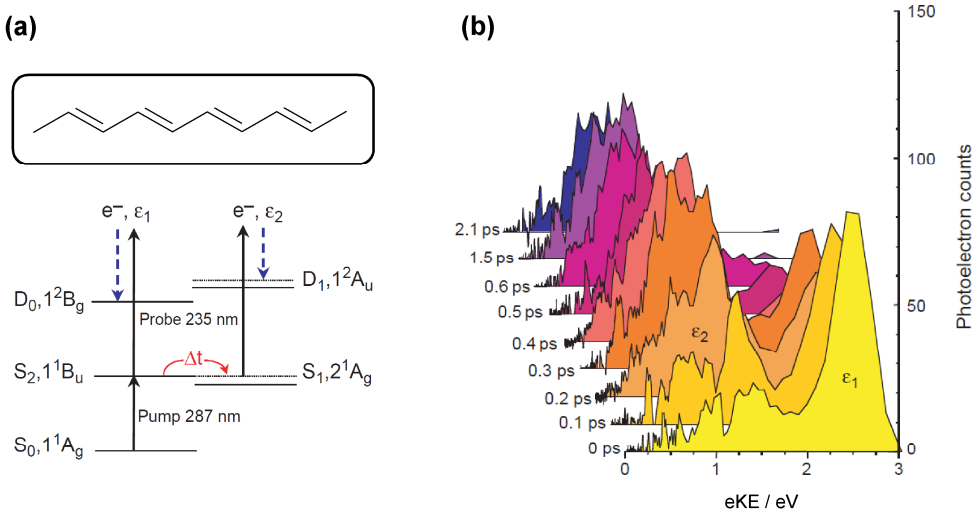

Figure 1.11: (a) State energy level diagram for the singlet states (S_n, n = 0,1,2) of neutral *all-trans*-decatetraene (*at*DT). Also shown are the first two doublet cation states, D_0 and D_1. A 287 nm (4.3 eV) pump pulse excites the S_2 state, while a second temporally delayed (Δt) probe pulse (235 nm, 5.25 eV) monitors the internal conversion from S_2 to S_1, generating *eKE* features ε_1 and ε_2. Shown inset above is the molecular structure of *at*DT. (b) Time-resolved photoelectron spectra of *at*DT when pumped and probed at 4.3 eV and 5.25 eV, respectively. Adapted by permission from Macmillan Publishers Ltd: *Nature*, reference [152], copyright 1999.

processes play in the ultrafast photo-dynamics of many biomolecules and protein chromophores such as DNA bases [27-33], amino acids [35], rhodopsin [83], and the photoactive yellow protein [36] to name a small selection.

An early highlighting example of such studies can be found in the work of Stolow and co-workers, where Type I Koopmans' correlations have been used to unravel the ultrafast dynamics occurring in the *all-trans*-decetetraene (*at*DT) molecule, shown inset in Figure 1.11a [152]. The dynamics of polyene species are particularly interesting as they represent excellent 'model' systems for the conjugated polyene groups of the chromophore in the rhodopsin protein [83,163]. In these experiments, *at*DT is excited from its S_0 (^1A_g) ground state to the electronic origin of the optically accessible S_2 (1^1B_u) state using a 287 nm (4.3 eV) pump pulse. The excited *at*DT system is subsequently probed using a 235 nm (5.25 eV) probe pulse. Non-adiabatic coupling *via* a vibrational mode of b_u symmetry leads to the S_2 state internally converting to a vibrationally hot S_1 (2^1A_g) state, which is optically inaccessible from the S_0 state as this transition is dipole forbidden. As the S_2 state correlates to the ground D_0 cation state in Koopmans' picture and S_1 to the D_1 excited cation state, one observes distinct changes in the temporally evolving photoelectron spectra. Figure 1.11b shows the time-resolved

spectra, where at t = 0 the dominant *eKE* feature at 2.5 eV (ε_1), corresponds to detachment from the neutral S_2 state. As time evolves (Δt) a broader feature centred at lower *eKE* (ε_2) can be seen to increase in amplitude and correlates to the $S_1 \rightarrow D_1 + e^-$ detachment process. These mirrored dynamics are characteristic of IC between two states, in this case occurring between S_2 and S_1. Integration of the signal in features ε_1 and ε_2 followed by fitting to an exponential decay and rise, respectively, enabled Stolow and co-workers to extract a time-scale for IC of $\tau_{IC} \approx 390$ fs.

Such experiments elegantly demonstrate the detailed insights into ultrafast dynamics one can obtain with the aid of Koopmans' correlations in TRPES experiments. However, such correlations can be less forthcoming when studying larger molecular systems, as photoelectron features can become significantly broader in energy due to larger Franck-Condon envelopes for electron detachment. Stolow and co-workers have demonstrated that in particularly favourable systems, varying vibrational overlaps to detachment can in principle be used to unravel non-adiabatic processes (Koopmans' Type II) [17]. However, extracting dynamics from such systems can become more abstract, particularly if convoluted spectral features possess similar detachment cross-sections, resulting in negligible temporal signal changes. In Chapter 5 we explore this scenario in greater detail and discuss how time-resolved PADs can be used to untangle ultrafast dynamics.

1.4.2 Investigations of Micro-solvation

Numerous TRPES experiments have been conducted on negatively charged solvent-solute clusters in the gas phase, allowing one to probe the onset of solution phase behaviour [50,51,143]. Studies by the Neumark group present classic examples of such experiments, where the excited state dissociation dynamics of homonuclear halogen dimer anions solvated by Ar atoms [57] and CO_2 molecules [58] ($X_2^-(Ar)_n$ and $X_2^-(CO_2)_n$, respectively) have been interrogated using TRPES. These experiments were prompted by precursor ion yield experiments carried out by Lineberger and co-workers, which monitored variations in the dissociation dynamics of $X_2^-(CO_2)_n$ clusters as a function of increasing n [56,164]. However, unlike TRPES these methods are unable to monitor the excited state wave packet dynamics along the entire dissociative reaction co-ordinate, ultimately leading to a loss of information in the long

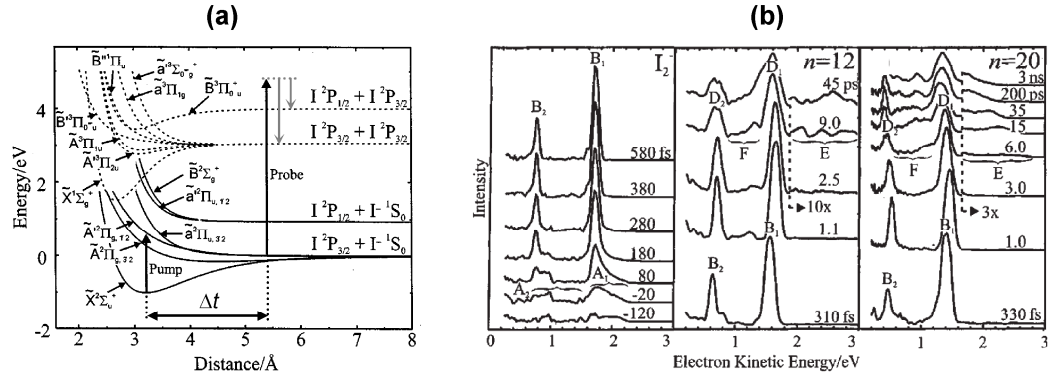

Figure 1.12: (a) Electronic potential energy surfaces of the I_2 anion (solid lines) and neutral I_2 (dashed lines). An ultrashort 780 nm (1.59 eV) pump pulse excites the I_2 anion into its $\tilde{A}'$ state. The subsequent dissociation dynamics are monitored using a time delayed 260 nm (4.74 eV) probe pulse as a function of increasing solvation number, *n*, when solvated with *n* Ar atoms. Photoelectron kinetic energies (downward grey arrows) generated at near complete dissociation, labelled B_1 and B_2 in (b), are also shown. (b) Time-resolved photoelectron spectra of the isolated I_2 anion (left) and the solvated species $I_2^-(Ar)_{12}$ and $I_2^-(Ar)_{20}$ (middle and right, respectively). Reprinted with permission from reference [57]. Copyright 1999, American Institute of Physics.

time dynamics.

Neumark and co-workers initially investigated the excited state dissociation of I_2^- solvated in Ar [57]. The electronic potential energy surfaces of isolated I_2^- are shown in Figure 1.12a, along with the pump-probe scheme used in the experiments. In bare I_2^- a 780 nm (1.58 eV) pump pulse initially forms an excited state wave packet on the dissociative $\tilde{A}'\left(^2\Pi_{g,1/2}\right)$ state, which is then monitored using a 260 nm (4.74 eV) probe pulse as the system evolves along the dissociative co-ordinate and produces isolated I^- $\left(^1S_0\right)$ and I $\left(^2P_{3/2}\right)$ products. At early times (*t* = 80 fs) the associated photoelectron spectrum (shown on the left in Figure 1.12b) shows two broad features, A_1 and A_2, which occur as a result of detachment from the transient $I_2^{-*}\left(\tilde{A}'\right)$. After 280 fs the excited state wave packet evolves to produce free I^- and I atoms, correlating to the two sharp features B_1 and B_2, which are characteristic of electron detachment from I^- producing neutral iodine in its two spin-orbit states, $^2P_{3/2}$ (B_1) and $^2P_{1/2}$ (B_2), separated by an energy of ~940 meV.

Upon solvation with 12 Ar atoms, $I_2^-(Ar)_{12}$, distinct changes in the temporal evolution of the photoelectron spectra are observed, which are shown in the middle panel of Figure 1.12b. Up until ~300 fs the photoelectron features described above evolve in a qualitatively similar manner as those observed in the unsolvated species,

although features B_1 and B_2 are red-shifted by ~150 meV. This is a direct result of the solvent-solute interaction energy between I^- and Ar, leading to a higher electron affinity. After 1 ps, features B_1 and B_2 evolve into the new broader features D_1 and D_2. These new signals arise from the detachment of electrons from I_2^{-*} in its weakly bound $\tilde{A}\left(^2\Pi_{g,3/2}\right)$ excited state to form neutral I_2 and are signatures of the recombination of the I^- and I fragments within the Ar solvent cluster. Such an effect, known as 'caging', is an inherent solution phase phenomena resulting from the interaction of the escaping dissociation products with the surrounding solvent molecules [165]. By studying the size evolution of these $I_2^-(Ar)_n$ species, Neumark and co-workers showed that the onset of caging behaviour is observed with as few as $n = 9$ Ar solvent atoms.

Recombination of the product atoms may also lead to the production of vibrationally hot ground state I_2^-, which is evidenced by the broad low intensity photoelectron features E and F for $t > 9$ ps. For $t > 45$ ps, no further temporal evolution of the photoelectron features is observed in the $I_2^-(Ar)_{12}$ species. However, for the larger $I_2^-(Ar)_{20}$ system, features E and F are seen to shift towards lower energies from 6 ps onwards, to as far out as 3 ns, and is indicative of vibrational cooling in the recombined ground state I_2^- chromophore. This is facilitated by the redistribution of the excess internal energy to the surrounding solvent cluster, and ultimately leads to the evaporation of Ar solvent atoms. This solvent evaporation process is unique to gas phase cluster species, and provides a window of insight into how energy redistribution is enabled by solvents in the bulk.

Analogous studies conducted on $I_2^-(CO_2)_n$ clusters were also compared to the results from $I_2^-(Ar)_n$ species [58]. Relative to the Ar solvent atoms, CO_2 solvent molecules have a much stronger interaction with the I_2^- chromophore. This enables the onset of caging dynamics to be observed at smaller cluster sizes ($n \geq 6$), and additionally leads a reduction in the observed recombination timescales. Comparative experiments such as these provide profound microscopic insights into how different solvents explicitly interact with solute molecules, interactions which can ultimately govern the outcome of a chemical reaction.

This and many other early femtosecond TRPES studies into micro-solvated species have since lead the way for many more gas phase investigations into a wide range of solvent mediated processes including charge delocalisation [166-168],

influences of solvation configurations on solute reactivity [62], and vibrational energy redistribution to solvents [59]. The most recent of these has been the observation of solvent-mediated electron transfer *via* a single CO_2 solvent molecule in the photo-dissociating IBr^- anion [169]. In isolated IBr^-, photo-induced dissociation along its $A'\left(^2\Pi_{1/2}\right)$ state exclusively generates I^- and Br as final products. However, these new studies conducted by Lineberger and co-workers show that following excitation to the weakly bound A' state, long range electron transfer (~7 Å) from I^- to Br may occur in the dissociating species across the bridging CO_2 solvent molecule on a timescale of 350 fs.

1.4.3 Electrospray Ionisation and Time-resolved Photoelectron Spectroscopy

In recent years there has be a greater drive to study the chemical dynamics of larger molecular species in the gas phase, particularly anions, which can be readily mass-separated using time-of-flight methods. From this perspective the coupling of ESI sources and photoelectron analysers has come into its own over the last decade. The wealth of spectroscopic information attainable from partnering these two experimental techniques was first demonstrated in the late 90s by the Wang group [138]. Since then, Wang and co-workers have recorded one-colour photoelectron spectra of numerous isolated molecular anions pertinent to organic, inorganic and biochemistry using nanosecond laser pulses, providing a plethora of new scientific understanding [170,171]. However, it has only been in the last few years that PES studies on ESI generated species have been logically extended into the time-domain. Here we briefly discuss the small ensemble of experiments which have to date interrogated the ultrafast dynamics of molecular anions produced *via* ESI using femtosecond TRPES.

Excited State Dynamics of the C_{60} Anion

Kappes and co-workers were the first to demonstrate femtosecond TRPES on large polyatomic anions generated through ESI [172]. In these experiments they monitored the ultrafast dynamics of the Buckminster-fullerene anion (C_{60}^-), following excitation from its ground state, $\tilde{X}^-\left(^2A_{2u}\right)$, to its second electronically excited state, $\tilde{B}^-\left(^2E_g\right)$, using a 775 nm (1.6 eV) pump pulse (see Figure 1.13a). Using a time-delayed 388 nm

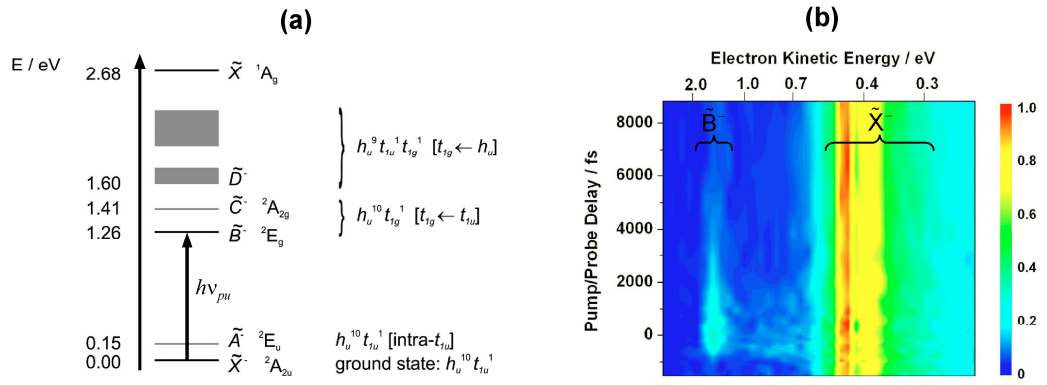

Figure 1.13: (a) State energy level diagram of C_{60}^- showing excitation from the ground state, $\tilde{X}^-$, to the second excited anion state, $\tilde{B}^-$, using an ultrashort pump pulse, $h\nu_{pu}$. Also shown is the vertical binding energy from the anion ground state to the neutral ground state, $\tilde{X}$. Valence molecular orbital configurations are shown on the right. (b) False-colour intensity plot showing the time-resolved photoelectron spectra of C_{60}^- obtained at pump and probe energies of 1.6 eV and 3.2 eV, respectively. Reprinted with permission from reference [172]. Copyright 2006, American Institute of Physics.

(3.2 eV) probe pulse, time-resolved photoelectron spectra were obtained, shown in Figure 1.13b as a false-colour intensity plot. Before t = 0, a single feature with an associated *eKE* of ~0.5 eV is observed, corresponding to the detachment of photoelectrons from the $\tilde{X}^-$ state. At t = 0, the spectra presents a new feature centred around an *eKE* value of ~1.6 eV, correlating to photoelectrons detached from the excited $\tilde{B}^-$ state. This excited state feature is observed to decay exponentially on a timescale of $\tau \approx 2.2$ ps, while the amplitude of the ground state feature is approximately time-independent, although one may have expected to observe some depletion around t = 0 due to a transfer of population from $\tilde{X}^-$ to $\tilde{B}^-$. The $1/\tau$ value corresponds to the rate of IC back to the ground state of the anion, with negligible IC observed to the excited $\tilde{A}^-\left(^2E_u\right)$ state as evidenced by the absence of additional photoelectron features at $t > 0$.

Ultrafast Dynamics of Multiply Charged Anions

Kappes and co-workers subsequently moved on to investigate the ultrafast dynamics of multiply charged anions (MCAs) [173,174]. Unlike species with only a single negative charge, isolated molecules possessing multiple excess charges often behave in a metastable manner, arising as a result of the delicate balance between repulsive long range ($e^- \cdots e^-$ interaction) and attractive short range ($\text{nuclear}^+ \cdots e^-$ interaction) electrostatic interactions. The resultant effect is the presence of a repulsive Coulomb

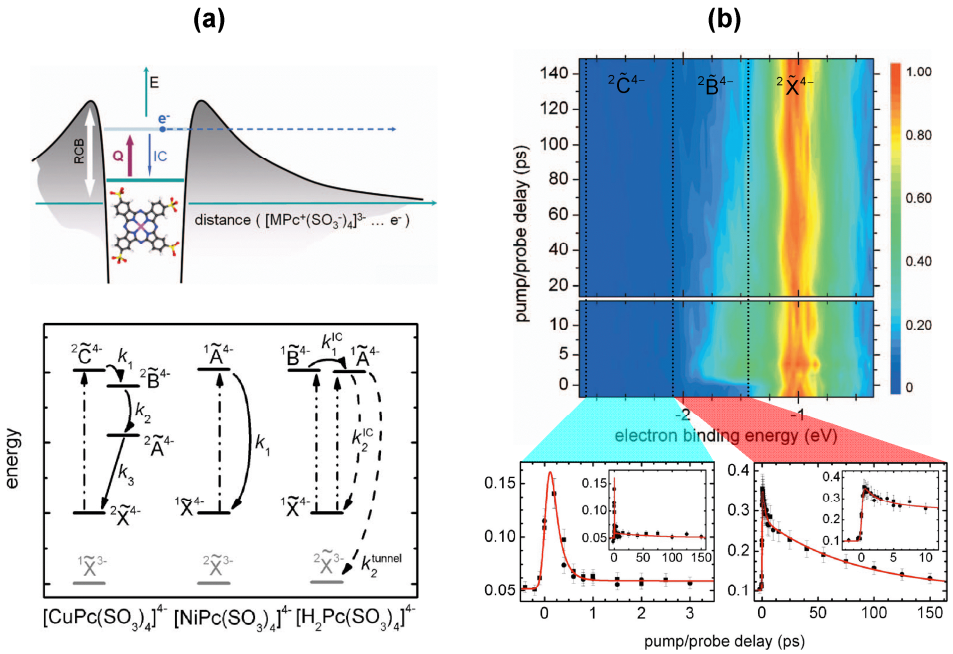

Figure 1.14: (a) Top: Schematic of the repulsive Coulomb barrier (RCB) along the $[MPc(SO_3)_4]^{3-}$ --- e^- co-ordinate. Also shown is the excitation from the metastable ground state to the Q band of the phorphyrin species, with the molecular structure of the copper containing species shown inset. Below are the molecular relaxation schemes observed for the Cu^{2+}, Ni^{2+} and free base (H_2) complexes. (b) Top: time-resolved photoelectron spectra of $[CuPc(SO_3)_4]^{4-}$ when pumped and probed at 1.6 eV and 3.2 eV, respectively. Bottom: integrated signal plots as a function of time for the $^2\tilde{C}^{4-}$ (left) and $^2\tilde{B}^{4-}$ (right) features, obtained over the electron binding energy ranges of –2.9 to –2.1 eV and –2.1 to –1.4 eV, respectively. Reprinted with permission from reference [173]. Copyright 2007, American Institute of Physics.

barrier (RCB), shown schematically at the top of Figure 1.14a. RCBs have the ability to drastically influence the molecular behaviour of MCAs, as exemplified by many of the early one-colour nanosecond PES studies conducted by Wang and co-workers, where they have observed processes such as excited state e^- tunnelling through the RCB, and even metastable MCAs which are able to store excess electronic energy as a result of their RCBs [171]. One of the classic examples known to display the latter of these phenomena are the metal containing phthalocyanine-tetrasulfonate tetra-anions, $[MPc(SO_3)_4]^{4-}$, with the Cu^{2+} containing species able to store an excess of 0.9 eV of energy, making it the most unstable MCA observed to date [175].

Prompted by these earlier studies, Kappes and co-workers first chose to investigate the ultrafast dynamics of a selection of $[MPc(SO_3)_4]^{4-}$ complexes, following excitation to their Q band absorption regions with a 775 nm (1.6 eV) pump pulse (see Figure 1.14a) [173]. The time-resolved photoelectron spectra measured for the

$[CuPc(SO_3)_4]^{4-}$ system are shown in Figure 1.14b (probe = 388 nm), which displays a single feature at a binding energy of –1 eV before $t < 0$ corresponding to detachment from its $^2\tilde{X}^{4-}$ ground state. Two new excited state features are observed at $t = 0$, observed in the binding energy ranges of –2.9 to –2.1 eV and –2.1 to –1.4 eV. The temporal evolution of these two features can be seen more clearly at the bottom of Figure 1.14b. The rapid decay of the low binding energy feature, followed by the concomitant rise of the higher binding energy feature on the same timescale is indicative of IC, which occurs from the excited $^2\tilde{C}^{4-}$ state to $^2\tilde{B}^{4-}$ on a timescale ≤250 fs (τ_1). The subsequent two-stage relaxation process to the ground state from the $^2\tilde{B}^{4-}$ state *via* the $^2\tilde{A}^{4-}$ is shown schematically in the bottom left panel of Figure 1.14a, and is confirmed by the bi-exponential decay of the higher binding energy feature with associated time constants of $\tau_2 \leq 250$ fs and $\tau_3 \approx 80$ ps, respectively ($k_n = 1/\tau_n$).

The ultrafast dynamics of the analogous Ni^{2+} containing and free base ($M = 2H^+$) species were also investigated, the former displaying comparatively simpler dynamics than the Cu^{2+} species, with its excited $^1\tilde{A}^{4-}$ state undergoing direct IC back to the $^1\tilde{X}^{4-}$ ground state in less than 250 fs (bottom middle panel, Figure 1.14a). The free base however, presents notably different dynamics. Following excitation to the $^1\tilde{B}^{4-}$ state IC to its near isoenergetic $^1\tilde{A}^{4-}$ state occurs in ~470 fs. Although, unlike the metal containing species the free base is also observed to undergo e^- tunnelling from the $^1\tilde{A}^{4-}$ state through the RCB to form the tri-anion in its ground state, $^2\tilde{X}^{3-}$ (bottom right, Figure 1.14a). This e^- tunnelling, which is in direct competition with IC back to $^1\tilde{X}^{4-}$ ground state, occurs on a timescale of ~70 ps with ~95 % of the $^1\tilde{A}^{4-}$ state population decaying in this manner.

The work of the Kappes group aptly demonstrates how ESI sources coupled with TRPES, provide a window of insight into the exotic dynamics occurring in MCAs. Most recently they have provided dynamical insights into Coulomb explosion processes occurring *via* excited state dissociation in the multiply charged $IrBr_6^{2-}$ species [174]. Upon excitation at 1.6 eV, they find that the excited state wave packet undergoes rapid IC to an intermediate state, enabling the molecule to dissociate over the RCB. As the resultant $IrBr_5^-$ and Br^- products are both negatively charged, the repulsive Coulomb interaction experienced by the fragments at short distances can be observed in the time-resolved photoelectron spectra as an energetic blue-shift of the characteristic *eKE* signal

of the Br^- photofragment, again highlighting how TRPES experiments are ideally suited to characterise these kinds of intriguing dynamics.

1.5 Overview of Thesis

In Chapter 1 we have provided the reader with an introduction to the fundamental concepts of gas phase spectroscopy and femtosecond time-resolved photoelectron spectroscopy experiments on gas phase anions. Specifically, we have described the recent innovations in these fields which have facilitated studies into larger molecular anions with the aid of electrospray ionisation sources, culminating with a glance into some of the more innovative and contemporary TRPES experiments performed in the past decade. In Chapter 2, we describe the development and construction of a new experiment for studying the spectroscopy and ultrafast dynamics of molecular anions, which utilises an electrospray ionisation source and an innovative new photoelectron imaging analyser for performing PES and TRPES. Data analysis of the acquired time-resolved photoelectron images is carried out using a newly developed image reconstruction algorithm, and Chapter 3 provides and in-depth description of this algorithm and the origins of the image reconstruction problem. Chapter 4 presents TRPES studies which have been carried out on the 7,7,8,8-tetracyanoquinodimethane (TCNQ) radical anion. In these pump-probe experiments we investigate the ultrafast non-adiabatic dynamics occurring between the first excited state of $TCNQ^-$ and its ground state. We also provide evidence for excited state wave packet dynamics. Following on from this, Chapter 5 then describes, for the first time, a new method for extracting ultrafast dynamical information from time-resolved PADs of isoenergetic photoelectron features; independent time-resolved features possessing the same or partially convoluted electron kinetic energies. To demonstrate this we utilise the time-resolved PADs observed in $TCNQ^-$ and extract time-scales for the non-adiabatic dynamics, and compare the results to the energetic analysis described in Chapter 4. We finally draw the thesis to a close with conclusions and present an outlook for future experiments in Chapter 6.

1.6 References

[1] A. H. Zewail, *J. Phys. Chem. A*, **104**, 5660 (2000).

[2] A. H. Zewail, *Angew. Chem. Int. Ed.*, **39**, 2587 (2000).

[3] N. F. Scherer, J. L. Knee, D. D. Smith, and A. H. Zewail, *J. Phys. Chem.*, **89**, 5141 (1985).

[4] M. J. Rosker, M. Dantus, and A. H. Zewail, *Science*, **241**, 1200 (1988).

[5] T. S. Rose, M. J. Rosker, and A. H. Zewail, *J. Chem. Phys.*, **88**, 6672 (1988).

[6] T. S. Rose, M. J. Rosker, and A. H. Zewail, *J. Chem. Phys.*, **91**, 7415 (1989).

[7] R. Berera, R. van Grondelle, and J. T. M. Kennis, *Photosynth. Res.*, **101**, 105 (2009).

[8] J. Shah, *IEEE J. Quantum Electron.*, **24**, 276 (1988).

[9] R. Schanz, S. A. Kovalenko, V. Kharlanov, and N. P. Ernsting, *Appl. Phys. Lett.*, **79**, 566 (2001).

[10] M. T. Zanni and R. M. Hochstrasser, *Curr. Opin. Struct. Biol.*, **11**, 516 (2001).

[11] S. H. Shim and M. T. Zanni, *Phys. Chem. Chem. Phys.*, **11**, 748 (2009).

[12] N. T. Hunt, *Chem. Soc. Rev.*, **38**, 1837 (2009).

[13] D. M. Sagar, C. D. Bain, and J. R. R. Verlet, *J. Am. Chem. Soc.*, **132**, 6917 (2010).

[14] Y. R. Shen, *Nature*, **337**, 519 (1989).

[15] K. B. Eisenthal, *Chem. Rev.*, **96**, 1343 (1996).

[16] P. Farmanara, V. Stert, W. Radloff, and I. V. Hertel, *J. Phys. Chem. A*, **105**, 5613 (2001).

[17] M. Schmitt, S. Lochbrunner, J. P. Shaffer, J. J. Larsen, M. Z. Zgierski, and A. Stolow, *J. Chem. Phys.*, **114**, 1206 (2001).

[18] J. A. Davies, K. L. Reid, M. Towrie, and P. Matousek, *J. Chem. Phys.*, **117**, 9099 (2002).

[19] S. H. Lee, K. C. Tang, I. C. Chen, M. Schmitt, J. P. Shaffer, T. Schultz, J. G. Underwood, M. Z. Zgierski, and A. Stolow, *J. Phys. Chem. A*, **106**, 8979 (2002).

[20] T. Schultz *et al.*, *J. Am. Chem. Soc.*, **125**, 8098 (2003).

[21] G. A. Worth, R. E. Carley, and H. H. Fielding, *Chem. Phys.*, **338**, 220 (2007).

[22] V. Blanchet, K. Raffael, G. Turri, B. Chatel, B. Girard, I. A. Garcia, I.

Wilkinson, and B. J. Whitaker, *J. Chem. Phys.*, **128**, 164318 (2008).

[23] A. Iqbal, L. J. Pegg, and V. G. Stavros, *J. Phys. Chem. A*, **112**, 9531 (2008).

[24] A. Iqbal, M. S. Y. Cheung, M. G. D. Nix, and V. G. Stavros, *J. Phys. Chem. A*, **113**, 8157 (2009).

[25] D. S. N. Parker, R. S. Minns, T. J. Penfold, G. A. Worth, and H. H. Fielding, *Chem. Phys. Lett.*, **469**, 43 (2009).

[26] A. Iqbal and V. G. Stavros, *J. Phys. Chem. A*, **114**, 68 (2010).

[27] S. Ullrich, T. Schultz, M. Z. Zgierski, and A. Stolow, *Phys. Chem. Chem. Phys.*, **6**, 2796 (2004).

[28] S. Ullrich, T. Schultz, M. Z. Zgierski, and A. Stolow, *J. Am. Chem. Soc.*, **126**, 2262 (2004).

[29] H. H. Ritze, H. Lippert, E. Samoylova, V. R. Smith, I. V. Hertel, W. Radloff, and T. Schultz, *J. Chem. Phys.*, **122**, 224320 (2005).

[30] E. Samoylova, H. Lippert, S. Ullrich, I. V. Hertel, W. Radloff, and T. Schultz, *J. Am. Chem. Soc.*, **127**, 1782 (2005).

[31] H. Satzger, D. Townsend, M. Z. Zgierski, S. Patchkovskii, S. Ullrich, and A. Stolow, *Proc. Natl. Acad. Sci. U. S. A.*, **103**, 10196 (2006).

[32] K. L. Wells, D. J. Hadden, M. G. D. Nix, and V. G. Stavros, *J. Phys. Chem. Lett.*, **1**, 993 (2010).

[33] N. L. Evans and S. Ullrich, *J. Phys. Chem. A*, in press (2010).

[34] J. M. Weber, I. N. Ioffe, K. M. Berndt, D. Loffler, J. Friedrich, O. T. Ehrler, A. S. Danell, J. H. Parks, and M. M. Kappes, *J. Am. Chem. Soc.*, **126**, 8585 (2004).

[35] A. Iqbal and V. G. Stavros, *J. Phys. Chem. Lett.*, **1**, 2274 (2010).

[36] I. R. Lee, W. Lee, and A. H. Zewail, *Proc. Natl. Acad. Sci. U. S. A.*, **103**, 258 (2006).

[37] G. Meijer, M. S. Devries, H. E. Hunziker, and H. R. Wendt, *Appl. Phys. B*, **51**, 395 (1990).

[38] M. G. H. Boogaarts and G. Meijer, *J. Chem. Phys.*, **103**, 5269 (1995).

[39] V. V. Golovlev, S. L. Allman, W. R. Garrett, N. I. Taranenko, and C. H. Chen, *Int. J. Mass Spectrom.*, **169**, 69 (1997).

[40] V. V. Golovlev, S. L. Allman, W. R. Garrett, and C. H. Chen, *Appl. Phys. Lett.*, **71**, 852 (1997).

[41] I. Bald, I. Dabkowska, and E. Illenberger, *Angew. Chem. Int. Ed.*, **47**, 8518 (2008).

[42] M. Smits, C. A. de Lange, S. Ullrich, T. Schultz, M. Schmitt, J. G. Underwood, J. P. Shaffer, D. M. Rayner, and A. Stolow, *Rev. Sci. Instrum.*, **74**, 4812 (2003).

[43] D. R. Miller, in *Atomic and Molecular Beam Methods*, edited by G. Scholes (Oxford University Press, Oxford, 1988), Vol. 1, pp. 14 - 53.

[44] J. H. Moore, C. C. Davis, and M. A. Coplan, *Building Scientific Apparatus*, 3rd ed. (Westview Press, Cambridge, MA., 2003).

[45] E. Wrede and S. E. Sanders, *Personal Communication* (2009).

[46] W. R. Gentry, in *Atomic and Molecular Beam Methods*, edited by G. Scholes (Oxford University Press, Oxford, 1988), Vol. 1, pp. 54 - 81.

[47] M. Kappes and S. Leutwyler, in *Atomic and Molecular Beam Methods*, edited by G. Scholes (Oxford University Press, Oxford, 1988), Vol. 1, pp. 380 - 415.

[48] A. W. Castleman and K. H. Bowen, *J. Phys. Chem.*, **100**, 12911 (1996).

[49] K. Muller-Dethlefs and P. Hobza, *Chem. Rev.*, **100**, 143 (2000).

[50] T. E. Dermota, Q. Zhong, and A. W. Castleman, *Chem. Rev.*, **104**, 1861 (2004).

[51] J. R. R. Verlet, *Chem. Soc. Rev.*, **37**, 505 (2008).

[52] J. P. K. Doye and D. J. Wales, *Science*, **271**, 484 (1996).

[53] D. J. Wales, J. P. K. Doye, M. A. Miller, P. N. Mortenson, and T. R. Walsh, *Adv. Chem. Phys.*, **115**, 1 (2000).

[54] V. Bonacic-Koutecky and R. Mitric, *Chem. Rev.*, **105**, 11 (2005).

[55] Y. M. Wang, B. C. Shepler, B. J. Braams, and J. M. Bowman, *J. Chem. Phys.*, **131**, 054511 (2009).

[56] V. Vorsa, S. Nandi, P. J. Campagnola, M. Larsson, and W. C. Lineberger, *J. Chem. Phys.*, **106**, 1402 (1997).

[57] B. J. Greenblatt, M. T. Zanni, and D. M. Neumark, *J. Chem. Phys.*, **111**, 10566 (1999).

[58] B. J. Greenblatt, M. T. Zanni, and D. M. Neumark, *J. Chem. Phys.*, **112**, 601 (2000).

[59] A. V. Davis, R. Wester, A. E. Bragg, and D. M. Neumark, *J. Chem. Phys.*, **119**, 2020 (2003).

[60] Y. Miller, G. M. Chaban, J. Zhou, K. R. Asmis, D. M. Neumark, and R. B.

Gerber, *J. Chem. Phys.*, **127**, 094305 (2007).

[61] T. E. Salter, V. Mikhailov, and A. M. Ellis, *J. Phys. Chem. A*, **111**, 8344 (2007).

[62] R. A. Relph *et al.*, *Science*, **327**, 308 (2010).

[63] G. Luttgens, N. Pontius, P. S. Bechthold, M. Neeb, and W. Eberhardt, *Phys. Rev. Lett.*, **88**, 076102 (2002).

[64] L. D. Socaciu, J. Hagen, T. M. Bernhardt, L. Woste, U. Heiz, H. Hakkinen, and U. Landman, *J. Am. Chem. Soc.*, **125**, 10437 (2003).

[65] M. L. Anderson, M. S. Ford, P. J. Derrick, T. Drewello, D. P. Woodruff, and S. R. Mackenzie, *J. Phys. Chem. A*, **110**, 10992 (2006).

[66] D. Harding, M. S. Ford, T. R. Walsh, and S. R. Mackenzie, *Phys. Chem. Chem. Phys.*, **9**, 2130 (2007).

[67] M. Niemietz, M. Engelke, Y. D. Kim, and G. Gantefor, *Appl. Phys. A*, **87**, 615 (2007).

[68] M. Niemietz, K. Koyasu, G. Gantefor, and Y. D. Kim, *Chem. Phys. Lett.*, **438**, 263 (2007).

[69] S. Wolf, G. Sommerer, S. Rutz, E. Schreiber, T. Leisner, and L. Woste, *Phys. Rev. Lett.*, **74**, 4177 (1995).

[70] N. Pontius, P. S. Bechthold, M. Neeb, and W. Eberhardt, *Phys. Rev. Lett.*, **84**, 1132 (2000).

[71] N. Pontius, G. Luttgens, P. S. Bechthold, M. Neeb, and W. Eberhardt, *J. Chem. Phys.*, **115**, 10479 (2001).

[72] N. Pontius, M. Neeb, W. Eberhardt, G. Luttgens, and P. S. Bechthold, *Phys. Rev. B*, **67**, 035425 (2003).

[73] A. E. Bragg, J. R. R. Verlet, A. Kammrath, O. Cheshnovsky, and D. M. Neumark, *J. Chem. Phys.*, **122**, 054314 (2005).

[74] J. R. R. Verlet, A. E. Bragg, A. Kammrath, O. Cheshnovsky, and D. M. Neumark, *J. Chem. Phys.*, **121**, 10015 (2004).

[75] O. F. Hagena, *Surf. Sci.*, **106**, 101 (1981).

[76] H. C. W. Beijerinck and N. F. Verster, *Physica C*, **111**, 327 (1981).

[77] U. Even, J. Jortner, D. Noy, N. Lavie, and C. Cossart-Magos, *J. Chem. Phys.*, **112**, 8068 (2000).

[78] R. R. Corderman and W. C. Lineberger, *Annu. Rev. Phys. Chem.*, **30**, 347

(1979).

[79] K. M. Ervin and W. C. Lineberger, in *Advances in Gas Phase Ion Chemistry*, edited by N. G. Adams and L. M. Babcock (JAI Press, Greenwich, 1992), Vol. 1, p. 121.

[80] D. M. Neumark, *Acc. Chem. Res.*, **26**, 33 (1993).

[81] A. Sanov and R. Mabbs, *Int. Rev. Phys. Chem.*, **27**, 53 (2008).

[82] R. Pincus and M. B. Baker, *Nature*, **372**, 250 (1994).

[83] R. W. Schoenlein, L. A. Peteanu, R. A. Mathies, and C. V. Shank, *Science*, **254**, 412 (1991).

[84] T. E. Meyer, G. Tollin, J. H. Hazzard, and M. A. Cusanovich, *Biophys. J.*, **56**, 559 (1989).

[85] G. R. Fleming and P. G. Wolynes, *Phys. Today*, **43**, 36 (1990).

[86] P. Ball, *Chem. Rev.*, **108**, 74 (2008).

[87] A. E. Bragg, J. R. R. Verlet, A. Kammrath, O. Cheshnovsky, and D. M. Neumark, *Science*, **306**, 669 (2004).

[88] A. E. Bragg, J. R. R. Verlet, A. Kammrath, O. Cheshnovsky, and D. M. Neumark, *J. Am. Chem. Soc.*, **127**, 15283 (2005).

[89] J. R. R. Verlet, A. E. Bragg, A. Kammrath, O. Cheshnovsky, and D. M. Neumark, *Science*, **307**, 93 (2005).

[90] M. A. Johnson and W. C. Lineberger, in *Techniques for the Study of Ion Molecules Reactions*, edited by J. M. Farrar and W. H. Saunders (John Wiley & Sons, New York, 1988), Vol. 20, pp. 591 - 635.

[91] E. De Hoffmann, J. Charette, and V. Stroobant, *Mass Spectrometry: Principles and Applications*. (John Wiley & Sons, New York, 1999).

[92] K. R. Asmis, T. R. Taylor, C. S. Xu, and D. M. Neumark, *J. Chem. Phys.*, **109**, 4389 (1998).

[93] D. Ray, N. E. Levinger, J. M. Papanikolas, and W. C. Lineberger, *J. Chem. Phys.*, **91**, 6533 (1989).

[94] J. M. Papanikolas, J. R. Gord, N. E. Levinger, D. Ray, V. Vorsa, and W. C. Lineberger, *J. Phys. Chem.*, **95**, 8028 (1991).

[95] J. M. Papanikolas, V. Vorsa, M. E. Nadal, P. J. Campagnola, H. K. Buchenau, and W. C. Lineberger, *J. Chem. Phys.*, **99**, 8733 (1993).

[96] D. W. Arnold, S. E. Bradforth, E. H. Kim, and D. M. Neumark, *J. Chem. Phys.*, **102**, 3510 (1995).

[97] L. A. Posey and M. A. Johnson, *J. Chem. Phys.*, **89**, 4807 (1988).

[98] J. M. Weber, J. Kim, E. A. Woronowicz, G. H. Weddle, I. Becker, O. Cheshnovsky, and M. A. Johnson, *Chem. Phys. Lett.*, **339**, 337 (2001).

[99] D. H. Paik, I. R. Lee, D. S. Yang, J. S. Baskin, and A. H. Zewail, *Science*, **306**, 672 (2004).

[100] T. Habteyes, L. Velarde, and A. Sanov, *Chem. Phys. Lett.*, **424**, 268 (2006).

[101] L. Velarde, T. Habteyes, and A. Sanov, *J. Chem. Phys.*, **125**, 114303 (2006).

[102] R. Middleton, *Nucl. Instrum. Methods*, **141**, 373 (1977).

[103] G. T. Caskey, R. A. Douglas, H. T. Richards, and H. V. Smith, *Nucl. Instrum. Methods*, **157**, 1 (1978).

[104] G. D. Alton, G. D. Mills, and J. Dellwo, *Rev. Sci. Instrum.*, **65**, 2006 (1994).

[105] G. D. Alton, *Rev. Sci. Instrum.*, **65**, 1141 (1994).

[106] H. Hotop, T. A. Patterson, and W. C. Lineberger, *Phys. Rev. A*, **8**, 762 (1973).

[107] H. E. Beske, A. Hurrle, and K. P. Jochum, *Fresen Z Anal Chem*, **309**, 258 (1981).

[108] J. R. Bacon and A. M. Ure, *Analyst*, **109**, 1229 (1984).

[109] M. Tabrizchi, T. Khayamian, and N. Taj, *Rev. Sci. Instrum.*, **71**, 2321 (2000).

[110] V. Dudnikov, *Rev. Sci. Instrum.*, **73**, 992 (2002).

[111] M. Schmidt, C. Ellert, W. Kronmuller, and H. Haberland, *Phys. Rev. B*, **59**, 10970 (1999).

[112] M. Karas, D. Bachmann, U. Bahr, and F. Hillenkamp, *Int. J. Mass Spectrom. Ion Processes*, **78**, 53 (1987).

[113] M. Karas and F. Hillenkamp, *Anal. Chem.*, **60**, 2299 (1988).

[114] M. Karas and F. H. Hillenkamp, in *Ion Formation from Organic Solids IV*, edited by A. Benninghoven (John Wiley & Sons, New York, 1988), p. 108.

[115] F. H. Hillenkamp, M. Karas, A. Ingeldoh, and B. Stahl, in *Biological Mass Spectrometry*, edited by A. L. Burlingame and J. A. McCloskey (Elsevier, Amsterdam, 1990), p. 49.

[116] *Electrospray Ionisation Mass Spectrometry: Fundementals, Instrumentation and Applications*, edited by R. B. Cole (John Wiley & Sons, New York, 1997).

[117] M. Dole, L. L. Mack, R. L. Hines, R. C. Mobley, L. D. Ferguson, and M. B. Alice, *J. Chem. Phys.*, **49**, 2240 (1968).

[118] M. Yamashita and J. B. Fenn, *J. Phys. Chem.*, **88**, 4451 (1984).

[119] M. Yamashita and J. B. Fenn, *J. Phys. Chem.*, **88**, 4671 (1984).

[120] J. B. Fenn, *Angew. Chem. Int. Ed.*, **42**, 3871 (2003).

[121] S. E. Rodriguez-Cruz, J. S. Klassen, and E. R. Williams, *J. Am. Soc. Mass Spectrom.*, **10**, 958 (1999).

[122] D. L. Zhan and J. B. Fenn, *Int. J. Mass Spectrom.*, **219**, 1 (2002).

[123] G. Schlosser, Z. Takats, and K. Vekey, *J. Mass Spectrom.*, **38**, 1245 (2003).

[124] L. B. Loeb, A. F. Kip, G. G. Hudson, and W. H. Bennett, *Phys. Rev.*, **60**, 714 (1941).

[125] R. J. Pfeifer and C. D. Hendricks, *AIAA J.*, **6**, 496 (1968).

[126] D. P. H. Smith, *IEEE Trans. Ind. Appl.*, **IA-22**, 527 (1986).

[127] I. Hayati, A. I. Bailey, and T. F. Tadros, *J. Colloid Interface Sci.*, **117**, 205 (1987).

[128] J. Fernandex de la Mora and I. G. Locertales, *J. Fluid Mech.*, **243**, 561 (1994).

[129] A. T. Blades, M. G. Ikonomou, and P. Kebarle, *Anal. Chem.*, **63**, 2109 (1991).

[130] G. I. Taylor, *Proc. R. Soc. London A*, **A280**, 383 (1964).

[131] J. M. Lopez-Herrera, A. Barrero, A. Boucard, I. G. Loscertales, and M. Marquez, *J. Am. Soc. Mass Spectrom.*, **15**, 253 (2004).

[132] P. Kebarle and L. Tang, *Anal. Chem.*, **65**, A972 (1993).

[133] A. W. Colburn, A. E. Giannakopulos, and P. J. Derrick, *Eur. J. Mass Spectrom.*, **10**, 149 (2004).

[134] A. Gomez and K. Tang, *Phys. Fluids*, **6**, 404 (1994).

[135] L. Tang and P. Kebarle, *Anal. Chem.*, **65**, 3654 (1993).

[136] Rayleigh, *Philos. Mag.*, **14**, 184 (1882).

[137] J. V. Iribarne and B. A. Thomson, *J. Chem. Phys.*, **64**, 2287 (1976).

[138] L. S. Wang, C. F. Ding, X. B. Wang, and S. E. Barlow, *Rev. Sci. Instrum.*, **70**, 1957 (1999).

[139] X. B. Wang and L. S. Wang, *Rev. Sci. Instrum.*, **79**, 073108 (2008).

[140] C. Hirlimann, in *Femtosecond Laser Pulses: Principles and Experiments*, edited by C. Rulliere (Springer, New York, 2005), pp. 25 - 56.

[141] A. Stolow, A. E. Bragg, and D. M. Neumark, *Chem. Rev.*, **104**, 1719 (2004).

[142] A. Assion, M. Geisler, J. Helbing, V. Seyfried, and T. Baumert, *Phys. Rev. A*, **54**, R4605 (1996).

[143] D. M. Neumark, *Annu. Rev. Phys. Chem.*, **52**, 255 (2001).

[144] A. Stolow, *Annu. Rev. Phys. Chem.*, **54**, 89 (2003).

[145] A. Stolow, *Int. Rev. Phys. Chem.*, **22**, 377 (2003).

[146] T. Suzuki and B. J. Whitaker, *Int. Rev. Phys. Chem.*, **20**, 313 (2001).

[147] L. Nugent-Glandorf, M. Scheer, D. A. Samuels, A. M. Mulhisen, E. R. Grant, X. M. Yang, V. M. Bierbaum, and S. R. Leone, *Phys. Rev. Lett.*, **87**, 193002 (2001).

[148] L. Nugent-Glandorf, M. Scheer, D. A. Samuels, V. M. Bierbaum, and S. R. Leone, *J. Chem. Phys.*, **117**, 6108 (2002).

[149] J. H. D. Eland, *Photoelectron Spectroscopy*. (Butterworth, London, 1984).

[150] M. Seel and W. Domcke, *J. Chem. Phys.*, **95**, 7806 (1991).

[151] M. Seel and W. Domcke, *Chem. Phys.*, **151**, 59 (1991).

[152] V. Blanchet, M. Z. Zgierski, T. Seideman, and A. Stolow, *Nature*, **401**, 52 (1999).

[153] T. Seideman, *Annu. Rev. Phys. Chem.*, **53**, 41 (2002).

[154] K. L. Reid, *Annu. Rev. Phys. Chem.*, **54**, 397 (2003).

[155] R. Mabbs, E. R. Grumbling, K. Pichugin, and A. Sanov, *Chem. Soc. Rev.*, **38**, 2169 (2009).

[156] M. Tsubouchi, B. J. Whitaker, L. Wang, H. Kohguchi, and T. Suzuki, *Phys. Rev. Lett.*, **86**, 4500 (2001).

[157] A. E. Bragg, R. Wester, A. V. Davis, A. Kammrath, and D. M. Neumark, *Chem. Phys. Lett.*, **376**, 767 (2003).

[158] C. Z. Bisgaard, O. J. Clarkin, G. R. Wu, A. M. D. Lee, O. Gessner, C. C. Hayden, and A. Stolow, *Science*, **323**, 1464 (2009).

[159] J. Lecointre, G. M. Roberts, D. A. Horke, and J. R. R. Verlet, *J. Phys. Chem. A*, **114**, 11216 (2010).

[160] D. R. Cyr and C. C. Hayden, *J. Chem. Phys.*, **104**, 771 (1996).

[161] J. Jortner, S. A. Rice, and R. M. Hochstrasser, *Adv. Photochem.*, **7**, 149 (1969).

[162] G. Stock and W. Domcke, *Adv. Chem. Phys.*, **100**, 1 (1997).

[163] B. S. Hudson, B. E. Kohler, and K. Schulten, in *Excited States*, edited by E. C. Lim (Academic, New York, 1982), Vol. 6.

[164] A. Sanov and W. C. Lineberger, *Phys. Chem. Chem. Phys.*, **6**, 2018 (2004).

[165] A. L. Harris, J. K. Brown, and C. B. Harris, *Annu. Rev. Phys. Chem.*, **39**, 341 (1988).

[166] A. V. Davis, M. T. Zanni, C. Frischkorn, and D. M. Neumark, *J. Electron Spectrosc. Relat. Phenom.*, **108**, 203 (2000).

[167] D. H. Paik, N. J. Kim, and A. H. Zewail, *J. Chem. Phys.*, **118**, 6923 (2003).

[168] D. E. Szpunar, K. E. Kautzman, A. E. Faulhaber, and D. M. Neumark, *J. Chem. Phys.*, **124**, 054318 (2006).

[169] L. Sheps, E. M. Miller, S. Horvath, M. A. Thompson, R. Parson, A. B. McCoy, and W. C. Lineberger, *Science*, **328**, 220 (2010).

[170] X. B. Wang, X. Yang, and L. S. Wang, *Int. Rev. Phys. Chem.*, **21**, 473 (2002).

[171] X. B. Wang and L. S. Wang, *Annu. Rev. Phys. Chem.*, **60**, 105 (2009).

[172] O. T. Ehrler, J. P. Yang, C. Hattig, A. N. Unterreiner, H. Hippler, and M. M. Kappes, *J. Chem. Phys.*, **125**, 074312 (2006).

[173] O. T. Ehrler, J. P. Yang, A. B. Sugiharto, A. N. Unterreiner, and M. M. Kappes, *J. Chem. Phys.*, **127**, 184301 (2007).

[174] C. Rensing, O. T. Ehrler, J. P. Yang, A. N. Unterreiner, and M. M. Kappes, *J. Chem. Phys.*, **130**, 234306 (2009).

[175] X. B. Wang and L. S. Wang, *Nature*, **400**, 245 (1999).

Chapter 2: Experimental Design and Construction of a New Photoelectron Imaging Spectrometer

The design and construction of a new photoelectron imaging spectrometer for studying the spectroscopy and ultrafast dynamics of molecular anions is considered. Here, we discuss the challenges which must be overcome to successfully couple an electrospray ionisation source to a photoelectron imaging spectrometer. Throughout this chapter, we then describe in detail the femtosecond laser system and experimental design and construction of the spectrometer, which incorporates an ion guide and trap, a Wiley-McLaren time-of-flight spectrometer, and a novel velocity map imaging arrangement for performing photoelectron imaging on anions. The instrument is calibrated using iodide anions, where we record both its time-of-flight and photoelectron spectra. The results of these calibration experiments are also compared to simulation results, performed using the Simion simulation package. Finally, we conclude by describing the experimental controls and the data acquisition control station, the latter of which has been developed in LabVIEW.

2.1 Experimental Overview

In this section we present the development and construction of a new experiment, which will probe the ultrafast dynamics and spectroscopy of molecular anions generated *via* electrospray ionisation (ESI) using time-resolved photoelectron imaging (TRPEI). We also spend time considering the challenges involved in coupling these two experimental methodologies together and how these may be overcome through the process of careful and considered experimental design. We follow on with a description of the femtosecond laser system used, including details of the optics arrangements, harmonic generation stages (second, third and fourth harmonics) and finally characterise the laser system in the time and frequency domains. A full description of the spectrometer succeeds this in Sections 2.3 to 2.5. We draw this chapter to a close by providing a complete description of the experimental controls and the data acquisition (DAQ) interface, which has been coded in LabVIEW 8.5.

2.1.1 Overview of Spectrometer

A full schematic of the gas phase spectrometer is presented in Figure 2.1, and is broadly defined into three regions; (i) source region, (ii) time-of-flight region, and (iii) detection region. Each of these three sections, including the components of the spectrometer contained within each region, are described in greater detail throughout Sections 2.3 to 2.5 of this chapter. This includes an in depth discussion of the development and design considerations behind each of the individual components, complete with relevant simulations using Simion 8.0. In Section 2.1.2, we first consider and describe the vacuum pumping systems utilised.

2.1.2 Vacuum Considerations

Primary Vacuum Pump Systems

One of the major drawbacks of ESI sources is that they must be operated at atmospheric

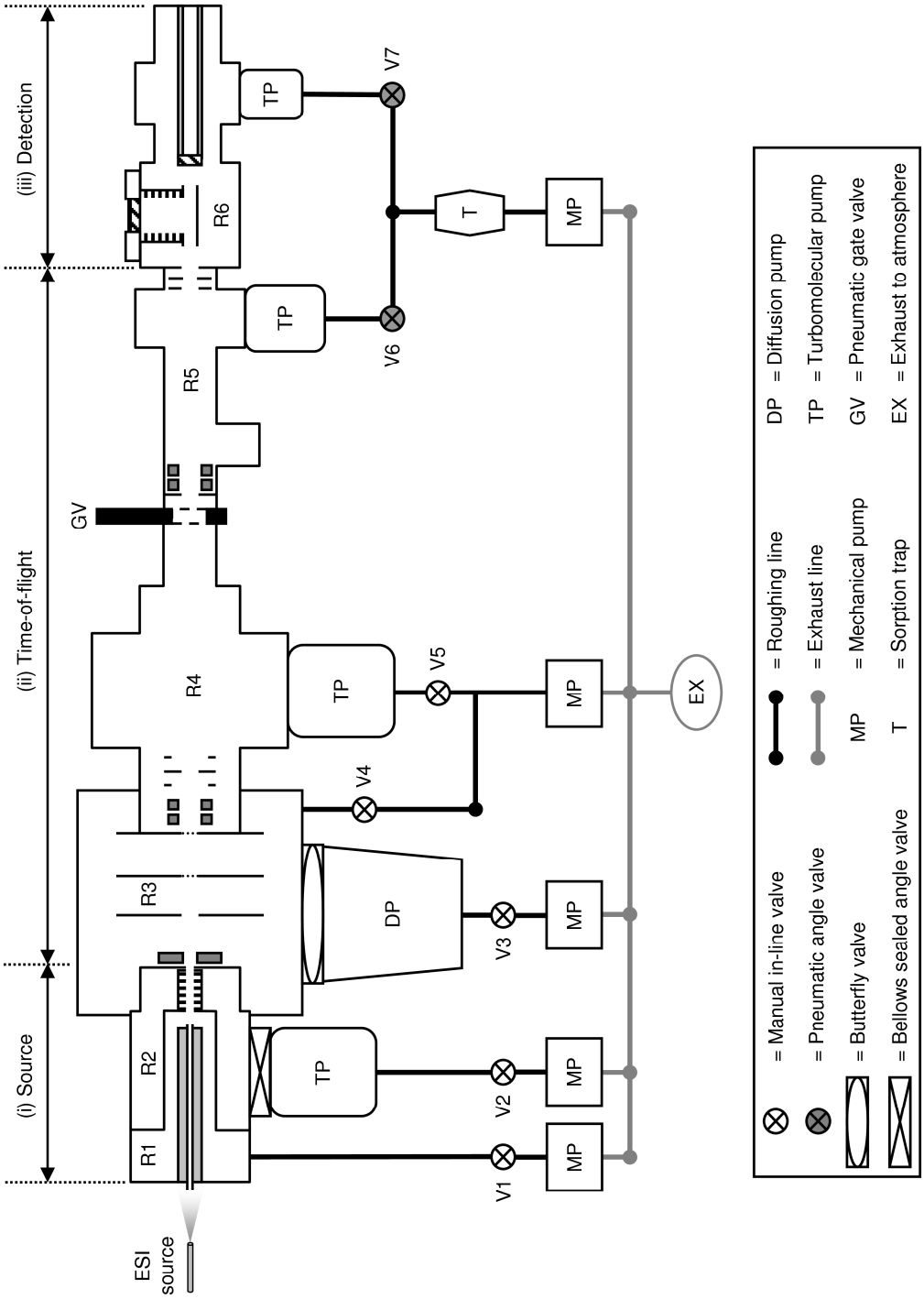

Figure 2.1: Schematic of the gas phase spectrometer. The spectrometer is defined into 3 distinct sections: (i) source, (ii) time-of-flight, and (iii) detection. The spectrometer itself consist of a total of 6 differentially pumped regions, labelled R1 to R6, defined by a series of differential apertures, with R1 open to atmosphere (ESI source) through a stainless steel capillary. The primary and foreline vacuum pump systems are also schematically shown, with a key for all vacuum components shown below.

conditions (760 Torr, 298 K), whereas photoelectron imaging must be performed under ultra-high vacuum (UHV) ($\leq 10^{-9}$ Torr) to attain feasible signal-to-noise levels in the measured photoelectron images. To evade this issue the spectrometer has been divided into six differentially pumped chambers, labelled R1 to R6 in Figure 2.1, each defined by a series of differential pinholes, the first of which (R1) is open to atmosphere through a stainless steel capillary. The specifications for each of these differential apertures, are presented in Table 2.1, where *d* are their inner diameters (i.d.) and in the case of capillaries, *L* is their associated length.

Table 2.1: Target base pressures, P_R, for each of the differentially pumped sections of the spectrometer. The dimensions of the differential capillaries/apertures leading into each of the regions are also given, where *d* is the diameter of the capillary/aperture and *L* is the capillary length.

Pressure region (*R*)	P_R / Torr	*d* / cm	*L* / cm
Atmosphere	760	-	-
R1	1.5	0.06	18
R2	1×10^{-3}	0.1	0.2
R3	5×10^{-6}	0.2	-
R4	3×10^{-7}	0.5	-
R5	2×10^{-8}	0.5	-
R6	5×10^{-9}	0.5	-

Designing the spectrometer in such a manner allows the final detection region (R6) to readily attain the desired UHV pressures through a sequential reduction of gas load in each successive region, provided one selects appropriate vacuum pumping systems. Table 2.1 also displays the *target* base pressures, P_R, for each of the spectrometer regions, and here we give consideration to the minimum pumping specifications required to obtain these pressures. We begin by calculating the gas conductance, C_R (in l s^{-1}), through each of the differential capillaries/pinholes, which then allows us to determine the maximum gas throughput into each subsequent region, Q_R (in Torr l s^{-1}), using [1]

$$Q_R = C_R \left(P_{R-1} - P_R \right). \tag{2.1}$$

Due to the relatively high pressure in R1, the gas flow in this region may be classed as a *viscous flow* regime, and hence the conductance through the capillary, C_R, is defined as [1]

$$C_R = 180\left(\frac{d^4}{L}\right)\left(\frac{1}{2}\left[P_{R-1} - P_R\right]\right). \tag{2.2}$$

The base pressure required for the second region, R2, however, fits into the transitional domain between the viscous and *molecular flow* regimes.[1] In the molecular flow regime the conductance becomes independent of pressure and for a capillary, C_R may be determined using [1]

$$C_R = 12\frac{d^3}{L}. \tag{2.3}$$

For the transitional pressure range in R2, equation (2.3) can be used to provide a conservative estimate for C_R.[2] The remaining pressure regions of the spectrometer (R3 to R6) may be definitively classed into the molecular flow regime, where C_R through these successive pinholes (defined as $d > L$), may be defined as [1]

$$C_R \approx 20\pi\left(\frac{d}{2}\right)^2. \tag{2.4}$$

Equations (2.2) and (2.4) are valid assuming that the input gas is primarily air at room temperature (298 K). Here, the spectrometer is open to atmosphere which justifies this assumption. A summary of these conductance and throughput calculations, based on the

[1] The transitional domain between viscous and molecular flow occurs over an approximate pressure range of 500 to 5 mTorr, and occurs when the mean free path of molecules becomes approximately equal to the dimensions of the vacuum chamber. A rigorous mathematical description of this transitional gas flow regime is non-trivial [1].

[2] For a viscous gas flow regime the conductance depends on both the gas pressure and the square of the cross-section of the conducting capillary (d^4). However, in the molecular flow regime, gas flow is independent of pressure and is proportional to d^3. It therefore follows that equation (2.3) will provide a conservative estimate for a capillary's conductance in the transitional regime between viscous and molecular flow.

parameters in Table 2.1, is shown in Table 2.2, where the minimum pumping speed requirements based on these results, $S_R^{\min}$, are determined using $S_R^{\min} = Q_R / P_R$.

Table 2.2: Calculation results for the capillary/aperture conductances, C_R, gas throughputs, Q_R, and minimum pumping speeds, $S_R^{\min}$, required to attain the base pressures, P_R, shown in Table 2.1. Calculations are based on the *d* and *L* parameters shown in Table 2.1 using equations (2.1) to (2.4).

Pressure region (*R*)	C_R / l s^{-1}	Q_R / Torr l s^{-1}	$S_R^{\min}$ / l s^{-1}
R1	4.9×10^{-2}	37.4	26.7
R2	6.7×10^{-2}	0.1	100
R3	0.6	3.1×10^{-3}	785.4
R4	3.9	1.6×10^{-5}	52.4
R5	3.9	1.2×10^{-6}	58.9
R6	3.9	7.9×10^{-8}	15.7

Table 2.3: Specifications of the primary vacuum pump systems used to evacuate each of the regions of the spectrometer, based on the minimum pumping speed/throughput requirements displayed in Table 2.2.

Pressure region (*R*)	Pump type	Pump model	S_R^{pump} / l s^{-1}	Q_R^{pump} / Torr l s^{-1}
R1	Mechanical	Oerlikon SV100B	28	42
R2	Turbomolecular	Oerlikon TW250S	250	0.25
R3	Diffusion	Oerlikon DIP3000	3000*	1.5×10^{-2}
R4	Turbomolecular	Edwards EXT250H	250	7.5×10^{-5}
R5	Turbomolecular	Oerlikon Turbovac 151	150	3.0×10^{-6}
R6	Turbomolecular	Oerlikon Turbovac SL80	80	4.0×10^{-7}

To reach the target base pressures in Table 2.1 the gas load (throughput) passing into

* The pumping speed of 3000 l s^{-1} for the DIP3000 diffusion pump is based on no conductance restraints. Due to conductance limitations from the butterfly valve (see Figure 2.1) and other spectrometer components, this may conservatively be estimated to be reduced to ~2000 l s^{-1}.

each region must be pumped away, i.e. the maximum gas throughput of the vacuum system must exceed the gas throughput into that region. Based on this and the results from the calculations in Table 2.2, the primary pumping systems selected for each differential region, together with their associated pumping speeds, S_R^{pump}, and maximum throughputs, Q_R^{pump}, are shown in Table 2.3. R1 is evacuated using a 100 m^3 hr^{-1} (~28 l s^{-1}) single stage mechanical pump (Oerlikon, SV100B). Due to the relatively high pressures required in this region and the large throughput, a single stage rotary pump is ideally suited for R1. For the second region of the spectrometer (R2) a 250 l s^{-1} turbomolecular pump (Oerlikon, TW250S) has been selected. The throughput in region 2 is particularly high (~0.25 Torr l s^{-1} at a pressure of 1×10^{-3} Torr), and when experiments are performed, the operational pressure and throughput in this region may be increased by up to an order of magnitude, which is not ideal for turbomolecular pumps. Alternatively, a pumping system capable of dealing with high throughputs, such as a roots blower, may have been selected, although such pumps do not offer comparable high pumping speeds (~250 l s^{-1}) at the target base pressure for R2 [1]. R3 of the spectrometer is pumped using a 3000 l s^{-1} diffusion pump (Oerlikon, DIP3000). This large vacuum pumping system has been specifically chosen to exceed the minimum primary pumping specifications for this region (see Table 2.2) so that in the future a molecular beam source, which will generate a significantly larger gas load than the existing ESI arrangement, may be readily incorporated into R3. In the event of this modification, the first two differentially pumped regions would be detached from the spectrometer. The remaining three differentially pumped regions of the instrument, R4 to R6, are all evacuated using turbomolecular pumps. As these regions (particularly R5 and R6) will constitute the UHV regions of the spectrometer, turbomolecular pumps have been selected over oil-based diffusion pump systems to ensure the UHV conditions required. These turbomolecular pump models and their pumping speeds are displayed in Table 2.3.

Table 2.4: Final base pressures measured in each region of the spectrometer, using the pump selection shown in Table 2.3.

Pressure region (*R*)	Final measured base pressure / Torr
R1	1.3
R2	2.5×10^{-3}

R3	1.2×10^{-6}
R4	1.6×10^{-7}
R5	5.1×10^{-9}
R6	3.8×10^{-9}

The final *measured* base pressures in each of the spectrometer regions are displayed in Table 2.4, when using the pumping systems in Table 2.3. When experiments are being performed, the pressure in R1 may be increased using a manual in-line mechanical valve (labelled V1 in Figure 2.1). Operational pressures in this first region are typically within the range of 3 to 10 Torr, and are discussed in more detail in Section 2.3.2. Similarly, the pressure in R2 may also be controlled using a bellows sealed angle valve, which is labelled in Figure 2.1, and the operational pressure in this region is commonly on the order of 10^{-2} Torr.

Foreline Vacuum Pump Systems

The primary vacuum systems in Table 2.3 are all connected to foreline vacuum pumping systems, with the exception of the SV100B single-stage mechanical pump used to evacuate R1 of the spectrometer. This pumping arrangement is shown schematically in Figure 2.1 and the pumping specifications of these foreline vacuum systems, which are all two-stage mechanical pumps, are shown in Table 2.5 below.

Table 2.5: Foreline vacuum pump specifications for each of the pressure regions of the spectrometer, where S_n^{fore} is the pumping speed of the associated two-stage mechanical pump in $m^3\ hr^{-1}$.

Pressure region (R)	Pump model	S_R^{fore} / $m^3\ hr^{-1}$
R2	Oerlikon D40B	40
R3	Oerlikon D25B	25
R4	Edwards RV12	12
R5/R6	Oerlikon D4B	4

These pumps, whilst also serving for foreline evacuation while the primary pumps are in operation, also function to ‘rough’ out the spectrometer prior to switching over to the

primary vacuum systems, as the primary pumps require an initial 'roughing' pressure, P_R^{rough}, which ranges from ~10^{-2} to 10^{-4} Torr depending on the primary pump specifications, before the spectrometer can be evacuated to the final base pressures. All regions evacuated by turbomolecular pumps are roughed out through their respective primary pump. The turbomolecular pump in R2 is backed by a 40 m^3 hr^{-1} mechanical pump (Oerlikon, D40B), where its relatively large pumping speed has been selected due to the high throughputs in this spectrometer region, while all other turbomolecular pumps are backed at their recommended pumping speeds. However, the third spectrometer region (R3), which is evacuated using a diffusion pump, must be roughed out directly and is performed using the RV12 two-stage mechanical pump, connected to R3 with an additional roughing line, as shown in Figure 2.1. Prior to opening the butterfly valve (see Figure 2.1) and switching over to the DIP3000 diffusion pump, the RV12 pump is isolated from R3 using a mechanical in-line valve, labelled V4 in Figure 2.1, enabling isolated backing of the EXT250H pump connected to R4. The DIP3000 system itself is backed by an individual 25 m^3 hr^{-1} mechanical pump (Oerlikon, D25B). The turbomolecular pumps connected to R5 and R6 (Turbovac 151 and SL80, respectively) are both backed by a single 4 m^3 hr^{-1} two-stage mechanical pump (Oerlikon, D4B). This foreline section also contains a sorption trap, labelled T in Figure 2.1, to reduce the amount of mechanical pump oil reaching R5 and R6 of the spectrometer, which can be detrimental to obtaining the desired UHV conditions in the detection region. Additionally, a pair of pneumatic angle valves (V6 and V7 in Figure 2.1) are placed prior to these two turbomolecular pumps, and serve to preserve the UHV conditions in R5 and R6, in conjunction with the pneumatic gate valve (Kurt J. Lesker, SG0250PCCF), labelled GV in Figure 2.1, in the event of vacuum pump failure. This vacuum interlock system is discussed in greater detail in Section 2.6.1.

Pressure Measurement

The pressures in each of the spectrometer regions are monitored using a variety of different pressure gauges. The pressure in the first region, R1, is independently monitored using a digital pirani gauge (InstruTech, CVM-211), capable of measuring the chamber pressure over a range of 10^2 to 10^{-2} Torr. R2's pressure is measured using a thermocouple gauge (Kurt J. Lesker, KJL-6000), operating over a pressure range of 10^{-1}

to 10^{-3} Torr. Similarly, the pressures in each individual foreline vacuum line are monitored using thermocouple gauges; 5 in total for each roughing line. Finally, the remaining regions of the spectrometer (R3 to R6) all contain thermionic ionisation gauges (Kurt J. Lesker, G100KQF25/G100F) for pressure measurement. These gauges operate over the wide pressure regime of 10^{-3} to 10^{-9} Torr and are particularly useful for the detection region compared to alternative magnetron gauges, as the magnetic fields produced by the latter can lead to detrimental distortions in the measured photoelectron trajectories. All thermocouple and ionisation gauges are connected to a pair of pressure gauge controllers (Kurt J. Lesker, KJLC6600), each capable of monitoring pressures from 4 thermocouple gauges and 2 ionisation gauges. A summary of the pressure gauges for each of the spectrometer regions is show below in Table 2.6.

Table 2.6: Summary of the gauge types used to monitor the pressures in each region of the spectrometer. Also shown are the pressure ranges over which each gauge operates.

Pressure region (*R*)	Gauge type	Operation range / Torr
R1	Pirani	10^{2} - 10^{-2}
R2/foreline	Thermocouple	10^{-1} - 10^{-3}
R3/R4/R5/R6	Thermionic ionisation	10^{-3} - 10^{-9}

2.2 Femtosecond Laser System

2.2.1 Laser System and Fundamental Beam Delivery

Before providing further details of the spectrometer, we first describe the laser system specifications and the optical layouts used to perform TRPEI. The femtosecond laser system is schematically shown in Figure 2.2 and consists of a commercial femtosecond titanium sapphire (Ti:Sapph) oscillator (Spectra-Physics, Tsunami) pumped by the second harmonic (532 nm) of a continuous wave (CW) Nd:YAG laser (Spectra-Physics, Millennia Pro). The oscillator outputs a 76 MHz pulse train centred at 800 nm (tunable from ~770 to ~830 nm) with a measured power of 0.5 W (~6 nJ/pulse) and a bandwidth of 50 nm. This seed beam is then temporally stretched and subsequently amplified using a second Ti:Sapph crystal in a regenerative amplifier (Spectra-Physics, Spitfire XP-Pro), pumped by the second harmonic (527 nm) of a 1 kHz pulsed Nd:YLF (Spectra-

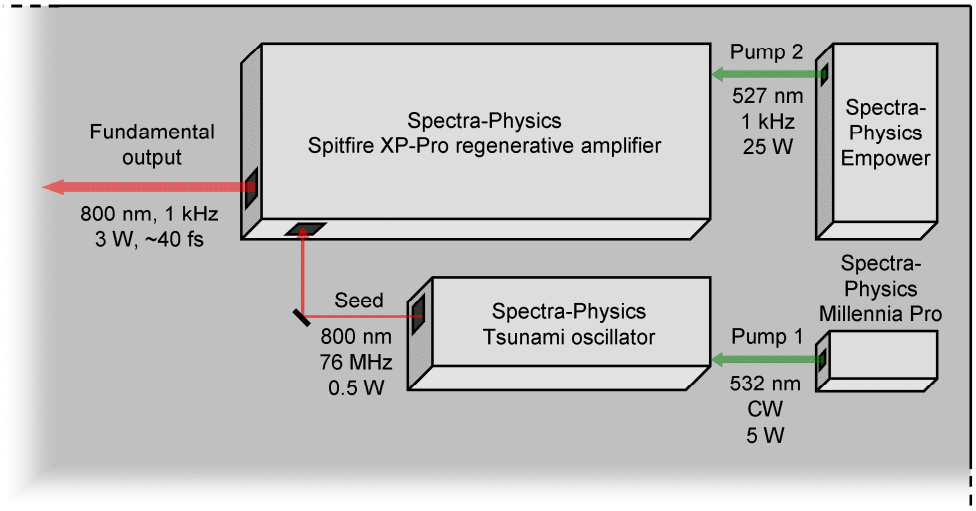

Figure 2.2: Layout of the femtosecond laser system used in conjunction with the gas phase spectrometer. The laser consists of two pump lasers (Spectra-Physics Millennia Pro and Empower), a femtosecond Ti:Sapphire oscillator (Spectra-Physics Tsunami) and a femtosecond Ti:Sapphire regenerative amplifier (Spectra-Physics Spitfire XP-Pro). Details of each of the laser outputs are displayed along with the specifications of the 800 nm fundamental emitted from the regenerative amplifier.

Physics, Empower). Following amplification, the pulses are then recompressed to generate a 1 kHz pulse train of ~40 fs pulses (full width at half maximum (FWHM)) centred at 800 nm with energies of 3 mJ/pulse (see Sections 2.2.4 and 2.2.5 for fundamental pulse characterisation) and possesses a polarisation which is horizontal with respect to the plane of the laser table (*p*-polarised).

The optical layout for the delivery and partitioning of the 800 nm fundamental is show schematically in Figure 2.3. Immediately after exiting the regenerative amplifier the fundamental enters a telescope, consisting of a concave/convex mirror pair and reduces the diameter of the beam from ~0.5 cm down to ~0.3 cm (FWHM). It is then subsequently divided into two separate 800 nm beams of equal energy (1.5 mJ/pulse) using a 50:50 beam splitter. One of these beams, labelled i in Figure 2.3, is used to pump the first of two optical parametric amplifiers (OPAs) (Light Coversion, TOPAS-C). The second beam with an energy of 1.5 mJ/pulse is manoeuvred towards a second 50:50 beam splitter, again producing a second pair of daughter beams, each with an energy of 750 μJ/pulse. The first of these, labelled ii in Figure 2.3, is guided into the input aperture of the second OPA system (Spectra-Physics, OPA-800C). Neither OPA system is utilised for any of the experiments described in the latter chapters of this

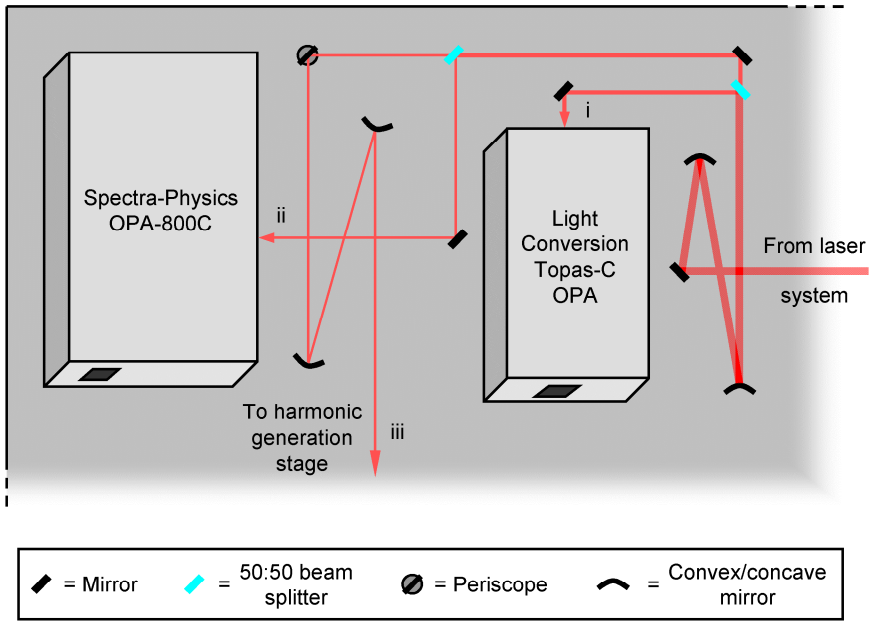

Figure 2.3: Layout of the fundamental beam delivery. The 800 nm fundamental (3 mJ/pulse) passes through a series of telescopes, beam splitters, and periscopes, to produce three separate beams: (i) the TOPAS-C OPA input beam (1.5 mJ/pulse), (ii) the OPA-800C input beam (750 μJ/pulse), and (iii) the harmonic generation stage input beam (750 μJ/pulse). An optics key is shown below the figure.

thesis and so are not discussed in any greater detail. A portion of the remaining 750 μJ/pulse beam, labelled iii in Figure 2.3, is used to pump a harmonic generation stage arrangement. Before entering this stage the beam height is reduced using an optical periscope, which also serves to rotate the laser polarisation by 90^{o} from *p*- to *s*-polarisation (vertical with respect to the plane of the laser table). Finally beam iii enters a second telescope, reducing the beam diameter further, from 0.3 cm to 0.2 cm.

2.2.2 Harmonic Generation Stage

The harmonic generation stage, which is loosely based on the designs of Nebel *et al*. [2] and Ringling *et al*. [3], is used to generate the higher harmonics of the 800 nm fundamental emitted from the regenerative amplifier, and is shown schematically in Figure 2.4. Harmonics of the fundamental up to and including the fourth are generated *via* non-linear processes in thin non-centrosymmetric (anisotropic) crystals, appropriately cut to the correct angle depending on the harmonic being generated, producing wavelengths of 400 nm, 266 nm, and 200 nm, respectively. The origins of

these non-linear processes can be understood in terms of the dielectric polarisation, $\vec{P}$, which is set up in a medium as the laser radiation passes through it [4]:

$$\vec{P} = \varepsilon_0 \left(\chi_1 \vec{E} + \chi_2 \vec{E}^2 + \chi_3 \vec{E}^3 + \ldots \right). \tag{2.5}$$

In equation (2.5) ε_0 is the permittivity of free space ($\varepsilon_0 = 8.8 \times 10^{-12}$ J^{-1} C^2 m^{-1}), χ_i are the i^{th} order susceptibilities, and $\vec{E}$ is the electric field vector of the laser pulse:

$$\vec{E} = E_0 \sin(\omega t), \tag{2.6}$$

where E_0 and ω are the electric field amplitude and frequency (in rads s^{-1}), respectively. At low electric field intensities only the first term in equation (2.5) dominates, and is responsible for optical phenomena such as reflection and refraction. However, the electric field intensity in femtosecond pulses (and other pulsed laser systems) is sufficiently high that E_0^2 becomes large enough to compensate for the small higher order susceptibility, χ_2, making this second term more significant. By substituting equation (2.6) into the first two terms of equation (2.5) the following relationship is arrived at [4]:

$$\begin{aligned} \vec{P} &= \varepsilon_0 \left[\chi_1 \left(E_0 \sin(\omega t) \right) + \chi_2 \left(E_0^2 \sin^2(\omega t) \right) \right] \\ &= \varepsilon_0 \left[\chi_1 \left(E_0 \sin(\omega t) \right) + \chi_2 \left(\frac{1}{2} E_0^2 \left\{ 1 - \cos(2\omega t) \right\} \right) \right], \end{aligned} \tag{2.7}$$

where the $\frac{1}{2}\left[1 - \cos(2\omega t)\right]$ term is arrived at from simple trigonometric identities and implies that laser light at twice the frequency (energy) of the incident light, 2ω, may be generated. Equation (2.7) displays the origins of the second harmonic generation (SHG) process, specifically used here to generate 400 nm laser pulses from the 800 nm fundamental. Although SHG is a one-colour two photon process, similar two-colour mixing methods may be used to perform sum frequency generation [4], enabling higher harmonics of the fundamental to be accessed, as discussed below.

Prior to entering the harmonic generation stage, the 800 nm input beam iii may be attenuated in energy depending on the desired energy output of the harmonics, and is

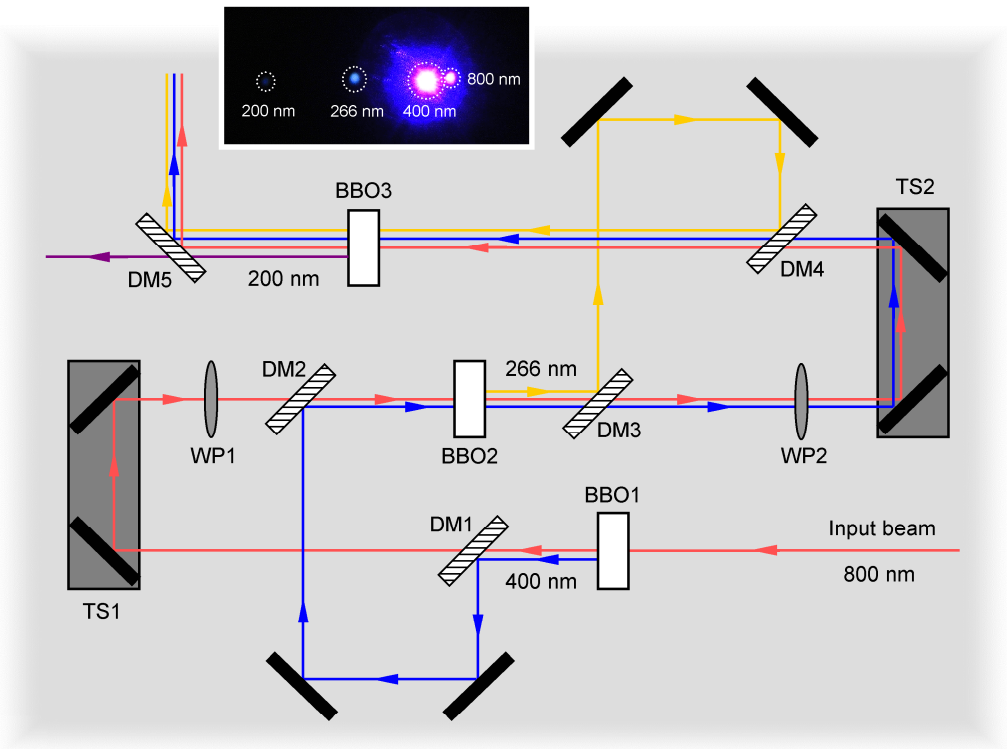

Figure 2.4: Optical layout of the harmonic generation stage used to generate the second (SHG, 400 nm), third (THG, 266 nm), and fourth (FHG, 200 nm) harmonics of the 800 nm fundamental. Harmonic generation is performed in thin type I β-barium borate (BBO) crystals of varying thicknesses, labelled BBO1 to BBO3, respectively. Harmonics are separated and recombined using dichroic mirrors (DM) and beam polarisations are controlled using $\lambda/2$ waveplates (WP). Maximum temporal overlap between the different harmonics in the BBO crystals in controlled using mirror pairs mounted on translation stages (TS). A labelled photograph of the output harmonics and the fundamental is show at the top of the schematic, where harmonics have been spatially dispersed using a quartz prism.

achieved using a variety of thin beam splitters. Here, a 190 mW beam of 800 nm passes through a 300 μm thick type I β-barium borate (BBO) crystal, labelled BBO1 in Figure 2.4, generating ~70 mW of 400 nm alongside the residual 800 nm beam, where the SHG is rotated by 90^{o} relative to the 800 nm input.

Third harmonic generation (THG) is performed through sum frequency mixing of the 400 nm and 800 nm beams in a second type I BBO crystal, which is 200 μm thick (BBO2 in Figure 2.4). Optimum conversion to 266 nm is achieved when the 400 nm and 800 nm pulses are spatially and temporally overlapped in BBO2. However, the 400 nm pulses are temporally retarded relative to the 800 nm pulses, as a result of group velocity delay (GVD) in BBO1. This GVD arises as a result of the varying refractive index of the crystal as a function of λ. To compensate for GVD in the crystal, the 400

nm and 800 nm beams emitted from BBO1 are separated using a dichroic mirror (DM1), and the 800 nm beam passed through a manual optical delay line (TS1), while the 400 nm beam remains on a fixed path length. By adjusting the path lengths to be equal using TS1, maximum temporal overlap in BBO2 may be attained. Additionally, a $\lambda/2$ waveplate (WP1) rotates the polarisation of the 800 nm beam by 90^{o} to match the 400 nm beam polarisation (*p*-polarisation), which is required for non-linear frequency conversion in type I BBO crystals. Both beams are finally recombined at a second dichroic mirror (DM2) and spatially overlapped in BBO2, producing the desired 266 nm output with a power of ~30 mW along with the remaining SHG and fundamental beams.

Fourth harmonic generation (FHG) is carried out using a similar method to that described for THG, where the 266 nm beam is split from the 400 nm and 800 nm beams using another dichroic mirror (DM3). The 400 nm and 800 nm beams pass through a $\lambda/2$ waveplate (WP2) and manual translation stage (TS2). These beams are then recombined with the 266 nm beam using a dichroic mirror (DM4), and spatially and temporally overlapped into a final 100 μm thick type I BBO crystal (BBO3). Four beams are emitted from BBO3: fundamental, SHG, THG, and the desired 200 nm FHG beam. After exiting the harmonic generation stage, the harmonics and fundamental may be separated using appropriate dichroic mirrors (e.g. DM5).

The BBO crystal thicknesses used in the harmonic stage have been selected to minimise dispersion effects. As femtosecond pulses are energetically broad, but temporally very short, when they pass through a medium of higher density, such as a BBO crystal, GVD causes the higher energy (frequency) components of the pulse to become temporally retarded relative to the lower energy components. The ultimate consequence of this dispersion is the undesired temporal broadening of the femtosecond pulse and the effect becomes more pronounced with increasing pulse energy. Hence, the BBO crystal thicknesses in the harmonic stage decrease as the order of the harmonic generation process increases to minimise this issue.

A labelled photograph of all 4 output beams is shown inset at the top of Figure 2.4, where the harmonics and fundamental have been spatially dispersed using a quartz prism. Table 2.7 presents a summary of the beam characteristics generated from the harmonic generation stage. No power or conversion efficiency measurements are available for the FHG beam as its wavelength is beyond the measurable wavelength

range of the power meter (Gentec-Eo, Uno).

Table 2.7: Summary of the 800 nm harmonics generated using the harmonic generation stage in Figure 2.4. Beam powers and conversion efficiencies are also listed.

Harmonic	Wavelength / nm	Power / mW	Conversion efficiency / %
Fundamental	800	190 ± 2	-
SHG	400	70 ± 2	37
THG	266	30 ± 2	16
FHG	200	-	-

2.2.3 Optical Delay Line and Pump-Probe Delivery

A pair of beams emitted from the harmonic generation stage is used for pump and probe pulses in time-resolved experiments. For the experiments described in the latter chapters of this thesis, the 800 nm fundamental and the 400 nm SHG beams are used as pump and probe, respectively. With reference to Figure 2.5, after exiting the harmonic generation stage the pump-probe beam pair is separated with a dichroic mirror. After

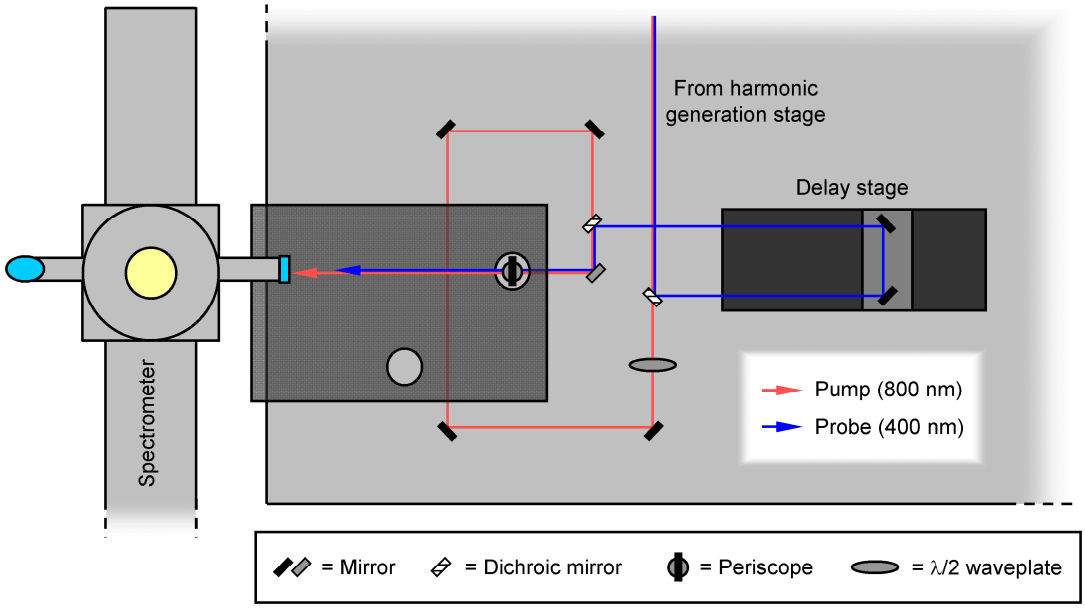

Figure 2.5: Schematic of the optical delay line and optics used for delivering the pump (800 nm) and probe (400 nm) to the detection region of the spectrometer.

separation, the probe pulses are passed along an optical delay line controlled by a motorised delay stage (Physik Instrumente, M-505), which is interfaced to a computer using a universal serial bus (USB) cable and controlled with a program written in LabVIEW 8.5 (see Section 2.6.3). The delay stage has a maximum translation distance of 15 cm, corresponding to a maximum time delay of ~1 ns between the pump and probe pulses. The delayed 400 nm probe beam is then collinearly recombined with the 800 nm pump beam at another dichroic mirror, which has been passed through a fixed delay line, containing a λ/2 waveplate. The λ/2 waveplate ensures that the pump's electric field vector polarisation is the same as the probe's, where both pump and probe polarisations are oriented parallel to the plane of the photoelectron imaging detector (*p*-polarised), described in Section 2.5.2. The pump-probe beam pair is then raised up to an optics platform, comparable in height to the detection region of the spectrometer, using a periscope containing dual-band dielectric mirrors (reflectivity >99 % at 400 nm and 800 nm). Finally, pump and probe pulses are sent unfocussed into the detection region (R6) of the spectrometer through a 1.5 mm thick CaF_2 window (1" diameter) where they perpendicularly intersect a beam of anions. Pump and probe pulses exit the chamber through a 2 mm thick fused silica window cut and mounted to the Brewster angle ($\theta \approx 55.5^{o}$) to reduce any undesired reflections back into the detection region.

2.2.4 Temporal Characterisation

Auto-correlation of the Fundamental

The temporal profile of the 800 nm fundamental may be characterised by measuring its intensity auto-correlation signal, I_{AC} [5]. Briefly, this is commonly performed by sampling a small portion of the fundamental beam, *I*, (<1 mW) and then partitioning this into two separate beams of equal intensity, from here on referred to as I' and I''. These beams are then *collinearly* overlapped in a thin BBO crystal to produce a second harmonic signal at 400 nm. By introducing a temporal delay, τ, between I' and I'', the intensity of the I_{AC} signal as a function of τ may be determined by the convolution relationship [5]:

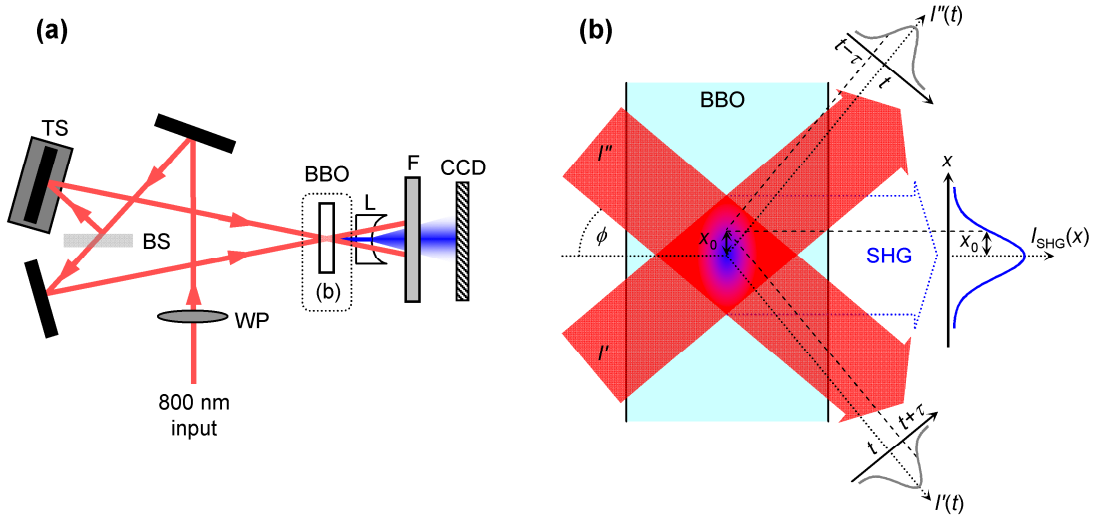

Figure 2.6: (a) Schematic of the delta single shot auto-correlator. A waveplate (WP) is used to select the polarisation of the 800 nm input beam, which is then divided into two beams of equal intensity, I' and I'', using a 50:50 beam splitter (BS). I' and I'' are then spatially overlapped in a BBO crystal at an angle of 2ϕ with respect to each other, resulting in SHG. The 400 nm SHG signal is then dispersed onto a charge coupled device (CCD) array using a lens (L) and the residual 800 nm beams filtered out (F). A mirror mounted on a translation stage (TS) may be used to introduce a temporal delay between I' and I'', and is used to temporally calibrate the auto-correlator. (b) shows a more detailed schematic of the SHG process, where the resultant Gaussian I_{SHG} profile is projected onto the CCD array. The measured I_{SHG} profile can be related to the desired I_{AC} profile through equation (2.10).

$$I_{AC} = \int I'(t) \cdot I''(t-\tau)\, dt\,. \tag{2.8}$$

For Gaussian laser pulses, the resultant convolution over τ will produce a measured Gaussian I_{AC} profile, where the FWHM of the I_{AC} profile, $\Omega(I_{AC})$, is related to the fundamental FWHM, $\Omega(I)$, through the relationship:

$$\Omega(I) = \frac{1}{\sqrt{2}}\Omega(I_{AC})\,. \tag{2.9}$$

Here however, we measure the temporal profile of the 800 nm fundamental using a single shot auto-correlator (Minioptic Technology, Delta Autocorrelator) connected to an oscilloscope (LeCroy, Wavesurfer 44Xs), enabling I_{AC} to be obtained in a single shot. A schematic of the single shot auto-correlator is displayed in Figure 2.6a. As with a standard auto-correlation measurement, the beam is first split into I' and I''. In a

single shot auto-correlation arrangement these two beams are instead overlapped in the BBO crystal *at an angle* of 2ϕ with respect to each other, rather than collinearly. This results in an SHG intensity profile, I_{SHG}, shown in Figure 2.6b, which is filtered from the residual I' and I'' beams, and dispersed onto and captured with a charge coupled device (CCD) array. The measured I_{SHG} profile is related to I_{AC} through [5]

$$I_{\mathrm{AC}} \propto I_{\mathrm{SHG}} = \int I'(t+\tau)\cdot I''(t-\tau)\,dt\,, \tag{2.10}$$

where the delay τ is now geometrically defined with respect to Figure 2.6b as

$$\tau = \frac{x_0 \sin\phi}{c}\,, \tag{2.11}$$

and c is the speed of light in m s^{-1}. By performing a temporal calibration of the auto-correlator a proportionality constant, K_{t}, may be obtained for equation (2.10), providing access to $\Omega(I_{\mathrm{AC}})$ through $\Omega(I_{\mathrm{AC}}) = K_{\mathrm{t}}\cdot\Omega(I_{\mathrm{SHG}})$, where we measure a value of K_{t} = 5.7 × 10^{-11}. From these single shot auto-correlation measurements, $\Omega(I)$ is finally obtained using equation (2.9), providing a measured temporal pulse width of 42 ± 10 fs for the 800 nm fundamental.

Cross-correlation of the Fundamental and Second Harmonic

The temporal resolution attainable in TRPEI experiments is ultimately governed by the temporal width of the pump-probe pulse pair, defined here as the 800 nm fundamental and the 400 nm SHG beam, respectively. The temporal width of this pulse pair can be measured *via* their intensity cross-correlation, I_{XC}, in a thin BBO crystal (200 μm thick), used to generate third harmonic signal. These measurements are performed in a similar manner to a standard auto-correlation measurement (not single shot), except the convolution of the two pulses is now defined as

$$I_{\mathrm{XC}} = \int I_{\mathrm{pu}}(t)\cdot I_{\mathrm{pr}}(t-\tau)\,dt\,, \tag{2.12}$$

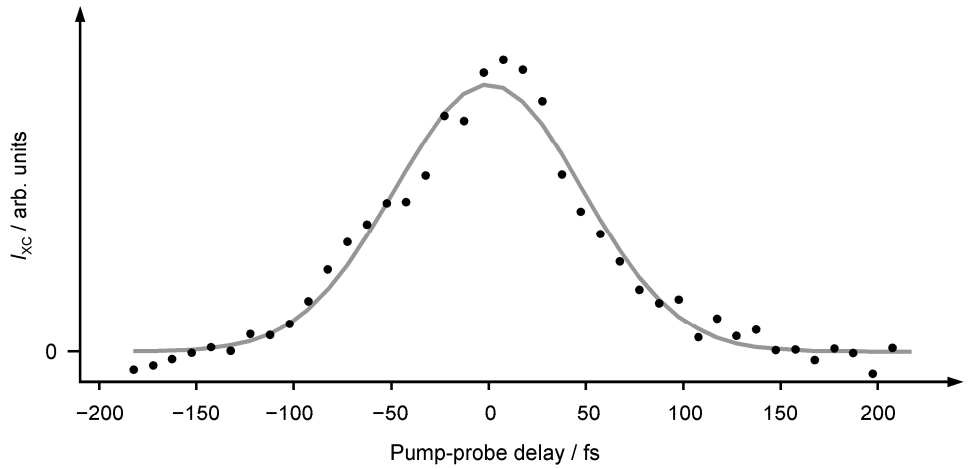

Figure 2.7: Third harmonic intensity profile, I_{XC}, produced from the cross-correlation of the fundamental (800 nm) and second harmonic (400 nm) in a 200 μm thick BBO crystal. The cross-correlation profile (solid circles) has been fitted to a Gaussian pulse profile (grey line), using a linear least squares fitting method. The measured FWHM of the power profile is 114 fs, corresponding to a temporal width of 80 ± 15 fs for the pulse pair.

where I_{pu} and I_{pr} are the intensities of the pump and probe beams, respectively. Here we determine their cross-correlation by measuring the intensity of the I_{XC} profile generated in the harmonic generation stage, using a fast photo-diode (Thorlabs, DET10A/M) connected to an oscilloscope. The measured I_{XC} profile is shown in Figure 2.7 as solid circles, with a least squares fit to a Gaussian profile shown as a solid grey line. Using an analogous relationship to that shown in equation (2.9), the FWHM of the cross-correlation power profile (114 fs) can be used to determine the FWHM of the pump-probe pulse pair, which provides a measured temporal width of 80 ± 15 fs. However, this measurement will provide an underestimate of the true temporal width of the pulse pair in a time-resolved experiment, as the pulses must pass through a CaF_2 window into the detection region of the spectrometer. This will have the effect of temporally stretching the pulses as a result of dispersion, discussed in Section 2.2.2. To attain a more accurate measurement of the pulse pair's temporal width, we may in principle measure the pump-probe cross-correlation within the detection region, using techniques such as above threshold electron detachment (ATD) from iodide anions. Using this method will take into account any additionally temporal dispersion, providing a more accurate cross-correlation measurement, although the method used to generate the profile in Figure 2.7 provides a sufficient estimate of the temporal

resolution in time-resolved experiments.

2.2.5 Frequency Characterisation

The frequency spectrum of the 800 nm fundamental is characterised using a fibre-optic UV-Visible spectrometer (Ocean Optics, Red Tide USB650), with a resolution of 2 nm, interfaced to a computer using a USB cable. The measured spectrum is shown in Figure 2.8 (black line), where the fundamental's frequency profile has been fitted to a Gaussian profile (dashed grey line, linear least squares fit), yielding a measured FWHM bandwidth of ~35 nm centred at a wavelength of 798 nm, correlating to an energy bandwidth of ~68 meV centred at 1.54 eV. For a transform limited femtosecond pulse with a Gaussian profile the time-bandwidth product (see equation (1.8) in Chapter 1) may be used to determine that, an energy bandwidth of 68 meV ($\Delta\nu$ ~ 1.6×10^{13} Hz) correlates to a temporal pulse width Δt ~ 30 fs. However, the temporal width of the pulse as measured by the single shot auto-correlator in Section 2.2.4 is 42 fs, indicating that the pulses are not truly transform limited, although the deviation is only ~10 fs from the expected transform limit value. A possible explanation for the deviation from the transform limit may be due to deviations from a truly Gaussian pulse profile, in either the time or frequency domains. Auto-correlation measurements indicate that minimal compensation is required for a non-Gaussian temporal profile, although the measured

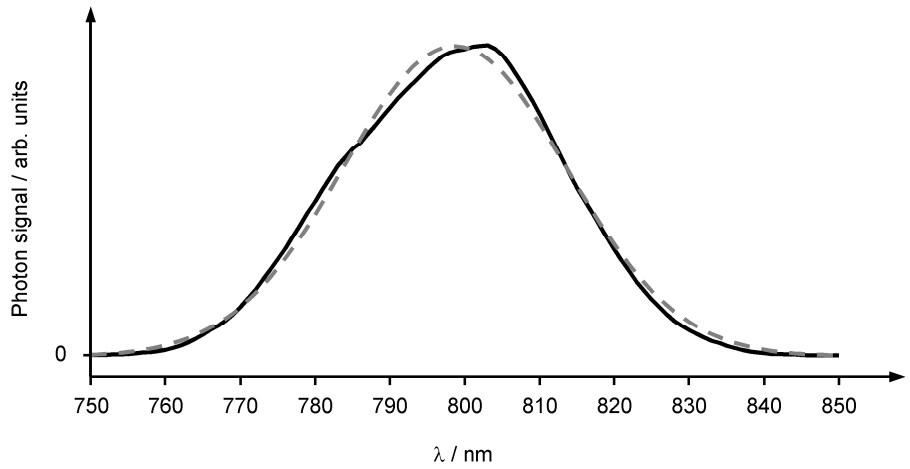

Figure 2.8: Frequency spectrum of the 800 nm fundamental pulses (black line). This spectrum has been fitted to a Gaussian profile (dashed grey line), using a linear least squares fitting method. The wavelength FWHM of the profile is measured to be ~35 nm (~68 meV) and is centred at 798 nm (1.54 eV).

frequency profile of the fundamental is not truly Gaussian and could potentially account for a divergence from the transform limit.

2.3 Source Region

Having presented an overview and characterisation of the femtosecond laser system used to perform TRPEI experiments, we now move on to describe the spectrometer in greater detail. We begin by describing the source region of the spectrometer, which consists of the first two differentially pumped chambers (R1 and R2).

2.3.1 Electrospray Ionisation Source

General Operation

An ESI source is used to generate the gas phase molecular anions of interest. The fundamental principles involved in this soft ionisation process have previously been described in detail in Section 1.2.3. The full ESI source arrangement, which operates at atmospheric pressure, is schematically shown in Figure 2.9a.

A solution containing the anions of interest is prepared and then drawn into in a quartz syringe (Supelco, Hamilton 1000 series). The concentration of the solution is variable depending on the molecular species of interest, but is usually in the range of 10^{-3} to 10^{-5} M. Similarly, the solvent used to make up the solution may also vary depending on the nature of the solute, although it commonly consists of a mixed methanol / water (MeOH / H_2O) solvent or pure acetonitrile (MeCN). The 0.72 mm o.d. syringe needle (Supelco, Hamilton 7780-04) is placed into a polyether ether ketone (PEEK) syringe fill port (VICI, C-VISF-1H), shown labelled in Figure 2.9a, which connects the syringe to a $\frac{1}{16}''$ o.d. PEEK transfer line (Supelco, Z227293). The solution is then flowed through this transfer line, which is connected to the ESI source, at a rate of 250 μl hr^{-1} using a syringe pump (World Precision Instruments, Aladdin 1000). The flowed solution subsequently enters the ESI source, which is shown in more detail in Figure 2.9b, and primarily consists of a stainless steel capillary (i.d. ≈ 100 μm). The ESI capillary is biased to a high negative voltage of approximately –3 kV using a commercial electrospray high voltage supply module (Applied Kilovolts,

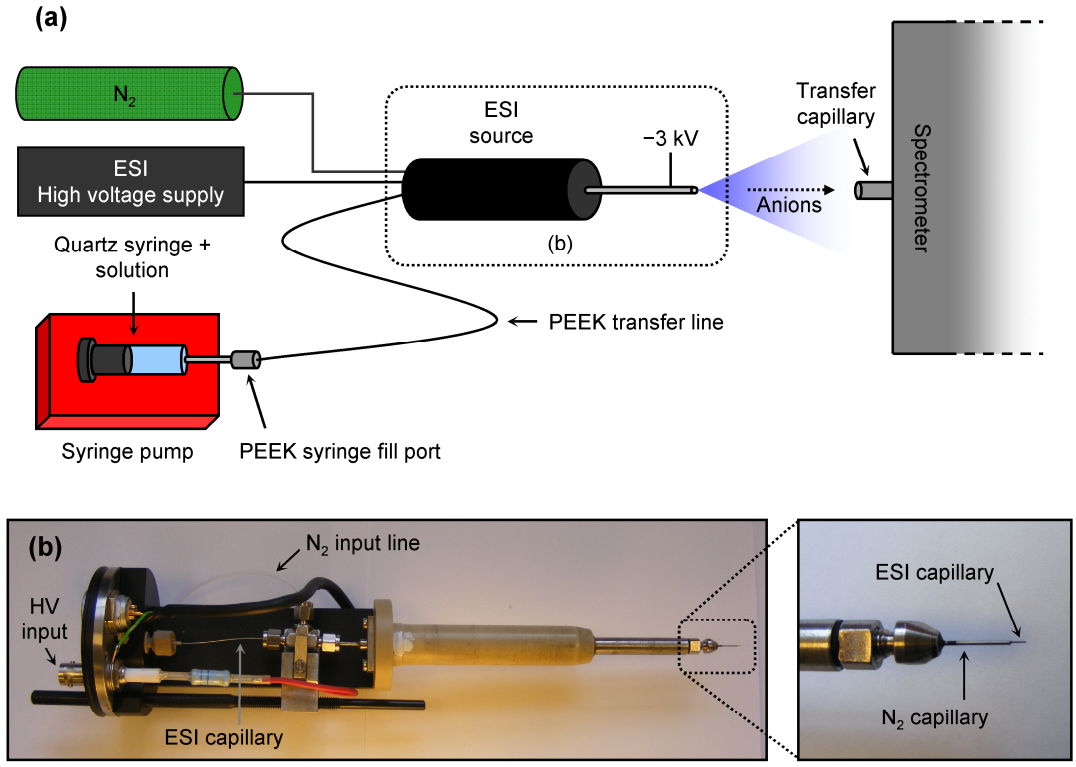

Figure 2.9: (a) Schematic of the electrospray ionisation (ESI) source arrangement used to generate molecular anions of interest. The source consists of a syringe pump and quartz syringe, a PEEK transfer line, and the ESI source, which operates at atmospheric pressure. (b) shows a photograph of the inside of the ESI source, with an enlarged view of the ESI tip on the right.

ES008RCP150) operating in constant current mode. As the flowed solution exits the tip of biased ESI capillary an aerosol of negatively charged droplets, containing the anions of interests, is generated. As shown in Figure 2.9b, the biased ESI capillary itself is housed within a second larger capillary, which may be used to delivery a constant flow of nitrogen drying gas at room temperature around the diverging ESI aerosol; this is commonly referred to as a nebulising gas. Nebulising gas is commonly used to enhance the degree of solvent evaporation from the anions of interest in outgoing aerosol plume, thus reducing the fraction of solvent/solute clusters entering the spectrometer. Here however, the nebulising gas has not been utilised. The tip of the ESI source is placed at a distance of ~1 cm from the entrance of a stainless steel capillary, which defines the interface between the ESI source and the first differentially pump region of the spectrometer (R1). The details of the capillary interface are described in more detail in Section 2.3.2.

Electrospray Source Characterisation

Measurements of the ion current emitted from the ESI source were performed using a Faraday cup placed immediately prior to the vacuum interface. Currents were measured using a picoammeter (EM Electronics, DC Picoammeter E26), capable of measuring currents as low as 0.1 pA. For the source characterisation, a 6 mM solution of NaI (Sigma-Aldrich, >99.5 %) in a mixed MeOH / H_2O (80:20, respectively) solvent was sprayed. The ESI high voltage supply module was set to a constant current of 0.21 μA producing a voltage of –2.9 kV on the ESI source. Under these source conditions, an ion current of ~0.2 μA was measured at the Faraday cup, in accordance with recent measurements by Colburn *et al*. [6]. As the measured voltage on the high voltage supply increases, the measured current at the Faraday cup also increases in an approximately linear manner, however, as the voltage and in turn electric field strength increases, the measured current becomes less stable. From these characterisation tests it was concluded that the optimum ESI voltage for the current source arrangement is approximately –3 kV.

Similar tests were also conducted by varying the properties of the NaI solution to gain an understanding of how these properties affect the stability of the ion source. In these tests, the concentration and solvent ratio prove to be crucial to the stability of the electrospray aerosol. With regards to the former, concentrations below 10^{-5} M and above 10^{-2} M generate notably unstable ion currents, where low concentrations also lead to a significant reduction in the measured ion current. For the latter, mixed solvents containing high fractions of H_2O (>50 %) generate unstable aerosols, in line with previous experimental observations and theoretical models of ESI, described in Section 1.2.3.

2.3.2 Vacuum Interface: Region 1

A cross-sectional schematic of the first differentially pumped region of the spectrometer (R1) is shown in Figure 2.10. The aluminium source chamber has been designed and manufactured in-house and contains R1 and a section of the second vacuum region of the spectrometer, R2. R1 is partitioned from R2 within the source chamber by a stainless steel tube which is sealed to the source chamber and the custom-made R2

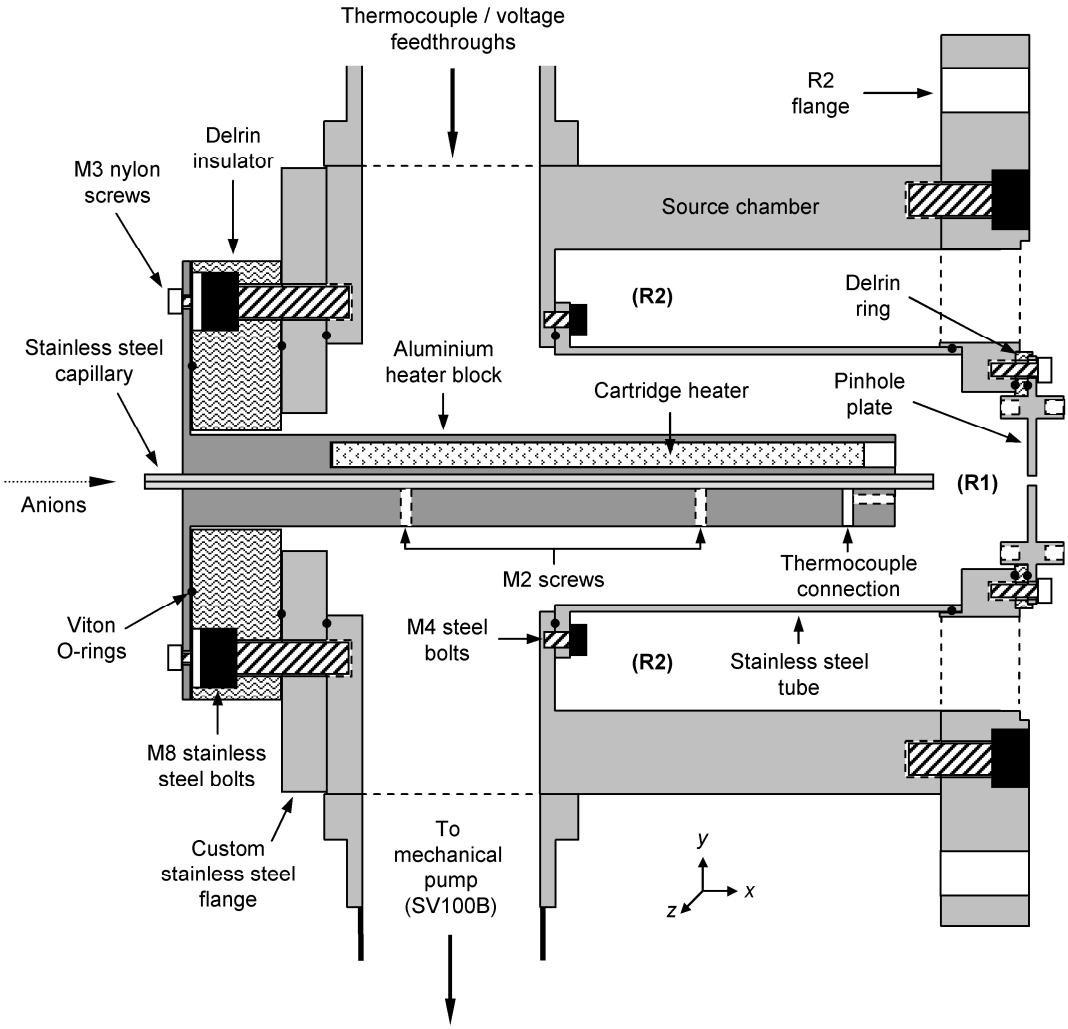

Figure 2.10: Cross-sectional schematic of the first vacuum region of the spectrometer (R1), which houses a heated capillary interface. Schematic is not-to-scale.

flange with Viton O-rings. The end of R1 is defined by a stainless steel pinhole plate (1 mm i.d.) mounted and sealed onto the R2 flange using M3 Teflon screws and Viton O-rings. The pinhole is electrically isolated from the flange using a Delrin insulator ring.

Heated Capillary Interface

Anions generated from the ESI source enter the first vacuum region through a stainless steel capillary (600 μm i.d., 18 cm long) mounted within an aluminium heater block (2.2 cm o.d., 16 cm long). The front of the heater block has a 10 cm diameter (dia.) plate, which is used to mount the heater block onto a Delrin block (2 cm thick) with a 2.4 cm dia. hole at its centre. This Delrin block is used to electrically isolate the heater

block assembly from the main source chamber, and is subsequently mounted onto the face of a stainless steel flange. The entire arrangement is bolted onto the front of the source chamber using M8 steel screws and is sealed to vacuum using a series of Viton O-rings. All tapped threads in the aluminium source chamber have Heli-coil inserts embedded within them to prevent the aluminium threads from being damaged by the steel bolts.

Anions are aerodynamically encouraged into the spectrometer through the heated capillary interface, which is biased at a negative DC voltage, typically –50 V, using a custom-made voltage supply, constructed in-house, and forms a chain of 4 DC voltages applied throughout the source region of the spectrometer. Each voltage output from the supply is floated on top of the previous in the chain. These DC voltages are from here on referred to as V_1 - V_4, where the heater voltage, V_4, is the largest in magnitude and the last in the series. V_1 - V_3 are described throughout the remainder of Section 2.3.

The stainless steel capillary is heated to a temperature of ~80 ^{o}C using the aluminium heater block, which contains an embedded cartridge heater (RS, 837-537). As anions pass through the capillary further solvent evaporation occurs, and the temperature at which the heater is set ultimately controls the extent of this desolvation process. Anions then exit the heated capillary into R1 and migrate towards the first differential pinhole, which defines the division between R1 and R2. This pinhole plate is placed at a voltage of V_3 ~ –40 V. By increasing the pressure in R1, the portion of anion current transferred through the first differential pinhole can be optimised through collisional focusing. In general, the pressure in R1 is increased to an operational pressure of ~5 Torr, by manually throttling an in-line mechanical valve (labelled V1 in Figure 2.1 on page 51) placed between R1 and the SV100B mechanical pump used to evacuate this region.

Capillary Temperature Control

The temperature of the heated capillary interface is monitored and controlled using a type K thermocouple connected to a proportional, integral, and derivative (PID) loop controller (West Instruments, 2300). The method of PID process control is well established [7,8] and is illustrated in Figure 2.11 with respect to controlling the temperature of the heated capillary. The basic premise of the control process is to

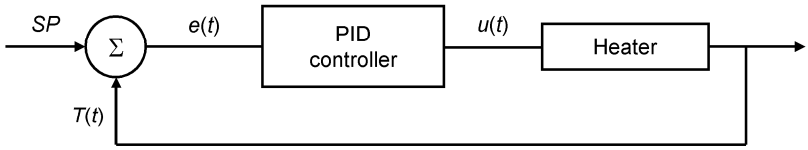

Figure 2.11: Proportional, integral, and derivative (PID) control loop process used to monitor and control the temperature of the heated capillary interface. A type K thermocouple monitors the temperature of the of the capillary, $T(t)$, and compares this with a set-point temperature, *SP*, to generate an error signal, $e(t)$. The controller then uses $e(t)$ to change the voltage, $u(t)$, applied to the heater and control $T(t)$.

measure the temperature of the heater, $T(t)$, as time progresses, and compare this to the desired set-point temperature, *SP*, to generate an error signal, defined as $e(t) = SP - T(t)$. The aim is then to minimise this error function to a value of $e(t) = 0$ as quickly as possible. Here this is achieved by generating a variable output from the controller, $u(t)$, to change the voltage applied to the heater cartridge, through a combination of the proportional, integral, and derivative control. Proportional control is the simplest component of the control process, and $u(t)$ is defined by $u(t) = K_P e(t)$ where K_P is a constant of proportionality. For this process the choice of K_P plays a vital role and can significantly affect the outcome of the control process. To understand this in better detail we now consider the temporal behaviour of the process. As the process aims to attain a value of $e(t) = 0$ as rapidly as possible, at early times the chosen value of K_P will be large. However, at longer times in the process large K_P values will lead to the process overshooting the *SP* value, and so a smaller K_P value is required, although small K_P values can lead to undesired slow response times. Finally at very long times, K_P must again be large to ensure that the $e(t) = 0$ condition is achieved, which leads to a steady-state offset between $T(t)$ and *SP*. From this analysis, it becomes apparent that the required form of K_P is not a constant and can potentially become quite complex. To alleviate this issue, integral and derivative control may be introduced in addition to proportional control.

Integral control studies the history of $e(t)$ and is proportional to the size of $e(t)$ over the duration of the error. As it measures the sum of $e(t)$ over time, integral control provides a measure of the steady-state offset introduced by proportional control, ultimately eliminating it. However, as it monitors the accumulated history of $e(t)$, rather than the present $e(t)$, it can lead to the controller moving past the ideal *SP* value.

To compensate for this additional overshoot, which occurs as a result of integral control, differential control is introduced. This control process looks at the rate of change of $e(t)$ over time, and reduces overshoot of *SP* by minimising the gradient of $e(t)$, although such control processes are particularly sensitive to noise in $T(t)$.

In a PID controller all three of the components described above are used and the final $u(t)$ term used to control $T(t)$ will be

$$u(t) = K_P e(t) + K_I \int_0^t e(t)dt + K_D \frac{de(t)}{dt}, \tag{2.13}$$

where K_I and K_D are constants which weight the integral and derivative terms, respectively. The PID control process may be optimised by careful selection of the three constants. Here these parameters have been optimised by a trail and error analysis of the heating process and have values of K_P = 0.1, K_I = 0.02 s^{-1}, and K_D = 0.2 s. Under these conditions the heating control process produces heater block temperatures stable to within ±1 ^oC. However, the type K thermocouple probe is embedded within aluminium heater block and does not directly measure the temperature of the stainless steel capillary interface. Independent temperature measurements of the transfer capillary itself using an external type K thermocouple probe, indicate that the temperature of the capillary is ~10 ^oC less than that of the aluminium heater block. Importantly though, these separate temperature measurements of the heated capillary show that its temperature is also stable to within ±1 ^oC.

2.3.3 Ion Guiding and Trapping: Region 2

A cross-sectional perspective of R2 is schematically shown in Figure 2.12. This region is partitioned from region 3 of the spectrometer (R3) by an aluminium top hat which is bolted into the R2 flange using M6 bolts. A stainless steel pinhole (1.8 mm dia.) plate defines the interface between R2 and R3, which is electrically isolated from and mounted onto the centre of the top hat using a Delrin insulator and M4 Nylon screws, respectively. The entire arrangement is sealed using Viton O-rings. As anions pass into R2 they enter an ion guide which we now subsequently describe in more detail.

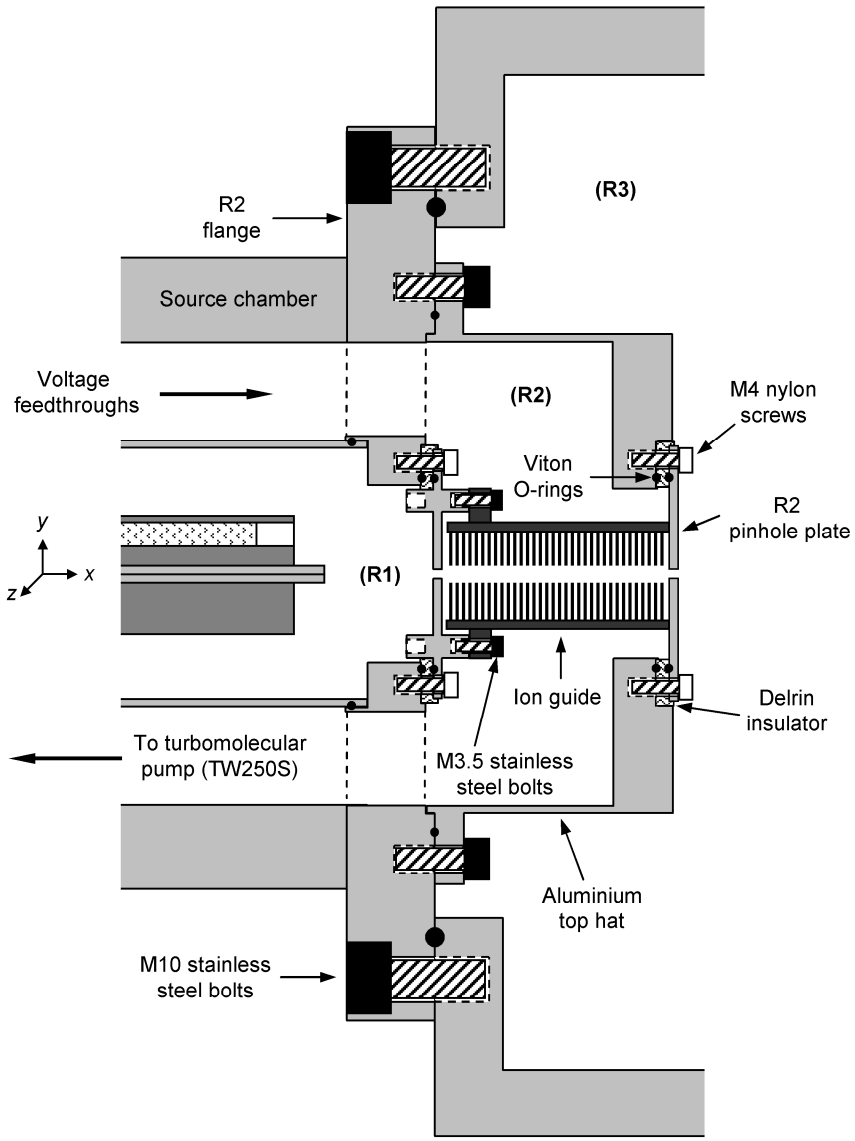

Figure 2.12: Cross-sectional schematic of the second region of the spectrometer (not to scale). Region 2 houses and ion guide and trap which is used to: (1) radially confine and focus the divergent anion beam; and (2) covert the continuous anion beam to a pulsed source, synchronous with the repetition rate of the femtosecond laser system (1 kHz).

The Need for Ion Guiding and Trapping

To successfully implement a photoelectron imaging detector into the spectrometer, an appreciable number of anions must be transferred to the detection region to generate an image of sufficient quality. When considering a one-colour photoelectron imaging experiment performed with the 1 kHz femtosecond laser system, described in Section 2.2, in conjunction with a pulsed anion source, we may estimate that ~10^3 ions per ion

packet are required to generate ~10 electrons per laser shot.[3] Similarly, for the same number of anions per packet one may conservatively anticipate that two orders of magnitude less electron signal (~0.1 electron per shot) will be observed in a two-colour TRPEI experiment, corresponding to ~10^2 electrons per second, which is ample to collect an individual image of reasonable quality (~10^4 total electron counts) over a duration of ~10 minutes.[4] However, one of the major drawbacks of the ESI method for anion generation is that the technique must be carried out at atmospheric pressure. As a result, the divergent anion beam produced from the source commonly passes through a successive number of differential apertures in the spectrometer, to enable the detection region to be at an appreciably low base pressure (~10^{-9} Torr) for photoelectron spectroscopy (PES) to be performed. This leads to a significant reduction of ion current in successive regions of the spectrometer. Experimental measurements show that in such a scenario, as little as 1 part in 10^6 of the original ion current generated at atmosphere reaches the detection region of the spectrometer [6]; for an initial current of 0.2 μA measured in Section 2.3.1 this translates to a conservative estimate of as little as 0.2 pA at the detection region. To circumvent this issue, ion guiding devices, such as hexapoles and radio-frequency (RF) only quadrupoles, are commonly utilised in the second pressure region of ESI spectrometers (typically 1 to 100 mTorr). Such devices provide viable alternatives to electrostatic ion optics (e.g. Einzel lenses) which are ineffective at such high pressures as a result of collisions between ions and background gases. Due to spatial restrictions, a compact ion guide based on the principles of an ion funnel [9,10] has been incorporated into the second differentially pumped vacuum region of the new spectrometer, which is loosely based on the ion funnel design implemented by Wyttenbach *et al.* [11]. Ion funnels consist of a series of planar electrodes with axisymmetric holes at their centre, where the holes reduce in size from the entrance to the terminus of the device. The guide described here differs from this

[3] This estimate is based on: (1) an unfocused 266 nm (4.66 eV) laser beam with a beam width at FWHM of 0.2 cm and an energy of 30 μJ/pulse; and (2) a cross-section for electron detachment, σ, of 10^{-17} cm^2. The number of electrons per laser shot, #e$^-$, may then be calculated using $\#e^- = N\sigma\gamma$, where γ is the number of photons per cm^2 in a single laser shot and N is the number of anions per packet.

[4] For a two-photon process, the cross-section for excitation, σ_{ex}, must also be included, and the number of electrons per shot can be determined using $\#e^- = N\sigma_{ex}\gamma_1\sigma\gamma_2$, where γ_1 and γ_2 are the number of photons per cm^2 per shot in the excitation and detachment pulses, respectively. Here we approximate this as $\#e^- = N\sigma^2\gamma^2$.

original design, as the holes at the centre of the electrodes are instead all equal in size. By applying a pair of out-of-phase RF voltages to alternating electrodes of the device, a pseudo Paul trapping effect is induced along the central axis of the device. This Paul trapping phenomenon [12] is considered in Figure 2.13. Applying an out-of-phase RF voltage pair in the configuration described above causes a 'saddle' potential to be generated between alternating electrodes of the device (t = 0 in Figure 2.13). At this point the anions will be attracted towards the positive region of the potential surface, +V, and gain kinetic energy. As time evolves and the potential produced by the RF voltages changes $(t = T/2)$, the region of the potential that was positive will now have 'flipped' to become negative, –V, converting the kinetic energy gained by the anions in this region into potential energy, and ultimately repelling them. Provided the frequency and amplitude of the RF voltages are sufficient, this sequential process causes anions to be confined around centre of the potential. In a Paul trap, anions are confined in all directions, whereas the potential generated in an ion funnel merely traps and focuses anions radially, allowing them to propagate along the central axis of device, hence the potential is only referred to a pseudo Paul trap. Utilising ion funnel based devices enables the portion of ion current transferred to the detector region to be enhanced by up to an order of magnitude [13], subsequently improving the quality and reducing the time required to obtain an acceptable photoelectron image.

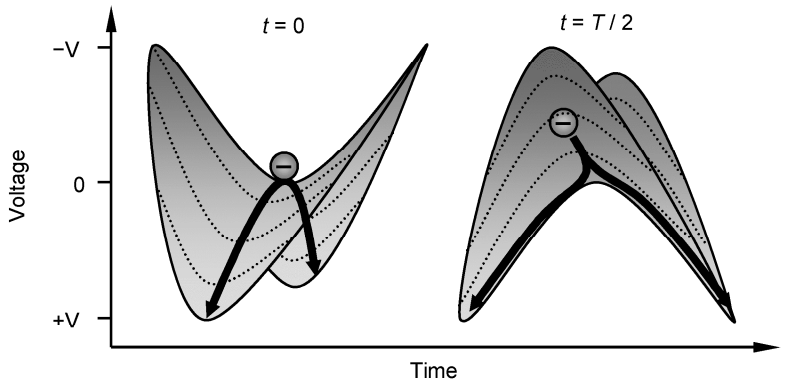

Figure 2.13: Schematic illustration of the Paul trapping phenomenon. A 'saddle point' potential is generated using a pair of out-of-phase RF voltages. Both RF voltages have a characteristic oscillation period of T. Initially (t = 0) anions gain kinetic energy as they are attracted towards the positive region (+V) of the 'saddle point' potential. As the RF voltages change with time ($t = T / 2$), the positive region of the potential 'flips' to become negative converting the anions kinetic energy into potential energy, thus repelling it towards the field free region at the centre of the potential. As this process repeats, it ultimately leads to the confinement of anions around the field free region of the potential.

In addition to the issue of ion current loss, anions generated from ESI sources are also continuous, whereas femtosecond laser systems are inherently pulsed and govern the repetition rate of the experiment. Hence, the anion source must first be converted into a pulsed source synchronous with the laser repetition rate (1 kHz). For laser systems with low repetition rates (<1 kHz), a standard method used to circumvent this issue is to implement a pulsed RF Paul trap. Analogous to the ion funnel device described above, these traps use a pair of pulsed out-of-phase RF voltages operating in the MHz frequency regime. One RF voltage is applied to a central ring electrode while the second is applied to a pair of 'end cap' electrodes (see Figure 2.11 in reference [14]). When the RF voltages are pulsed on, ions are radially confined leading to their accumulation around the centre of the trap. When pulsed off, ions are encouraged to exit the trap by applying appropriate DC voltages to the end caps. However, instabilities in the pulsed RF voltages arise at high repetition rates (≥1 kHz), making these traps difficult to implement into experiments which use femtosecond laser systems. Due to this technological restriction, the ion guide implemented in R2 has been adapted to incorporate a low voltage pulsed DC trap at its terminus, which conveniently avoids the need for any pulsed RF voltages. This trap enables anions to be efficiently trapped at a 1 kHz repetition rate, and a similar method has previously been used by Wyttenbach *et al*., with a measured unit trapping efficiency [11]. Based on the minimum projected ion current at the detection region of 0.2 pA in continuous mode and a unit trapping efficiency, approximately 10^3 ions per packet at 1 kHz may be expected, in line with the required anion number estimates discussed above.

Design, Construction and Operation of the Ion Guide

The ion guide consists of 33 steel electrodes mounted between two custom designed printed circuit boards (PCBs). These individual components are shown in Figures 2.14a to 2.14c. The electrodes, shown in Figure 2.14a, have dimensions of 11.98 mm × 19.08 mm × 0.20 mm (width × height × thickness). All electrodes have an axisymmetric hole at their centre (3.20 mm diameter) to allow the passage of anions along the central axis of the guide and are equally spaced by 1.47 mm. Holes at the top and bottom of the electrodes (3.0 mm diameter), have also been incorporated for assembling the ion guide. 0.5 mm wide pins at the top and bottom of the electrodes allow them to be soldered to

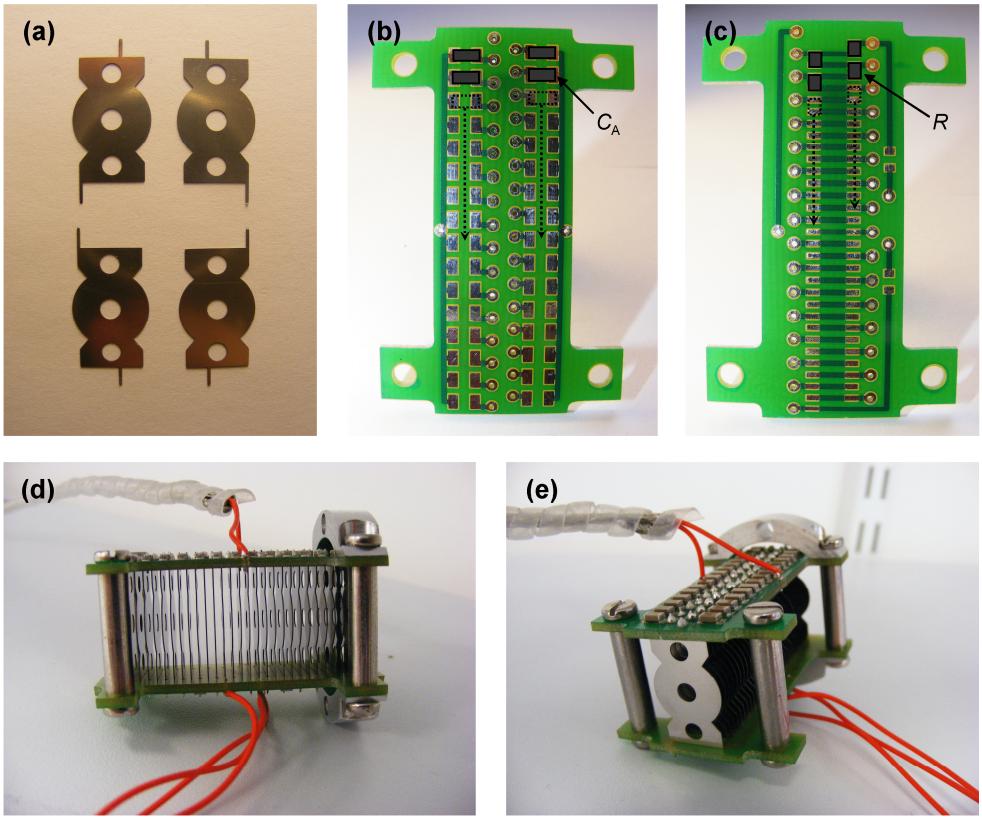

Figure 2.14: (a) Electrodes used in the ion guide, shown in the four unique configurations. Top (b) and bottom (c) printed circuit boards (PCBs) used for the ion guide. Also shown on (b) and (c) are the positions of the surface mounted capacitors, C_A, and resistors, R. (d) and (e) show photographs of the ion guide incorporated into the second region of the spectrometer, shown from a side (d) and end elevation (e). No photographs are to scale.

the copper tracks (0.5 mm wide) on the PCBs, and can potentially be arranged in four unique configurations (see Figure 2.14a), although only two are utilised for the ion guide. The copper track arrangements on the top and bottom PCBs are shown in Figures 2.14b and 2.14c, respectively. Both PCBs have dimensions of 50.0 mm × 33.1 mm × 1.6 mm (length × width × height) and are held together by four stainless steel rods (19.08 mm long, 5.00 mm diameter) tapped at either end for M3 screws. A pair of custom made mounts are attached to the top and bottom of the guide at its entrance using the stainless steel rods, and the entire ion guide assembly is mounted onto the R1 stainless steel pinhole plate with M3.5 screws. Photographs of the complete ion guide assembly are shown in Figures 2.14d and 2.14e from side and front elevations, respectively.

A diagram of the ion guide circuit is displayed in Figure 2.15. With reference to

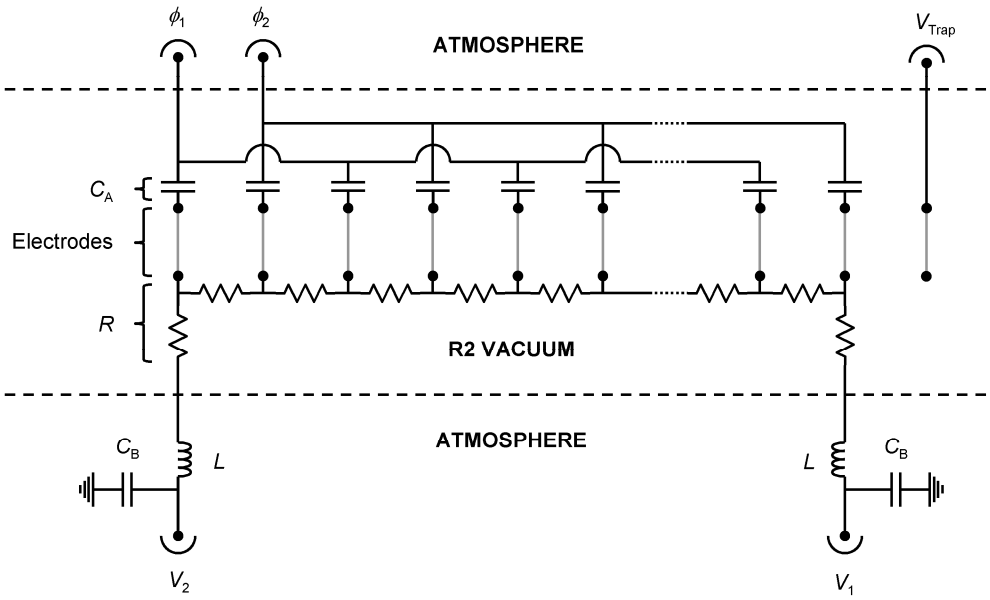

Figure 2.15: Circuit diagram for the ion guide. DC voltages generated from a custom-made power supply are applied to the first and penultimate electrodes of the guide, V_2 and V_1, respectively. RF voltages, ϕ_1 and ϕ_2, are coupled to the electrodes using a series of 100 pF capacitors, C_A. These capacitors also serve to form a resistor-capacitor (RC_A) circuit with a series of 1 MΩ resistors, to decouple the DC voltage from the RF power supply. Similarly, RF voltages are decoupled from the DC power supply using two inductor-capacitor (LC_B) circuits. A pulsed voltage, V_{Trap}, is applied to the final isolated electrode of the guide, which forms an ion trap.

this figure the first and penultimate electrodes of the device are placed at separate DC voltages, V_2 ~ –35 V and V_1 ~ –20 V, respectively. By placing a series of 1 MΩ surface mounted resistors, *R* (TYCO, CRG0805F1M0), between each of the first 32 electrodes, as schematically illustrated in Figure 2.14c, a DC voltage ramp is generated. The axial potential gradient of the voltage ramp causes the anions to propagate towards the exit of the guide. In addition to these DC potentials, a pair of RF voltages, ϕ_1 and ϕ_2 (1-2 MHz, 100-250 V_{pp}), are applied to the electrodes. Alternating electrodes have an RF voltage applied to them which is out-of-phase from the previous electrode, leading to the radial confinement and focusing of anions along the central axis of the guide. The pair of RF voltages are generated using a commercial self-oscillating power supply (Ardara Technologies, PSRF-100) and are coupled to the DC voltage ramp using 100 pF capacitors rated at 3 kV, C_A (PHYCOMP, 225002111536), shown in Figure 2.14b. The capacitors and resistors which make up this resistor-capacitor (RC) circuit are surface mounted onto the top and bottom PCBs, respectively. Similarly, the RF voltages must also be decoupled from the custom-made DC power supply. This is achieved with two

inductor-capacitor (LC) circuits, where the capacitors, C_B (Vishay, 222237520104), and inductors, L (EPCOS, B82144A2105J), are rated at 100 nF and 1 mH, respectively. These LC circuits are implemented outside the spectrometer and in between the DC power supply and the ion guide.

The final electrode of the ion guide is electrically isolated from the first 32 electrodes, and serves to form an electrostatic trap in which anions can be accumulated for ~1 ms, prior to them being extracted and injected into the next differentially pumped region of the spectrometer (R3). To close the trap, it is placed at a voltage, V_{Trap}, more negative than the end of the DC voltage ramp (V_1), typically –50 to –80 V. The trap is then opened by pulsing V_{Trap} to a voltage which is less negative than the end of the voltage ramp. This pulsed voltage is generated using a custom built fast voltage pulser, which has been designed and constructed in-house. It takes ~2.5 μs to empty the trap, and the main source of ion loss in the current trapping arrangement occurs as a result of space-charge repulsion due to the small dimensions of the trap, discussed below. The m/z range over which the trap operates can be roughly tuned by modifying the amplitudes of the RF voltages. Additionally, ions contained within the trap will be in

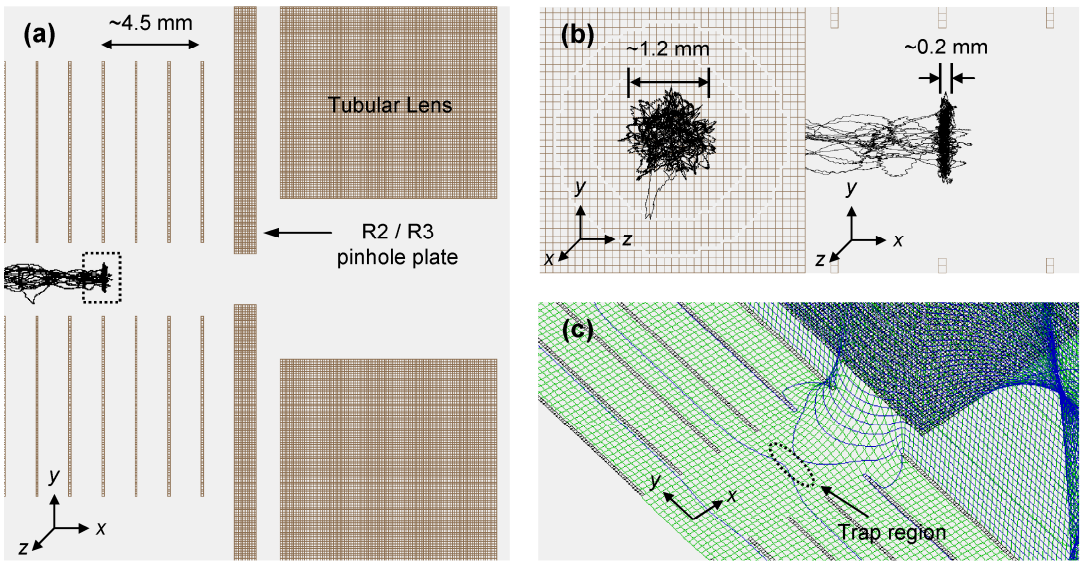

Figure 2.16: (a) Simulation of the ion trap incorporated at the end of the ion guide in region 2 of the spectrometer. The simulation parameters used are displayed in Table 2.8. Singly charged anions with a masses of 127 amu were simulated for a total flight period of 1 ms. (b) displays the ion trap along the axis of the ion guide (x co-ordinate) towards its exit (left) and from a cross-sectional perspective (right). (c) shows the (absolute) potential energy surface generated by the DC voltages in the ion trap region. Electric field lines are shown in blue.

thermal equilibrium with the background gas in R2 of the spectrometer, as a result of the numerous collisions they undergo during their passage through the ion guide. This provides an approximate internal temperature of 298 K for anions ejected from the trap.

The ion trap has been modelled using the Simion 8.0 simulation package. In this simulation RF voltages, DC voltages, and the trap pressure are controlled by a command script coded in Lua. A copy of this script code is provided in Appendix A. The results of the simulation are presented in Figure 2.16 and the associated simulation parameters are displayed Table 2.8. Anions were simulated for a total flight period of 1 ms for 20 singly charged anions of mass 127 amu. These simulations indicate that the ion trap is situated ~4.5 mm from the exit of the guide and has approximate dimensions of 1.2 mm × 0.2 mm (diameter × width), providing an estimated trap volume of ~0.2 mm^3. Although the simulation does not take into account repulsive space-charge effects, this simulated trap volume may be used to estimate the total number of ions which may be stored in the trap. Based on the space-charge limit of ~10^3 ions per mm^3 [15,16], we therefore estimate that the ion trap may only accommodate ~200 ions.

Table 2.8: Simulation parameters used for modelling the ion trap (results shown in Figure 2.16). The initial energy imparted to the anions is defined by a Gaussian distribution where the FWHM of the distribution is displayed in parentheses next to the centre of the energy distribution.

Simulation parameter	Value
V_{Trap}	–60 V
V_1	–20 V
V_2	–35 V
RF voltage	100 V_{pp}
RF frequency	1 MHz
Trap pressure	1×10^{-2} Torr
Initial ion energy (FWHM)	0.5 eV (0.2 eV)

2.4 Time-of-Flight Region

The time-of-flight (TOF) region of the spectrometer consists of three differentially pumped vacuum sections (R3 - R5). The first of these vacuum regions (R3) is shown schematically Figure 2.17, and is constructed from a custom stainless steel cube

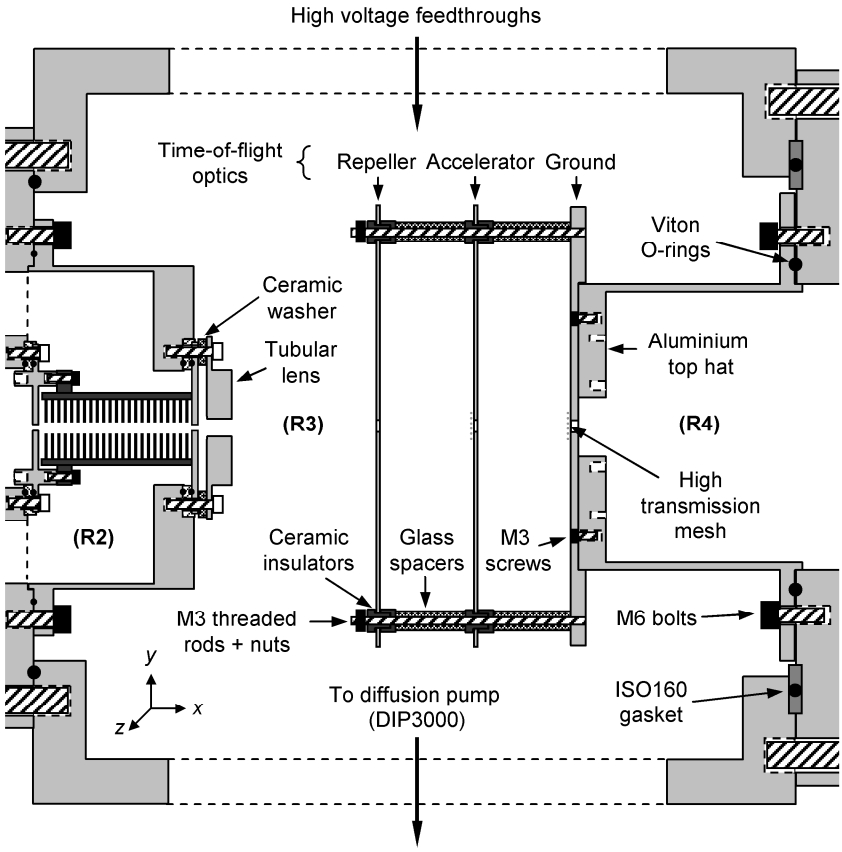

Figure 2.17: Cross-sectional diagram of the third region of the spectrometer (not to scale). Region 3 houses an electrically grounded tubular lens to collimate the pulsed anion beam, injected from the ion trap, into the centre of a collinear Wiley-McLaren time-of-flight (TOF) spectrometer.

chamber (Kurt J. Lesker) with 5 ISO160 vacuum ports and a custom designed port on the remaining face, onto which the source region of the spectrometer is bolted using M10 bolts *via* the R2 flange (see Figure 2.12). R3 is partitioned from the next region of the spectrometer (R4) by an aluminium top hat, which is bolted and sealed onto the inside face of an ISO160F to ISO100F zero length reducer flange, using M6 bolts and a Viton O-ring, respectively. This flange is then bolted and sealed to the main cube chamber, on the face opposite the source region. The differential interface between R3 and R4 is defined by a 5 mm diameter aperture at the centre of the ground plate of the TOF optics, which are described in more detail in Section 2.4.2.

2.4.1 Ion Packet Injection

Anions are pulsed out of the trap in region 2 and into the third vacuum region of the

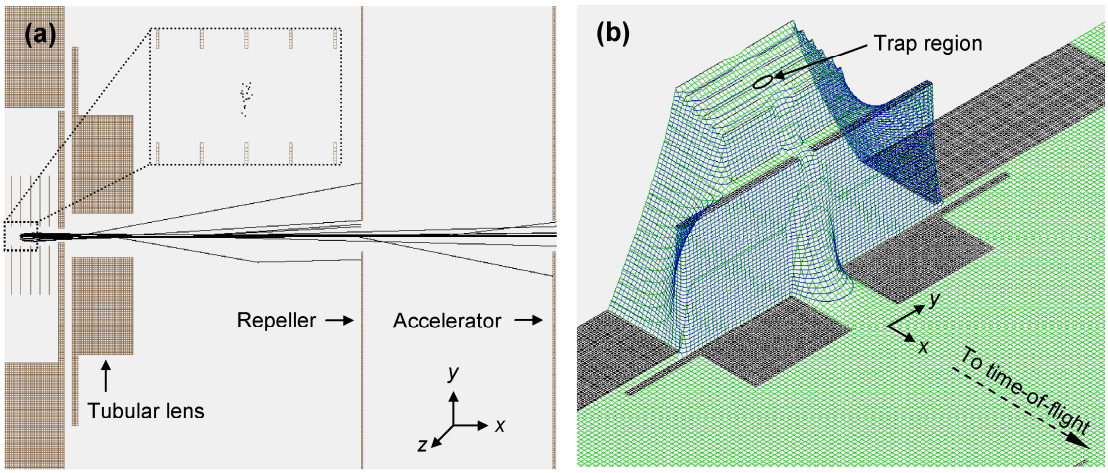

Figure 2.18: (a) Simion simulation of the anion injection process for 20 singly charged anions, each with a mass of 127 amu. Anion trajectories are shown in black and their initial positions in the trap region of the ion guide are shown inset (black dots). (b) Electric potential surfaces and field lines (blue lines) produced by the DC voltages. For visual clarity the absolute values of the electric field potentials are displayed here. Simulation parameters are shown in Table 2.9.

spectrometer through a 1.8 mm diameter pinhole, which also has the pulsed trap voltage, V_{Trap}, applied to it. As the anion packet enters this region of the spectrometer it is collimated into the centre of a collinear Wiley-McLaren TOF spectrometer, with the aid of an electrically grounded tubular lens, which has an i.d. of 7.0 mm. The lens is mounted directly in front of the pinhole plate using M3 Nylon screws and is electrically isolated from the plate using M4 ceramic washers (0.9 mm thick). All anions are ejected from the trap with the same energy, which is defined by the negative DC voltage offset applied to the penultimate electrode of the ion guide, V_1. Collimation of the ion packet into the TOF arrangement is controlled by varying the voltage to which the trap is pulsed open. Simion 8.0 has been used to simulate this injection process. The results and simulation parameters (controlled using the Lua script in Appendix A) are displayed in Figure 2.18 and Table 2.9, respectively. Analogous to the ion trap simulations (Section 2.3.3), 20 singly changed anions, each with a mass of 127 amu, have been simulated. For computational expense, and due to the cylindrical symmetry of the model around the *x*-axis, anions have only been generated in the *xy* Cartesian plane. The initial positions of the anions within the trap region (shown in Figure 2.16) have been designated based on a two-dimensional (2D) Gaussian distribution, with standard deviations from the centre of the trapping region of σ_x = 0.1 mm and σ_y = 0.5 mm,

along the x and y Cartesian axes, respectively. The injection process is displayed in Figure 2.18a, with the initial positions of anions within the trap region shown inset, and the electric field potential surface and field lines (blue lines) presented in Figure 2.18b. The results of these simulations indicate that ~70 % of anions pulsed out of the trap are successfully collimated into the centre of the TOF optics. However, these simulations neglect detrimental space-charge repulsion effects within the trap and are only valid in the absence of a pressure differential between the two regions. Experimentally this is not the case, although observations from experiment indicate that these simulations provide a good qualitative model for the ion injection process (see Section 2.5.1).

Table 2.9: Simulation parameters used for modelling the anion injection process into region 3 (Simulation results are displayed in Figure 2.18). The initial energy imparted to the anions is defined by a Gaussian distribution where the FWHM of the distribution is displayed in parentheses next to the centre of the energy distribution.

Simulation parameter	Value
V_{Trap}	–15 V
V_1	–20 V
V_2	–35 V
RF voltage	100 Vpp
RF frequency	1 MHz
Pressure	4×10^{-6} Torr
Initial ion energy (FWHM)	0.5 eV (0.2 eV)

2.4.2 Time-of-flight Mass Spectrometer: Region 3

Wiley-McLaren Time-of-Flight Mass Spectrometry

A Wiley-McLaren TOF mass spectrometer [17] is used to temporally focus anions according to their mass-to-charge (m/z) ratio at the detection region of the spectrometer. As shown in Figure 2.19, the arrangement consists of repeller, V_r, accelerator, V_a, and ground electrodes and a field free drift region of length, D, with an ion detector placed at its terminus. By pulsing the accelerator and repeller plates to high voltages ($V_r > V_a$) when the anion packet is at the centre of these two plates, anions will be accelerated into the field free drift region with an energy, U, defined as

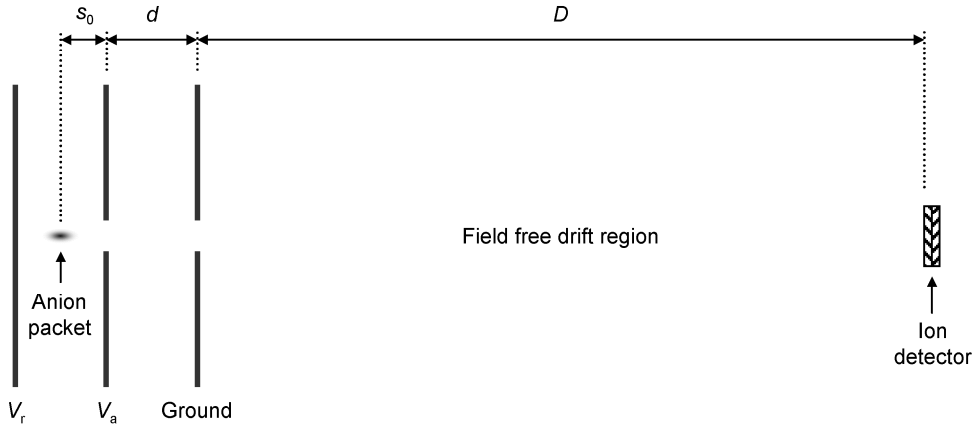

Figure 2.19: Illustration of a Wiley-McLaren time-of-flight (TOF) mass spectrometer. The arrangement consists of three electrodes; repeller, accelerator and ground. V_r and V_a are separated by a distance of $2s_0$ and V_a and ground are spaced apart by a distance d. Anions are accelerated into a field free drift region of length D, by pulsing the repeller and accelerator plates to voltages V_r and V_a, respectively ($V_r > V_a$). By varying the ratio V_r / V_a, anions of the same mass-to-charge (m/z) ratio may be temporally resolved and focused at the ion detector.

$$U = zs_0E_r + zdE_a + \bar{U}_i, \tag{2.14}$$

where E_r and E_a are the electric fields in the repeller and accelerator regions in V cm^{-1}, respectively, s_0 is half the length of the repeller region in cm, d is the length of the accelerator region in cm, z is the charge number on the anion, and $\bar{U}_i$ is the average initial energy of the anions in eV. When anions accelerated into the drift region have initial energies of $\bar{U}_i$ = 0 eV, their flight time to the ion detector, t (in μs), will be determined by their m/z ratio, and may be formally defined as [17]

$$t = 1.02\sqrt{\frac{m}{2U}}\left(2s_0k_0^{\frac{1}{2}} + \frac{2k_0^{\frac{1}{2}}}{k_0^{\frac{1}{2}}+1}d + D\right), \tag{2.15}$$

where m is the anion mass in amu, k_0 is expressed as

$$k_0 = \frac{s_0E_r + dE_a}{s_0E_r}, \tag{2.16}$$

and the constant 1.02 has units of cm^{-1} $amu^{-0.5}$ $eV^{0.5}$ μs. The physical outcome of this process is a mass spectrum of anions temporally resolved according to their *m*/*z* ratio. However, for the arrangement in the new spectrometer described here, anions are pulsed into the repeller region of the TOF optics with an initial kinetic energy, governed by the voltage applied to the penultimate electrode of the ion guide ($\bar{U}_i = V_1$). In this scenario, equation (2.15) will provide an over estimate for anion flight times.

Anions pulsed into the TOF arrangement will inherently have some initial spatial distribution about the centre of the acceleration region, Δs, determined by the spread in their initial kinetic energies, which can potentially lead to significant temporal broadening in the measured anion signals and reduce the resolution of the spectrometer. By tuning the electric field ratio, E_r/E_a, it is possible to compensate for this temporal broadening, and achieve the desired temporal focusing of anions of the same *m*/*z* at the same distance along the field free drift region, D_F, which is determined by [17]

$$D_F = 2s_0 k_0^{\frac{3}{2}} \left(1 - \frac{1}{k_0 + k_0^{\frac{1}{2}}} \frac{d}{s_0} \right). \tag{2.17}$$

The overall resolution of the TOF spectrometer, M_s, must also be considered, and is ultimately governed by the spread in anion kinetic energies, which is determined from their initial spatial distribution in the repeller region, Δs:

$$M_s \approx 16 k_0 \left(\frac{s_0}{\Delta s} \right)^2. \tag{2.18}$$

In equation (2.18) the mass resolution is defined as $M_s = m/\Delta m$ and is valid in the limits of $k_0 \gg 1$ and $k_0 \gg d/s_0$. To meet these conditions and attain an appreciable resolution from the TOF spectrometer, s_0 must be large than Δs. Additionally, D_F must be large to ensure $k_0 \gg 1$ as it depends on the ratio D_F/s_0, as shown in equation (2.17). Provided D_F and d are sufficiently large, particularly heavy masses can be readily resolved, which is ideal when studying large anionic species, such as biomolecules, in the gas phase. For the TOF spectrometer described here we estimate that M_s = 750

using equation (2.18).[5] However, equations (2.17) and (2.18) are only valid when $\bar{U}_i$ = 0, which is not the case here and as such the value predicted using equation (2.18) will not be equal to the experimentally observed resolution. Experimentally, we observe the TOF spectrometer resolution to be $M_s \approx 250$, as shown in Section 2.5.1, where the discrepancy between the experimental and predicted resolution is a direct result of $\bar{U}_i \neq 0$.

Design and Simulation of the Time-of-Flight Spectrometer

The TOF optics implemented in region 3 of the spectrometer have been illustrated in more detail in Figure 2.17. Unlike the original arrangement utilised by Wiley and McLaren [17], the anions are injected into the TOF optics collinearly, rather than the commonly chosen perpendicular arrangement. This arrangement has two immediate benefits: (1) no compensation for the transverse kinetic energy of the anions is required, as described by Wang and co-workers [18]; and (2) less spatial alignment of the accelerated anion beam is needed as it passes through the field free region of the spectrometer. It is important to note though, that collinearly oriented TOF arrangements are not without issues. Firstly, the effects of the initial anion energy distributions are far more pronounced in collinear arrangements than in perpendicular arrangements. $\left(\Delta s_{\text{collinear}} > \Delta s_{\text{perpendicular}}\right)$. Also, any neutral species present within the ion source are free to propagate along the axis of the TOF spectrometer to the detection region, a scenario avoided when using perpendicular arrangements. In such cases, electrons may also be detached from these residual neutrals when laser pulses possess enough energy, leading to undesired noise shots in the recorded photoelectron images. Here however, we do not observe any evidence of neutrals reaching the detection region of the spectrometer.

The stainless steel repeller and accelerator plates are 0.5 mm thick and have a diameter of 140 mm. Both plates have a 5 mm aperture at their centre, allowing accelerated anions to pass along the central axis of the spectrometer (defined as the *x*-axis in Figure 2.17 on page 85). The stainless steel ground plate has a diameter of 140 mm, a thickness of 5 mm, and has a 5 mm hole at its centre. This plate is mounted onto

[5] M_s has been determined using equation (2.18), based on the dimensions and voltages of the TOF spectrometer: d = 3 cm, s_0 = 1.5 cm, V_r = –2.3 kV, V_a = –2.0 kV, and Δs = 0.8 cm. Δs is obtained from the results of the ion packet injection simulations shown in Figure 2.18.

the front face of the aluminium top hat (which partitions R3 from R4) using M3 screws. To eliminate unwanted electric field distortions, these screws are countersunk so that the heads of the screws are flush with the surface of the ground electrode. The repeller and accelerator plates have four 3.2 mm equi-spaced holes at a diameter of 120 mm. These holes allow the two plates to be mounted on four M3 threaded rods, which are screwed into the ground electrode. Adjacent electrodes are spaced apart from each other by a distance of 30 mm, using glass spacers and ceramic insulators. The latter also serve to electrically isolate the repeller and accelerator electrodes. To prevent detrimental electrostatic lensing effects as anions pass through the TOF optics, high transmission stainless steel mesh (TWP, Berkley CA, 88 % transmission) has been placed over the central apertures of the accelerator and ground electrodes. Simulations suggest that the effect of electric field distortions from the aperture in the repeller electrode is negligible; hence, no mesh has been added to this plate.

Anions are accelerated out of the TOF optics and into a 1.3 m drift tube (consisting of R4 and R5 of the spectrometer) by pulsing the repeller and accelerator plates to voltages of –2.3 kV and –2.0 kV, respectively, for a period of 100 μs. These negative high voltages are generated using two commercial high voltage supply modules (Applied Kilovolts, HP2.5NIS025) connected to a pair of MOSFET high voltage pulsers (Behlke, HTS 50-06). Pulses have a fast rise time of ~50 ns and exponentially decay with a time constant of ~50 μs. The TOF arrangement may also be operated in a positive polarity mode using a second pair of high voltage modules (Applied Kilovolts, HP2.5PIS025), and by rewiring the high voltage pulsers.

Simion simulations of the temporal focussing process are shown in Figure 2.20 for 50 singly charged anions with masses of 127 amu, using the TOF voltages described above. The initial positions of the anions in the anion packet are shown in Figure 2.20a (black dots), and have been generated with a 2D Gaussian distribution at the centre of the repeller region of the TOF optics, with standard deviations of σ_x = 4 mm and σ_y = 1 mm in the *xy* Cartesian plane. Anions are born with an initial kinetic energy of U_i = 20 eV along the central axis of the spectrometer (*x*-axis), as a result of the kinetic energy imparted to them from the ion packet injection process. The electric field potentials (blue lines) generated by the TOF high voltages are shown in Figure 2.20b, together with the initial trajectories of the anions as they enter the drift tube (black

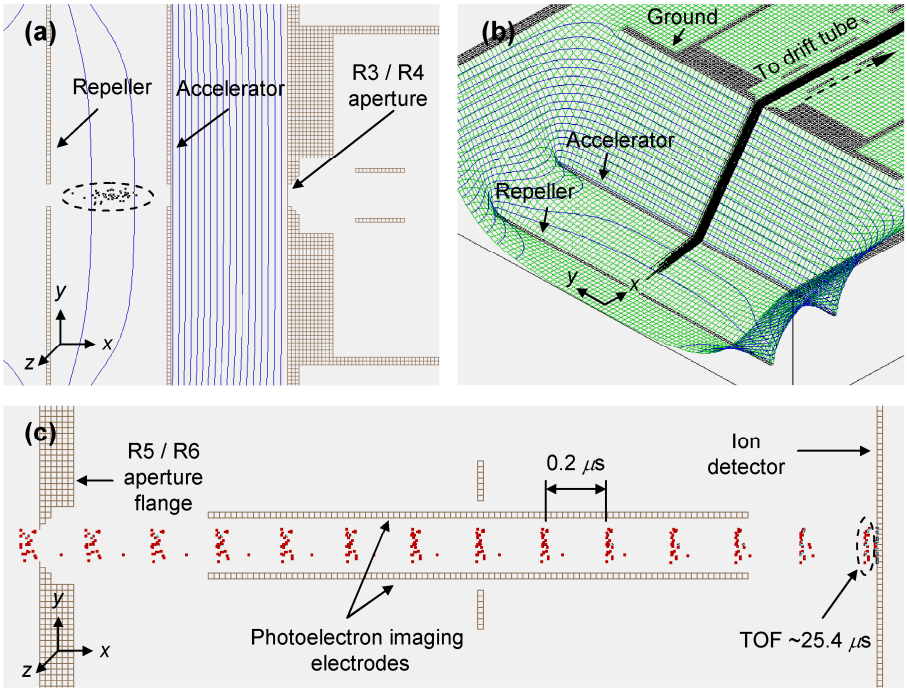

Figure 2.20: Simion simulations of the time-of-flight (TOF) optics and the temporal focusing process. (a) Initial positions of the 50 singly charged anions (mass = 127 amu). Anions are generated with a 2D Gaussian distribution at the centre of the repeller region of the TOF optics (σ_x = 4 mm, σ_y = 1 mm), and have initial energies of 20 eV along the central axis of the spectrometer (x-axis). (b) Potential surface and electric field lines (blue lines) generated when the repeller and accelerator electrodes are pulsed to voltages of –2.3 kV and –2.0 kV, respectively. Black lines indicate the initial trajectories of anions as they are accelerated into the drift tube. (c) Temporal focusing of the anion packet in the detection region of the spectrometer occurs at a distance of 1.3 m. Red dots are time markers (spaced by 0.2 μs) showing the temporal evolution of the anion packet, which has a total flight time of ~25.4 μs to the ion detector.

lines). Figure 2.20c displays the temporally focused anion packet at the end of a flight distance of 1.3 m in the detection region of the spectrometer. The temporal evolution of the anion packet is indicated by the time markers (red dots), spaced apart by 0.2 μs. The simulation results predict that anions of mass 127 amu have a total flight time to the ion detector of ~25.4 μs, with an associated spatial distribution of 1.6 mm, correlating to a temporal anion packet width of ~35 ns and a simulated TOF spectrometer resolution of $M_s \approx 360$. A comparison of this simulation result to the predicted focal distance, D_F, from equation (2.17) can be made using the dimensions of the TOF optics and voltages applied to the electrodes. These calculations predict a temporal focal distance of 1.44 m, which is close to the simulated distance of 1.3 m. Analogous to the calculations performed at the start of this section, this discrepancy arises because equation (2.17) have been derived based on the assumption that $U_i = 0$. As $U_i = 20$ eV, equation (2.17)

over-estimates the true D_F value of the TOF spectrometer described here.

2.4.3 Ion Beam Focussing: Regions 4 and 5

Regions 4 (R4) and 5 (R5) of the spectrometer make up the field free drift region of the TOF spectrometer, and are displayed in Figure 2.21. R4 consist of a six-way ISO100 cross. The end of this cross is connected to an ISO100 to 4-1/2" CF adaptor nipple with a pneumatic gate valve (Kurt J. Lesker, SG0250PCCF) attached to the CF flange. This gate valve is controlled by the vacuum interlock system described in to Section 2.6.1, which serves to: (1) isolate the detection region of the spectrometer during maintenance

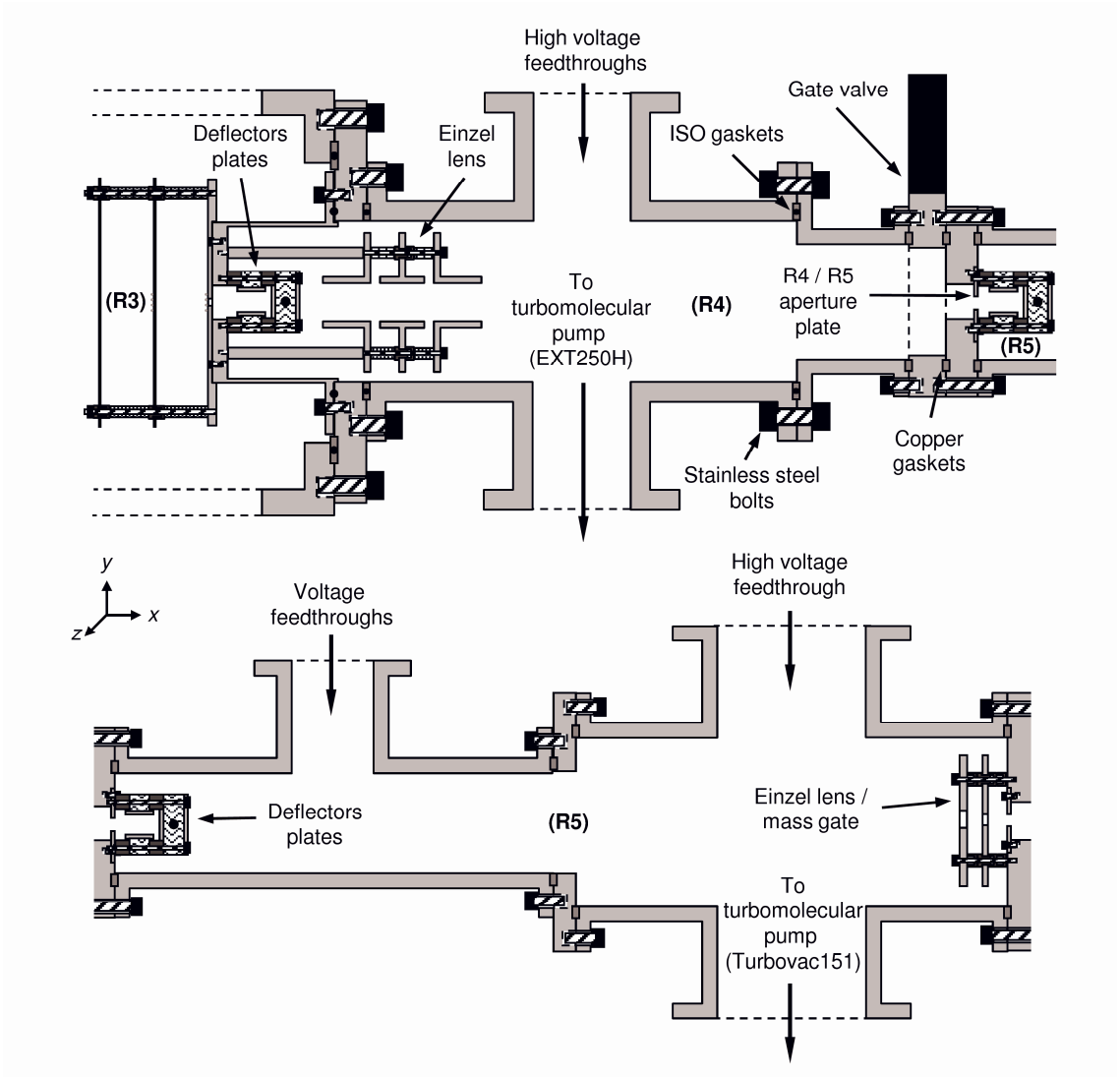

Figure 2.21: Cross-sectional schematics of the fourth (R4, top) and fifth (R5, bottom) differentially pumped regions of the spectrometer (schematics not to scale). R4 and R5 house spatial focusing optics and form the majority of the TOF drift tube.

in R1 to R4; and (2) isolate the detection region in the event of any of the vacuum pump systems failing. R4 and R5 are partitioned by a stainless steel plate with a 5 mm hole at the centre, which is bolted onto the centre of a zero-length 4-1/2" CF adaptor. R5 is constructed from a 4-1/2" CF tee and a four-way 6" CF cross, bolted together by a zero-length CF adaptor. R5 and R6 (the detection region) are separated by another 5 mm diameter aperture mounted onto the centre of a zero-length 6" CF adaptor.

Ion Beam Deflectors

Ions are spatially aligned along the field free drift tube and through the successive differential apertures using two sets of ion beam deflectors, which are able to manipulate the trajectory of the ion beam along the *y* and *z* Cartesian axes of the spectrometer. These deflector plates, shown in Figure 2.21, are placed at the start of regions 4 and 5. Each set consists of two pairs of stainless steel plates oriented perpendicularly with respect to each other. Each plate has dimensions of 30 mm × 14 mm × 2 mm (length × width × thickness), and have an M2 tap their centres. These plates are then mounted onto electrically insulting Teflon blocks using M2 screws. Each deflector set is then mounted to the spectrometer on four M3 threaded rods, where horizontal and vertical deflector pairs are spaced apart using ceramic spacers. DC voltages with the same magnitude but opposite polarities are applied to each plate in the deflector pairs. These DC voltage pairs are generated from a custom-made power supply, which has been constructed in-house and is capable of producing 4 DC voltage pairs in total.

Einzel Lenses and Mass Gate

Two Einzel lenses are used to spatially focus anions at the laser-ion interaction point in the detection region of the spectrometer (see Figure 2.21). The first of these is housed in R4 and consists of three cylindrical electrodes. All three electrodes have an i.d. of 20 mm. The central electrode has a length of 16 mm while the two end electrodes are both 20 mm long. The Einzel lens arrangement is mounted on four stainless steel rods, which are screwed into the rear face of the top hat partitioning R3 and R4. The ends of the tubular electrodes are spaced apart by 8 mm using ceramic insulators, which also

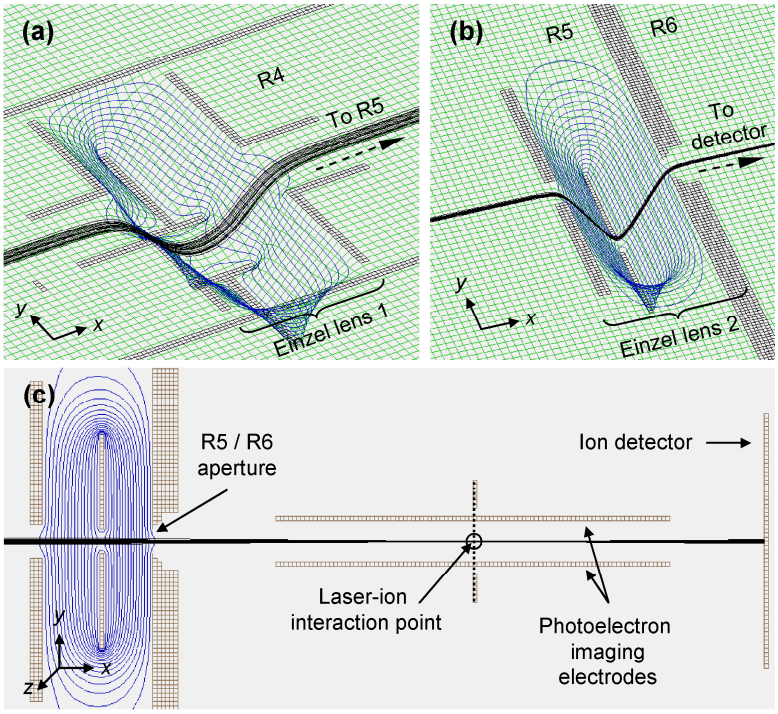

Figure 2.22: Simion simulation of the spatial focusing optics incorporated in regions 4 and 5 of the spectrometer. Simulation parameters are described in Section 2.4.2 and anion beam trajectories are shown by the black lines. Electric field lines are shown in blue. (a) Simulation of the first Einzel lens in region 4, where the central electrode is placed –700 V. (b) Second Einzel lens simulation when set at a voltage of –1 kV. (c) Spatial focus of the anion beam at the laser-ion interaction point in the detection region.

electrically isolate the central electrode.

The second Einzel lens is placed at the end of R5, and consists of two plate electrodes which have dimensions of 80 mm × 3 mm and 60 mm × 1 mm (diameter × thickness), and have 7 mm and 5 mm apertures at their centres, respectively. Both are mounted in front of the zero-length 6" CF adaptor at the end of R5 (which acts as a second ground electrode) on four M3 threaded rods. Ceramic spacers are used to space the electrodes apart by 14 mm and electrically isolate the second plate electrode.

High voltages of –700 V and –1000 V, are applied to the central electrode of each of the Einzel lenses, respectively, using two commercially available high voltage supply modules (Applied Kilovolts, HP2.5RIS025). Simion simulations of the spatial focusing process are displayed in Figure 2.22 for 20 anions with masses of 127 amu. Anions are accelerated into the TOF drift tube with the same simulation parameters as those described for the temporal focusing simulations presented in Section 2.4.2. The simulation results, shown in Figure 2.22c, indicate that by applying the high voltages

stated above to the Einzel lens pair, the anion packet is well focused at the laser-ion interaction point of the detector region.

The second Einzel lens may also be utilised as a mass gate to ensure that a single temporally resolved anion packet of specific *m*/*z* ratio is probed by the femtosecond laser pulses in the detection region. This is achieved by applying a high offset voltage (–3 kV) to the second Einzel lens, and then rapidly pulsing it back to the lens voltage at the time of arrival of the *m*/*z* anion packet of interest for a period of ~70 ns. This high voltage pulse is generated using a solid state pulser (DEI, PVX-4140) capable of producing stable high voltage pulses with minimal ringing, and rise and fall times of ≤25 ns.

2.5 Detection Region

The detection region of the spectrometer (R6) houses a photoelectron imaging detector arrangement and an ion detector to monitor and record TOF spectra. This region of the spectrometer is illustrated in Figure 2.23a and consists of a 6" CF cube chamber and a 6" to 4-1/2" CF four-way reducer cross.

The detection region also contains two sets of laser baffles, which are oriented perpendicular to the anion beam axis (*x*-axis), and are shown in Figure 2.23b. These baffles serve to reduce the number of stray laser photons interacting with the photoelectron imaging electrodes. This is particularly critical when utilising laser pulses in the UV energy regime, as this is above the work-function of the μ-metal electrodes (≤4.5 eV). Without light baffles this process leads to the generation of undesired photoelectron noise, which significantly reduces the signal-to-noise levels in photoelectron images. Each conical laser baffle has an o.d. of 16 mm and a 4 mm aperture at their centre for the laser to propagate through. Individual baffles are spaced apart by 15 mm stainless steel spacers, inside a 15.5 cm long stainless steel tube (16 mm i.d.). All baffle components are coated using a vacuum compatible carbon spray (Edelgraphit) and the arrangements are mounted onto the inside faces of two 6" CF flanges with stainless steel tubes at their centres (16 cm long, 1" o.d.). The entrance and exit laser windows (described in Section 2.2.3) are sealed onto the ends of each of these tubes using Torrseal low vapour pressure resin (Varian, 9530001), respectively.

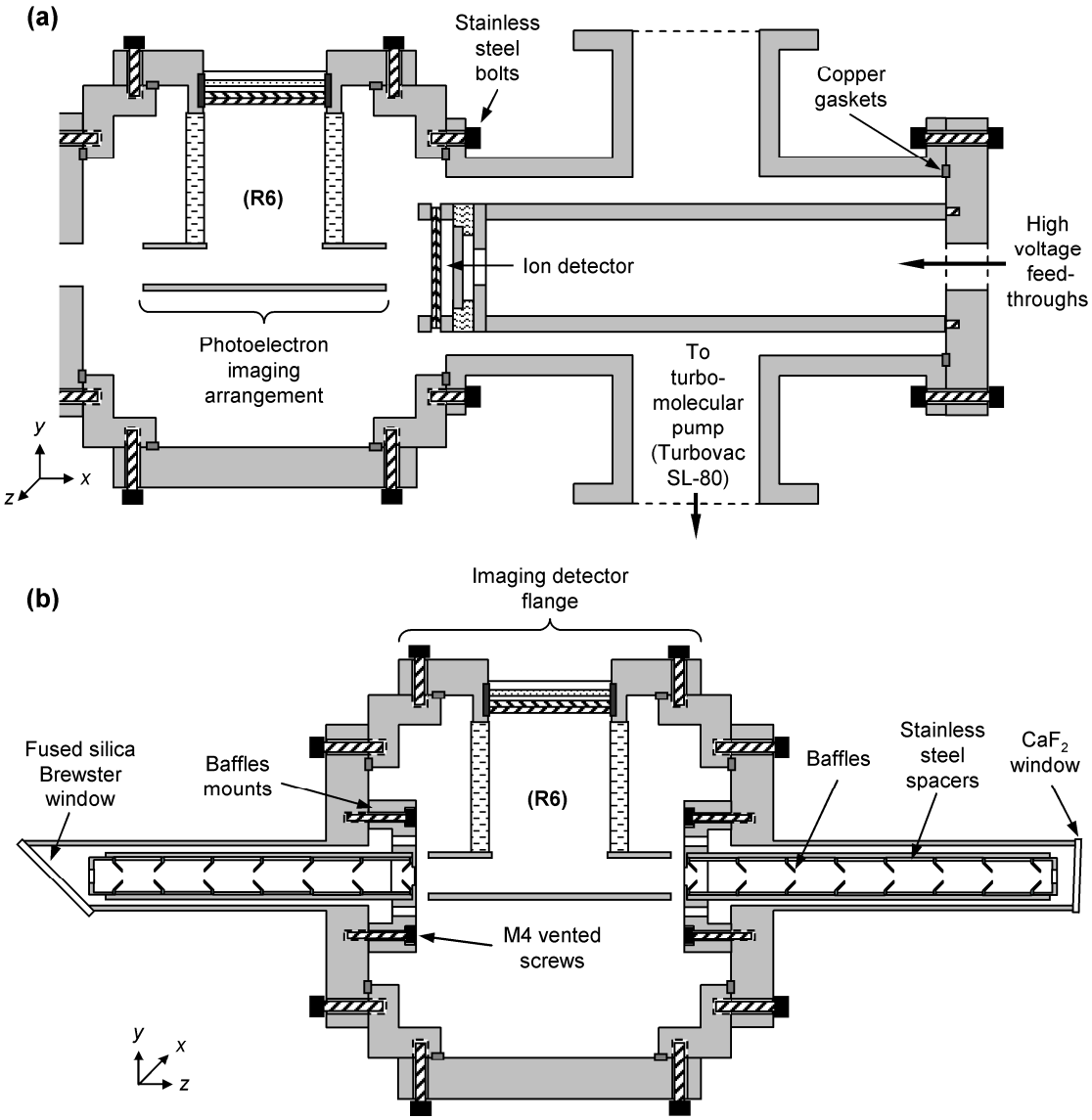

Figure 2.23: (a) Cross-section schematic (*xy* plane) of the detection region of the spectrometer (R6), which incorporates the photoelectron imaging arrangement and an ion detector for the TOF mass spectrometer. (b) Cross-sectional schematic (*yz* plane) of the laser baffles, which are oriented perpendicular to the anion beam axis (*x*-axis). The anion beam axis is oriented into the page and schematics are not to scale.

In their current form, the laser baffles are relatively ineffective, and a significant degree of laser induced noise is observed when recording photoelectron images at photon energies of ≥4.66 eV (266 nm), which we discuss in Section 2.5.2. For laser baffles to work efficiently, the baffles coating should ideally possess a low reflectance (<5 %) at photon energies of 4.66 eV and greater. However, the graphite carbon coating chosen here possesses a reflectance of ~50 % at photon energies of 4.66 eV and higher

[19], leading to large amounts of undesired light scattering. Additionally, the edge of the aperture at the centre of the conical baffles should also be a 'knife-edge' finish, to reduce any additional light scattering; this is unfortunately not the case here. Currently, we are developing a new set of electro-formed copper laser baffles with oxidised surfaces, which are loosely based on the designs in reference [20] and should overcome both of the issues discussed above.

2.5.1 Time-of-Flight Ion Detector

Design and Construction of the Microchannel Plate Ion Detector

Anions are detected using a voltage matched pair of microchannel plates (MCPs) (Photonis, MCP 40/12/10/8/D 60:1), with an active area of ~12 cm^2 (4 cm diameter). When struck by an anion, an electron cascade is generated through the pores of the MCP. By biasing the rear of the MCP pair at a high positive voltage, electrons are ejected from the rear of the device onto an anode placed at a higher positive voltage than the rear MCP. The electron current on the anode is subsequently measured using an oscilloscope.

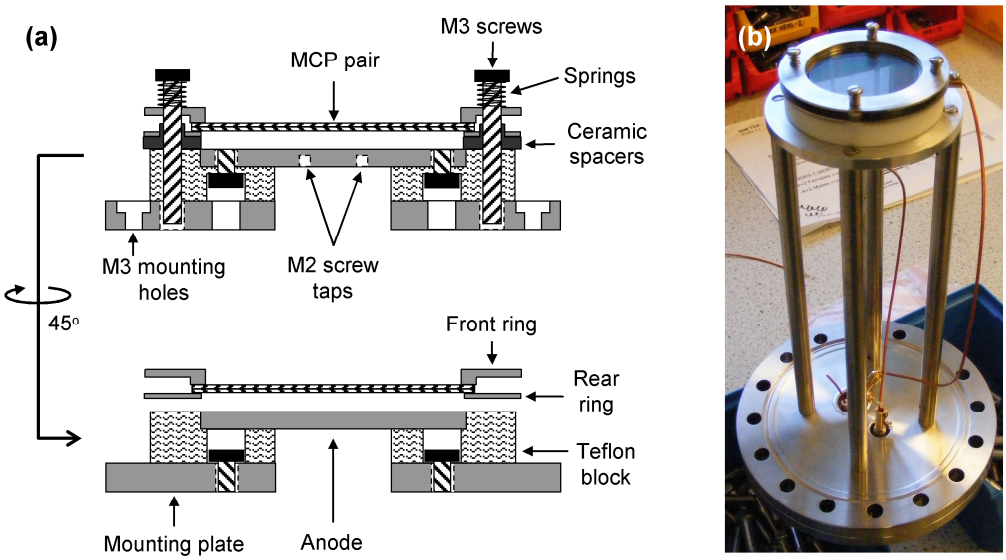

Figure 2.24: (a) Cross-sectional schematics of the ion detector mounting arrangement. The bottom schematic has been rotated by 45° around the vertical axis, with respect to the top schematic. (b) Complete ion detector arrangement mounted on the rear high voltage feedthrough flange of the detection region.

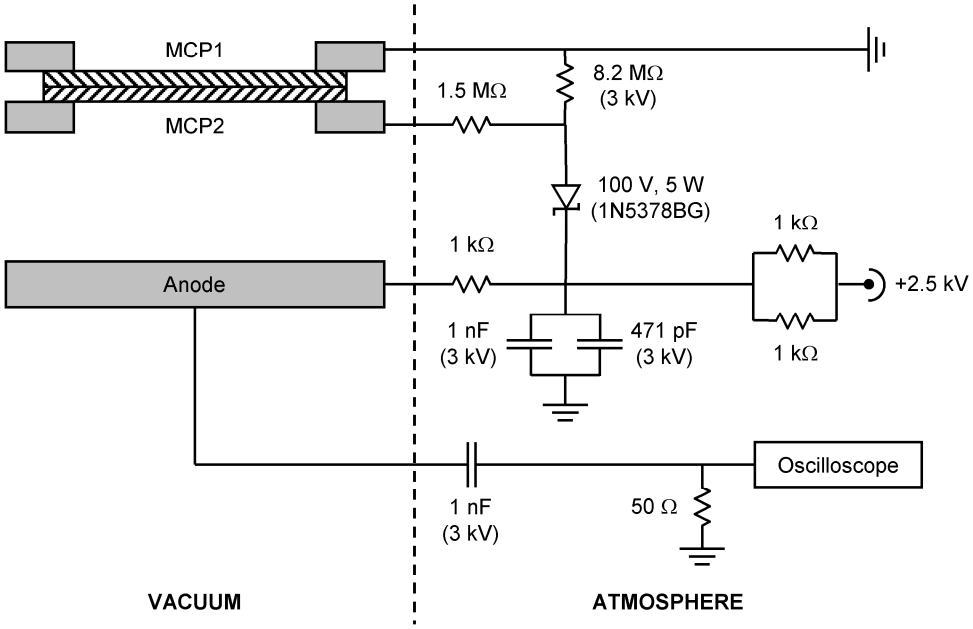

Figure 2.25: Voltage divider circuit used to couple the high voltage power supply output (+2.5 kV) to the rear MCP (MCP2) and the collection anode. The circuit also aids to maintain a fixed voltage difference of ~100 V between MCP2 and the anode, using a Zener diode in a reverse biased configuration. A high-pass resistor capacitor (RC) circuit is used to decouple the amplified electron signal from the anode high voltage, prior to measurement with an oscilloscope. Conversely, a low-pass RC arrangement is used to decouple the high frequency signal from the high voltage power supply module.

The MCPs are positioned in a mount constructed in-house. The mount schematics and final MCP arrangement are displayed in Figure 2.24a and Figure 2.24b, respectively. The plates are mounted between two stainless steel rings in front of a stainless steel anode plate, which is itself mounted onto an electrically isolating Teflon block. The Teflon block is screwed onto the front face of a stainless steel mounting plate, while the MCPs and stainless steel rings are held in place by 4 M3 stainless steel screws, which are attached to the rear mounting plate through the Teflon block. The rear ring is electrically isolated and spaced apart from the anode plate by 3 mm using four ceramic spacers, whereas the front ring is electrically grounded *via* the stainless steel screws. The arrangement is gently compressed together with the aid of four springs placed over the M3 screws, and the whole MCP assembly is screwed onto four M3 tapped stainless steel rods (20 cm long) which are mounted onto the end flange of the detection region.

A single high voltage power supply module (Applied Kilovolts, HP2.5PAA025) is used to apply positive high voltages onto the MCP arrangement by means of the circuit

shown in Figure 2.25. The high voltage is partitioned onto the collection anode and the rear MCP (labelled MCP2) using a series of resistors, which form a voltage divider circuit. A Zener dioide (On Semiconductor, 1N5378BG), rated at a Zener voltage of 100 V, has been placed in a reverse biased configuration between MCP2 and the anode to ensure that the voltage difference between them is maintained at ~100 V. When the power supply output is set to +2.5 kV, the voltages measured on the anode and the rear MCP (labelled MCP2) are +2.24 kV and +2.10 kV, respectively. The high voltage applied to the anode is decoupled from amplified electron signal using a 1 nF capacitor (Panasonic, ECKA3F102KBP) and the signal is then monitored on an oscilloscope (LeCroy, Wavesurfer 44Xs) *via* a 50 Ω coupling. Conversely, the high frequency signal is decoupled from the high voltage power supply with the aid of a low-pass RC filter circuit, consisting of a 1 kΩ (Tyco Electronics, ROX1SJ100K) resistor and a 1 nF plus 471 pF (Panasonic, ECKA3F471KBP) capacitor pair arranged in parallel to ground.

Calibration: Time-of-flight Spectrum of Iodide

The TOF spectrometer has been calibrated and tested by spraying a 6 mM solution of NaI in a mixed MeOH / H_2O solvent (80:20, respectively) from the ESI source, as described in Section 2.3.1. Anions are trapped and focused in the ion guide and pulsed into the TOF arrangement. The accelerator and repeller electrodes are then pulsed to voltages of –2.3 kV and –1.96 kV, respectively, and accelerated anions are then detected using the ion detector in R6, where the recorded TOF spectrum is displayed in Figure 2.26a. The peak at 25.24 μs corresponds to I^-, with an associated *m*/*z* ratio of 127. This measured time-of-flight correlates excellently with the predicted flight time of ~25.4 μs from the Simion simulations (Section 2.4.2). Using this peak as a reference mass, m_1, with a known flight time, t_1, it is possible to determine the masses of some of the other unknown anion peaks, m_2, present in the spectrum from the relationship

$$m_1 = m_2 \left(\frac{t_1}{t_2} \right)^2 , \tag{2.19}$$

where the remaining variable, t_2, is the flight time of the unknown peak. Using equation (2.19) and the I^- reference peak, the anion peak adjacent to it, with a flight

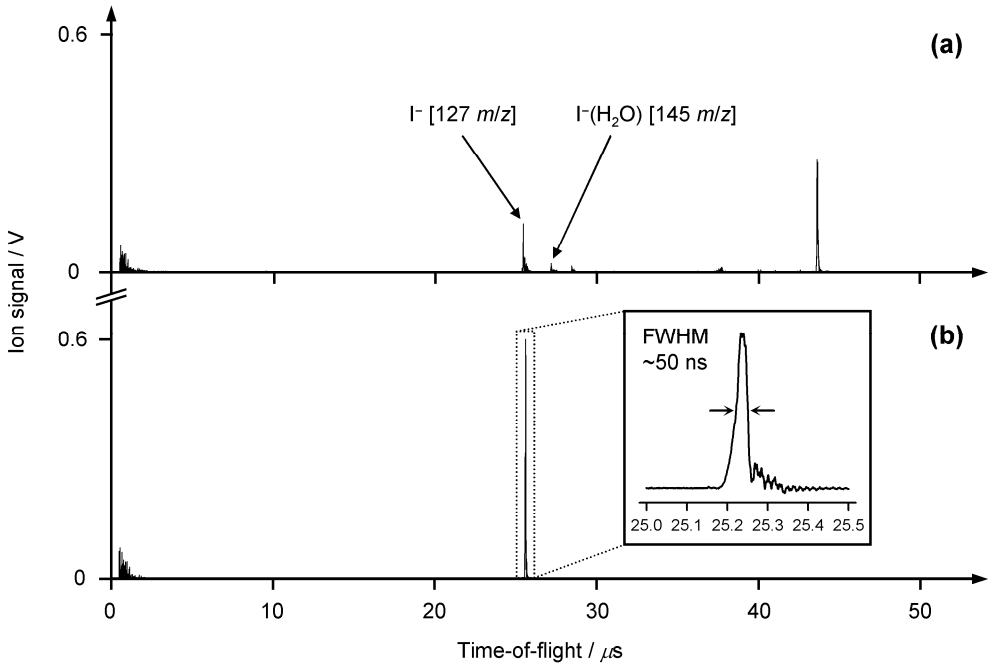

Figure 2.26: (a) Time-of-flight (TOF) spectrum obtained from spraying a 6 mM solution of NaI in a mixed MeOH / H_2O solvent (80:20, respectively). Peaks have been identified using equation (2.19) and the I^- peak as a reference, which has an associated TOF of ~25.2 μs. (b) TOF spectrum of an optimised I^- anion packet. The temporal profile of the peak is shown inset, and has an associated temporal FWHM value of ~50 ns. Equation (2.20) provides an estimate of ~130 anions per packet.

time of 27.0 μs, is determined to have an associated *m*/*z* value of 145. This corresponds to the *m*/*z* of the mono-hydrated species, $I^-(H_2O)$. However, it is not possible to assign the *m*/*z* ratio of the most prominent peak in the spectrum at ~44 μs. This issue originates from the fact that when anions are pulsed out of the ion trap into the TOF optics, they all have the same kinetic energy, resulting in a distribution of injection times (velocities) governed by their *m*/*z* ratio. This leads to a TOF spectrum which only contains the small range of ion masses optimised into the TOF arrangement. Additionally, the broad spatial distribution of *all* different *m*/*z* anions within the repeller region leads to a distortion in the ideal flight times of anions depending on the time period they spend in the repeller region, thus preventing a complete conversion of the TOF spectrum into an ideal mass spectrum; anions with large *m*/*z* ratios take longer to exit the TOF optics. Although, the immediate advantage of this effect is that by tuning the voltages in the first two regions of the spectrometer (V_1 - V_4, V_{Trap}, ϕ_1 and ϕ_2, defined in Section 2.3) and the time delay between opening the ion trap and pulsing the TOF high voltages, ΔT, particular peaks within the TOF spectrum can be optimised as shown

in Figure 2.26b. Here, a six-fold increase in I^- signal has been achieved, which is particularly advantageous for optimising the number of anions transmitted to the detection region in TRPEI experiments. All values for the optimised experimental parameters used to record the I^- calibration spectrum in Figure 2.26b are summarised below in Table 2.10.

Table 2.10: Optimised experimental parameters used to record the I^- calibration TOF spectrum in Figure 2.26b.

Spectrometer component	Variable	Optimised value
ESI source	V_{ESI}	–2.9 kV
	I_{ESI}	0.21 μA
	Solution flow rate	250 μl hr^{-1}
Heated capillary	T	80 ^{o}C
	V_4	–55 V
Source region pressures	P_{R1}	5 Torr
	P_{R2}	1×10^{-2} Torr
R1/R2 pinhole plate	V_3	–50 V
Ion guide	V_1	–40 V
	V_2	–48 V
	ϕ_1 and ϕ_2	120 V_{pp}, 1 MHz
Ion trap	V_{Trap} (Open)	–26.7 V
	V_{Trap} (Closed)	–48.5 V
Trap timing	ΔT	9.2 μs
	Open duration	2.0 μs
Deflector set 1	V_y	3.1 V
	V_z	–1.3 V
Deflector set 2	V_y	0.5 V
	V_z	–0.8 V
Einzel lenses	Einzel 1	–950 V
	Einzel 2	not used

The experimental resolution of the TOF spectrometer may be determined from the width of the 127 amu I^- peak in Figure 2.26b, which is measured to be ~50 ns (FWHM) (see inset in Figure 2.26b). This temporal width may be converted into a Δm value of 0.5 amu using equation (2.19), providing a measured resolution $\left(M_s = m/\Delta m\right)$ of M_s = 254 for the TOF spectrometer.

An estimate for the number of I^- anions, N, in the anion packet can also be established by using

$$N = \frac{\Delta t V}{RGe}, \tag{2.20}$$

where V is the measured anion signal in volts, R is the 50 Ω coupling impedance of the oscilloscope, Δt is the temporal FWHM of the anion peak in seconds, G is the measured gain of the ion detector, and e is the elementary charge on an electron (e = 1.602 × 10^{-19} C). When the rear of the MCPs is biased to +2.1 kV the gain is known to be G = 2.4 × 10^7 [21],[6] and the measured I^- signal and peak width in Figure 2.26b are 0.6 V and ~5 × 10^{-8} s, respectively. Using these values, a value of $N \approx 160$ is obtained. Recalling from the simulations in Section 2.3.3 that a total of ~200 anions may be accommodated in the ion trap, that there is an ~30 % loss when injecting the ion packet into the TOF optics (see Section 2.4.1), and that there is only ~77 % total ion transmission through the mesh in the TOF optics, we may predict the total number of anions reaching the ion detector. Based on these values we estimate that ~110 anions may reach the ion detector, assuming no additional ion loss at differentially apertures along the TOF drift region, which compares well to the experimentally determined number of 160 anions.

2.5.2 Photoelectron Imaging Detector

Detection of Photoelectrons

When implementing PES, two valuable pieces of information can potentially be

[6] The gain of the MCP pair at +2.1 kV has been extrapolated from the measured gain of 2.8 × 10^7 at 2.4 kV (provided by Photonis) using a standard gain curve for the chevron MCP pair in reference [21].

obtained from the emitted photoelectrons: (1) electron kinetic energies (*eKE*s), which provide information about the internal structure of the species being probed; and (2) photoelectron angular distributions (PADs). PADs can provide insight into the nature of the orbitals from which the photoelectrons have been detached [22-24], helping to construct a more complete description of the system being studied. In addition to these, it is also advantageous to maintain a high collection efficiency of photoelectrons, ideally approaching unity.

Over the past few decades a number of techniques have been developed for analysing photoelectrons, which include hemispherical analysers [25] and TOF methods [26], such as magnetic bottle analysers [27]. Hemispherical analysers effectively scan the *eKE* making this detection approach particularly time consuming, despite the excellent energy resolution it offers, while the latter TOF methods have the disadvantage of exceptionally low collection efficiencies ($\ll 1$ %), although this is not the case for magnet bottle analysers. These photoelectron analysers use a magnetic field (~1 T) generated from a permanent magnet to parallelise photoelectrons towards a detector placed at the terminus of a magnetically shielded flight tube containing a guiding magnetic field (1×10^{-3} T) generated by electro-magnets (solenoids). With careful design of the permanent magnet shape, near unit (4π steradian) collection efficiencies can be achieved [18,28]. However, the method has a number of drawbacks: (1) it suffers from reduced energy resolutions at low *eKE*s; (2) undesired Doppler broadening of *eKE* features is observed unless ions are decelerated before laser-ion interaction [18]; and most significantly (3) it is unable to measure the additional PADs.

In recent years there has been a significant shift towards photoelectron imaging techniques. This powerful detection methodology not only provides 4π steradian collection efficiency (where the detection efficiency is only limited by the efficiency of the detector), but also allows simultaneous access to *eKE*s and PADs. Imaging detection techniques were pioneered by Chandler and Houston in the late 80s for analysing the angular distributions in photofragmentation studies [29]. The method was soon thereafter expanded to the analysis of photoelectrons by Helm and co-workers [30], and coupled with the advent of greatly improved energy and angular resolution through Eppink and Parker's velocity map imaging (VMI) technique [31], photoelectron imaging (PEI) has since become an invaluable tool for extracting both the energetic and

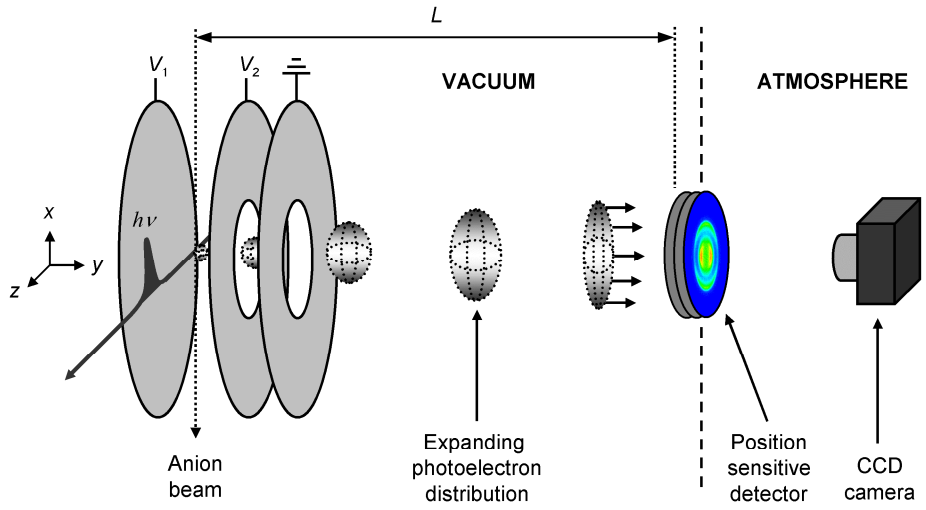

Figure 2.27: Schematic of a standard velocity map imaging (VMI) arrangement used for detecting photoelectrons. A series of negatively biased Wiley-McLaren type gridless electrodes are used to project the radially expanding 3D photoelectron distribution towards a position sensitive detector. The 2D projection of the photoelectron distribution is subsequently captured using a charge coupled device (CCD).

angular information attainable from time-resolved PES (TRPES) experiments.

Briefly, a standard VMI arrangement may be implemented with a series of Wiley-McLaren type gridless electrodes. Such an arrangement is illustrated in Figure 2.27. Upon photodetachment, the expanding Newton spheres of electrons are projected onto a position sensitive detector, most commonly a pair of MCPs coupled to a phosphor screen, by applying a pair of negative voltages to the first two electrodes ($V_1 > V_2$). The light generated from the phosphor screen provides a measure of the resultant 2D projection and subsequently captured using a CCD camera. By implementing an image deconvolution algorithm, which we discuss in detail in Chapter 3, the original three dimensional (3D) photoelectron distribution may be reconstructed, providing access to the desired one dimensional (1D) photoelectron spectrum and PADs.

Principles of Velocity Map Imaging

The principles behind the acceleration of the charged particle distribution towards a position sensitive detector in VMI are governed by the temporal focusing conditions introduced in Section 2.4.2, specifically, equation (2.17). Here we specifically consider the application of VMI for analysing photoelectrons, although all subsequent analysis

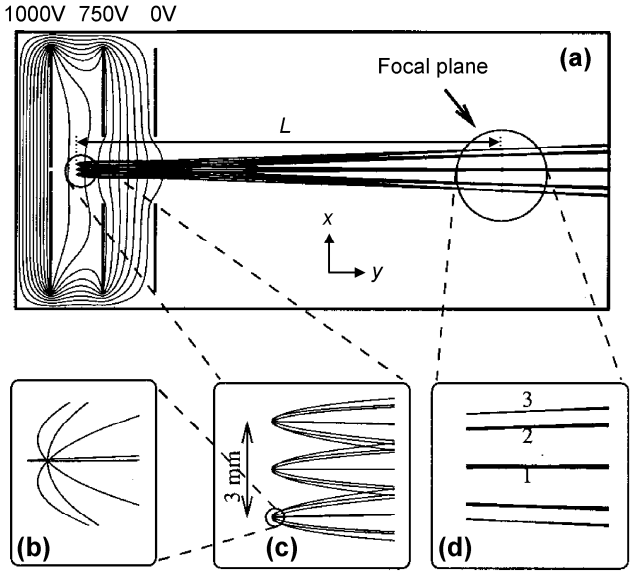

Figure 2.28: (a) Simion trajectory simulations of Eppink and Parker's original velocity map imaging (VMI) arrangement, showing the electric field lines and charged particle trajectories. Simulations were performed for charged particles with an initial energy of 1 eV. (b) shows the initial trajectory distributions of the particles, repeated at 3 different origins, each separated by 1.5 mm, in the repeller region of the VMI electrodes (c). (d) shows the velocity mapped trajectories of the three different particle velocities at the imaging detector focal plane (L = 36 cm). Reprinted with permission from reference [31]. Copyright 1997, American Institute of Physics.

may be readily expanded to charged particles of different masses and charges. Provided the V_1/V_2 ratio is optimised, all photoelectrons will be temporally focused at the detector plane distance, defined by the flight tube length, L, regardless of their original position in the laser-ion interaction volume. This gives rise to the observed '*pancaking*' of the 3D photoelectron distribution along the VMI axis (y-axis), as schematically illustrated in Figure 2.27. The time-of-flight of the photoelectrons, t^{e}, to the detector can be defined as

$$t^{e} \approx \frac{L}{v_y^{e}} \approx L\sqrt{\frac{m_e}{2eV_1}}, \tag{2.21}$$

where v_y^{e} is the velocity component of the photoelectrons along the VMI axis, m_e is the mass of an electron (m_e = 9.11 × 10^{-31} kg), and e is the charge on an electron (e = 1.602 × 10^{-19} C). In turn, the radial size, r, of a photoelectron distribution at the detector, with associated kinetic energy, eKE, may be determined from

$$r \approx v_x^{\mathrm{e}} t^{\mathrm{e}} \approx L\sqrt{\frac{eKE}{eV_1}}\,. \tag{2.22}$$

Equation (2.22), implies that $eKE \propto r^2$, which will prove vital when extracting the desired 1D photoelectron spectrum for the 2D image, as discussed later in this section. However, equations (2.21) and (2.22) only consider the scenario of Wiley-McLaren electrodes, which generate homogeneous electric fields, where no velocity mapping is achieved. The gridless electrodes in Eppink and Parker's original design lead to the formation of an electrostatic lens (similar to the Einzel lenses described in Section 2.4.3), causing all photoelectrons with the same velocity vectors, $\left\{v_x^{\mathrm{e}}, \left|v_y^{\mathrm{e}}\right|, v_z^{\mathrm{e}}\right\}$, to be focused onto the same position of the detector, regardless of their initial positions within the laser-ion interaction volume. For velocity mapping, equation (2.22) transforms to become

$$r \approx aL\sqrt{\frac{eKE}{eV_1}}\,, \tag{2.23}$$

where a is a velocity mapping magnification factor, dependent on the apparatus. For most apparatus $0.9 < a < 1.4$, and determines the velocity mapping properties of the arrangement. This elegantly eliminates detrimental Doppler broadening and can potentially allow VMI analysers to obtain resolutions as high as $\Delta E/E \approx 0.4$ % [32]. This process is illustrated by the original Simion trajectory simulations performed by Eppink and Parker [31], displayed in Figure 2.28a, where $V_1/V_2 \approx 1.3$ and L = 36 cm. 3 sets of 8 charged particles are generated at 3 different origins, separated by 1.5 mm. Particles are ejected from their origins with 1 eV of energy and their initial trajectories are distributed by 45° in the xy-plane (Figures 2.28b and 2.28c). The trajectories at the focal plane, shown in more detail in Figure 2.28d, clearly demonstrate that particles with the same velocities (ejection angles), 1 (0° / 180°), 2 (45° / 135°), and 3 (90° / 270°), are focused at the same positions on the detector plane, respectively.

Development of a New Velocity Map Imaging Arrangement for Photoelectron Imaging of Anions

Photoelectron VMI arrangements based on Eppink and Parker's original design, and oriented perpendicular to the anion beam axis (*x*-axis), require a potential difference of ~250 V between the repeller (V_1) and acceleration (V_2) electrodes to image 1 eV electrons at a distance of L = 36 cm (see Figure 2.28). For neutrals this is not an issue, however, for charged anion beams this voltage difference is ample enough to divert the beam trajectory into the VMI electrodes, prior to reaching the laser-ion interaction volume. To bypass this issue, many VMI arrangements used for performing photoelectron imaging on anions, rapidly pulse the voltages V_1 and V_2 on *just before* the time of laser-ion interaction. Pulsing the plate voltages on just before the time of ion-laser interaction, rather than when there is an exact temporal overlap, avoids the photodetached electrons from being distorted by the initial ringing of the high voltage pulses. Motivated to avoid this problem, and negate the need for controlling and purchasing costly high voltage pulsers, we have developed a new VMI arrangement which uses low DC voltages and abstains from large electric fields in regions where the anion beam propagates.

This arrangement is shown in Figure 2.29a, and consists of two μ-metal electrodes, a resistive glass tube (Photonis, Fieldmaster RGPT63.5-48.26/49.9) coupling the accelerator electrode voltage to the grounded face of the detector flange, and an MCP + P43 phosphor screen detector mounted into a 6" CF flange (Photek Ltd., VID240). The whole arrangement is magnetically shielded with μ-metal tubing (Magnetic Shields Ltd.) (79 mm i.d., 0.5 mm thick) and mounted from the detector flange using stainless steel rods and Teflon mounting rings. The two electrode plates, shown in more detail in Figure 2.29b, are spaced apart by 1.6 cm using stainless steel spacers and ceramic washers. Each has an o.d. of 9.6 cm and a 1.0 mm thickness, and both plates have radial magnetic shielding which interlocks without touching each other. Apertures of 1.6 cm × 1.6 cm are present in the radial shield, to allow the anion and laser beams passage through the VMI arrangement. The accelerator plate has a large opening at its centre (4.4 cm diameter) which generates an inhomogeneous electric field lens between the two electrodes, allowing electrons to be accelerated towards and focused onto the imaging detector MCPs, placed at a distance of 6.5 cm from the laser-

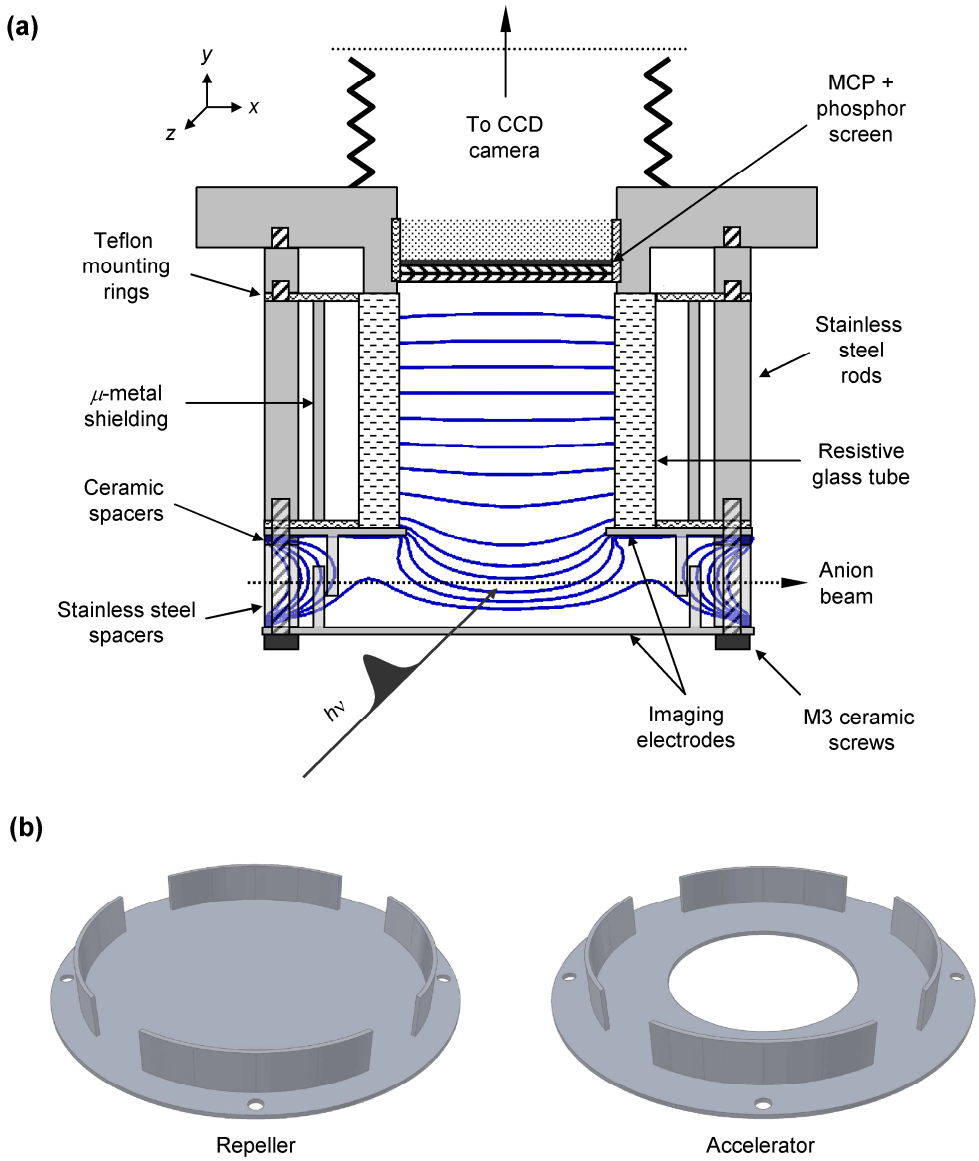

Figure 2.29: (a) Cross-sectional schematic of the new velocity map imaging (VMI) arrangement incorporated in the detection region of the spectrometer. The schematic is shown with respect to the *xy*-plane of the spectrometer and is not to scale. Electric field lines calculated using Simion 8.0 are shown in blue for repeller and accelerator voltages of –254 V and –250 V, respectively. (b) Schematics of the repeller and accelerator VMI electrodes (not to scale).

ion interaction point. A resistive glass tube (4.83 cm i.d, 63.5 cm o.d., 4.99 cm long) is used to generate a linear electric field gradient from the accelerator plate voltage, V_2, to the grounded face of the detector flange. The glass tube is similar in principle to a single pore of an MCP, and acts as an infinite chain of electrodes coupled to each other with a series of resistors. The outside of the tube is sand-blasted to electrically isolate it from the tube ends, which are nickel coated to allow electrical contact at the accelerator plate

and the grounded detector face, respectively. It is this tube which has enabled the exceptionally compact design of our VMI detector stack to be realised, from a two-fold perspective. Firstly, it avoids the need for space consuming UHV compatible resistors, and secondly, and most importantly, the tube eliminates undesired achromatic aberrations, which originate from electric field distortions at the start of the field free VMI flight region in Eppink and Parker style VMI arrangements (see field lines in Figure 2.28). To compensate for these aberrations, traditional VMI arrangements are forced to place the imaging detector at a reasonable distance from the point of laser-ion interaction (L = 36 cm in Figure 2.28). Here however, the electric field is homogenous and has a linearly decreasing gradient from the accelerator voltage to grounded face of the detector, thus elegantly eliminating any detrimental achromatic aberrations and allowing the detector to be placed significantly closer to the laser-ion interaction position (L = 6.5 cm).

The new VMI arrangement has been simulated using Simion 8.0 where the resistive glass tube has been modelled using a series of closely stacked ring electrodes. The results from these simulations are shown in Figure 2.30a. The dimensions of the VMI stack have been specifically chosen to realise low electric field gradients within the region between the repeller and accelerator plates. Simulation test results, shown in Figure 2.30b, show how the VMI voltage ratio, V_1/V_2, required to map 5 eV electrons at a distance of L = 6.5 cm onto a 40 mm diameter detector, varies with the ratio of the aperture size in the accelerator plate, D, to the distance between the electrode pair, d; D/d. As D/d increases, the ratio V_1/V_2 begins to decrease until it reaches unity at a value of D/d = 2.8. For the design described here D = 4.4 cm and d = 1.6 cm, providing a ratio of D/d = 2.75, thus allowing $V_1 \approx V_2$. For the simulations presented in Figure 2.30a, V_1 = –254 V and V_2 = –250 V. By placing the VMI electrodes at approximately the same voltages (to within ~2 %) realises the small electric field gradients required for minimal anion beam deflection. With reference to Figure 2.30a, this is exemplified by the trajectory of a simulated 2 keV anion beam (beige lines), which deviates off-axis by $<2^{o}$. The simulated electric field potentials from these simulations are also shown in Figure 2.29a (blue lines). Figure 2.30a additionally displays the simulated trajectories of photoelectrons, which have been born with a 2D Gaussian distribution in the xy plane (σ_x = σ_y = 0.5 mm) at the laser-ion interaction

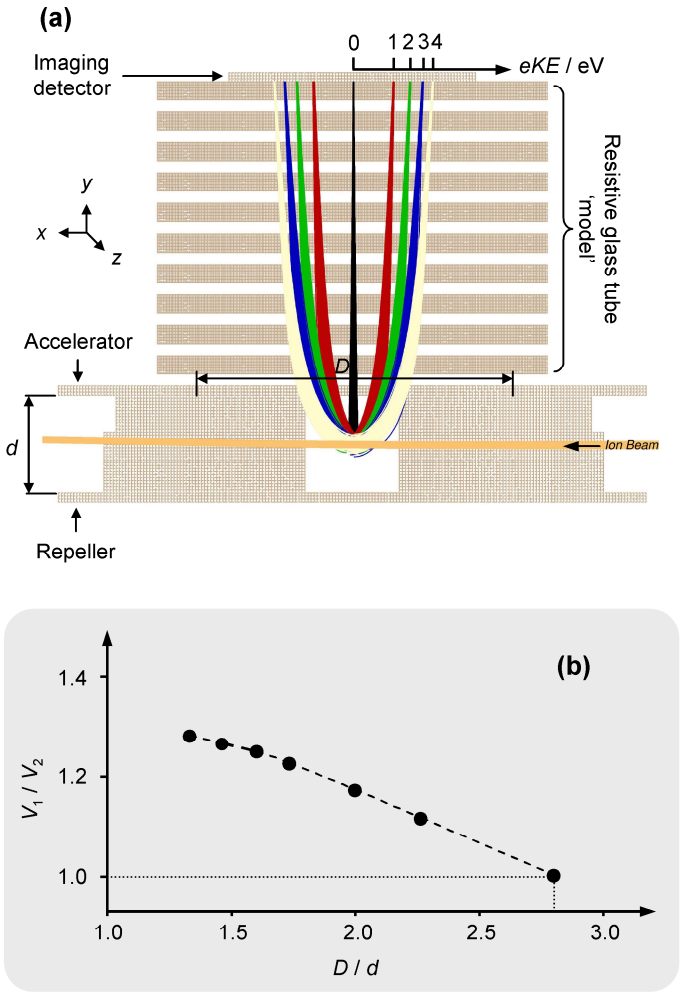

Figure 2.30: (a) Simion photoelectron trajectory simulations in the new imaging arrangement, conducted for electron kinetic energies (*eKE*s) of 0 (black), 1 (red), 2 (green), 3 (blue), and 4 eV (cream). 50 photoelectrons have been simulated for each energy, with a 2D Gaussian distribution about the laser-ion interaction point (σ = 0.5 mm). The simulation is displayed as a cross-sectional view through the *xy*-plane with the front section of the VMI stack cut away. Voltages of –254 V and –250 V have been applied to the repeller and accelerator plates, respectively (electric field lines displayed in Figure 2.29a). Under these conditions, a 2 keV anion beam (beige), traversing from right to left, is deflected off-axis by <2°. (b) shows how the ratio V_1/V_2 varies as a function of the ratio D/d, where *D* is the size of the aperture in the accelerator electrode and *d* is the distance between the two VMI electrodes (shown labelled in (a)).

position. 5 sets of 50 electrons are generated, where each set has *eKE* values of 0, 1, 2, 3, and 4 eV, respectively. These simulations indicate that an energy resolution of $\Delta E/E$ = 5 % is achievable with this arrangement. At the VMI electrode voltages applied in these simulations, it is possible to image photoelectrons with energies of up to 5 eV on the 40 mm diameter imaging MCPs, whilst maintaining an energy resolution of 5 %. Although this resolution value is not as good as most other photoelectron VMI arrangements, we note that this new arrangement was not designed with exceptionally

high energy resolution in mind, due to its application to femtosecond TRPEI experiments.

Imaging Calibration: Photoelectron Images of Iodide

The imaging arrangement has been calibrated using the well-known photoelectron spectra of iodide at 400 nm (3.10 eV) and 266 nm (4.66 eV). A packet of iodide anions is transferred to the detection region of the spectrometer using the methodology described in Section 2.5.1. As the anion packet passes through the centre of the VMI arrangement, it is perpendicularly intersected by a femtosecond laser pulse, generating photoelectrons. The electric field polarisation vectors, $\boldsymbol{\varepsilon}$, of both the 400 nm and 266 nm laser pulses are set parallel to the plane of the imaging detector, and have energies of ~80 μJ/pulse and ~30 μJ/pulse, respectively. Both beams have power densities of ~1 × 10^{10} W cm^{-2} at the laser-ion interaction region. The velocities of the ejected photoelectrons (speed and angle) are mapped onto the imaging detector MCPs, by placing the repeller and accelerator voltages at –254 V and –250 V, respectively, using a pair of commercial power supply units (Applied Kilovolts, HP2.5NIS025). This electron current is then amplified as it is accelerated towards the rear of the MCP pair, by biasing the rear MCP at +1.4 kV using a high voltage supply module (Applied Kilovolts, HP2.5PIS025). The amplified current is then further accelerated and impinges on the phosphor screen, which is placed at a high voltage of +4.5 kV with a second high voltage supply (Applied Kilovolts, HP010PIS025). As the electron signal strikes the phosphor, light is emitted and captured using a CCD camera (Basler, A312f) and lens (Computar, M2514-MP FA). The lens has a focal length of f = 25 mm and focal ratio of F = 1.4 (10 % of light passed), and the entire arrangement is placed at a distance of 18.5 cm from the imaging detector window, where is it isolated from external light sources in a custom-made mounting system. The CCD camera is interfaced to a data acquisition program written in LabVIEW 8.5 (see Section 2.6.3) on a personal computer, *via* a firewire cable. Raw photoelectron images are recorded for 8.75 × 10^5 laser shots at 400 nm and 3.5 × 10^6 laser shots at 266 nm. Images are then passed through a polar onion-peeling (POP) reconstruction algorithm to obtain 1D radial spectra, which are then converted into the desired photoelectron spectra. To achieve this conversion, the radial axis, r, is first converted into *eKE* space by squaring

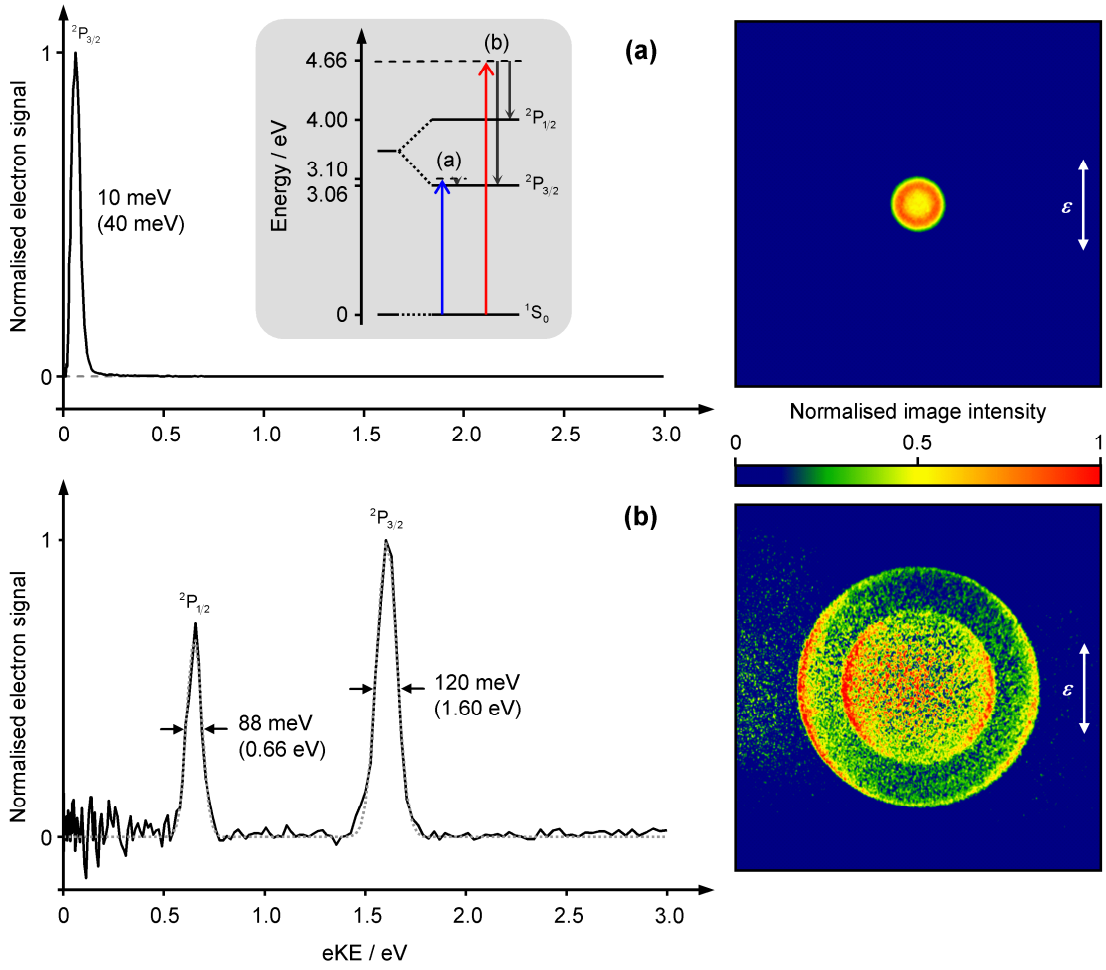

Figure 2.31: (a) Photoelectron spectrum and raw photoelectron image produced by detachment of electrons from I^- at 400 nm (3.10 eV). The single peak at ~40 meV corresponds to detachment from the $^1S_0$ anion ground state to the $^2P_{3/2}$ state of the neutral. Shown inset is an energy level diagram of the $^1S_0$ ground state of iodide and the spin-orbit states, $^2P_{3/2}$ and $^2P_{1/2}$, of neutral iodine. The detachment process in (a) is shown by the blue arrow, and electron kinetic energies are shown by the downward dark grey arrows. (b) shows the photoelectron spectrum and raw photoelectron image produced when electrons are detached from iodide at 266 nm (4.66 eV). The two peaks at 0.66 eV and 1.60 eV correlate to detachment to the $^2P_{1/2}$ and $^2P_{3/2}$ neutral states, respectively. This detachment process is labelled (b) (red arrow) on the inset energy level diagram in (a). The energy FWHM of the two features, shown adjacent to the two peaks, have been determined from least squares Gaussian fits (dotted grey line), providing a resolution of $\Delta E/E$ = 7.5 % for the feature at 1.60 eV.

all radii, r^2, and can understood from the relationship $r \propto \sqrt{eKE}$ shown in equation (2.22). A proportionality constant is then identified by calibrating the energy axis relative to a photoelectron feature of known energy, which in this case is chosen to be the $^2P_{3/2}$ spin-orbit state feature in the I^- spectrum at 266 nm, and has an associated energy of 1.60 eV (see Figure 2.31). The intensity scale must also be scaled as a result of the transformation from r to eKE and is performed through the relationship

$I(eKE) = I(r)/r$, where $I(eKE)$ and $I(r)$ are the signal intensity scales for photoelectron and radial spectra, respectively.

Figure 2.31 shows the 1D photoelectron spectra and raw photoelectron images collected by detaching electrons from I^- at 400 nm (3.10 eV) and 266 nm (4.66 eV). The laser polarisation vector, $\boldsymbol{\varepsilon}$, is indicated by the white arrows. Also shown inset is an energy level diagram of the spin-orbit states of neutral iodine, $^2P_{3/2}$ and $^2P_{1/2}$, and the singlet ground state of iodide, $^1S_0$.

Calibration experiments carried out at 400 nm (Figure 2.31a) yield a low energy isotropic feature at the centre of the image due to the *s*-wave like nature of the emitted electrons, corresponding to an orbital angular momentum of $l = 0$. These low energy electrons have an associated *eKE* of ~40 meV, and are produced by photodetachment from iodide's $^1S_0$ ground state, to the lowest energy $^2P_{3/2}$ spin-orbit state of neutral iodine. The associated energy width (FWHM) of this photoelectron feature is ~10 meV, corresponding to an energy resolution $\gg 5$ %. However, below *eKE*s of 1.2 eV the resolution is limited by the energy bandwidth of the femtosecond laser pulses (35 nm, 68 meV).

The results from the 266 nm calibration experiments are shown in Figure 2.31b. Photodetachment at this photon energy leads to the generation of two features in the captured image, corresponding to the two accessible spin-orbit states in iodine, $^2P_{3/2}$ and $^2P_{1/2}$. Both ring intensities have associated perpendicular anisotropies relative to the laser polarisation, which can be understood in terms of interference between *s*- and *d*-partial electron waves ($l = 0$ and 2, respectively). As the *eKE* increases, the cross-section, σ, for generating electrons with higher allowed *l* values increases, as predicted by the Wigner threshold law [33]

$$\sigma \propto eKE^{\left(l+\frac{1}{2}\right)}. \tag{2.24}$$

Unlike the 400 nm calibration experiments, a considerable amount of background photoelectron signal is observed in experiments at 266 nm, due to stray laser photons detaching electrons from the VMI electrodes. To reduce the impact of this laser related noise signal, a background image (laser off) acquired over the same number of shots

(3.5×10^6) has been subtracted from the experimental image to produce the raw photoelectron image presented in Figure 2.31b. The signal fluctuation observed at low *eKE* values (<0.5 eV) in the photoelectron spectrum is due to residual background electron signal. The two peaks at 0.66 eV and 1.60 eV are associated with electrons generated *via* detachment to the neutral $^2P_{1/2}$ and $^2P_{3/2}$ states, respectively. These *eKE*s translate accordingly to electron binding energies of 4.00 eV for the $^2P_{1/2}$ state and 3.06 eV for the $^2P_{3/2}$ state. Using the energy FWHM of these peaks (shown adjacent to the peaks in Figure 2.31b), this translates to an energy resolution of $\Delta E/E$ = 7.5 %, which corroborates reasonably well with the predicted energy resolution from the Simion trajectory simulations of $\Delta E/E$ = 5 %.

2.6 Experimental Controls

We close Chapter 2 by describing the experiment control systems, which include the vacuum interlock system, control of experimental timings, and finally the DAQ interface developed in LabVIEW 8.5. We begin by describing the vacuum interlock system.

2.6.1 Vacuum Interlock System

In the event that any of the vacuum pump systems fail, the spectrometer has been interlocked using a series of emergency logic protocols, controlled from a custom-made interlock control box. The primary aims of this interlock system are to isolate and preserve the UHV conditions in R5 and R6 of the spectrometer, and prevent any damage to the delicate ion and imaging detector arrangements housed in R6 in the event of vacuum failure. With reference to Figure 2.32, the 12 V interlock control box is connected to the pressure set-point relays (SP1 to SP4) within the pair of pressure gauge controllers (described in Section 2.1.2). The first of these gauge controllers (gauge controller 1) monitors the pressures in R5 and R6 of the spectrometer, using a pair of ionisation gauges (IG5 and IG6, respectively). Additionally, it also monitors the pressure of the backing line behind the R5 and R6 turbomolecular pumps (TMPs), *via* a thermocouple gauge (TC56). The second gauge controller monitors the pressures in R2 to R4, and the set-point relay, SP4, is specifically connected to the ionisation gauge on

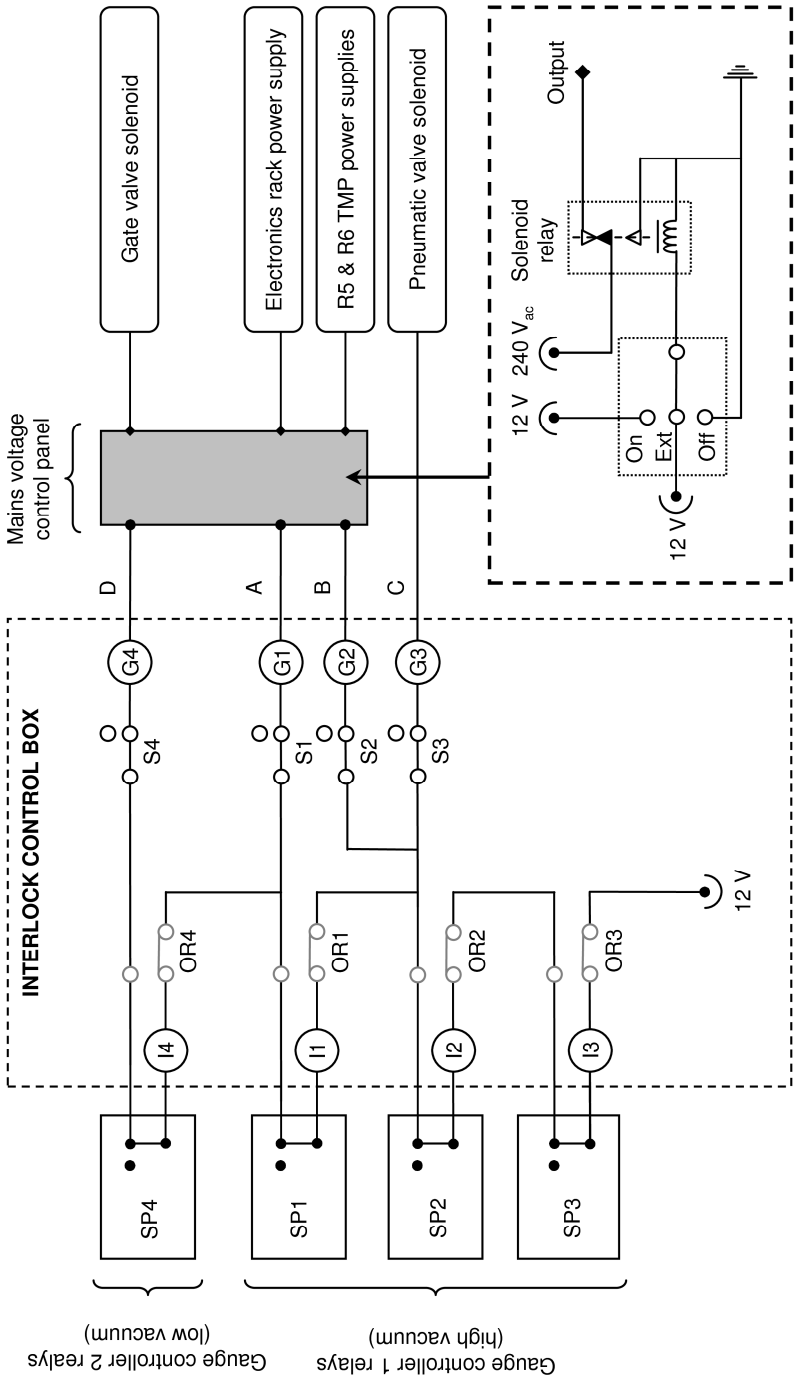

Figure 2.32: Schematic of the vacuum interlock control circuit. The arrangement consists of a 12 V interlock control box, which houses LED set-point breach indicators (I1 to I4), set-point override switches (OR1 to OR4), and control switches and indicators (S1 to S4 and G1 to G4, respectively) for the four 12 V outputs (A to D). This box is connected to the pressure set-point relays (SP1 to SP4) in the pair of pressure gauge controllers, which control the 12 V outputs. Outputs A, B and D drive solenoid relays (shown inset, bottom right) in a mains voltage control panel. All output voltages used operate spectrometer components, which are respectively labelled.

R4 of the spectrometer (IG4). The components in the interlock circuit diagram are all displayed in their normal operation configurations (no set-point breaches). In this normal operation configuration, the interlock control box supplies four 12 V outputs (A to D) which are then used to control various components of the spectrometer, which may be manually operated using switches S1 to S4, respectively, on the front panel of the interlock box. Each of the controlled components associated with S1 to S4 are shown below in Table 2.11.

Table 2.11: Spectrometer devices controlled using the four 12 V outputs (A to D) from the interlock control box.

12 V output (control switch)	Device(s) controlled
A (S1)	Electronics rack
B (S2)	R5 & R6 TMPs
C (S3)	Pneumatic angle valves
D (S4)	Pneumatic gate valve

Output C is used to drive a 12 V 4-way solenoid valve (Humphrey, 410 series) which is used to actuate a pair of pneumatic angle values (Kurt J. Lesker, SA0100PVQF) in the R5/R6 roughing line (labelled V6 and V7 in Figure 2.1 on page 51). The remaining three 12 V outputs (A, B, and D) are used to drive externally (Ext) controllable 12 V solenoid relays in a mains voltage (240 V_{ac}) control panel (shown inset in Figure 2.32). These solenoid relays provide the required 240 V_{ac} to drive each of the relevant spectrometer components. The interlock control of these solenoid relays may also be manually overridden using three way rotary control switches (On, Off, or Ext) on the front of the mains control panel. Output B controls power to the R5 and R6 TMPs, while output A collectively controls power to high voltage supplies for the imaging detector, ion detector, VMI electrodes, and mass gate. These are collectively referred to as the electronics rack. Finally, output D drives another 4-way solenoid valve (Humphrey, 410 series), used to actuate the pneumatic gate valve (Kurt J. Lesker, SG0250PCCF).

In the event that any of the pressure set-points are breached the corresponding set-point relays in the pressure gauge controllers switch to their open positions, removing the 12V output from that region of the interlock circuit. The pressure set-points, their

associated pressure gauges, and the actions taken upon these set-points being breached are summarised in Table 2.12. Set-point breaches are monitored using the LED indicators (I1 to I4, respectively) on the front interlock panel, which extinguish in the event of a set-point breach. Set-point breaches may be manually overridden using a series of override switches, OR1 to OR4. The override switches also serve to allow R5 and R6 to be evacuated from atmosphere safely when reactivating the primary and foreline vacuum pump systems. To evacuate the high vacuum regions of the spectrometer from atmosphere, the override switches OR2 and OR3 must be switched from their normal configurations (shown in Figure 2.32) to their override positions, enabling the pneumatic angle valves in the foreline region to be opened and allowing the R5 and R6 TMPs to be started when R5 and R6 attain an appropriate roughing pressure. OR1 and OR4 should remain in their normal configurations during this period to ensure that the pneumatic gate valve remains shut and that no power is supplied to the electronics rack. When R5 and R6 finally reach pressures of ~10^{-8} Torr, OR2 and OR3 may be switched back into their normal positions, ensuring that the interlock system is operational.

Table 2.12: Pressure set-point values (SP1 to SP4), their associated control pressure gauges, and the actions taken upon on a set-point breach.

Pressure set-point / Torr	Control pressure gauge	Breach actions
SP1 = 1×10^{-6}	IG5	Close gate valve Shut down electronics rack
SP2 = 1×10^{-5}	IG5	SP1 actions + Close inline valves Shut down R5 & R6 TMPs
SP3 = 5×10^{-2}	TC56	SP2 actions
SP4 = 1×10^{-5}	IG4	Close gate valve

2.6.2 Timing Considerations

Accurate timing between all pulsed voltage components of the experiment is critical for optimising both the ion signals in TOF spectra and photoelectron signals for TRPEI. The latter relies on the temporal overlap of pump and probe laser pulses with a specific m/z anion packet of interest. The laser pulses are switched out of the amplification

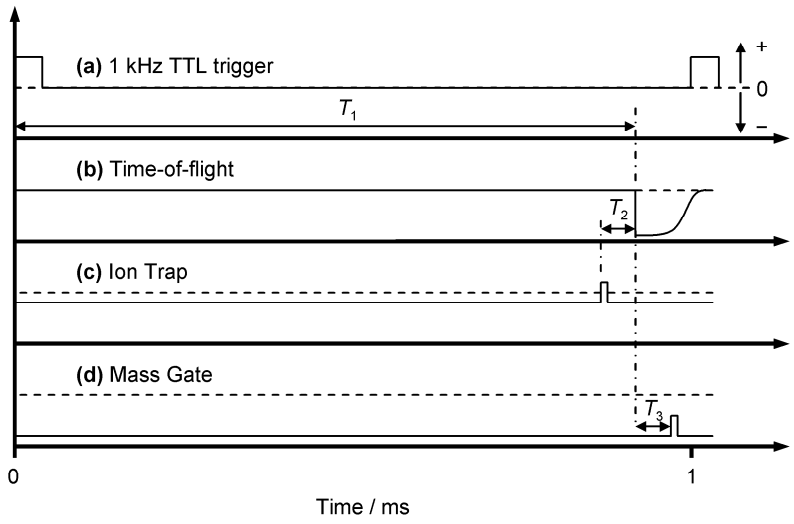

Figure 2.33: Timing sequence used for performing time-resolved photoelectron imaging (TRPEI) experiments. The 1 ms delay cycle is triggered (t = 0) using a 1 kHz TTL signal (a) generated from the laser Pockels cell driver. The time-of-flight (TOF) electrode voltages are pulsed on at a time delay, T_1, from t = 0 (b), formally defined by equation (2.25). By varying T_1 a specific m/z anion packet can be temporally overlapped with the pump and probe laser pulses in the imaging detector. Anions are unloaded at a delay time of $T_1 - T_2$, relative to t = 0 (c). Finally, the mass gate may be pulsed to its Einzel lens voltage at a delay T_3, relative to T_1, allowing a single anion packet into the detection region.

cavity in the regenerative amplifier using high voltage Pockels cells, which are triggered at a rate of 1 kHz with a TTL signal. This signal is subsequently used as the reference trigger (t = 0) for defining all experimental time delays. As the 76 MHz seed output from the oscillator is not locked to the 1 kHz repetition rate of the regenerative amplifier Pockels cells, this leads to a jitter of 13 ns on the delay cycle trigger, although this is not a major issue as the temporal duration of an ion packet (~50 ns) is sufficiently long for this not to cause a problem.

The timing sequence for the experiment is schematically displayed in Figure 2.33 and is controlled using a single digital delay generator (Highland Technology, P400), triggered by the 1 kHz TTL pulses. The delay generator defines all temporal delays and voltage pulse durations, where applicable for the latter. At a delay time T_1, the repeller and acclerator TOF electrodes are pulsed to voltages of –2.3 kV and –2.0 kV, respectively, for a period of 100 μs. By varying T_1, accelerated anions of specific m/z ratios can be temporally overlapped with the next laser pulse in the 1 kHz pulse train at the laser-ion interaction region of the photoelectron imaging arrangement. T_1 is formally defined as

$$T_1 = \frac{1}{r} - TOF \ , \tag{2.25}$$

where r is the repetition rate of the experiment and TOF is flight time of the anion packet of interest. Anions are pulsed into the TOF optics at a delay time $T_1 - T_2$ relative to $t = 0$. T_2 is formally defined by the flight time of the ion packet of interest from the trap exit to the centre of the repeller of the TOF optics, and is dependent of the anions m/z ratio. At this negative T_2 time delay relative to T_1, the ion trap voltage is pulsed open for a period of typically 1.0 to 2.5 μs. When anions exit the trap, they enter region 3 with a velocity spread dependant on their m/z ratio, and by varying T_2 and the duration the trap is open, it is possible to optimise a particular mass range of anions into the TOF spectrometer. Immediately prior to the anions entering the detection region, the mass gate may be pulsed to its Einzel lens voltage (–1 kV) at a time delay T_3 relative to T_1. By varying T_3 a single anion packet of specific m/z ratio may be allowed to enter the detection region of the spectrometer, whilst all other negatively charged species are gated out. For the experiments described in thesis however, the mass gate function is not used. Finally, the anion packet of interest is intersected with the next laser pulse in the 1 kHz laser pulse train (t = 1 ms in Figure 2.33).

2.6.3 Data Acquisition Interface

Overview of the Data Acquisition Control Station

TRPEI experiments are controlled from a purpose built DAQ control station on a PC, coded in LabVIEW 8.5. The LabVIEW program interfaces to and controls two major components: (1) the imaging CCD camera (Basler, A312f); and (2) the optical delay stage (Physik Instrumente, M-505), through firewire and USB cables, respectively. The basic premise of the control station is to move the optical delay stage to a defined number of temporal pump-probe delays, and at each delay the CCD camera output is integrated for a user defined number of laser shots. In this manner, a series of temporally evolving photoelectron images are then saved onto the DAQ PC. This aforementioned experimental loop is then reiterated, and all photoelectron images recorded at the same delays are summed together. This process is repeated until the user

is satisfied that the signal-to-noise ratio in the desired 1D radial spectra is acceptable. The signal-to-noise is monitored on-the-fly (at a rate of ~1 Hz) by incorporating the polar-onion peeling algorithm (POP) we have developed into the DAQ control station. The POP algorithm is explained in detail in Chapter 3. Resultant 1D radial spectra for each temporal delay are also saved to the DAQ PC.

The details of the control and operation of the optical delay line and CCD camera, which operate in tandem to each other, are described in greater detail below.

Optical Delay Line Control

The optical delay stage used has a minimum step size of 0.05 μm, correlating to a temporal delay of 0.3 fs, and has a measured precision of 0.004 % over a delay of 170 ps. The delay stage is primarily controlled using the virtual instruments (VIs) provided by Physik Instrumente, some of which have been modified to increase the efficiency of the control station. An operation chart of the delay stage control process is presented in Figure 2.34. Before an experimental run begins, the delay stage interface is initialised and a delay routine file (written in ASCII format), containing all desired temporal delays (in fs), is called into memory. Following this, the position of the stage corresponding to the temporal overlap of the pump and probe laser pulses (t = 0) is defined for the remainder of the experiment. This position is located prior to an experiment by spatially overlapping the pump and probe laser pulses in an appropriate thin non-centrosymmetric crystal (e.g. BBO), and optimising the sum frequency output on a fast photo-diode (Thorlabs, DET10A/M) by varying the delay stage position. Although a more accurate method to obtain t = 0 would be to perform above threshold detachment on Γ^- within the detection region itself, the method used here provides an ample estimate for t = 0, and any error in this value may be accounted for in the temporal fits during data analysis. The control station itself consists of three loops, each embedded within each other. The first of these loops defines the number of times the complete experimental delay routine is repeated and runs for a total of n_1 iterations, where each individual iteration, i_1, corresponds to a single experimental run. Embedded within this first loop is the delay cycle loop which runs over n_2 iterations, where n_2 is defined as the total number of temporal delays in the delay routine file. Here a time delay, $t(i_2)$, is read from the delay file, and then converted into the corresponding delay

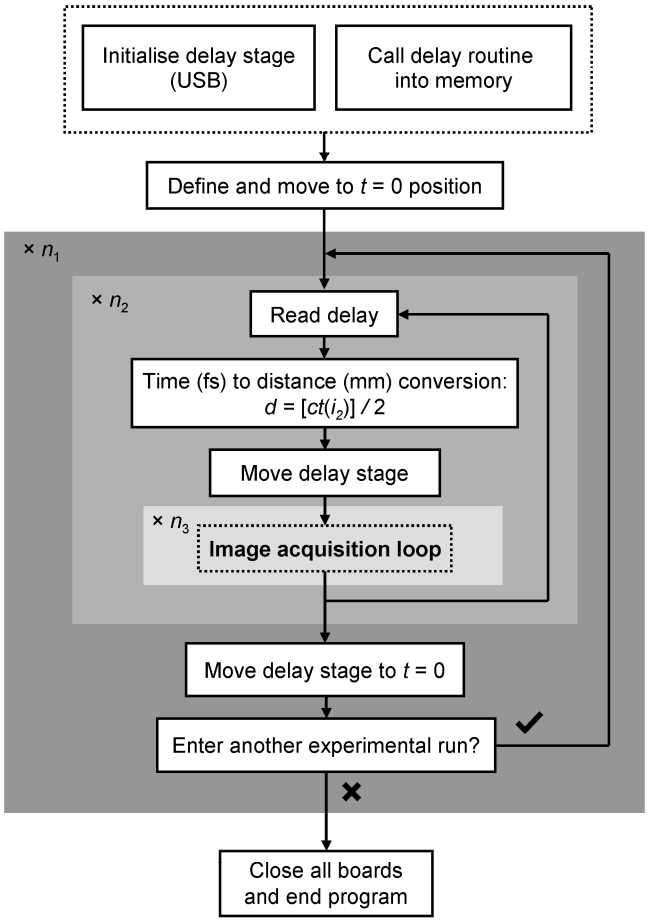

Figure 2.34: Operations chart of the delay stage control process coded in LabVIEW 8.5. The process begins by initialising the delay stage USB interface and loading an ASCII delay file into memory. The position (in mm) on the delay stage correlating to the temporal overlap of the pump and probe laser pulses (t = 0) is then defined for the remainder of the experiment. The first of three loops (dark gray) is then entered, which runs over n_1 iterations and defines the total number of times the experimental delay routine is repeated. The delay stage loop (intermediate gray) is then entered. This loop runs for n_2 iterations, where n_2 is defined by the total number of temporal delays and each iteration, $t(i_2)$, corresponds to an individual delay. At each iteration, the delay stage is moved to the appropriate delay and a photoelectron image is acquired in the image acquisition loop (ligh gray). At the end of each delay cycle, the delay stage is reset to its t = 0 position and a Boolean operation is used to decide whether the experimental cycle (dark gray loop) is repeated or the program terminated.

stage position, d (in mm), using the relationship $d = \left[ct(i_2) \right] / 2$, where c is the speed of light in air in mm fs^{-1} (c = 2.99 × 10^{-4} mm fs^{-1}). The delay stage is then moved to the appropriate delay position. The factor of a ½ is present because the probe beam enters and exits the delay stage along the same direction (see Figure 2.5 in Section 2.2.3), and hence the stage is only required to move half the distance. All temporal delay positions are defined absolutely with respect to the t = 0 position, rather than incrementally moving to the next delay position with respect to the last delay. By using this method,

the error accrued in temporal delay positions as the delay cycle progresses is significantly reduced. Before moving to the next delay position, the control station enters an image acquisition loop, which is described in the next subsection. When the delay routine is completed, the delay control process moves back into the experimental run loop where the delay stage position is reset to t = 0. A user activated Boolean operation is then finally used to decide whether another iteration of the complete delay sequence is required. The outcome of this Boolean operation may be decided at any time during the current experimental iteration. If true, then another experimental run is performed, increasing the value of n_1 by 1. Conversely, if false, all interfaces are closed and the DAQ program ended.

CCD Camera Control

The CCD camera has an 8 mm (diagonal) sensor and a resolution of 782 × 582 pixels. Each pixel has a size of 8.3 μm × 8.3 μm, where each pixel equates to 8 bits, corresponding to a total of 3.64 Mbits per image (0.45 Mb). The camera control process operates alongside the delay stage control, shown in Figure 2.34, in the three control station loops. Each of these loops may not proceed to its next iteration or be completed until *both* the delay stage and camera control VIs within them end. A flow diagram of the camera control process is shown in Figure 2.35, and begins by initialising the CCD camera firewire interface. This involves initiating the CDD camera and then selecting a region-of-interest on the CCD sensor, of size $p_x \times p_y$ (in pixels), where p_x and p_y are the number of pixels in the x and y co-ordinate directions, respectively. In conjunction to this, user defined experiment details are called into memory, which include an experiment name and date. These details are used to automatically generate appropriate folder and file names for the photoelectron images recorded during a TRPEI experiment. Images are recorded as a two-dimensional array of integers, where the image arrays have a size of $p_x \times p_y$, and are here in referred to as the matrices $\mathbf{P}(t)$ at each temporal delay, t. The final component of the initialisation process requires a basis set for the POP algorithm to be called into memory, which is described in greater detail in Section 3.2.3 of this thesis. Following initialisation, the first loop, which runs over a total of n_1 iterations, is activated. This then leads into the delay cycle loop described above. If the current iteration of the experimental loop is i_1 = 1, then a new empty

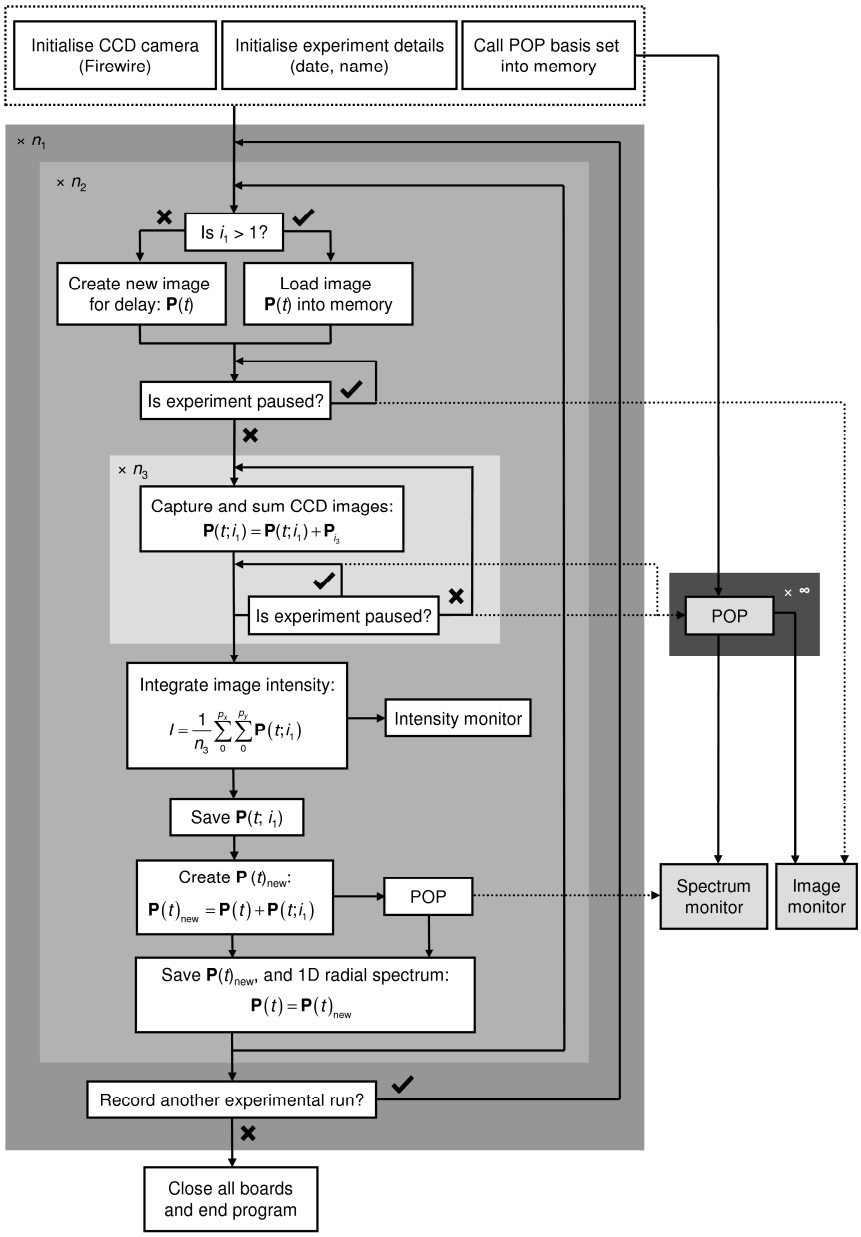

Figure 2.35: Operations chart for acquiring images from the CCD camera in the DAQ control station, which runs in tandem to the delay stage control process presented in Figure 2.34. The process begins by initialising the CCD camera, experiment details, and the basis set for the polar onion-peeling (POP) routine. The three loops which are sequentially entered are the same three loops presented in Figure 2.34. The experimental loop (dark grey) runs for n_1 user defined iterations, and defines the total number of times a delay cycle is repeated. At the start of the delay cycle loop (intermediate grey), an image, $\mathbf{P}(t)$, is either created or called from memory, depending on which iteration the outer experimental loop is at, i_1. In the image acquisition loop (light grey), n_2 individual images, $\mathbf{P}_{i_3}$, are acquired and summed from the CCD camera to generate the integrated image, $\mathbf{P}(t;i_1)$. The delay loop is then re-entered where the total intensity of the image is determined and sent to an intensity monitor on the front panel of the DAQ control station. $\mathbf{P}(t;i_1)$ is then saved to the DAQ PC, and added to the image array $\mathbf{P}(t)$, to generated $\mathbf{P}(t)_{\text{new}}$. $\mathbf{P}(t)_{\text{new}}$ is then passed through the POP algorithm, and the derived 1D radial spectrum and raw photoelectron image are saved to memory, such that $\mathbf{P}(t)=\mathbf{P}(t)_{\text{new}}$. At the end of a complete delay cycle, the experimental loop is re-entered, where a user controlled Boolean operation governs whether the DAQ process ends or another delay cycle is entered. During image acquisition, POP is also run independently allowing on-the-fly access to the 1D spectrum as it is acquired.

image array, $\mathbf{P}(t)$, is created for the current temporal delay of the delay routine, $t(i_2)$. Alternatively, if $i_1 > 1$, then the relevant saved $\mathbf{P}(t)$ is called into memory for the current iteration of the delay cycle loop. The process then enters the image acquisition loop which acquires and sums together a total of n_3 individual camera images, $\mathbf{P}_{i_3}$, to generate the integrated image, $\mathbf{P}(t;i_1)$. The CCD camera is operated in free-running mode (un-triggered) and each iteration, i_3, takes ~0.7 s, corresponding to approximately 700 laser shots per image ($\mathbf{P}_{i_3}$) at a laser repetition rate of 1 kHz. After exiting this loop, the resultant image, $\mathbf{P}(t;i_1)$, is integrated using

$$I = \frac{1}{n_3}\sum_{0}^{p_x}\sum_{0}^{p_y}\mathbf{P}(t;i_1), \tag{2.26}$$

to measure the total intensity of the photoelectron image, *I*. This value of *I* is then sent to an image intensity monitor display on the front panel of the control station. By monitoring *I* for each temporal delay of an experiment the user can monitor and optimise the total photoelectron signal over the duration of a TRPEI experiment. $\mathbf{P}(t;i_1)$ is then saved to the DAQ PC before it is added to the $\mathbf{P}(t)$ which was created or loaded into memory at the start of the current delay iteration, to generate $\mathbf{P}(t)_{\text{new}}$. $\mathbf{P}(t)_{\text{new}}$ is subsequently deconvoluted and converted into a 1D radial spectrum using the POP algorithm, where finally, the 1D spectrum and $\mathbf{P}(t)_{\text{new}}$ are saved to the DAQ PC, so that $\mathbf{P}(t) = \mathbf{P}(t)_{\text{new}}$. The same Boolean operation described at the end of the delay stage control process is then used to determine whether another repeat of the complete delay cycle is required, or all interfaces are terminated and the control station closed.

The experiment control station may also be paused at any stage of a TRPEI experiment using a Boolean operation. This allows the user to pause the DAQ process should either the anion beam signal or photoelectron imaging signal need to be optimised, without acquiring any null data. To aid in this process, the POP algorithm is also operated in parallel to the aforementioned control loops. In this manner, the user is provided with on-the-fly access to the 1D radial spectrum of the current accumulating image, $\mathbf{P}(t;i_1)$, as the experiment progresses. This process is represented by the dotted arrows in Figure 2.35. Through Boolean operations (not displayed in Figure 2.35) either the currently accumulating radial spectrum or the spectrum from the previous delay

iteration can be observed on the spectrum monitor on the control station front panel. Analogously, either the currently accumulating photoelectron image, or the previous photoelectron image may also be observed on the front panel.

2.7 Summary

In this chapter we have described the development, construction, and commissioning of a new photoelectron imaging spectrometer, designed to study the spectroscopy and ultrafast dynamics of molecular anions. The experiment consists of an electrospray ionisation source coupled to a time-of-flight mass spectrometer and a novel compact photoelectron imaging detector arrangement. We began by considering the vacuum pumping systems required to enable the successful coupling of an ESI source, which operates at atmospheric pressure, to a photoelectron imaging detector, which must be operated under ultra-high vacuum conditions.

Following on from this the femtosecond laser system used to perform time-resolved photoelectron imaging was described in detail, where we characterise the fundamental pulses in both the time and frequency domains, and conclude that pulses nearly transform limited. Similarly, the temporal width of the pump-probe pulse pair (800 nm and 400 nm, respectively) was determined to be ~80 fs.

Particular detail was then paid to describing the ion guide and TOF spectrometer, the former of which converts the continuous anion beam into a pulsed source synchronous with the repetition rate of the femtosecond laser system, using a low voltage DC trap. Simion simulations have been used to model the ion trap, which indicate that it may accommodate a total of ~200 anions. The TOF spectrometer was calibrated by spraying a solution of NaI, to record a calibration TOF spectrum of I^-. The results from these calibration experiments corroborate well with the predicted values for spectrometer resolution and for the number of anions reaching the detection region of the spectrometer, both of which we attained from Simion simulations.

A new compact velocity map imaging spectrometer for performing PEI on anions has also been described. The novelty of the design stems from the incorporation of a resistive glass tube and the low electric field gradients generated in regions where the anion beam propagates. This results in minimal deflection of the anion beam as it

traverses through the arrangement, allowing the use of low DC voltages rather than costly high voltage pulsers. The arrangement was calibrated using the well-known photoelectron spectra of I^- at 400 nm and 266 nm, and has a resolution of $\Delta E/E = 7.5$ %.

Finally, we drew this chapter to a close by describing the experiment control systems, which include a vacuum interlock system, the experimental timing procedures, and the DAQ control station. The DAQ, developed in LabVIEW 8.5, also incorporates a polar onion-peeling reconstruction algorithm, which provides on-the-fly access to the 1D photoelectron spectra as images are acquired. In Chapter 3, we move on to describe this algorithm in greater depth.

2.8 References

[1] J. H. Moore, C. C. Davis, and M. A. Coplan, *Building Scientific Apparatus*, 3rd ed. (Westview Press, Cambridge, MA., 2003).

[2] A. Nebel and R. Beigang, *Opt. Lett.*, **16**, 1729 (1991).

[3] J. Ringling, O. Kittelmann, F. Noack, G. Korn, and J. Squier, *Opt. Lett.*, **18**, 2035 (1993).

[4] W. Demtroder, in *Laser Spectroscopy: Basic Concepts and Instrumentation* (Springer, New York, 1998), pp. 222 - 365.

[5] L. Sarger and J. Oberle, in *Femtosecond Laser Pulses: Principles and Experiments*, edited by C. Rulliere (Springer, New York, 2005), pp. 195 - 222.

[6] A. W. Colburn, A. E. Giannakopulos, and P. J. Derrick, *Eur. J. Mass Spectrom.*, **10**, 149 (2004).

[7] G. F. Franklin, J. D. Powell, and A. Emami-Naeini, *Feedback Control of Dynamics Systems*. (Prentice Hall, New Jersey, 1986).

[8] A. Datta, M. T. Ho, and S. P. Bhattacharyya, *Structure and Synthesis of PID Controllers*. (Springer, London, 2000).

[9] S. A. Shaffer, K. Q. Tang, G. A. Anderson, D. C. Prior, H. R. Udseth, and R. D. Smith, *Rapid Commun. Mass Spectrom.*, **11**, 1813 (1997).

[10] S. A. Shaffer, D. C. Prior, G. A. Anderson, H. R. Udseth, and R. D. Smith, *Anal. Chem.*, **70**, 4111 (1998).

[11] T. Wyttenbach, P. R. Kemper, and M. T. Bowers, *Int. J. Mass Spectrom.*, **212**,

13 (2001).

[12] W. Paul and H. S. Steinwedel, *Z. Naturforsch.*, **8a**, 448 (1953).

[13] T. Kim *et al.*, *Anal. Chem.*, **72**, 2247 (2000).

[14] E. De Hoffmann, J. Charette, and V. Stroobant, *Mass Spectrometry: Principles and Applications*. (John Wiley & Sons, New York, 1999).

[15] E. Fischer, *Z. Phys.*, **156**, 1 (1959).

[16] S. H. Guan and A. G. Marshall, *J. Am. Soc. Mass Spectrom.*, **5**, 64 (1994).

[17] W. C. Wiley and I. H. Mclaren, *Rev. Sci. Instrum.*, **26**, 1150 (1955).

[18] L. S. Wang, C. F. Ding, X. B. Wang, and S. E. Barlow, *Rev. Sci. Instrum.*, **70**, 1957 (1999).

[19] E. A. Taft and H. R. Philipp, *Phys. Rev.*, **138**, A197 (1965).

[20] J. E. Butler, *Appl. Opt.*, **21**, 3617 (1982).

[21] J. L. Wiza, *Nucl. Instrum. Methods*, **162**, 587 (1979).

[22] T. Seideman, *Annu. Rev. Phys. Chem.*, **53**, 41 (2002).

[23] K. L. Reid, *Annu. Rev. Phys. Chem.*, **54**, 397 (2003).

[24] A. Sanov and R. Mabbs, *Int. Rev. Phys. Chem.*, **27**, 53 (2008).

[25] A. A. Bengali, S. M. Casey, C. L. Cheng, J. P. Dick, P. T. Fenn, P. W. Villalta, and D. G. Leopold, *J. Am. Chem. Soc.*, **114**, 5257 (1992).

[26] S. W. Allendorf, D. J. Leahy, D. C. Jacobs, and R. N. Zare, *J. Chem. Phys.*, **91**, 2216 (1989).

[27] P. Kruit and F. H. Read, *J. Phys. E*, **16**, 313 (1983).

[28] O. Cheshnovsky, S. H. Yang, C. L. Pettiette, M. J. Craycraft, and R. E. Smalley, *Rev. Sci. Instrum.*, **58**, 2131 (1987).

[29] D. W. Chandler and P. L. Houston, *J. Chem. Phys.*, **87**, 1445 (1987).

[30] C. Bordas, F. Paulig, H. Helm, and D. L. Huestis, *Rev. Sci. Instrum.*, **67**, 2257 (1996).

[31] A. T. J. B. Eppink and D. H. Parker, *Rev. Sci. Instrum.*, **68**, 3477 (1997).

[32] S. J. Cavanagh, S. T. Gibson, M. N. Gale, C. J. Dedman, E. H. Roberts, and B. R. Lewis, *Phys. Rev. A*, **76**, 052708 (2007).

[33] E. P. Wigner, *Phys. Rev.*, **73**, 1002 (1948).

Chapter 3: Charged Particle Image Reconstruction using Polar Onion-peeling

A method to reconstruct full three dimensional (3D) photofragment/photoelectron distributions from their two dimensional (2D) projection onto a detection plane is presented, for processes in which the expanding Newton sphere has cylindrical symmetry around the axis parallel to the projection plane. The method is based on: (1) onion-peeling in polar co-ordinates in which the contribution to the 2D projection from events outside the plane bisecting the Newton sphere are subtracted in polar coordinates at incrementally decreasing radii; and (2) ideas borrowed from the basis set expansion method in polar co-ordinates (pBASEX), which are used to generate 2D projections at each incremental radius for the subtraction. The method is then compared to other reconstruction algorithms, where it is shown to be as good as the pBASEX method in terms of accuracy, is devoid of centerline noise common to reconstruction methods employing Cartesian co-ordinates, and it is computationally cheap allowing images to be reconstructed as they are being acquired in a typical imaging experiment. We close by discussing the integration of the algorithm into the LabVIEW data acquisition control station.

3.1 Image Reconstruction: A Conceptual Overview

3.1.1 The Need for Image Reconstruction

The results obtained from charged particle imaging experiments [1-3], and more specifically, photoelectron imaging [4], offer experimentalists access to detailed information about both the charged particle velocities, which may be readily translated into kinetic energy distributions, and a quantitative measure of their angular distributions as a function of velocity. To extract this information from the captured images, we must first consider how the original three dimensional (3D) charged particle distribution is transformed during the velocity map imaging (VMI) [5] process.

Figure 3.1 considers a 3D Newton sphere of charged particles, $F(r,\theta,\phi)$, which may be integrated over all θ and ϕ to produce the associated one dimensional (1D) velocity spectrum, $I(v)$, through

$$I(v) \propto \int_0^{2\pi}\int_0^{\pi} F(r,\theta,\phi) d\theta d\phi, \tag{3.1}$$

where $v \propto r$. In a standard VMI arrangement, $F(r,\theta,\phi)$ is accelerated along the flight

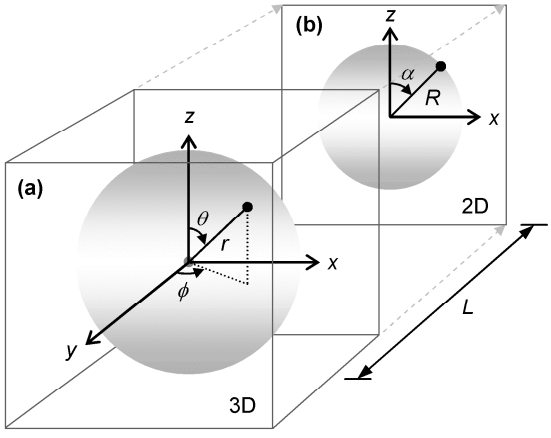

Figure 3.1: (a) Three dimensional (3D) Newton sphere of charged particles, $F(r,\theta,\phi)$, which exhibits cylindrical symmetry about the *z*-axis. (b) Two dimensional (2D) projection, $G(R,\alpha)$, produced from mapping (a) onto a 2D position sensitive detector in the *xz* Cartesian plane, parallel to the *z*-axis.

axis (*y*-axis), for a length *L*, where it then impinges on a two dimensional (2D) position sensitive detector, in the *xz* Cartesian plane. This projection process leads to a reduction in dimensionality, causing the azimuthal (ϕ) component of $F(r,\theta,\phi)$ to become convoluted in the plane of the captured 2D image, $G(R,\alpha)$, resulting in an apparent loss of information. If we are to obtain $I(v)$, then we must first identify a method to extract $F(r,\theta,\phi)$ directly from the measured $G(R,\alpha)$, and here-in lies the fundamental premise of the image reconstruction problem.

3.1.2 Image Reconstruction Methods

Since the development of charged particle imaging techniques, there have been a number of approaches developed for solving the image reconstruction problem. These commonly involve the use of a computer coded algorithm to reconstruction the original 3D distribution from the measured 2D image. Reconstruction algorithms may be classed into two categories; inversion methods, and forward convolution techniques, both of which are reviewed in reference [6]. The former rely on $G(R,\alpha)$ containing a cylindrical axis of symmetry, so that the axis parallel to this will incorporate a sufficient amount of information to mathematically reconstruct $F(r,\theta,\phi)$. Figure 3.2 displays schematically the basic premise behind these methods. The vital step in these algorithms is to obtain a 'central slice' through the original 3D distribution at $\phi = 0$, $F(r,\theta,\phi=0)$, which may then be used to extract $F(r,\theta,\phi)$ and subsequently obtain $I(v)$. For photoelectron and photofragment imaging, the polarisation of the laser electric field

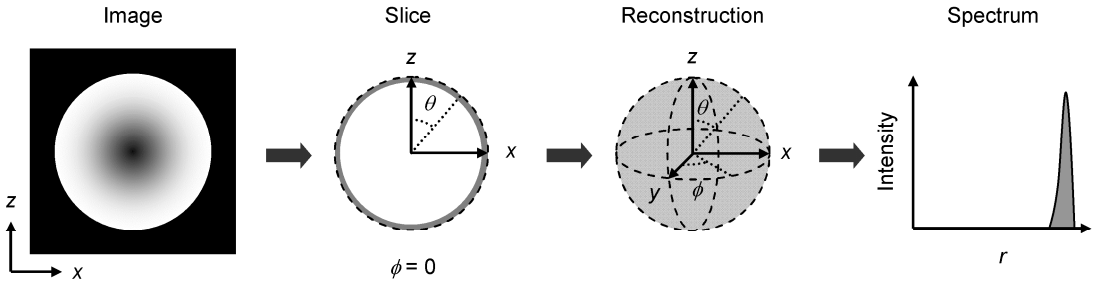

Figure 3.2: Schematic of an image reconstruction process using an inversion method. An image, $G(R,\alpha)$, is passed through the inversion reconstruction algorithm to generate a central slice through the original 3D distribution, $F(r,\theta,\phi=0)$. Provided the original 3D distribution possesses cylindrical symmetry about ϕ, it can be reconstructed from the slice. The desired 1D spectrum can then be obtained using equation (3.1).

vector, $\boldsymbol{\varepsilon}$, induces this cylindrical symmetry axis, which corresponds to the z-axis with respect to Figures 3.1 and 3.2. The $F(r,\theta,\phi=0)$ slice may also be obtained experimentally, with the aid of elegant slice imaging techniques [7-10]. These techniques commonly take one of two approaches: (1) the detector is 'gated' so that it only detects the central slice through the charged particle distribution; or (2) for photofragments a sheet laser beam may be used to preferentially ionise the central slice. However, these techniques are experimentally more involved and for light particles such as photoelectrons, technological limitations make the former approach exceptionally challenging, while the later is simply not applicable to photoelectrons. As such, there are currently no published results for slice imaging on photoelectrons.

Imaging may also be used to measure differential scattering cross-sections and bi-molecular collision products [11], resulting from crossed molecular beam experiments. However, in these experiments the interaction time between the two molecular beam pulses (100's μs) is significantly longer than the ionising laser pulse duration (10's ns). As a result, scattered particles with small velocities in the lab frame remain in the laser-ion interaction region to be ionised, while those with large lab frame velocities escape the interaction volume before ionisation occurs. This can ultimately lead to a measured charged particle distribution which is very often not cylindrically symmetric. Additionally, the spatial orientation of the product quantum state distributions in such scattering experiments may also yield images which are non-cylindrically symmetric [6]. Here, forward convolution approaches must instead be utilised [12-16], where a 3D charged particle distribution is simulated based on known differential cross-sections. This distribution is subsequently projected into 2D dimensions, to generate a convoluted image, hence the term forward convolution. The simulated image is then compared with the experimental image, and the cross-sections iteratively optimised until there is good agreement between simulation and experiment.

Abel Inversion and BASEX Methods

A mathematically exact method used for recovering the 3D charged particle distribution is the inverse Abel integral [6]. This method is commonly performed in Cartesian co-ordinates, where the projection of the 3D distribution onto a 2D plane can be expressed as

$$G(x,z) = \int_{-\infty}^{\infty} F(x,y,z)dy\,, \tag{3.2}$$

where $F(x,y,z)$ and $G(x,z)$ are the 3D distribution and 2D projection in Cartesian co-ordinates, respectively. By considering a single row through this 2D image at $z = z_0$, this single row, $g(x;z_0)$, may be expressed as

$$g(x;z_0) = 2\int_{0}^{\infty} f(x,y;z_0)dy = 2\int_{x}^{\infty} \frac{f(r;z_0)\,r}{\sqrt{r^2 - x^2}}dr\,, \tag{3.3}$$

where the function $f(x,y;z_0)$ represents a 2D slice through the original 3D distribution at z_0. $f(x,y;z_0)$ is then expressed in terms of polar co-ordinates, $f(r;z_0)$, through the relationship $r^2 = x^2 + y^2$. Equation (3.3) is known as the Abel integral and if one can recover the functions $f(r;z_0)$ for each row z, it is possible to reconstruct the original 3D distribution. By transforming equation (3.3) into the inverse Abel function

$$f(r;z_0) = \frac{1}{\pi}\int_{r}^{\infty} \frac{dg(z_0)}{dx}\frac{dx}{\sqrt{x^2 - r^2}}\,, \tag{3.4}$$

via the Fourier transform convolution theorem, the functions $f(r;z_0)$ can be recovered for each $g(x;z_0)$, although equation (3.4) is cumbersome to solve due to the singularity at $r^2 = x^2$. The most commonly employed algorithm to perform this integral is the Fourier-Hankel algorithm [6]. However, this inversion method leads to the commonly observed centre-line noise at $x = 0$ in the deconvoluted central slice, the intensity of which is magnified by the derivative within the integral. Additionally, this algorithm is computationally slow and takes 7.0 s to deconvolute a 512 × 512 pixels image on a PC with a 1.7 GHz processor [17].

A robust method to circumvent the use of equation (3.4) directly is to employ basis set functions with analytically known inverse Abel transforms, $b_k(r)$, to construct each $f(r;z_0)$, using

$$f(r;z_0) = \sum_{k=0}^{K-1} a_k b_k(r;z_0)\,, \tag{3.5}$$

where K is the total number of basis functions and a_k are their weighting co-efficients. This basis set expansion method (BASEX), developed by Reisler and co-workers [18], is accurate and can handle relatively noisy images. As a result it has been widely adopted, even though it still suffers from the same Cartesian noise at $x = 0$ as the Fourier-Hankel algorithm. However, as the basis functions used to generate $f(r;z_0)$ have a different symmetry to the original distribution, $F(r,\theta,\phi)$, the inversion time is significantly increased, taking 64.0 s to invert a 512 × 512 pixels image on a 1.7 GHz processor [17]. A variation on this method, pBASEX [17], instead uses polar basis functions which include the Legendre polynomials

$$I(\theta) = \sum_n \beta_n P_n \cos(\theta), \tag{3.6}$$

to which the angular distributions of the photofragments are fitted. In equation (3.6), β_n are the anisotropy parameters which describe the angular distributions and $P_n \cos(\theta)$ are Legendre polynomials of order n. For experiments recorded with linearly polarised laser light, only even values of n need be considered. pBASEX also has the advantage of producing a reconstructed image in which the centre line noise at $x = 0$, generated in Cartesian reconstruction methods, is instead restricted around the centre spot of the image ($r = 0$). Additionally, reconstructed images are naturally smoothed, particularly angularly, as a result of the idealised polar basis functions so that the images are visually very attractive. As the pBASEX basis functions have the same symmetry as the charged particle distribution (both polar co-ordinates) the computation time is significantly enhanced, taking only 1.3 s to reconstruct the same image described above at the same processor speed [17].

Vrakking's Method

The method of Vrakking may also be used to invert measured 2D images [19]. Here, an initial 3D charged particle distribution is simulated based on the radial and angular distributions in the measured 2D image. It is in principle similar to the forward convolution methods described above, in so much that the algorithm calculates a 2D projection of the trail 3D distribution, and then compares this with the measured

experimental image. A correction factor is then generated from this comparison and applied to the simulated image. This process is then iteratively repeated until there is agreement between simulated and experimental images. As was the case with pBASEX, this method treats the inversion radially which eliminates the centreline noise issue observed in Cartesian methods. However, this method is computationally even slower than the Abel inversion and BASEX methods, taking 3 minutes to invert an image of 300 × 300 pixels using a 950 MHz processor [6]. It is worth noting that the concepts of this algorithm have recently been modified by Renth *et al*. [20], to develop new methods based on cross validation and iterative regularisation, which combine features of both BASEX and the iterative method.

Onion-peeling Methods

Another approach to the reconstruction problem is the so-called onion peeling method. It explicitly considers the Jacobian for projecting the original 3D charged particle distribution, $F(r,\theta,\phi)$, onto the 2D detector plane, $G(x,z)$, when it is accelerated from within a uniform electric field, *F*, over a flight distance, *L* [4,6,21]. With reference to Figure 3.1 on page 131, the trajectories of a 3D distribution of charged particles with velocity *v*, may be described in terms of the Euler angles in spherical polar co-ordinates, (θ,ϕ), for a given velocity (radius, *r*). This 3D distribution is then impacted onto a 2D Cartesian plane (the detector) where particles will have Cartesian impact co-ordinates at the detector defined as (x,z). Using Newtonian mechanics, the impact co-ordinates (x,z) may be determined from their original velocity vectors in spherical polar co-ordinates, (r,θ,ϕ). Rearrangement of the relationships obtained for x and z subsequently allows one to extrapolate the original (r,θ,ϕ) trajectories associated with each (x,z) component of the measured 2D image, which in principle enables access to the original 3D distribution. However, for the impact co-ordinate solutions to remain sufficiently simple to solve the problem, the initial energy of the charged particles, E_k, must be significantly less that the energy the particles gain from being accelerated in the electric field, *qFL*, where *q* is the particles charge (i.e. $E_k < qFL$); this problem has been investigated in some detail by Helm and co-workers [4,22]. Experimentally, the condition $E_k < qFL$ is regularly attained in most VMI arrangements, although inhomogeneous fields in these arrangements can complicate matters. Additionally, the

method described above is only valid if the original 3D distribution contains a single E_k component (single *r*). In reality, it is much more likely that the charged particles will possess a distribution of E_ks, a scenario which results in (x,z) positions associated with smaller E_ks in the recorded image containing contributions from larger E_k components, for all E_ks less than the largest E_k feature. In Cartesian co-ordinates, the method of onion-peeling seeks to alleviate this problem by first calculating the contribution of the largest E_k feature (largest *x*) in the 2D image, and then subtracting it, where the E_k contribution is calculated using the Jacobian for the charged particle projection process (see reference [6]). This process is then incrementally repeated along the deceasing *x*-direction (smaller E_k), until $x = 0$ is reached and all E_k components have been accounted for. By retaining the largest E_k component associated with each (x,z) throughout the process, the vital central slice, $F(r,\theta,\phi=0)$, will be generated. This onion-peeling method, originally developed by Bordas *et al.* [4], is appealing because it is intuitively simple and computationally very fast, taking 0.7 s to deconvolute a 512 × 512 pixels image on a 1 GHz processor [17]. However, in Cartesian co-ordinates it suffers from error accumulation because one must start at the outermost point on the detector (largest *x*) where the signal is smallest due to the Jacobian in going from 3D spherical co-ordinates (the laser-matter interaction system) to 2D Cartesian (the detection system). This problem can be alleviated by onion-peeling in polar co-ordinates (POP) [23], in which the error at large radii is reduced and error accumulation is not a major concern. Additionally, it relaxes the need for a high kinetic energy at the detector with respect to the initial energy [23]. Like pBASEX and the iterative methods, POP reduces the centreline noise to a spot around the centre of the image. However, POP as developed by Zhao *et al.* [23] is slow, thus losing a lot of onion-peeling's appeal. Additionally, POP has not been directly compared to other methods and onion-peeling in general is perceived to be inferior to pBASEX and many other methods in terms of accuracy and its handling of noise [6].

3.1.3 Towards Real-time Charged Particle Image Reconstruction

One of the drawbacks of imaging methods is that visual inspection of a 2D image during data acquisition (DAQ) often does not provide the user with information on the quality of the desired 1D spectrum, $I(v)$, or angular distributions. In contrast, the direct

provision of the speed distribution through time-of-flight (TOF) methods, such as magnetic bottle analysers [24,25], is very attractive as it provides instant feedback during DAQ. This is in part because at large radii, the signal appears weaker as it is dispersed over a larger area, while signal at smaller radii is confined to a smaller area, causing the centre of the image to typically be very bright. Additionally, the 2D image contains the cylindrically symmetric azimuthal (ϕ) contribution, which carries no useful information. As a result, the observation of small signals in congested regions of a radial spectrum can be difficult, as is the case, for example, in time-resolved photoelectron imaging (TRPEI) experiments, where pump-probe signals can commonly be an order of magnitude less in total intensity than single photon features [26]. Hence, access to the radial spectrum during DAQ allows a user to optimise signals and determine the quality of a 1D spectrum, without the need for using an off-line reconstruction method. For this to be a feasible prospect, the reconstruction algorithm must operate on a comparable timescale to the image acquisition process in a standard DAQ program, which is commonly ~1 Hz. When considering the image reconstruction methods described in Section 3.1.2, many of these algorithms operate on a timescale >1 Hz, as summarised in Table 3.1 below.

Table 3.1: Summary of the computational speeds for the inversion algorithms described throughout Section 3.1.2. Inverted image sizes and associated processor speeds are also provided.

Inversion algorithm	Image size / pixels	Processor speed	Computation time / s
Fourier-Hankel	512 × 512	1.7 GHz	7.0
BASEX	512 × 512	1.7 GHz	64
pBASEX	512 × 512	1.7 GHz	1.3
Vrakking	300 × 300	950 MHz	~180
Onion-peeling	512 × 512	1 GHz	0.7

The only current algorithms that operate on a sufficient timescale to meet this criterion are the pBASEX and the Cartesian onion-peeling algorithms, which will reconstruct an image in 1.3 s and 0.7 s, respectively. The issue with the latter is that Cartesian onion-peeling results in undesired centreline noise at $x = 0$ and handles noise poorly for the reasons discussed in the previous section, which detracts from the beneficial speed of

the algorithm. pBASEX however, operates in polar co-ordinates and does not generate centreline noise, in addition to the fact that it copes well with image noise. We must also consider that to support a truly online reconstruction method, the reconstruction algorithm should ideally be readily incorporable into existing DAQ software. Much modern DAQ software, such as that described in Section 2.6.3, is now coded in LabVIEW, as a result of its versatile virtual instrument (VI) coding platform, which is particularly intuitive for experimentalists. With this in mind, pBASEX in its current form cannot be readily incorporated as a VI into LabVIEW DAQ, despite its attractive computational efficiency.

Motivated by this restriction, this Chapter presents the development and computational details of an image reconstruction routine based on onion-peeling in polar co-ordinates, which enables 'real-time' (~1 Hz) image processing while retaining the accuracy of other reconstruction methods. We specifically describe how we overcome the limitations of the computational speed of POP by employing the basis set concepts utilised for BASEX and pBASEX. The method is a computationally cheap and an intuitively simple reconstruction method for on-the-fly image reconstruction during DAQ. Additionally, we show that POP is as accurate as pBASEX and has certain important advantages over the latter.

Section 3.2 describes the POP method along with a thorough description of the computational details. In Section 3.3, the method is compared with other methods for simulated images with low signal-to-noise levels and large variations in the intensities of features. We also compare the reconstruction of an experimentally obtained image and close by considering the integration of the POP algorithm into the existing DAQ software described in Chapter 2.

3.2 Onion-peeling in Polar Co-ordinates: POP

3.2.1 Fundamental Concepts of the Polar Onion-peeling Method

Using Figure 3.1 as a reference, we consider a 3D radial distribution, $F(r,\theta,\phi)$, that is cylindrically symmetric around the *z*-axis; for photoionisation and photodissociation experiments, this will correspond to the radiation polarization vector, $\boldsymbol{\varepsilon}$. In charged

particle imaging, $F(r,\theta,\phi)$ is mapped onto the 2D detector plane parallel to z, producing the measured distribution, $G(R,\alpha)$. For charged particles emitted with a radial (speed) distribution described by a delta function, $\delta(r)$, the image $G(R,\alpha)$ has signal at radii smaller than the radius defined by the velocity of the photoproducts (i.e. at $R < r$). This signal originates from the ϕ-dependence of the charged particle cloud, which may be calculated and subtracted away from $G(R,\alpha)$ for all $R < r$, leaving only the radial delta function, $\delta(r)$, at $R = r$. The resultant distribution is equivalent to a slice through the 3D distribution, $F(r,\theta,\phi=0)$, and from this, the full 3D distribution can be recovered because of the inherent cylindrical symmetry around the z-axis of $F(r,\theta,\phi)$. In the case of broad or congested radial distributions, the same strategy holds. The 2D projection $G(R,\alpha)$ can be expressed as the sum of the individual 2D projections, $g(r;R,\alpha)$, for all r-components of the full 3D distribution, $F(r,\theta,\phi)$:

$$G(R,\alpha) = \int_0^{r_{\max}} g(r;R,\alpha)dr, \tag{3.7}$$

where $R \le r$ and the semicolon in $g(r;R,\alpha)$ is used to indicate that the 2D projections are given at specific radii, r. Analogous to the case of the radial delta function, $F(r,\theta,\phi=0)$ can be recovered by removing the contributions of ϕ for $R < r$, starting at $r = r_{\max}$ and incrementally decreasing in steps of dr until $r = 0$ is reached. At each r, $g(r;R,\alpha)$ is subtracted from $G(R,\alpha)$, which effectively 'peels away' the ϕ-contributions at each r; hence, the term onion-peeling. POP was first introduced by Zhao *et al.* [23], and the method presented here is in essence equivalent, however, the main restriction of their method has been its computational expense and general applicability. The cause of this arises from the need to simulate an entire 3D distribution at each radial increment. The 2D projection of this simulated distribution, $g_{\text{fit}}(r;R,\alpha)$, is then used in the subtraction.

The method we describe here fundamentally differs from that of Zhao *et al.* [23] in how $g_{\text{fit}}(r;R,\alpha)$ is generated. In order to retain the low computational expense of onion-peeling, we borrow ideas from the basis set expansion methods [17,18], in which basis sets are used in order to fit the experimental 2D data. In a similar spirit, the POP method described here uses the concept of basis sets to allow for the very efficient

calculation of $g_{\text{fit}}(r;R,\alpha)$, as described in Section 3.2.3.

3.2.2 Conversion between Cartesian and Polar Co-ordinate Systems

Cartesian to Polar Conversion

Prior to the start of the POP algorithm, the Cartesian image, $G(x,z)$, containing pixels of dimensions $dx \times dz$ where $dx = dz = 1$, must be converted to polar co-ordinates by mapping the Cartesian grid, defined by the CCD, onto a polar array, $G(R,\alpha)$, with pixels of size $dR \times d\alpha$. This pixel conversion process is adapted from a similar method used by Wrede [27], and is described with respect to Figure 3.3. In order to retain a similar amount of information in polar co-ordinates, the polar pixel is chosen to be of a similar size as the Cartesian pixel: $dRd\alpha \approx dxdz = 1$. As the differential area remains the same, the number of polar pixels required to define a given R will scale as R, as illustrated in Figure 3.3a. Prior to the conversion process, $G(x,z)$ first undergoes a four way folding process, to generate a single symmetrised image quadrant, $G_q(x,z)$, and this process is described in more detail in Section 3.2.3. For a symmetrised Cartesian quadrant, the number of polar pixels at each R equates to the integer part of $\frac{1}{2}\pi(R+1)$. The origins of this relationship stem from the fact that one needs to define the circumference length of a 90° arc, defined as $\frac{1}{4}(2\pi R) = \frac{1}{2}\pi R$. The factor of +1 then simply originates from the fact that the smallest value of R is $R = 0$, and a single polar pixel is required to define this minimum R. As an example, for the pixel column $R = 1$, the number of polar pixels equates to 3 using the above relationship.

Figure 3.3b illustrates how the signal in a polar pixel, $I(R,\alpha)$, is determined *via* its fractional overlap with the four surrounding Cartesian pixels. This process is best conceptually understood by rotating the polar pixel by α about its pivot. The absolute centre of the polar pixel is first expressed in Cartesian co-ordinates, (x_p, z_p), using

$$\begin{aligned} x_p &= R\sin\alpha \\ z_p &= R\cos\alpha \end{aligned}. \tag{3.8}$$

From these decimal co-ordinates, the co-ordinates of the Cartesian pixel, (x_c, z_c), that lies on the centre of the polar pixel are determined by rounding x_p and z_p to the nearest

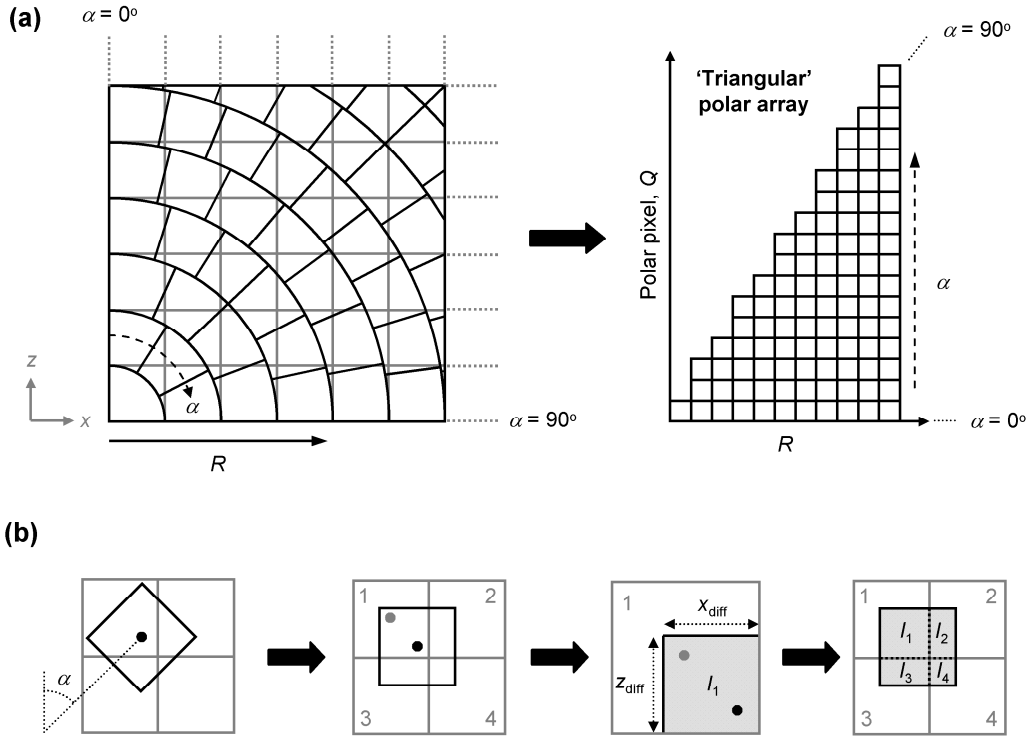

Figure 3.3: (a) Schematic representation of the Cartesian pixel array, $G_q(x,z)$, shown in gray and the overlaid array of polar pixels, $G(R,\alpha)$, shown in black. This polar array is then represented as a 'triangular' array of polar pixels, Q, as show on the right. (b) Schematic of the Cartesian to polar conversion process. A polar pixel, (R,α), is rotated about its central pivot (black dot) by α, and the Cartesian pixel in which its centre lies is determined (pixel 1). The intensity contribution of this pixel, I_1 (grey shaded area), to the polar pixel intensity is then determined using x_{diff} and z_{diff}, which are calculated using equation (3.10). Finally, the remaining intensity contributions from Cartesian pixels 2, 3 and 4 (I_2, I_3 and I_4, respectively) are determined to calculate the final polar pixel intensity. With reference to the methodology described in this section, this example is shown for a translational move of x +1 and z – 1.

integers, respectively. The fractional intensity contribution from this Cartesian pixel, defined as I_1, to the total polar pixel intensity, $I(R,\alpha)$, can the be determined from

$$I_1 = I(x_c, z_c)\cdot[x_{\text{diff}}\, z_{\text{diff}}], \tag{3.9}$$

where

$$\begin{aligned} x_{\text{diff}} &= 1-|x_c - x_p| \\ z_{\text{diff}} &= 1-|z_c - z_p| \end{aligned}, \tag{3.10}$$

and $I(x_c, z_c)$ is the total signal of the Cartesian pixel at (x_c, z_c). The next three Cartesian pixels that overlap with the polar pixel are identified using a series of simple comparisons between x_c and x_p, and z_c and z_p. With respect to x_c and x_p, if $x_c > x_p$ then the *x* co-ordinate translation will be *x* – 1, whereas if $x_c < x_p$ then the move will be *x* + 1. This process is then repeated for the *z* co-ordinate, and the remaining three fractional Cartesian intensities can then be calculated using

$$\begin{aligned} I_2 &= I(x_c \pm 1, z_c) \cdot \left[(1 - x_{diff}) z_{diff} \right] \\ I_3 &= I(x_c, z_c \pm 1) \cdot \left[x_{diff} (1 - z_{diff}) \right] \\ I_4 &= I(x_c \pm 1, z_c \pm 1) \cdot \left[(1 - x_{diff})(1 - z_{diff}) \right] \end{aligned} , \tag{3.11}$$

where the total intensity of the polar pixel will be

$$I(R, \alpha) = I_1 + I_2 + I_3 + I_4 . \tag{3.12}$$

When this process is completed for all polar pixels, the resulting raw polar image, $G(R, \alpha)$, is thus a triangular array because the number of angles, α, at which pixels can be defined scales linearly with *R*. Although not the traditional representation of a 2D image, it provides a convenient and intuitive display as one can simply read off the radial distribution along the *R* axis and the angular distribution by comparing the signal levels along the angular axis.

The main source of error in this polar to Cartesian conversion arises from the assumption that the polar pixel has the same dimensions as the Cartesian pixel. This becomes less pronounced as *R* increases and because the onion-peeling peels from the outer radius inwards, the errors are not cumulative and only present a problem at small *R*. However, the noise introduced by the reconstruction method is also greatest at small *R*. Thus, noise accumulation only occurs at small *R* and the error introduced by the polar conversion is not significant.

Polar to Cartesian Back Conversion

At the end of the POP algorithm, the desired 2D slice, $F(r, \theta, \phi = 0)$, is produced in an array of polar pixels. This deconvoluted polar image may then be converted back into

Cartesian space with a back conversion algorithm, which is similar to that of the Cartesian to Polar conversion described above, although it does possess some vital conceptual differences. With respect to Figure 3.3a, these differences originate for the fact that the total number of pixels at each *R*, $P(R)$, varies as a function of *R*, whereas the Cartesian array is square. For the basis of this analysis we now describe the polar pixels in terms of (R,Q), rather than (R,α), where Q is the polar pixel number at *R* and is determined from the integer part of $\alpha/\left[\frac{\pi}{2}/\{P(R)-1\}\right]$.

Figure 3.4 shows how the signal associated with a Cartesian pixel, $I(x,z)$, is determined from four overlapping polar pixels. We begin in a similar manner as the forward conversion process, by rotating the Cartesian pixel about its centre by α and locating the absolute centre of (x,z) in the polar frame using

$$\begin{aligned} R_{\mathrm{c}} &= \sqrt{x^2+z^2} \\ \alpha_{\mathrm{c}} &= \tan^{-1}\left(\frac{x}{z}\right), \end{aligned} \tag{3.13}$$

where the associated Q_{c} is evaluated from

$$Q_{\mathrm{c}} = \frac{\alpha_{\mathrm{c}}}{\left[\frac{\pi}{2}/P(R_{\mathrm{p}})-1\right]}. \tag{3.14}$$

However, when $z = 0$, the quotient $x/z = \infty$, which poses a computational problem. To alleviate this issue, when $z = 0$, α_{c} is automatically defined as $\pi/2$ rather than using the relationship in equation (3.13). The centre of the polar pixel, $(R_{\mathrm{p}},Q_{\mathrm{p}})$, on which the centre of (x,z) lies is then determined by rounding R_{c} and Q_{c} to the nearest integers. The intensity contribution from this first polar pixel, I_{a}, can then be calculated in an analogous manner to equations (3.9) and (3.10), such that

$$I_{\mathrm{a}} = I(R_{\mathrm{p}},Q_{\mathrm{p}})\cdot[R_{\mathrm{diff}}Q_{\mathrm{diff}}], \tag{3.15}$$

where $I(R_{\mathrm{p}},Q_{\mathrm{p}})$ is the intensity of the polar pixel and

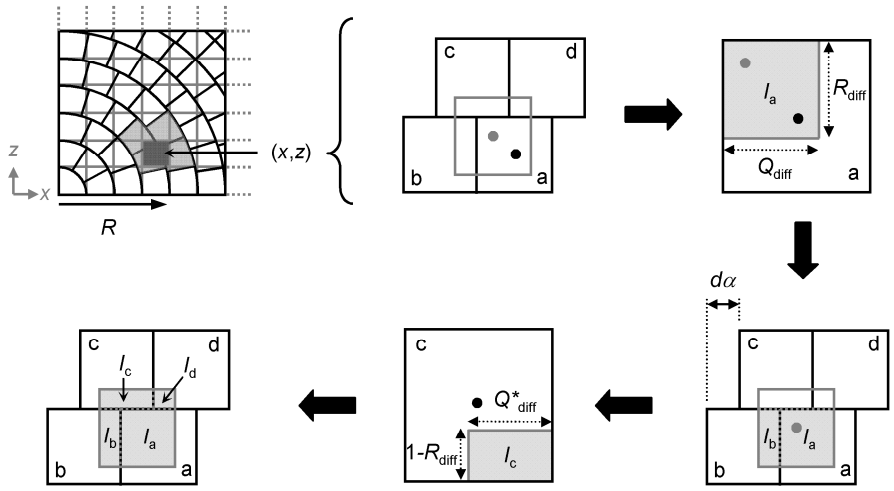

Figure 3.4: Overview of the polar to Cartesian back conversion process used at the end of the POP algorithm. The signal assigned to a Cartesian pixel, labelled (x,z) and shown in dark grey (top left), is calculated from its fractional overlap with the four surrounding polar pixels, labelled a to d (light grey, top left). This process is shown schematically, where the factional intensity contribution from the first polar pixel, I_a, is determined using Q_{diff} and R_{diff}, which are obtained using equation (3.16). I_b is then calculated in a similar manner, however, due to the angular difference, $d\alpha$, between the two rows of radial pixels, a new Q^*_{diff} must be used to calculate I_c and I_d, rather than the original Q_{diff}. The origins of this are described in this section. The associated Cartesian pixel intensity is then simply the sum of I_a, I_b, I_c, and I_d.

$$\begin{aligned} R_{diff} &= 1 - \left| R_p - R_c \right| \\ Q_{diff} &= 1 - \left| Q_p - Q_c \right| \end{aligned} . \qquad (3.16)$$

The second polar pixel to contribute to the total Cartesian pixel intensity is determined from a translation in the Q co-ordinate at R_p. If $Q_c > Q_p$ then a move of Q + 1 is introduced, while for $Q_c < Q_p$ the move will be Q – 1, resulting in a partial intensity contribute from the second polar pixel of

$$I_b = I\left(R_p, Q_p \pm 1\right) \cdot \left[R_{diff}\left(1 - Q_{diff}\right)\right]. \qquad (3.17)$$

To proceed further with the conversion process, we must now consider how the Cartesian pixel overlaps with the remaining two polar pixels, and this is where the back conversion differs conceptually from the original forward conversion method. To do

this, we first obtain the required move in the R co-ordinate by comparing R_c and R_p, analogous to the Q co-ordinate move described above. However, the pixel at $(R_p \pm 1, Q_p)$ will not be defined by the same α as the pixel at (R_p, Q_p). This angular difference, defined as $d\alpha$ in Figure 3.4, is a direct result of the variation in $P(R)$ as a function of R, and can result in a different Q_c at $R_p \pm 1$, which we label Q_c^*. This can be determined from

$$Q_c^* = \frac{\alpha_c}{\left[\frac{\pi}{2} \Big/ P(R_p \pm 1) - 1\right]} \tag{3.18}$$

where the associated Q_p^* is again evaluated by rounding Q_c^* to the nearest integer. A corrected value of Q_{diff}^* is then obtained using an analogous relationship to the one shown in equation (3.16), allowing the correct intensity contributions, I_c and I_d, from the remaining polar pixels to be evaluated using

$$\begin{aligned} I_c &= I(R_p \pm 1, Q_p^*) \cdot \left[(1 - R_{diff}) Q_{diff}^*\right] \\ I_d &= I(R_p \pm 1, Q_p^* \pm 1) \cdot \left[(1 - R_{diff})(1 - Q_{diff}^*)\right] \end{aligned}. \tag{3.19}$$

In equation (3.19), $Q_p^* \pm 1$ is decided based on a comparison between Q_c^* and Q_p^*, as described above. The total intensity of the Cartesian pixel is then simply

$$I(x, z) = I_a + I_b + I_c + I_d . \tag{3.20}$$

In a similar manner to the forward conversion process, errors in the polar to Cartesian back conversion are most prominent at small R, where the polar and Cartesian pixel sizes are not necessarily equal. In addition to this, at small R, some Cartesian pixels may have a minor overlap with more than four polar pixels, and the rotation about α at the start of the back conversion routine generally neglects this. However, the POP algorithm itself compresses noise to the centre of the image at small R and so the information in this region of the polar array is not particularly critical. In the reconstruction algorithm however, no further image processing is carried out post back conversion, and it is used for presentational and visual aids only, even though the

quality of the resultant Cartesian image is visual very attractive.

3.2.3 Polar Onion-peeling: Computational Method

Image Centring and Four-way Folding

Prior to the beginning of the onion-peeling algorithm, the centre of the raw Cartesian image, (x_0, z_0), is identified, by manually inspecting a four-way folded Cartesian quadrant of the original image. In principle, it is possible to incorporate an automated image centring process into the POP algorithm (e.g. the Bordas criterion [4]), although at present this has not been implemented. The symmetrised Cartesian image quadrant, $G_q(x,z)$, generated from the folding process has the additional benefit of being a quarter of the size of the original raw image, which significantly reduces the computation time of the subsequent POP method (see Section 3.3.1), while still retaining all vital signal and angular information. When the centre of the image has been indentified, the pixel intensities in the folded Cartesian quadrant, $I_q(x,z)$, are determined from the sum of four Cartesian pixels in the 2D image:

$$I_q(x,z) = I(+\delta_x,+\delta_z) + I(+\delta_x,-\delta_z) + I(-\delta_x,+\delta_z) + I(-\delta_x,-\delta_z), \qquad (3.21)$$

for all $x > 0$ and $z > 0$, and where

$$\begin{aligned} \pm\delta_x &= x_0 \pm x \\ \pm\delta_z &= z_0 \pm z \end{aligned}. \qquad (3.22)$$

For pixels in the quadrant that lie along $x = 0$ and $z = 0$, respectively, a similar approach is taken:

$$\begin{aligned} I_q(x=0,z) &= 2\left[I(x_0,+\delta_z) + I(x_0,-\delta_z)\right] \\ I_q(x,z=0) &= 2\left[I(+\delta_x,z_0) + I(-\delta_x,z_0)\right] \end{aligned}. \qquad (3.23)$$

Finally the pixel intensity at $I_q(x=0,z=0)$ is obtained from

$$I_q\left(x=0,z=0\right)=4\left[I\left(x_0,z_0\right)\right]. \tag{3.24}$$

The resultant raw Cartesian quadrant is then transformed into the raw polar image array, $G\left(R,\alpha\right)$, using the method described in Section 3.2.2.

Onion-peeling Process

The raw polar image $G\left(R,\alpha\right)$ corresponds to the sum over all *r* components as defined previously in equation (3.7). As long as there is no signal at radii larger than the detector, the outermost ring will contain no contribution from ϕ and the substitution

$$g\left(r;R,\alpha\right)=h\left(r,\theta\right), \tag{3.25}$$

at $R = r$ is valid. Starting at the outermost radius, $h\left(r_{\max},\theta\right)$ is fitted to the well known angular distribution [28,29]

$$I\left(\theta\right)=N\left(r\right)\sum_n \beta_n\left(r\right)P_n\left[\cos\theta\right], \tag{3.26}$$

where $P_n\left[\cos\theta\right]$ is the n^{th} order Legendre polynomial. The fit provides $N\left(r\right)$, an intensity factor, and $\beta_n\left(r\right)$, the anisotropy parameters describing the charged particle angular distributions. The integer *n* is determined by the physics of the process. The fitting can be performed using standard linear least squares methods, such as singular value decomposition, as used in pBASEX. For TRPEI experiments, we are primarily concerned with two-photon processes, hence at present our program only fits up to $n = 4$, where the fit is performed directly, although in principle it would not be demanding to expand the fitting process to higher order Legendre terms.

The values of $N\left(r\right)$ and $\beta_n\left(r\right)$ extracted from the fit may then be used to calculate the distribution $g_{\text{fit}}\left(r_{\max};R,\alpha\right)$, which is then subtracted from $G\left(R,\alpha\right)$ for all $R \le r_{\max}$:

$$G^*(R,\alpha) = G(R,\alpha) - g_{\text{fit}}(r;R,\alpha). \tag{3.27}$$

$G^*(R,\alpha)$ is a modified polar image containing $G(R,\alpha)$ for $R < r_{\max}$. The process is incrementally repeated for $r = r_{\max} - dr$ until r = 0 is reached. Upon completion, $G^*(R,\alpha)$ represents a 2D polar array of all the residuals from the subtraction. The desired 2D slice, $F(r,\theta,\phi=0)$, is constructed by retaining $h(r,\theta)$ in equation (3.25) at each increment. Note that either the experimental $h(r,\theta)$ or the fitted $h_{\text{fit}}(r,\theta)$ may be used to construct $F(r,\theta,\phi=0)$. The choice does not affect the ultimate radial spectrum produced, however, the latter smoothes angular noise in a similar manner as pBASEX [17] does and presents visually very attractive images, although it also discards real experimental angular noise.

Basis Set Methods

In the interest of computational expense, direct numerical simulation of $g_{\text{fit}}(r;R,\alpha)$ is avoided as it is time consuming and is the main limitation to the speed of Zhao *et al.*'s original algorithm. The approach taken here uses ideas from BASEX, in which basis functions are used in order to fit the experimental 2D data. For basis functions, POP uses idealised radial distribution functions, $b_r(R)$, produced by angular integration of perfectly isotropic images. The generation of $b_r(R)$ is schematically shown in Figure 3.5. To retain consistency with the experimental image acquisition, the basis functions are generated by simulating images for all values of *r* onto a Cartesian grid. A single simulated image at *r* is created by generating a finite number, *m*, of random particle trajectories, (r,θ,ϕ), and projecting them onto a Cartesian grid, (x,z), where

$$\begin{aligned} x &= r\sin\theta\sin\phi \\ z &= r\cos\theta \end{aligned}. \tag{3.28}$$

The target pixel position (x,z) is attained from the integer components of the values from equation (3.28). The intensity to be added to pixel (x,z) is then determined using

$$I = \left(1 + \frac{\beta_2}{2}\left[3\cos^2\theta - 1\right]\right)\sin\theta. \tag{3.29}$$

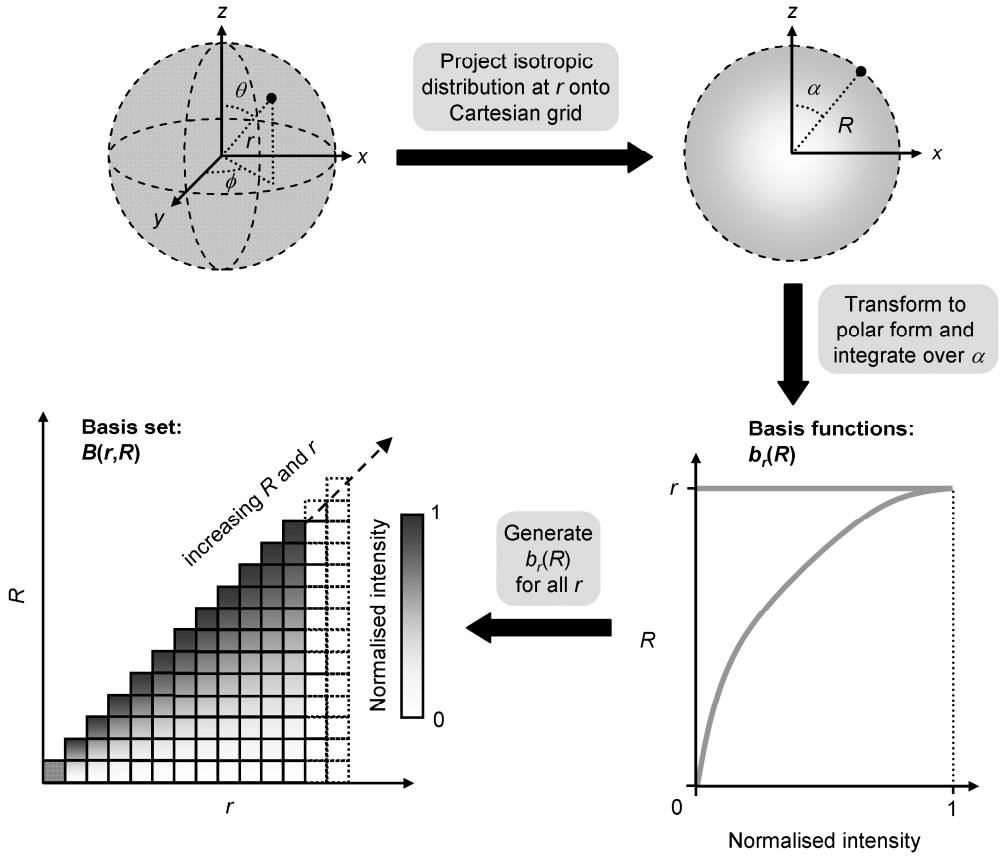

Figure 3.5: Schematic of the basis set construction process. Perfectly isotropic distributions ($\beta_2 = 0$) are simulated for each *r* and then projected onto a Cartesian grid to generate the associate 2D image. Each image contains a total of *m* randomly generated charged particle trajectories. The images are then integrated over all α to produce the basis functions, $b_r(R)$. The intensity in each $b_r(R)$ is normalised such that the intensity at $R = r$ is unity. All basis functions, each defined at a different *r*, are then collated into a single array to form the basis set, $B(r,R)$, which is itself a 2D triangular array.

Equation (3.29) is arrived at from equation (3.26), where only the even terms of the Legendre polynomial up to $n = 2$ are considered, and the intensity factor $N(r) = 1$. The factor of $\sin\theta$ accounts for the reduction in dimensionality during the projection. For an isotropic distribution, $\beta_2 = 0$ and equation (3.29) simply becomes

$$I = \sin\theta . \tag{3.30}$$

After *m* trajectories, the resultant isotropic image is then four-way folded into a single quadrant, transformed to polar form using the method described in Section 3.2.2, and integrated over angle α to produce $b_r(R)$. Here each basis function is generated from

an isotropic image, simulated for a total of $m = 1 \times 10^8$ trajectories to ensure basis functions of sufficient quality. The time taken to simulate an individual $b_r(R)$ scales linearly with m. A basis set, $B(r,R)$, is constructed from basis functions generated at all possible r, and $B(r,R)$ is consequently a 2D triangular array, as displayed in Figure 3.5. All basis functions are normalised such that the intensity at $R = r$ is unity. Importantly, $B(r,R)$ is generated only once using a stand alone LabVIEW program and then supplied to the reconstruction routine. The time taken to construct a single $B(r,R)$ scales linearly with respect to $m \times r$ and the overall size of the basis set $B(r,R)$ is determined by the size of the CCD (in pixels) used in the experiment. It may also be readily extended to sub-pixel resolution, attainable through centroiding of events [30]. The $B(r,R)$ generated here is capable of handling images as large as 1024 × 1024 pixels. In contrast, the basis functions in BASEX and pBASEX are defined by the width of the Gaussian functions used, which affects the reconstructed 3D distribution and consequently introduces an additional parameter.

The method used to obtain $g_{\text{fit}}(r;R,\alpha)$ from the associated $b_r(R)$ is described with respect to Figure 3.6. During the POP routine, the relevant basis function $b_r(R)$ is retrieved from the $B(r,R)$ basis set, which is called into memory only once at the start of the routine or a DAQ run and remains in memory for the entire duration of the DAQ. An idealised perfectly isotropic polar image, $g_{\text{ideal}}(r;R,\alpha)$, is then constructed from $b_r(R)$ using

$$g_{\text{ideal}}(r;R,\alpha) = \rho(r,R)\, b_r(R). \tag{3.31}$$

The number of polar pixels at each R, $P(R)$, as described in Section 3.2.2, along with their associated intensities is reintroduced to $g_{\text{ideal}}(r;R,\alpha)$ through the factor $\rho(r,R)$. Numerically, $\rho(r,R)$ is defined as the ratio of the number of polar pixels at r to R and accounts for the fact that in the polar image, the number of polar pixels changes with respect to R (i.e. the polar image is a 2D 'triangular' array). The idealised image $g_{\text{fit}}(r;R,\alpha)$ with experimentally observed anisotropy, $\beta_n(r)$, and intensity, $N(r)$, is then generated through

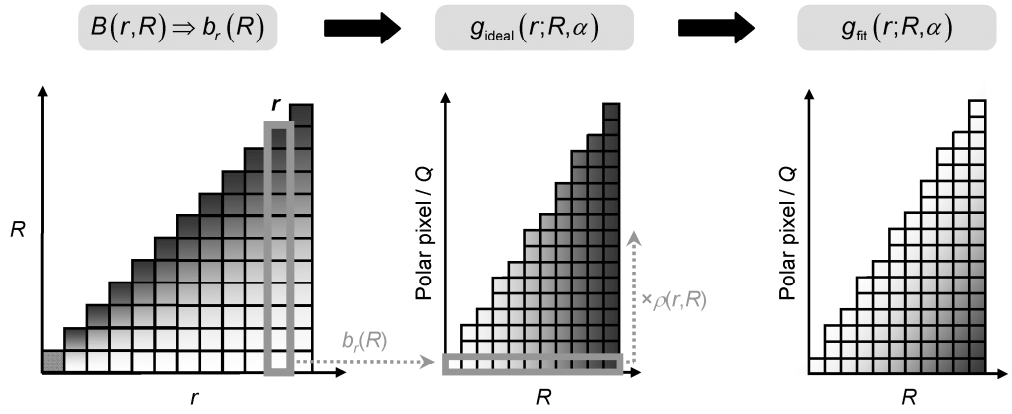

Figure 3.6: Reconstruction of $g_{\text{fit}}(r;R,\alpha)$ from a basis function, $b_r(R)$, during the polar onion-peeling (POP) routine. The appropriate basis function, $b_r(R)$, at r is called from the basis set, $B(r,R)$. An idealised isotropic polar image, $g_{\text{ideal}}(r;R,\alpha)$, is the produced from $b_r(R)$ through the factor $\rho(r,R)$, using equation (3.31). $g_{\text{fit}}(r;R,\alpha)$ is then generated from $g_{\text{ideal}}(r;R,\alpha)$ with equation (3.32). The correct anisotropy, $\beta_2(r)$, and intensity scaling, $N(r)$, are introduced to $g_{\text{fit}}(r;R,\alpha)$ from the fit to the outer ring $h(r,\theta)$, determined in equation (3.26).

$$g_{\text{fit}}(r;R,\alpha) = g_{\text{ideal}}(r;R,\alpha)\,N(r)\sum_n \beta_n(r)\,P_n\left[\frac{R}{r}\cos\alpha\right], \tag{3.32}$$

where the parameters $N(r)$ and $\beta_n(r)$ have been obtained from the fit of the outer ring, $h(r,\theta)$, in equation (3.26). The factor of R/r in equation (3.32) accounts for the transformation of co-ordinate system from (r,θ,ϕ) to (R,α), as represented at the start of this chapter in Figure 3.1. Particle positions in both the 3D and 2D co-ordinate systems share a common z component (i.e. $z(\text{2D}) = z(\text{3D})$), both of which are formally defined in equations (3.8) and (3.28), respectively. By equating these two relationships, $\cos\theta$ may be defined in terms of $\cos\alpha$:

$$\cos\theta = \frac{R}{r}\cos\alpha\,. \tag{3.33}$$

The image $g_{\text{fit}}(r;R,\alpha)$ generated through equation (3.32) is identical to that produced *via* the method implemented by Zhao *et al.* [23], but has avoided direct simulation of the image as part of the reconstruction, resulting in a much more efficient algorithm.

3.2.4 Effects of Image Pixilation

POP subtracts the ϕ-contribution to each ring successively, ultimately leading to the slice $F(r,\theta,\phi=0)$. This is valid if the radial width of each increment tends to zero, i.e. $dr \to 0$. However, pixilation of the image by the CCD means that at every subtraction, some ϕ-component is not accounted for over the polar pixel width, *dR*, resulting in the retention of a slice $F(r,\theta,\phi\approx 0)$. Similar pixilation effects have been noted by Loock and Manzhos when performing onion-peeling in Cartesian co-ordinates [21].

Figure 3.7 explores the general functionality of the missing ϕ-component in more detail. To do this, images with a single pixel width radial feature at various *r* have been simulated, using the method described in Section 3.2.3, where each image contains the same number of random charged particle trajectories, *m*. The images are then reconstructed using the POP algorithm and the radial spectrum, $I(r)$, obtained from the resultant $F(r,\theta,\phi\approx 0)$ using

$$I(r) = \int_0^{2\pi} F(r,\theta,\phi\approx 0) r\sin\theta d\theta, \tag{3.34}$$

where $r\sin\theta$ is the Jacobian. In Figure 3.7, the ratio of the peak intensity at a fixed *r* (arbitrarily chosen as *r* = 200) to the peak intensity at varying *r* is plotted as a function

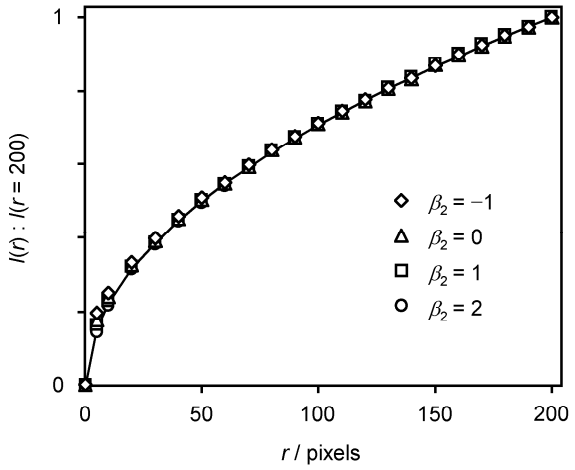

Figure 3.7: Ratio of the peak intensity at *r* = 200, $I(r=200)$, to the peak intensity of varying *r*, $I(r)$, as a function of *r*, for various angular distributions, β_2. This represents the approximate $\sqrt{r}$ functionality (solid black line) of the residual ϕ-contribution associated with $F(r,\theta,\phi\approx 0)$ arising from pixilation, and displayed in Figure 3.8. At small *r*, a β-dependent deviation from this functionality is observed, which can be understood with respect to Figure 3.8.

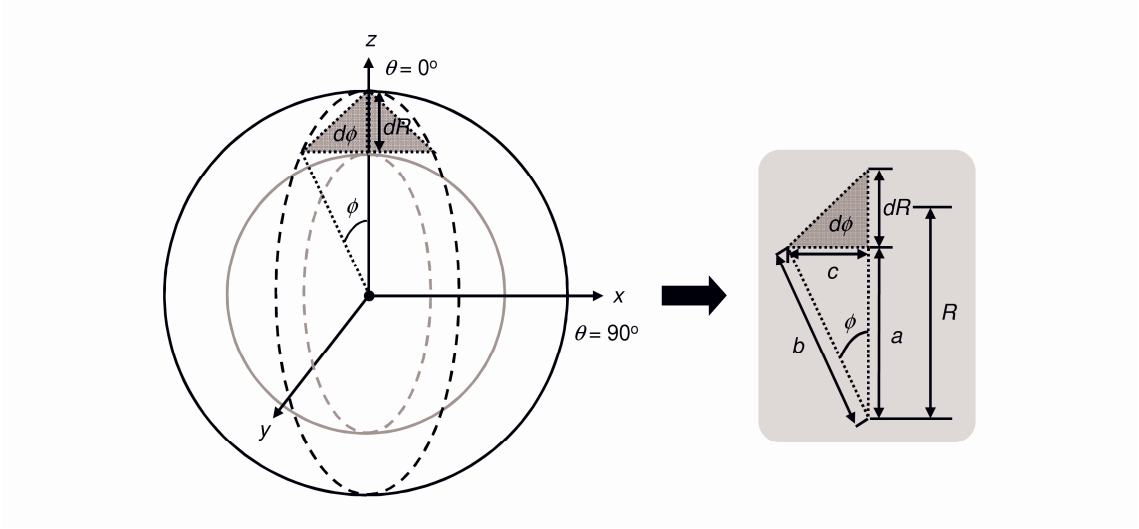

Figure 3.8: Representation of the remaining ϕ-contribution for the pixel width, dR, in the resultant 'slice' from the POP algorithm, $F(r,\theta,\phi \approx 0)$. The area of the triangle, $d\phi$, provides an approximation for this remaining ϕ-contribution, which can be calculated and accounted for when converting $F(r,\theta,\phi \approx 0)$ into the desired 1D radial spectrum. $d\phi$ is calculated using simple Pythagorean geometry, with respect to illustration on the right. The apparent β-dependence observed in Figure 3.7 can be understood from the schematic on the left, as dR is not truly constant as a function of θ.

of r, where the different symbols correspond to different anisotropy parameters for the simulated images. If the slice $F(r,\theta,\phi = 0)$ contains no ϕ-component, then the ratio should be unity and independent of r, which we observe is not the case. Instead, the ratio possesses a $\sqrt{r}$ functionality, the origins of which can be understood with respect to Figure 3.8. The missing ϕ-component, $d\phi$, at a given R is perpendicular to the $R\alpha$-plane (along the y axis) and its area will depend on R. To a first approximation, the ϕ-component can be described as a triangle (in the yz plane), the area of which can be determined by the following simple analysis. The length of c in Figure 3.8 is first calculated using the simple Pythagorean relationship

$$c^2 = b^2 - a^2, \tag{3.35}$$

where

$$\begin{aligned} a &= R - \frac{dR}{2} \\ b &= R + \frac{dR}{2} \end{aligned}. \tag{3.36}$$

Substituting equations (3.36) into equation (3.35), produces $c = \sqrt{2RdR}$, which reduces to $\sqrt{2R}$ when dR = 1, as defined here. The area of the triangle, $d\phi$, can then be evaluated as $\frac{1}{2}\sqrt{2R}$, although the total missing ϕ-contribution is actually $2d\phi = \sqrt{2R}$, and is hence proportional to $\sqrt{R}$. This scaling is shown in Figure 3.7 (when dR = 1) as a solid black line through the data. Despite the rather rough approximation, it appears to capture the behaviour very well particularly at large R. The observed β-dependence at small R originates from the θ-dependence on the omitted volume and can in principle be accounted for. However, in practice, this is cumbersome and ultimately presents only a small error and only at small R, where noise is naturally accumulated using polar reconstruction methods.

Thus, in order to reconstruct the full 3D distribution from the slice $F(r,\theta,\phi \approx 0)$, the standard $r\sin\theta$ scaling factor becomes weighted by a factor of $1/\sqrt{r}$, resulting in a final scaling of $\sqrt{r}\sin\theta$, which accurately recovers the full 3D distribution.

3.2.5 Polar Onion-peeling Algorithm: Computational Overview

A schematic flow chart of operations for the POP algorithm is presented in Figure 3.9. Briefly, the raw Cartesian image, $G(x,z)$, is folded into a single quadrant of a quarter of the size, $G_q(x,z)$, which is then converted into polar form, $G(R,\alpha)$, using the method described in Section 3.2.2. The polar quadrant is then passed through the onion-peeling process, which removes the ϕ-contribution associated with each decreasing radial increment using $g_{\text{fit}}(r;R,\alpha)$. $g_{\text{fit}}(r;R,\alpha)$ is generated from a basis set, $B(r,R)$, of basis functions, $b_r(R)$, using the intensity, $N(r)$, and anisotropy parameters, $\beta_n(r)$, obtained from the fit to the outermost ring, $h(r_{\max},\theta)$ (see equation (3.26)). The subtraction process is then repeated until the centre of the image is reached (r = 0). By retaining $h(r_{\max},\theta)$ at each radial increment the desired slice, $F(r,\theta,\phi=0)$, is generated at the end of the routine, which may then be used to generated the desired 1D radial spectrum, $I(r)$. Finally, the resultant $F(r,\theta,\phi=0)$ in polar form may be back converted into Cartesian co-ordinates using the polar to Cartesian back conversion methodology described in Section 3.2.2.

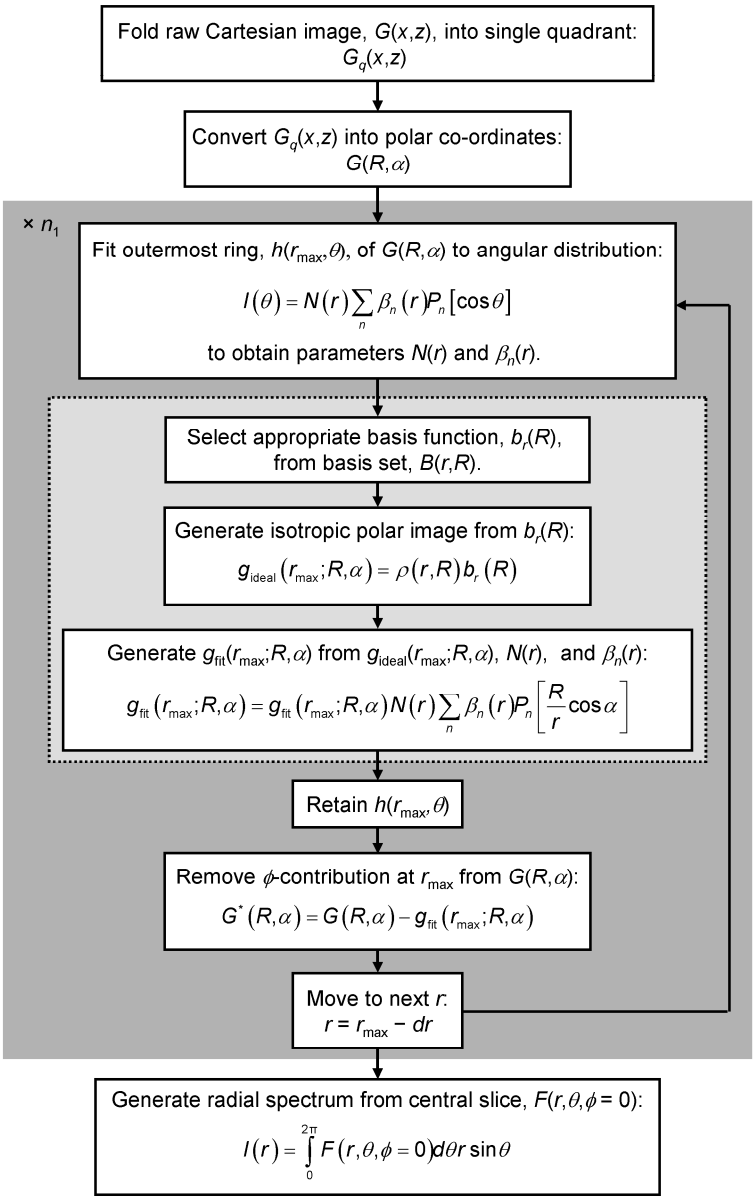

Figure 3.9: Flow chart of operations for the polar onion-peeling algorithm. The raw Cartesian image, $G(x,z)$, is first folded into a single quadrant, $G_q(x,z)$, and then converted into an array of polar pixels, $G(R,\alpha)$. The onion-peeling process is then initiated (dark grey loop). For the first iteration the outermost ring at r_{max}, $h(r_{max},\theta)$, is fitted to an angular distribution to extract an intensity factor, $N(r)$, and anisotropy parameters, $\beta_n(r)$. Basis functions, $b_r(R)$, are then used to generate $g_{fit}(r_{max};R,\alpha)$ from the fit parameters $N(r)$ and $\beta_n(r)$. This basis function expansion process is represented by the light grey region of the flow chart. $g_{fit}(r_{max};R,\alpha)$ is then subtracted from $G(R,\alpha)$ to remove the ϕ-contribution associated with r_{max}. This is repeated for n_1 iterations at each dr decrement until $r = 0$ is reached. $h(r,\theta)$ is then retained at each r to generate $F(r,\theta,\phi=0)$. When $r = 0$ is reached, the resultant slice $F(r,\theta,\phi=0)$ is then integrated over θ to generate the desired 1D radial spectrum, $I(r)$.

3.3 Performance and Application of the Polar Onion-peeling Algorithm

3.3.1 Algorithm Performance: Speed and Scaling

Application to 'Real-time' Image Reconstruction

The primary motivation for developing POP stems from the desire to observe the radial distribution in conjunction with DAQ. In a typical experiment, DAQ does not require the read-out of the CCD at every shot. Specifically, most ultrafast pump-probe experiments operate at 1 kHz, which far exceeds the read-out rate from most CCDs. Hence, often the CCD is exposed for several laser shots and data transferred at 1 Hz or less. Because this timescale is comparable to that required for POP, reconstruction may be performed in parallel to DAQ, providing direct feedback on the progress of the experiment. We demonstrate the point by simulating a radial spectrum in a typical TRPEI experiment. Typically, ~1 electron per shot is collected at 1 kHz for single photon features (features A and B in Figure 3.10), while a pump-probe signal is often at least an order of magnitude less probable (feature C in Figure 3.10).

Images in the first column of Figure 3.10 are simulated by randomly sampling a 3D distribution of photoproducts with predetermined anisotropy parameters and Gaussian radial distributions, as described by the method in Section 3.2.3. This is then projected onto a 256 × 256 pixel Cartesian grid, representing the CCD. The three processes, labelled peaks A, B, and C in Figure 3.10, correspond to radial distributions at r = 40, 75, and 90 pixels and anisotropy parameters of β_2 = –0.5, 1.0, and 0.0, respectively. Also included are 0.5 electrons per shot of random events on the Cartesian grid to simulate the effect of white Cartesian noise (e.g. stray electrons or dark counts).

The first row in Figure 3.10 shows the simulation after only 1 s of data acquisition, corresponding to 1×10^3 electrons in peaks A and B. The central column represents $F(r,\theta,\phi=0)$ following POP and retaining $h_{\text{fit}}(r,\theta)$. This is displayed in polar co-ordinates as the 'triangular' array described in Section 3.2.2, where the diagonal corresponds to the angle $\theta = \pi/2$. For clarity, negative values arising from over subtraction have been set to zero in the display. Despite the low signal level,

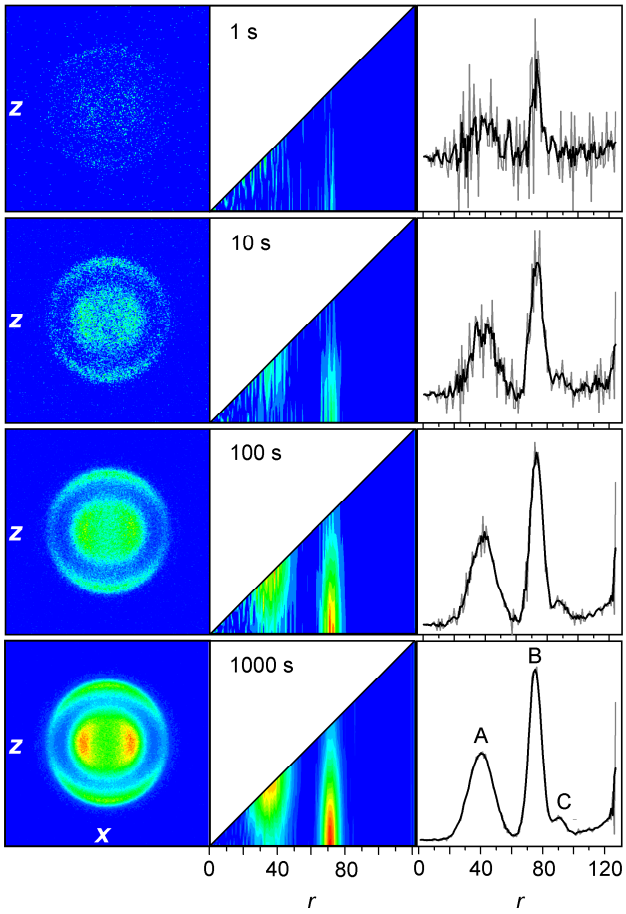

Figure 3.10: Simulated images for a typical time-resolved photoelectron imaging (TRPEI) experiment (left column) have been generated over an increasing data acquisition time: 1 to 1000 s. Deconvolution of these images using POP generates $F(r,\theta,\phi=0)$ (middle column), and angular integration of $F(r,\theta,\phi=0)$ over θ subsequently yields the associated radial spectra (right column, grey line). The solid black line in the radial spectra represents a 3 point running average. Features A and B correspond to single photon processes producing 1 electron per shot at 1 kHz (1×10^3 electrons after 1 s). Feature C corresponds to a pump-probe feature with an order of magnitude less signal than A and B. Cartesian white noise has been simulated in the images with the addition of 0.5 electrons per shot of random events.

features A and B can be clearly identified. In the right column of Figure 3.10, the corresponding radial spectrum (grey line) is presented along with a 3 point running average (black line); peaks A and B can be readily identified and hence optimised during DAQ (at a 1 Hz rate). The second row shows the same data, but after 10 s collection; 1×10^4 electrons in features A and B. Although it is now also clear from the raw Cartesian image that there are two distinct rings, the radial spectrum shows the additional presence of feature C, which is not immediately apparent from the raw image.

At larger radii, the effects of the 0.5 counts per shot of random Cartesian noise

result in a rising baseline and an oscillation near the detection edge (large *r*). These oscillations arise because the Cartesian noise does not possess ϕ-contributions. As a result, the first increment over subtracts, which is compensated for in the next iteration leading to an oscillation in the fit parameter $N(r)$ from equation (3.26). After 100 s, the radial distribution shows clearly all the features present and $F(r,\theta,\phi=0)$ provides a convenient visual aid to the anisotropy of features A and B. After 1000 s, corresponding to 1×10^6 counts in A and B, the effect of radial smoothing is no longer noticeable.

Figure 3.10 highlights the benefit of direct access to the radial spectrum. As data is collected, even small signals may be observed, allowing real-time optimisation of experimental parameters during a time-resolved imaging experiment. Additionally, instant information about the quality of the spectrum is provided. It can be seen that after 100 s of collection, the spectrum may be of acceptable quality, whereas after 10 s, it is not and at 1000 s the improving signal-to-noise is no longer noticeable. In many cases the angular distribution is the observable of interest. Although $F(r,\theta,\phi=0)$ provides a visually attractive image and shows the anisotropy clearly, it must be remembered that this is a fit and provides no information about the quality of that fit. During DAQ, POP can provide a convenient measure of the confidence in the measured β_n parameters. In Figure 3.10, for example, the standard deviation in β_2 from the fit in equation (3.26) can be calculated directly. At pixel *r* = 75 it is 94.3 %, 36.7 %, 9.9 %, and 3.4 % after 1 s, 10 s, 100 s, and 1000 s, respectively. Hence, POP allows the determination of a target confidence level in real-time. More generally, the residuals array, $G^*(R,\alpha)$, defined in equation (3.27), may be used to set general predetermined criteria for the quality of an image and its reconstruction.

Computational Speed and Scaling

The computational speed of POP scales as R^3. For a 256 × 256 pixel image POP takes 0.6 s on a PC with a 2.0 GHz processor, readily attaining the 1 Hz speed criterion set out in Section 3.1.3. The speed of the algorithm can be further improved in a number ways. For example, the Cartesian to polar image conversion, producing $G(R,\alpha)$, can be binned into larger α or *R* intervals. The binning in larger α intervals is particularly useful. The effective box car averaging over α only has a minor effect on the angular fit

to equation (3.26) (β_n will be slightly underestimated), particularly when high order anisotropy terms are required. The increase in computational speed would scale linearly with the number of α intervals in this case. Binning in larger *R* intervals would increase the speed significantly. For example, a 2 pixel bin would lead to a 2^3 fold increase in computation speed. However, this will also lead to a loss of radial resolution, which may or may not be a major concern, depending on specific applications. Generally, if POP is used as a diagnostic tool during DAQ, re-binning in larger *R* intervals is ideal and allows for true real-time image processing during DAQ.

3.3.2 Reconstruction of Simulated Images

In Figure 3.11 we compare the accuracy of POP against other commonly used methods. Specifically, we have chosen to compare primarily to pBASEX as Garcia *et al*. [17] provide a thorough evaluation of pBASEX relative to the commonly used methods of BASEX and the Fourier-Hankel algorithm, which makes use of the inverse Abel transform. In general, pBASEX performs better than the inverse Abel method whilst it is comparable to BASEX, except for images where the anisotropy parameters in equation (3.26), β_n, possess non-even integer values of *n*, for which pBASEX outperforms BASEX [17]. Figure 3.11a shows a 256 × 256 pixel simulated image containing 5 radial features, labelled 1 to 5, in which a total number of 7.4×10^5 events have been randomly generated based on predefined angular and radial Gaussian distributions (σ_r). The simulation parameters used for each of the features in the image are defined in Table 3.2.

Table 3.2: Image simulation parameters for features 1 to 5 in Figure 3.11. Radial features, *r*, are simulated with a Gaussian distribution, σ_r, and anisotropy parameters β_1 and β_2. The number of shots, *m*, in each feature is also displayed.

Peak	*r*	σ_r	β_1	β_2	Shots / *m* × 10^5
1	15.5	1.8	0.0	0.6	0.4
2	34.2	6.5	–0.1	–0.4	2.0
3	56.1	2.9	0.2	–0.8	2.0
4	94.6	1.3	–0.3	0.4	2.0
5	100.1	0.5	0.1	0.6	1.0

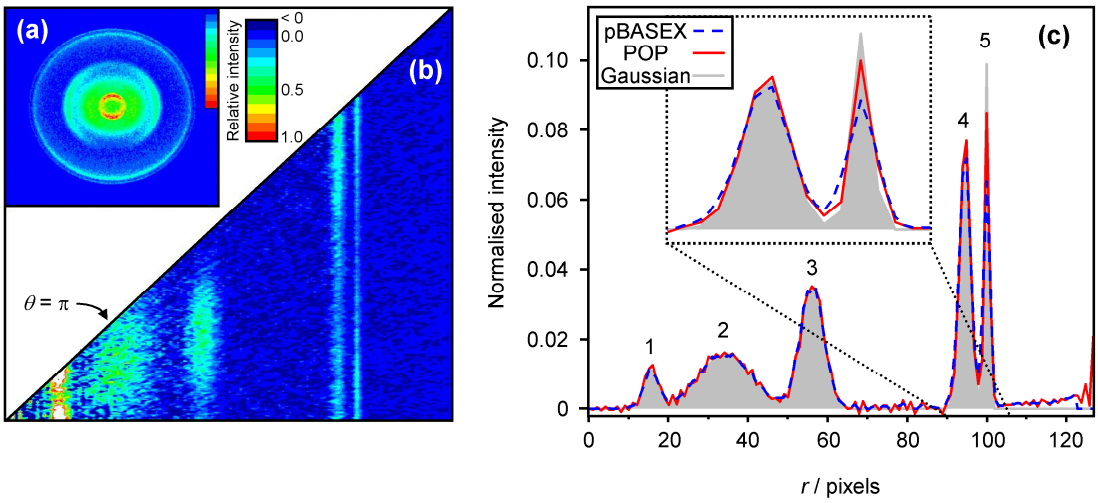

Figure 3.11: (a) Simulated image of a photoionisation event. (b) Reconstructed slice generated using POP by retaining the raw data, $h(r,\theta)$. (c) Comparison of the radial spectra associated with (a) when calculated using pBASEX (blue dashed) and POP (solid red). For visual clarity the peaks around r = 95 have been expanded in the inset. Shown in grey is the expected radial distribution based on the radial Gaussian distributions in Table 3.2.

In addition to these features, 1×10^5 counts of Cartesian noise have also been added. The reconstructed slice from POP is shown in Figure 3.11b, where the originally measured $h(r,\theta)$ is retained to show the true nature of the measured noise from the raw 2D image. This is in contrast to Figure 3.10 and pBASEX, which only show a fit to the data and as a result, these do not provide any indication of the quality of the angular image. Also, unlike the images simulated in Figure 3.10, non-even integer values of n are used for the anisotropy parameters, β_1 and β_2, the angle spanned by the $F(r,\theta,\phi=0)$ is now $0 \le \theta \le \pi$ and is shown in Figure 3.11b. To facilitate this change, the raw Cartesian image, $G(x,z)$, is folded in half, rather than four-way folded, using a similar method to that described in Section 3.2.3. Additionally, the Cartesian to polar conversion process in Section 3.2.2 simply determines the number of polar pixels at each R, $P(R)$, from the integer part of $\pi(R+1)$, rather than $\frac{1}{2}\pi(R+1)$.

In Figure 3.11c, the recovered 1D radial distribution (normalised to the total integrated intensity) is shown, along with that obtained using pBASEX and the expected radial distribution based on the input parameters of the simulation in Table 3.2. Both methods are able to reproduce the radial positions to sub-pixel resolution. Similarly, the extracted anisotropy parameters, β_1 and β_2, presented in Table 3.3, are accurate to less than one decimal place in both cases. The major noticeable difference in the spectra of

Figure 3.11c is the peak intensities of the peaks around r = 95 pixels, which is highlighted in the inset. POP appears to do better in terms of absolute peak height and width, reproducing the expected distribution more closely than pBASEX. The other noticeable difference is that the baseline noise between features is less for pBASEX, which is a consequence of the radial width of the Gaussian function contained in its basis set, which essentially smoothes the image.

Table 3.3: Comparison between the anisotropy parameter values obtained by POP and pBASEX upon reconstruction of Figure 3.11a. Also presented are the expected values used to simulate the image in Figure 3.11a.

Peak	β_1			β_2		
	Simulation	POP	pBASEX	Simulation	POP	pBASEX
1	0.00	–0.02	0.00	0.60	0.63	0.57
2	–0.10	–0.10	–0.11	–0.40	–0.42	–0.40
3	0.20	0.20	0.19	–0.80	–0.78	–0.78
4	–0.30	–0.30	–0.29	0.40	0.39	0.38
5	0.10	0.09	0.07	0.60	0.64	0.59

3.3.3 Reconstruction of Experimental Images

Figure 3.12 presents an experimentally measured image which has been reconstructed using POP and pBASEX to provide the radial spectra shown. The image in Figure 3.12a, measured by Bellm and Reid, has been obtained by resonance-enhanced multi-photon ionisation of *para*-difluorobenzene from the S_0 ground state, *via* the 5^1 vibrational level in the S_1 state [17]. This particular image has been chosen as it was used as a direct comparison to photoelectron TOF data and was also used by Garcia *et al*. in their evaluation of pBASEX with respect to the inverse Abel and BASEX methods. From this evaluation, they observe that the measured anisotropy parameters, β_2 and β_4, obtained from all three of these inversion algorithms are comparable to the experimental TOF measurements, to within the estimated error bars of ±0.1. However, for the Cartesian based BASEX and inverse Abel algorithms to generate satisfactory anisotropy measurements, the centre-line noise region must be negated and calculation of the anisotropy parameters is only performed over the range $20^\circ \le \theta \le 60^\circ$. In

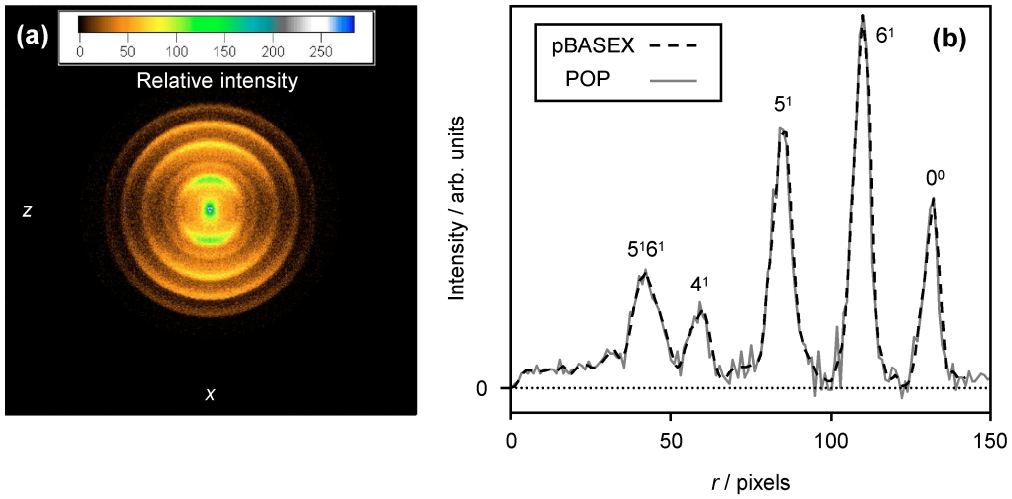

Figure 3.12: (a) Experimental image generated using (1 + 1′) resonance-enhanced multi-photon ionisation of *para*-difluorobenzene from the S_0 ground state *via* the 5^1 vibrational level in the S_1 state. (b) Comparison of the radial spectra calculated using pBASEX (dashed black) and POP (solid grey) from the experimentally obtained image in (a). Image in (a) reprinted with permission from reference [17]. Copyright 2004, American Institute of Physics.

addition, all three methods consistently produce values larger than the TOF data, which they tentatively attribute to the poorer angular resolution in photoelectron TOF analysers.

Radial spectra obtained using either POP or pBASEX produce very similar results both in terms of peak positions and intensities, as shown in Figure 3.12b. The anisotropy parameters extracted from POP can be compared directly with those presented by Garcia *et al*. [17] and Bellm and Reid [31], and are shown in Table 3.4. POP obtains values which are consistent with other methods, including the experimental TOF measurements of Bellm and Reid [31].

Table 3.4: Anisotropy parameters obtained from the reconstruction of Figure 3.12a using POP and pBASEX [17]. Experimental values, obtained using a photoelectron time-of-flight spectrometer, are shown in the TOF columns [31].

Peak	β_2			β_4		
	POP	pBASEX	TOF	POP	pBASEX	TOF
5^16^1	1.13	1.12	-	0.04	–0.02	-
4^16^1	0.64	0.67	-	0.03	0.00	-
5^1	1.12	1.09	0.95	–0.04	0.00	0.11
6^1	1.08	1.14	0.96	–0.10	–0.09	0.16
0^0	0.99	1.04	0.83	–0.07	–0.04	0.08

3.3.4 Integration into Data Acquisition Software

The POP procedure has been developed as a drop-in subroutine (subVI) for use in the LabVIEW DAQ program describe in detail at the end of Chapter 2 (Section 2.6.3). Most coding has however been written using a C language syntax within a formula node interface, which provides clarity and versatility for any potential users; the POP C code is provided in Appendix B. A flow diagram of how POP has been integrated into the LabVIEW DAQ software is displayed in Figure 3.13. At each temporal delay in the DAQ program, individual images are collected from the CCD camera (Basler, A312f) at a rate of ~1.5 Hz (~0.7 s for a single image), where the image acquisition process iteratively acquires and sums a predefined number of individual images for each delay. At the end of each iteration, the DAQ supplies the currently acquiring image to the POP routine, which operates separately from the DAQ routine allowing independent image processing. The POP routine is placed within a 'while loop' which continuously operates until the entire imaging DAQ routine has finished. To ensure maximum computational efficiency of POP the basis set is loaded in memory only once at the start of the DAQ run, and then called as required. For each iteration of the while loop the acquiring image supplied from the DAQ first undergoes a 2 × 2 pixel binning process into a Cartesian array of exactly half the size of the original image. This binning process significantly increases the computation time as this equates to a two-fold binning in R, leading to a relative 8-fold increase of the computation time of the POP routine,

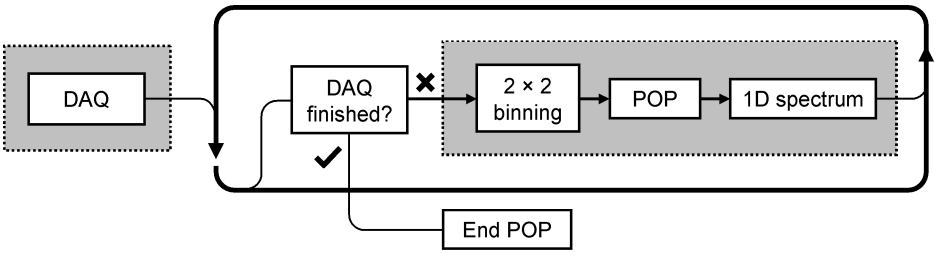

Figure 3.13: Flow diagram of how the polar onion-peeling (POP) subroutine has been integrated into the existing LabVIEW data acquisition (DAQ) program (shown in Figure 2.35), to enable on-the-fly access to 1D radial spectra. The currently acquiring image is supplied from the DAQ routine to the independently operating POP subroutine, which is placed in a 'while loop' (bold black arrows); this while loop operates for the entire duration of the DAQ run. The acquiring image first undergoes a 2 × 2 pixel binning process and then passes through the POP routine, allowing on-the-fly access to the 1D radial spectrum.

ensuring reconstruction times of <1 Hz. The radially binned image is then passed through the POP subroutine, providing on-the-fly access to 1D radial spectrum as it is acquired. In principle the LabVIEW platform also allows for parallelisation of the DAQ and the image reconstruction using a dual core processor, common to most modern PCs, although this has currently not been implemented in the imaging DAQ software.

3.4 Summary

In summary, a method to reconstruct the full 3D charged particle distribution from its measured 2D projection in VMI experiments has been developed. It is based on the method of Zhao *et al*., which performs an onion-peeling of the projection in polar co-ordinates, but has been greatly improved in terms of computational speed by using a basis set of radial distribution functions, which allow for the efficient calculation of 2D projections required in the onion-peeling subtraction. As a result, POP can be used for the reconstruction of the full 3D Newton sphere alongside DAQ in typical experiments, providing the user with instant on-the-fly access to the 1D radial and angular spectra rather than the convoluted 2D image. This is particularly useful in applications where signals are small or obscured by large backgrounds, or in applications requiring long DAQ times, both of which are often the case in TRPEI experiments. Despite the improvements in computational speed, the quality of the reconstruction is comparable to the widely used pBASEX method.

3.5 References

[1] D. W. Chandler and P. L. Houston, *J. Chem. Phys.*, **87**, 1445 (1987).

[2] A. J. R. Heck and D. W. Chandler, *Annu. Rev. Phys. Chem.*, **46**, 335 (1995).

[3] M. N. R. Ashfold *et al.*, *Phys. Chem. Chem. Phys.*, **8**, 26 (2006).

[4] C. Bordas, F. Paulig, H. Helm, and D. L. Huestis, *Rev. Sci. Instrum.*, **67**, 2257 (1996).

[5] A. T. J. B. Eppink and D. H. Parker, *Rev. Sci. Instrum.*, **68**, 3477 (1997).

[6] A. T. J. B. Eppink, S. M. Wu, and B. J. Whitaker, in *Imaging in Molecular Dynamics: Technology and Applications*, edited by B. J. Whitaker (Cambridge

University Press, Cambridge, 2003), pp. 65 - 112.

[7] K. Tonokura and T. Suzuki, *Chem. Phys. Lett.*, **224**, 1 (1994).

[8] C. R. Gebhardt, T. P. Rakitzis, P. C. Samartzis, V. Ladopoulos, and T. N. Kitsopoulos, *Rev. Sci. Instrum.*, **72**, 3848 (2001).

[9] D. Townsend, M. P. Minitti, and A. G. Suits, *Rev. Sci. Instrum.*, **74**, 2530 (2003).

[10] J. J. Lin, J. G. Zhou, W. C. Shiu, and K. P. Liu, *Rev. Sci. Instrum.*, **74**, 2495 (2003).

[11] S. J. Greaves, R. A. Rose, and A. J. Orr-Ewing, *Phys. Chem. Chem. Phys.*, **12**, 9129 (2010).

[12] A. G. Suits, L. S. Bontuyan, P. L. Houston, and B. J. Whitaker, *J. Chem. Phys.*, **96**, 8618 (1992).

[13] L. S. Bontuyan, A. G. Suits, P. L. Houston, and B. J. Whitaker, *J. Phys. Chem.*, **97**, 6342 (1993).

[14] N. Yonekura, C. Gebauer, H. Kohguchi, and T. Suzuki, *Rev. Sci. Instrum.*, **70**, 3265 (1999).

[15] K. T. Lorenz, M. S. Westley, and D. W. Chandler, *Phys. Chem. Chem. Phys.*, **2**, 481 (2000).

[16] M. S. Westley, K. T. Lorenz, D. W. Chandler, and P. L. Houston, *J. Chem. Phys.*, **114**, 2669 (2001).

[17] G. A. Garcia, L. Nahon, and I. Powis, *Rev. Sci. Instrum.*, **75**, 4989 (2004).

[18] V. Dribinski, A. Ossadtchi, V. A. Mandelshtam, and H. Reisler, *Rev. Sci. Instrum.*, **73**, 2634 (2002).

[19] M. J. J. Vrakking, *Rev. Sci. Instrum.*, **72**, 4084 (2001).

[20] F. Renth, J. Riedel, and F. Temps, *Rev. Sci. Instrum.*, **77**, 033103 (2006).

[21] S. Manzhos and H. P. Loock, *Comput. Phys. Commun.*, **154**, 76 (2003).

[22] J. Winterhalter, D. Maier, J. Honerkamp, V. Schyja, and H. Helm, *J. Chem. Phys.*, **110**, 11187 (1999).

[23] K. Zhao, T. Colvin, W. T. Hill, and G. Zhang, *Rev. Sci. Instrum.*, **73**, 3044 (2002).

[24] P. Kruit and F. H. Read, *J. Phys. E*, **16**, 313 (1983).

[25] L. S. Wang, C. F. Ding, X. B. Wang, and S. E. Barlow, *Rev. Sci. Instrum.*, **70**,

1957 (1999).

[26] A. E. Bragg, J. R. R. Verlet, A. Kammrath, O. Cheshnovsky, and D. M. Neumark, *J. Am. Chem. Soc.*, **127**, 15283 (2005).

[27] E. Wrede, *Personal Communication* (2009).

[28] R. N. Zare, *Angular Momentum: Understanding Spatial Aspects in Chemistry and Physics*. (Wiley, New York, 1988).

[29] K. L. Reid, *Annu. Rev. Phys. Chem.*, **54**, 397 (2003).

[30] B. Y. Chang, R. C. Hoetzlein, J. A. Mueller, J. D. Geiser, and P. L. Houston, *Rev. Sci. Instrum.*, **69**, 1665 (1998).

[31] S. M. Bellm and K. L. Reid, *Chem. Phys. Lett.*, **395**, 253 (2004).

Chapter 4: Spectroscopy and Dynamics of the 7,7,8,8-Tetracyanoquinodimethane Radical Anion

The photoelectron spectrum of the 7,7,8,8-tetracyanoquinodimethane (TCNQ) radical anion has been measured at 3.1 eV. Additionally, the ultrafast relaxation dynamics of the first excited state (1^2B_{3u}) of $TCNQ^-$ have been studied using time-resolved photoelectron imaging, which reveals that it undergoes internal conversion back to the ground state ($^2B_{2g}$) with an associated lifetime of 650 fs and shows evidence of coherent nuclear motion.

4.1 Introduction to the 7,7,8,8-Tetracyanoquinodimethane Radical Anion

4.1.1 Application to Charge-transfer Chemistry

Following the observations in the early 1960s that certain organic salts of the 7,7,8,8-tetracyanoquinodimethane (TCNQ) radical anion show electrical conductivity approaching that of bulk metals [1,2], the field of charge-transfer (CT) complexes and the chemists' ability to develop efficient conductive organic complexes has become one of the corner-stone goals of modern chemistry [3,4]. TCNQ, shown in Figure 4.1a, is a planar organic molecule with D_{2h} symmetry and has a conjugated π system, which, together with the highly electron withdrawing cyano groups, leads to a high electron affinity. In the condensed phase, TCNQ based CT salts owe their high conductivities to a π-π stacking motif (schematically illustrated in Figure 4.1b) resulting in the *spatial* and *energetic* overlap between their respective π orbitals. This is exemplified by the complex of the tetrathiofulvane (TTF) radical cation and the TCNQ radical anion, illustrated in Figure 4.1b, which is commonly regarded as the benchmark CT complex [5]. At a temperature of 66 K it possesses a conductivity of $1.47 \times 10^4\ \Omega^{-1}\ \mathrm{cm}^{-1}$,

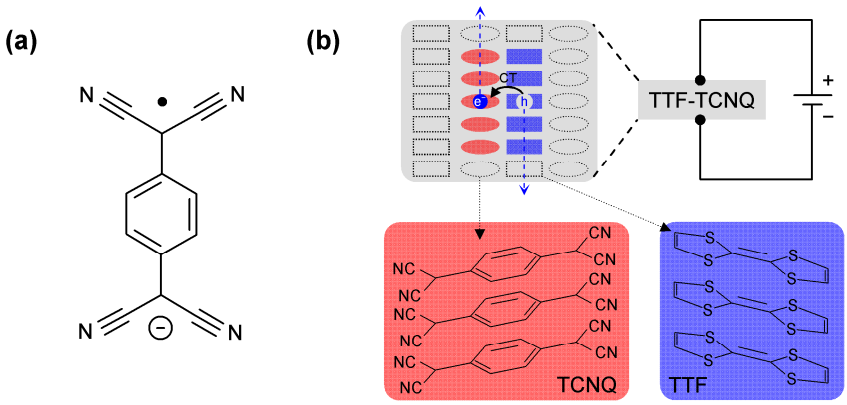

Figure 4.1: (a) Molecular structure of the 7,7,8,8-tetracyanoquinodimethane (TCNQ) radical anion. (b) Schematic illustration of the charge-transfer (CT) process when TCNQ is complexed with tetrathiofulvane (TTF) in the bulk. Both TCNQ and TTF are arranged in a π-π stacking motif (inset bottom), where TTF and TCNQ stacks are alternately aligned next to each other in the extended crystal structure. CT from TTF to TCNQ takes place to leave an electron hole (h) on TTF while transferring the electron (e^-) to TCNQ, forming $TCNQ^-$ and TTF^+. Electrons then flow through the TCNQ stack towards the positive terminal of the circuit, whereas holes flow through the TTF stack towards the negative terminal.

approaching that of copper at room temperature ($6 \times 10^5\ \Omega^{-1}\ cm^{-1}$) and for this reason the term '*organic metal*' has become widely used to describe these highly conductive organic salts [6].

TCNQ based complexes remain at the focus of much ongoing interdisciplinary research and there has been a large amount of effort invested into the derivatisation of complexes such as TTF-TCNQ with the aim of increasing their conductivities to that of bulk metals [6,7]. This includes, for example, the covalent linking of donor and acceptor molecules for application to high efficiency solar cells [8,9]. To date, enhancing the conductive properties of these complexes has proved to be somewhat empirical. Additionally, salts of $TCNQ^-$ with alkali metal cations possess interesting spin lattice properties at low temperatures (<66 K) [10,11], causing a dramatic conductor to insulator transition. More generally, molecules derived from TCNQ have found wide ranging applications in, for example: non-linear optics [12], liquid crystal displays [13], and organic light-emitting devices [14].

4.1.2 Motivations for Studying the TCNQ Radical Anion

Despite the broad interest in TCNQ complexes, it is rather surprising that there are virtually no experimental studies into the electronic structure and relaxation dynamics of the fundamental $TCNQ^-$ building block. Here we report the photoelectron spectrum of the isolated TCNQ radical anion at 3.1 eV (400 nm), which provides insight into the structure of the anion and the neutral. Furthermore, we study the ultrafast relaxation dynamics of photo-excited $TCNQ^-$, yielding molecular level information about the flow of energy in the molecule. The detailed knowledge of the molecular and electronic structure, as well as relaxation dynamics gained through such experiments, are prerequisites to further the understanding of not only the CT mechanism, but to ultimately guide the development of new CT complexes and other novel materials based on TCNQ.

4.1.3 Electronic Structure and Spectroscopy of TCNQ

The electron affinity of TCNQ has been determined to be 2.8 ± 0.1 eV through collisions of neutral TCNQ with fast caesium atoms [15,16]. The gas phase

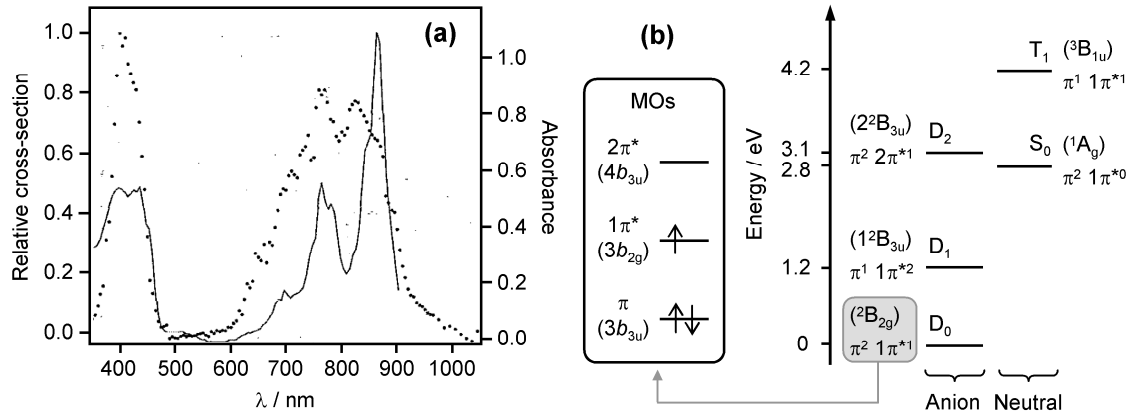

Figure 4.2: (a) Gas phase photodetachment (black dots) and solution phase UV-Vis absorption (solid line) spectra recorded by Brauman and co-workers [17,18]. (b) State energy level diagram for the anion and neutral states of TCNQ. Presented in parentheses are the term symbols associated with each state and their electronic configurations are shown below. The valence molecular orbitals (MOs) are shown on the left, where orbital symmetries are given in parentheses. The spectra in (a) are reprinted with permission from reference [18]. Copyright 1994, American Institute of Physics.

photodetachment spectrum shown in Figure 4.2a, recorded by Brauman and co-workers, reveals strong absorptions around 3.1 eV (400 nm) and 1.2 eV (1030 nm) [17,18], and the spectrum closely resembles the absorption spectrum of $TCNQ^-$ in solution [19]. These two features can be understood in terms of the electronic state energy level diagram, presented in Figure 4.2b. The lower energy band is a broad feature (1.2 – 2.2 eV) that exhibits two dominant vibrational progressions arising from a core excitation involving a $\pi^1 1\pi^{*2} \leftarrow \pi^2 1\pi^{*1}$ transition, as indicated in Figure 4.2b, where we use the labelling D_0, D_1 and D_2 to indicate the doublet states of the anion and S_0 and T_1 for the ground and first excited state of the neutral TCNQ, respectively. The $D_2 \leftarrow D_0$ transition at 3.1 eV is an outer excitation promoting the $1\pi^{*1}$ electron to the higher lying $2\pi^*$ orbital.

In addition to these experimental studies, there have been a number of theoretical investigations of isolated TCNQ and its derivatives, in both its anion and neutral states [20-26]. The TCNQ radical anion is unusual because it possesses a bound excited electronic state, a characteristic not commonly associated with anions. In $TCNQ^-$, this arises from a combination of the high binding energy of the excess electron and the conjugated π system. However, the large size of $TCNQ^-$ and the fact that it contains cyano (CN) groups makes the task of performing accurate quantum calculations challenging, particularly in its excited states.

Early *ab-initio* studies focused on the first few excited doublet states of the TCNQ radical anion, which were thought to be bound with respect to the singlet ground state of the neutral, $S_0\left(^1A_g\right)$ [20]. Later, Skurski and Gutowski calculated the vertical excitation energy of the D_1 $\left(1^2B_{3u}\right)$ state to be 1.24 eV above the D_0 $\left(^2B_{2g}\right)$ ground state at the CI/PM3 level of theory [22], which correlates well with the experimentally observed features in the UV-Vis [19] and photodetachment spectra [18] at 1.2 eV. However, calculations involving the higher lying D_2 $\left(2^2B_{3u}\right)$ excited state, which corresponds to an outer excitation, were less consistent with experiment, as some studies determine it to be bound [22] while others predicted it to be unbound [20,26] with respect to the neutral. The experimentally observed $D_2 \leftarrow D_0$ transition occurs at 3.1 eV [17-19], so that the second excited D_2 state is unbound by about 0.3 eV, thus highlighting the difficulties involved in accurately calculating electronic excitation energies in large molecules such as $TCNQ^-$.

To probe the electronic structure of TCNQ, we employ photoelectron imaging (PEI) of the isolated radical anion which, as well as measuring the outgoing electron's kinetic energy (*eKE*), also provides access the photoelectron angular distributions (PADs) [27]; we explore these PADs in greater detail in Chapter 5. In its time-resolved variant, a femtosecond laser pulse excites $TCNQ^-$ into its first excited state and the electron is removed using a second ultrashort probe pulse, which projects the dynamically evolving system onto correlated final states of the neutral. As discussed in Chapter 1, photoelectron spectroscopy (PES) has relaxed selection rules. However, final states must be accessible within Koopmans' theorem (see Section 1.3.3 in Chapter 1), which argues that the electronic configuration of the initial state following photodetachment must not change when accessing the final state [28,29]. In the specific case of $TCNQ^-$, the neutral state that TCNQ will be left in is determined by the electronic structure of the anion state from which the electron is removed.

4.2 Experiment Details

4.2.1 Generation of TCNQ Radical Anions

The experiment is described in detail in Chapter 2 and only an overview of the details

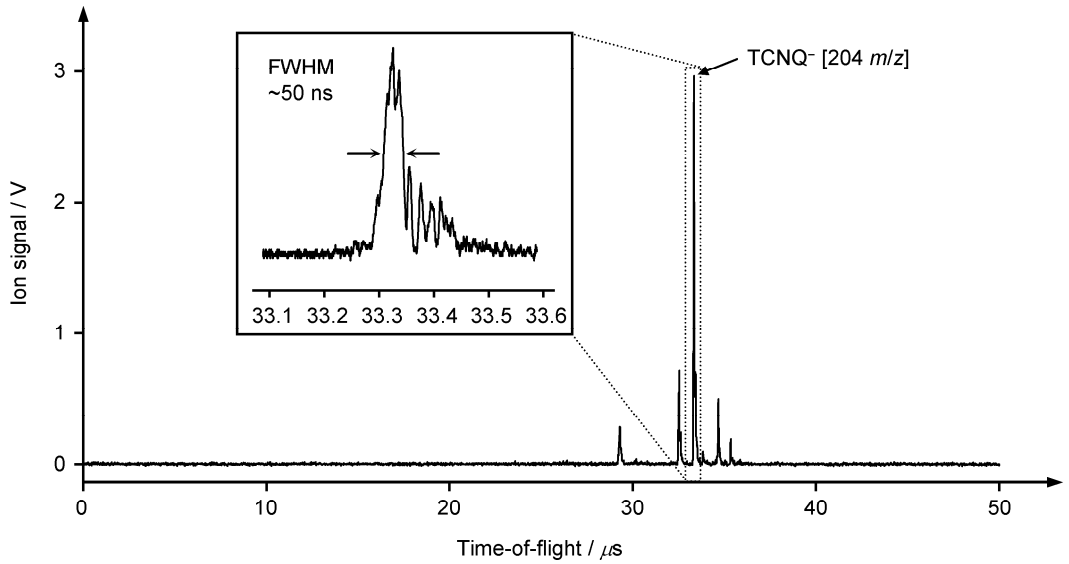

Figure 4.3: Time-of-flight (TOF) spectrum of the TCNQ radical anion, obtained using the experimental parameters in Table 4.1. The $TCNQ^-$ peak at 33.3 μs has an associated temporal full-width at half maximum (FWHM) of 50 ns (shown inset), and corresponds to m/z = 204 amu.

specific to this experiment are provided here. TCNQ anions are generated through electrospray ionisation (ESI). A 1 mM solution of TCNQ (Sigma-Aldrich) in pure acetonitrile is pumped at a flow rate of 250 μl hr^{-1} through the stainless steel ESI needle, which is biased at –3 kV. Anions enter the first vacuum region *via* the stainless steel capillary which is heated to 80 ^oC, and pressures in the first and second vacuum regions of the spectrometer are throttled to 3.6 Torr and 7.2 mTorr, respectively. Anions are then radially confined in the ion guide, where they are subsequently accumulated at its terminus in the DC trap. The temperature of the ions within the trap is approximately room temperature (298 K), as a result of thermalising collisions with background gas molecules. They are then injected collinearly into the Wiley-McLaren time-of-flight (TOF) spectrometer at a 500 Hz repetition rate, which is half the repetition rate of the femtosecond laser system. The TOF spectrum, shown in Figure 4.3, is monitored using the multichannel plate (MCP) ion detector, the rear of which is biased at 2.1 kV. The TOF spectrum is dominated by a peak at 33.3 μs, corresponding to m/z = 204 amu. Based on the measured signal of 3 V and a temporal full-width at half maximum (FWHM) of 50 ns, we calculate that a single TCNQ ion packet contains approximately

800 anions (see equation (2.20) in Section 2.5.1).[1] A summary of the spectrometer parameters used to record the TOF spectrum of $TCNQ^-$ is presented below in Table 4.1.

Table 4.1: Spectrometer parameters used to record the TOF spectrum of the TCNQ radical anion in Figure 4.3.

Spectrometer component	Variable	Optimised value
ESI source	V_{ESI}	–2.9 kV
	I_{ESI}	0.20 μA
	Solution flow rate	250 μl hr^{-1}
Heated capillary	T	80 ^{o}C
	V_4	–48 V
Source region pressures	P_{R1}	3.6 Torr
	P_{R2}	7.2 mTorr
R1/R2 pinhole plate	V_3	–47 V
Ion guide	V_1	–40 V
	V_2	–45 V
	ϕ_1 and ϕ_2	195 V_{pp}, 1 MHz
Ion trap	V_{Trap} (Open)	–38.1 V
	V_{Trap} (Closed)	–43.2 V
Trap timing	ΔT	12.3 μs
	Open duration	2.3 μs
Deflector set 1	V_y	0.6 V
	V_z	–1.4 V
Deflector set 2	V_y	0.7 V
	V_z	–3.2 V
Einzel lenses	Einzel 1	–918 V
	Einzel 2	–1400 V

[1] A comparison with ion trap simulations and experimentally obtained mass spectra of iodide in Chapter 2 indicates that the $TCNQ^-$ ion packet contains 4 times more than the predicted ion trap capacity limit. We tentatively attribute this discrepancy to differences between the modelling parameters of the Simion ion trap simulation and the experimental parameters used in these $TCNQ^-$ experiments.

4.2.2 Laser Arrangement and Photoelectron Imaging

Laser pulses are derived from the commercial femtosecond laser system (Spectra-Physics, Spitfire XP-Pro) described in Section 2.2. The 800 nm fundamental (1.5 eV) is used as a pump in time-resolved experiments and has an associated bandwidth of ~30 nm (~60 meV). Probe pulses are generated by frequency doubling in a 300 μm thick type-I β-Barium Borate (BBO) crystal. The 400 nm (3.1 eV) probe pulses are delayed relative to pump pulses using a motorised delay stage (Physik Instrumente, M-505) before being recombined and sent unfocussed into the vacuum chamber. The polarisation of the laser electric field vector, $\boldsymbol{\varepsilon}$, was set parallel to the photoelectron imaging detector plane and pulse energies of the pump and probe are measured to be 120 μJ/pulse and 70 μJ/pulse, respectively. The power densities of both pulses are on the order of ~1 × 10^{10} W cm^{-2} and the temporal width of the pulse pair for these experiments is determined to be 100 fs from their cross-correlation in a second 200 μm thick type-I BBO crystal.

Photoelectrons are collected using the velocity map imaging (VMI) arrangement described in Section 2.5.2. Raw images are recorded over 1.75 × 10^5 laser shots, and photoelectron spectra are obtained by subtraction of the superfluous azimuthal contribution to the raw image using the polar onion-peeling (POP) routine described in Chapter 3. The photoelectron energy scale is calibrated using the photoelectron spectrum of iodide at 266 nm, presented in Section 2.5.2.

4.3 Photoelectron Spectrum of the TCNQ Radical Anion at 3.1 eV

4.3.1 Interpretation and Assignment of the Photoelectron Spectrum

The photoelectron spectrum of the TCNQ radical anion following detachment at 3.1 eV is presented in Figure 4.4a, which shows two features centred at 0.2 eV and 2.0 eV, labelled A and B, respectively. Also shown in Figure 4.4b is the raw photoelectron image acquired over 1.75 × 10^5 laser shots (left half) together with the deconvoluted central slice through the three dimensional photoelectron cloud (right half), where the laser polarisation vector, $\boldsymbol{\varepsilon}$, is shown by the white arrow. The one-colour detachment scheme is shown with respect to the state energy level diagram in Figure 4.4c, where

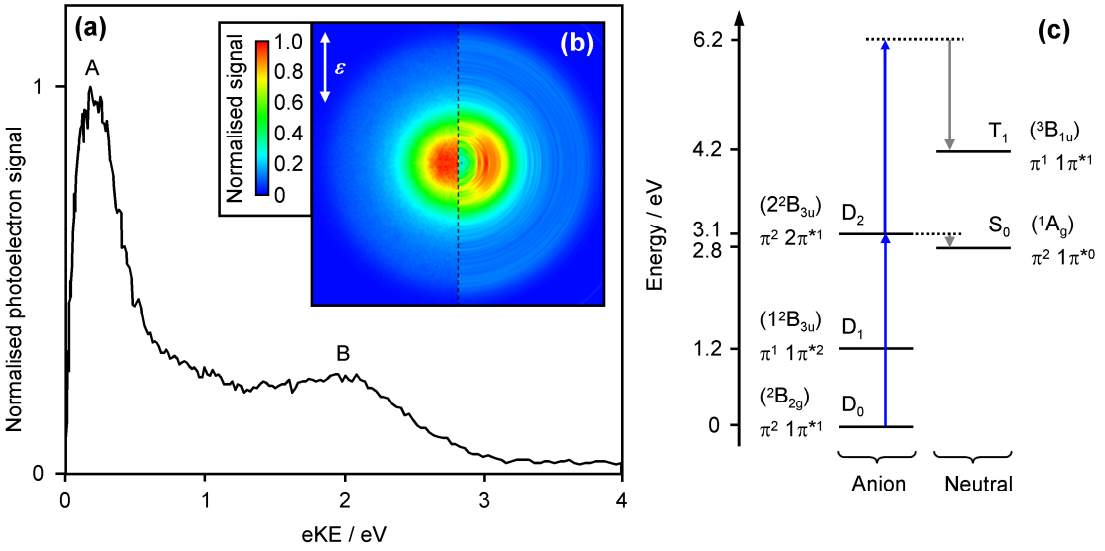

Figure 4.4: (a) Photoelectron spectrum of the TCNQ radical anion recorded at 3.1 eV (400 nm). (b) Raw photoelectron image (left) acquired over 1.75 × 10^5 laser shots and the slice through the centre of the deconvoluted electron image (right). The laser polarisation direction, $\boldsymbol{\varepsilon}$, is indicated in the top left of the image by the white arrow. (c) State energy level diagram for the anion and neutral states of TCNQ, showing the one-colour detachment scheme. Vertical blue arrows indicate one- and two-photon detachment at 3.1 eV and grey downward arrows represent the subsequent electron kinetic energies (*eKE*s) for features A and B in (a).

blue arrows represent 3.1 eV photons and downward grey arrows represent *eKE*s. The low energy feature in the photoelectron spectrum, labelled A, corresponds to excitation from the D_0 ground state of the anion to the D_2 state, which promptly autodetaches to the S_0 neutral ground state. This provides a detachment energy of 2.9 eV, which is in good agreement with the measured electron affinity of 2.8 ± 0.1 eV [15,16].

The broader kinetic energy feature around 2.0 eV (labelled B in Figure 4.4a) is somewhat unexpected. The photon energy of 3.1 eV is resonant with the D_2 state and as such, this photoelectron peak could be explained in terms of resonance-enhanced two-photon detachment *via* the D_2 state, which has a large excitation cross-section ($\sigma \approx 1 \times 10^{-16}$ cm^2) [30]. Recalling that the D_2 state primarily possesses a $\pi^2 2\pi^{*1}$ configuration (see Figure 4.4c), Figure 4.5 explores the electron detachment process from the $\pi^2 2\pi^{*1}$ character in terms of Koopmans' theorem. In Koopmans' picture, this $\pi^1 1\pi^{*2}$ component of the D_2 state correlates to the neutral in its S_0 state following detachment of an electron from the $2\pi^*$ $(4b_{3u})$ orbital, thus generating photoelectrons around 3.5 eV; this is not observed in the photoelectron spectrum.

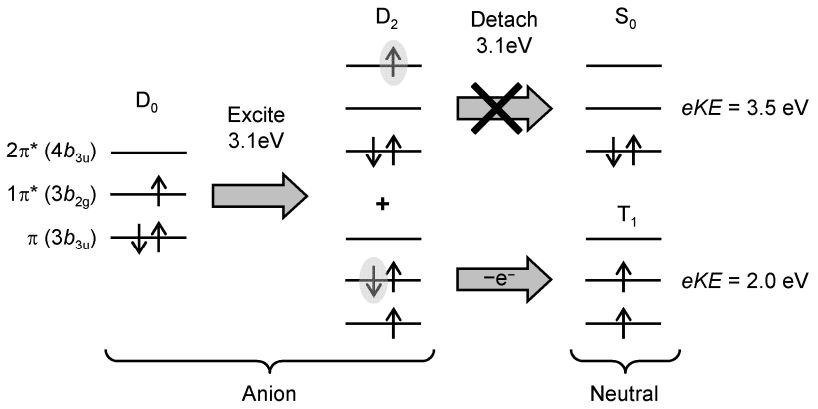

Figure 4.5: Type I Koopmans' correlations for electron detachment in $TCNQ^-$ following excitation from the D_0 anion ground state to the D_2 excited state at 3.1 eV. The D_2 state has contributions from two electronic configurations: the outer excited $\pi^2 2\pi^{*1}$ and the core excited $\pi^1 1\pi^{*2}$. The $\pi^2 2\pi^{*1}$ configuration correlates to the S_0 neutral ground state following electron detachment with a second 3.1 eV photon, and would generate photoelectrons at 3.5 eV; this is not observed in the photoelectron spectrum. The core excited $\pi^1 1\pi^{*2}$ contribution corresponds to the excited T_1 state of the neutral. This electron detachment process given rise to the 2.0 eV feature (B) in the measured photoelectron spectrum in Figure 4.4a.

Theoretical investigations predict that the D_2 state is not a 'pure' state and has contributions from more than one electronic configuration. Skurski and Gutowski [22], as well as Brauman and co-workers [18], calculate that there is a small admixture of the core excited $\pi^1 1\pi^{*2}$ configuration to the D_2 state (8 % and 15 %, respectively). Albeit a small contribution, Figure 4.5 shows how this core excited configuration correlates to the T_1 $\left({}^3B_{1u}\right)$ excited state in the neutral following detachment from the $1\pi^*$ $\left(3b_{2g}\right)$ orbital, and we assign the 2.0 eV feature to this process. It is important to note that this core excited contribution to the D_2 state does not correlate to the S_0 neutral ground state in Koopmans' picture (see Figure 4.5) and thus the excess electron does not undergo rapid autodetachment. The measured 2.0 eV provides an estimated energy of ~1.4 eV for the highly spin-forbidden $T_1 \leftarrow S_0$ transition. In an attempt to verify this value, we have measured the UV-Vis absorption spectrum of neutral TCNQ over a range of 600 nm to 900 nm (1.37 eV - 2.06 eV) using spectroelectrochemical analysis,[2] as presented in Figure 4.6. However, this shows no absorption in the spectral region around 1.4 eV up to 2.06 eV, indicating that the $T_1 \leftarrow S_0$ transition is optically dark, as

[2] Spectroelectrochemical analysis was performed using a 0.1 mM solution of TCNQ (Sigma Aldrich) in pure acetronitrile and a quartz electrolytic cell (1 cm pathlength). The UV-Vis absorption spectrum was recorded for the anion and the neutral using a UV-Vis absorption spectrometer with a 1 nm resolution.

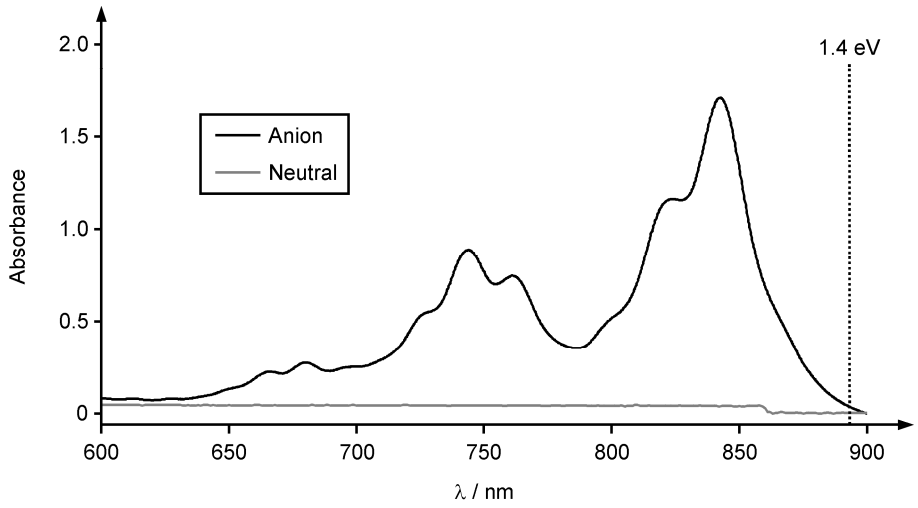

Figure 4.6: UV-Vis absorption spectrum of neutral TCNQ (grey line) and its anion (black line) from 600 nm to 900 nm (1.37 eV to 2.06 eV), recorded by performing a spectroelectrochemical analysis on a 0.1 mM solution of TCNQ in pure acetonitrile. The series of vibrational features starting at ~875 nm in the anion spectrum correspond to the $D_1 \leftarrow D_0$ transition. No features at 1.4 eV are present in the neutral spectrum, indicating that the $T_1 \leftarrow S_0$ transition is optically dark, as anticipated for a spin-forbidden transition.

expected for a spin-forbidden transition.

When considering the integrated intensity of the broad 2.0 eV feature (feature B), it is similar to that of the sharper feature A at 0.2 eV, which contradicts the prediction that only a small contribution of the D_2 state is of the core excited $\pi^1 1\pi^{*2}$ character. However, this is not a true reflection on the state contributions, as the cross-section for photodetachment to the T_1 state relative to the S_0 state may be different. Based on our time-resolved photoelectron spectra, which we discuss in Section 4.4, the cross-section for photodetachment from the $\pi^1 1\pi^{*2}$ configuration to the T_1 state is observed to be comparatively large and can explain the large intensity observed in feature B at 2.0 eV.

4.3.2 TCNQ Electronic State Potentials

In Figure 4.7 we explore the relative potential energy surfaces of both the anion and the neutral states of TCNQ, with respect to the features observed in the photoelectron spectrum and UV-Vis absorption spectrum of $TCNQ^-$. In the photoelectron spectrum, the feature around 2.0 eV is much broader than the feature at 0.2 eV. The narrow width of the latter suggests that the potential energy surfaces associated with the D_2 and S_0 states are similar, as schematically shown in Figure 4.7, and hence, there is little

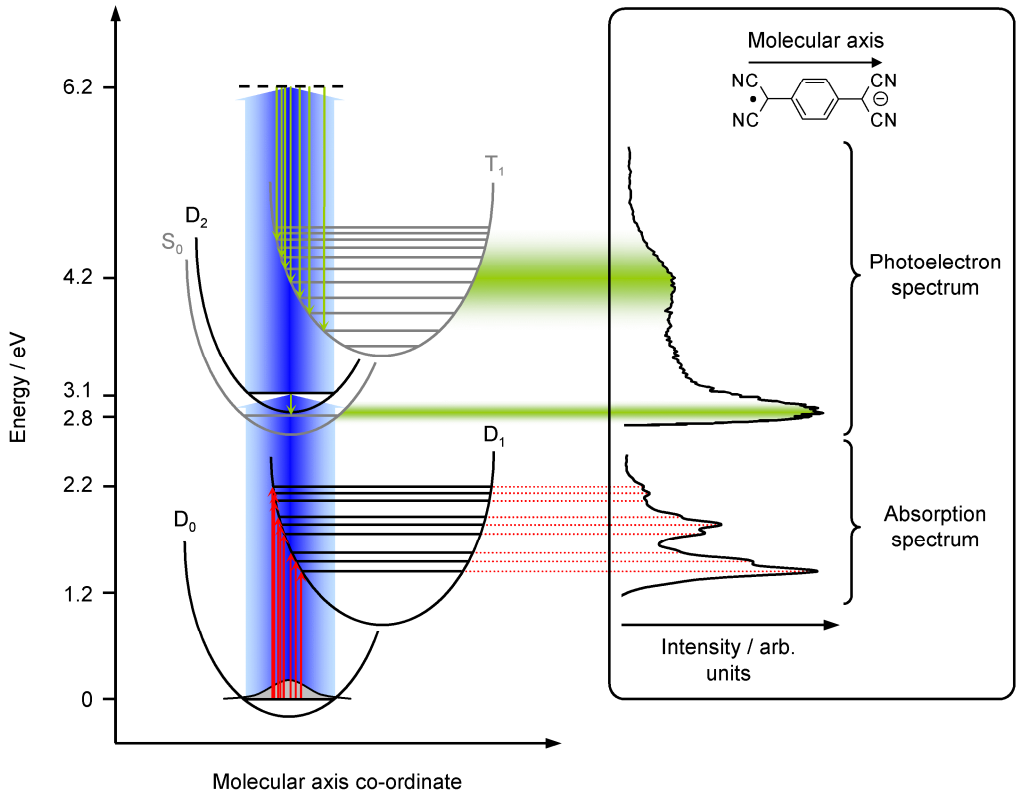

Figure 4.7: Schematic illustration of the relative potential energy surfaces of the TCNQ anion (black) and neutral (grey) states with respect to the molecular axis co-ordinate (shown inset above). Resonance-enhanced two-photon detachment *via* the D_2 state at 3.1 eV (thick blue arrows), results in the photoelectron features at 2.0 eV and 0.2 eV (downward green arrows). This is shown with relation to the measured photoelectron spectrum on the right. Absorption from the D_0 anion ground state to the D_1 excited anion state (red arrows) is also shown, with respect to the broad absorption feature observed in the UV-Vis absorption spectrum over an energy range of 1.2 eV to 2.2 eV (right).

vibrational energy transfer to the neutral following excitation and electron autodetachment. This is supported by theoretical calculations which suggest that the D_0, D_2, and S_0 states all have similar geometries [22]. The lack of major geometric change in going from the D_0 state to D_2 state is reinforced by the relatively narrow peak at 3.1 eV in the UV-Vis absorption [19] and gas phase photodetachment spectra [17,18]. This is in contrast to the $D_1 \leftarrow D_0$ transition, which as shown in Figure 4.7 displays clear vibrational progressions, making the observed feature starting at 1.2 eV very broad in both the gas and solution phase spectra. The width of the photoelectron feature at 2.0 eV suggests that there is a major geometric change in the photodetachment from the D_2 to T_1 state, which is also schematically illustrated in Figure 4.7. This is again in line with theoretical work that calculates the T_1 state to

become elongated along the long molecular axis (see inset in Figure 4.7) with respect to the D_0 and D_2 states due to its additional anti-bonding character [22]. Interestingly, the T_1 state geometry is very similar to that of the D_1 [22], which is evidenced by the photoelectron spectra observed in the time-resolved experiments in Section 4.4.

4.4 Dynamics of the 1^2B_{3u} Excited State

4.4.1 Time-resolved Photoelectron Spectra

The lifetime and relaxation dynamics following excitation to the 1^2B_{3u} state (D_1) of $TCNQ^-$ have been studied using time-resolved photoelectron imaging, employing pump and probe pulse energies of 1.5 eV (800 nm) and 3.1 eV (400 nm), respectively. The pump photon is resonant with the $D_1 \leftarrow D_0$ transition, while the probe removes the excited electron, thus yielding a series of time-resolved photoelectron spectra. The

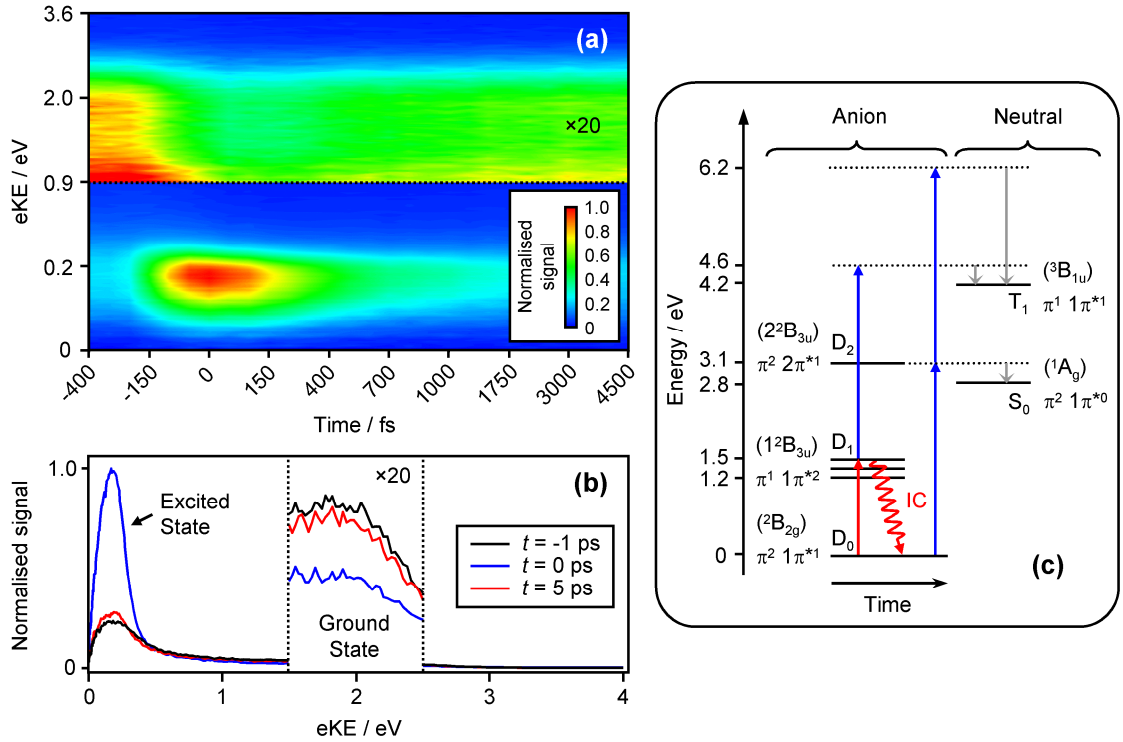

Figure 4.8: (a) Normalised false-colour intensity plot of the measured photoelectron spectra as a function of pump-probe delay (time, *t*) using pump and probe energies of 1.5 eV and 3.1 eV, respectively. (b) Individual photoelectron spectra showing the ground and excited state features at pump-probe delays of *t* = –1 ps, 0 ps, and 5 ps. (c) Energy level diagram of the electronic states showing the pump-probe scheme, where red arrows represent pump photons (1.5 eV), blue arrows are the probe photons (3.1 eV), and grey downward arrows are electron kinetic energies (*eKE*s).

probe wavelength is chosen to be resonant with the D_2 state so that the feature around 2.0 eV provides a clear signature of the ground state dynamics. The time-resolved photoelectron spectrum is shown in Figure 4.8a as a normalised false-colour intensity plot, where the measured photoelectron spectra have been plotted as a function of pump-probe delay (time, *t*). To aid in the analysis of the $TCNQ^-$ excited state dynamics and for clarity, individual photoelectron spectra are also presented at three different pump-probe delays in Figure 4.8b: $t = -1$ ps, 0 ps, and 5 ps. The pump-probe scheme for the experiment is also displayed in Figure 4.8c.

Before the excited state is prepared ($t < 0$), the photoelectron spectrum is identical to that of the one-colour spectrum in Figure 4.4a. This indicates that the pump does not induce any resonance-enhanced two-photon detachment because the D_1 state does not correlate to the S_0 neutral state. This is in contrast to the photodetachment spectrum measured by Brauman and co-workers [17,18], who used a continuous light source. In these experiments it was proposed that a second photon could be absorbed after the excited state has relaxed through internal conversion (IC), producing $TCNQ^-$ in a vibrationally excited D_0^* ground state. Excitation from the D_0^* state does correlate to the S_0 state and hence, it was concluded that $TCNQ^-$ loses its excess electron through ground state autodetachment following the absorption of a second photon. In the experiments described here, the excitation pulse is short, such that there is insufficient time for the excited state to undergo IC before absorbing additional photons. To confirm Brauman and co-workers hypothesis, we have conducted time-resolved experiments where the pump and probe both have energies of 1.5 eV. If the hypothesis suggested above is correct, one may expect that after a sufficient time delay, Δt, between the two pulses, photoelectrons associated with detachment from the vibrationally hot ground state to S_0 would be observed. However, over a time delay of 10 ps we observe no photoelectron signal in the measured images. We show later, in Section 4.4.2, that this is ample time for the D_1 state to have relaxed back to the ground state. To account for the signal observed in the photodetachment spectrum at 800 nm a three photon process must instead be invoked, as illustrated in Figure 4.9. Following IC between D_1 and D_0^*, we suggest that a second photon excites the vibrationally hot ground state back into a vibrationally excited D_1^* state, which may then internally convert back to a highly vibrationally excited D_0^{**} state. From here two detachment pathways are available to the

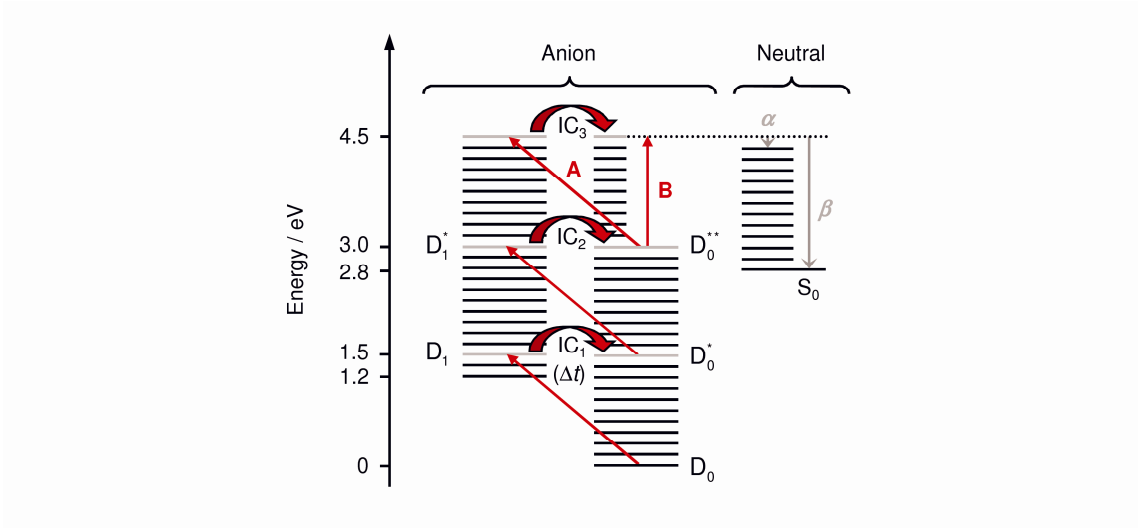

Figure 4.9: Proposed three photon absorption processes for detaching electrons at 800 nm (1.5 eV). A first photon (thin red arrows) excites population from the D_0 ground state into the D_1 excited state, which then undergoes internal conversion (IC_1) back to a vibrationally hot ground state, D_0^*, after a time Δt. A second photon does not lead to photodetachment, but rather excites D_0^* into a vibrationally hot D_1^* state, which internally coverts (IC_2) back to a highly vibrationally excited ground state, D_0^{**} . Finally, a third photon may lead to indirect, A, or direct, B, detachment of an electron from D_0^{**} to generate neutral TCNQ in its correlated S_0 ground state (grey arrows, α and β).

system. The first of these is labelled A is Figure 4.9. Here, a third 1.5 eV photon excites $TCNQ^-$ into a highly vibrationally excited D_1 state, which may then again internally convert back to a hot D_0 ground state. From here, vibrationally mediated autodetachment may occur to generate low energy photoelectrons (labelled α in Figure 4.9). Alternatively, process B in Figure 4.9 may occur, resulting in direct electron detachment from D_0^{**} to the correlated S_0 state of the neutral *via* the absorption of a third 1.5 eV photon. This generates high energy photoelectrons around 1.8 eV (labelled β in Figure 4.9). To differentiate between processes A and B, one must ultimately conduct a time-resolved three pulse experiment (pump-pump-probe), where all three pulses have energies of 1.5 eV.

When pump and probe pulses are temporally overlapped (t = 0), as shown in Figure 4.8c, a large increase in photoelectron signal is observed at 0.2 eV. Additionally, the feature at 2.0 eV is depleted. The latter is a direct measure of the D_0 ground state population as the only process that can produce photoelectrons at this kinetic energy is resonance-enhanced two-photon detachment *via* the D_2 excited state. Depletion in this feature indicates that some population has been transferred from the D_0 ground state to the D_1 excited state by the pump pulse. The new feature around 0.2 eV is assigned to

the detachment of electrons from the excited D_1 state to the T_1 state of the neutral, with which it is correlated in Koopmans' picture (see Figure 4.5). The observed kinetic energy around 0.2 eV is obtained by subtracting the detachment energy and the S_0 to T_1 energy gap from the total photon energy absorbed.

At long time in Figure 4.8b, t = 5 ps, the photoelectron spectrum indicates that the excited state population has decayed, while a recovery in the ground state is observed.

4.4.2 Lifetime of the 1^2B_{3u} Excited state

Exploring the dynamics in further detail, Figure 4.10 shows the integrated intensities of the excited and ground state features over the spectral ranges of 0.15 eV to 0.40 eV and 1.65 eV to 2.25 eV, respectively. The mirrored dynamics signify that population is transferred from the excited state directly to the ground state, and thus suggests that IC is being observed. We also highlight that the excited state feature at 0.2 eV is convoluted with some residual signal arising from the D_0 ground state, which will also recover with time. However, because of the relatively large cross-section for detachment from the D_1 state $\left(D_1 \rightarrow T_1 + e^-\right)$, the dynamics of the ground state contributing to this feature cannot be discerned from the D_1 state dynamics.

The integrated intensity of the ground state peak as a function of pump-probe delay (Figure 4.10a, open diamonds) can be fitted using a single exponential function

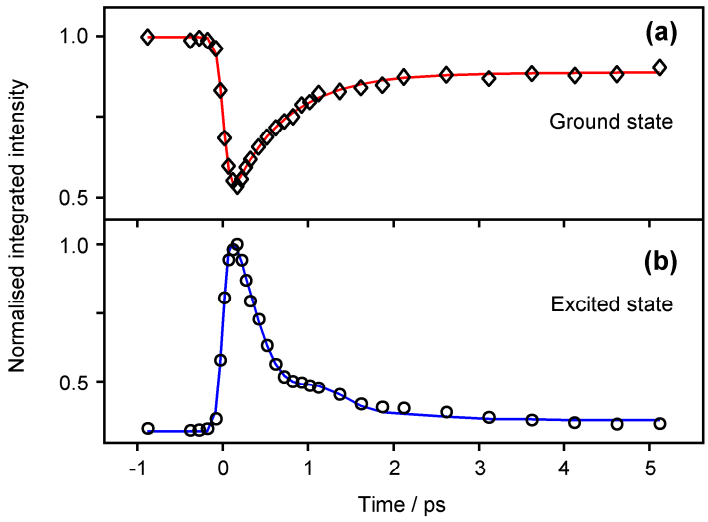

Figure 4.10: Integrated intensities of (a) the ground (open diamonds) and (b) the excited state (open circles) features as a function of pump-probe delay (time, t). Solid red and blue lines are fits to equations (4.1) and (4.2), respectively, following convolution with the Gaussian instrument response function.

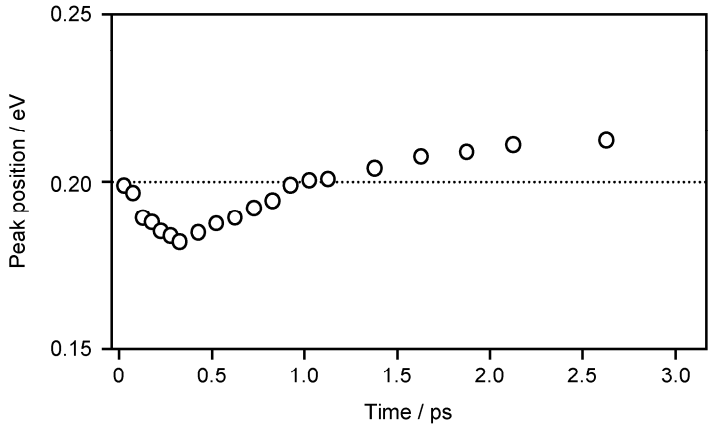

Figure 4.11: Peak position of the excited state feature in the time-resolved photoelectron spectra. The centre of the photoelectron feature (open circles) has been determined by fitting the peak to a Gaussian energy distribution using a least squares fitting method.

convoluted with the Gaussian instrument response function (see Appendix C for details of the convolution). The latter describes the temporal cross-correlation of the pump and probe laser pulses. Prior to convolution, the exponential fit function, $f(t)$, has the form

$$\begin{aligned} f(t) &= C_0, \quad t < 0 \\ f(t) &= 1 - \left[A_1 \exp(-t/\tau) + C_1 \right], \quad t \geq 0 \end{aligned}, \tag{4.1}$$

where A_1 is the amplitude of the exponential and τ corresponds to the lifetime to the D_1 excited state. The constants C_0 and C_1 represent a measure of the initial ($t < 0$) and final ($t \gg 0$) ground state populations, respectively. C_1 is observed to be less than C_0, suggesting that not all the population has recovered and will be discussed later. The fit, shown in Figure 4.10a as a solid red line, yields a measured lifetime of $\tau = 640 \pm 50$ fs for the ground state population recovery.

The excited state peak dynamics, displayed in Figure 4.10b as open circles, could also potentially be described by a single exponential fit function. However, such a description does not capture the apparent reduced decay rate around 1 ps. Given the broad bandwidth of the pump pulse, a coherent superposition of vibrational levels will be excited, leading to coherent nuclear motion of $TCNQ^-$ on the D_1 state. Evidence for nuclear motion can be extracted from the time-resolved photoelectron spectra which show a small red shift of ~10 meV in the photoelectron peak position at ~400 fs, as shown in Figure 4.11. The central position of the excited state photoelectron feature has

been obtained by fitting the peak to a Gaussian energy distribution using a least squares fitting method. To account for vibrational dynamics in the population decay, we have included a periodic modulation of the exponential fit with the resultant functional form

$$\begin{aligned} g(t) &= C_0, \quad t < 0 \\ g(t) &= A_1 \exp(-t/\tau) + A_2 \cos(\omega t + \phi) \exp(-t/\tau_d) + C_1, \quad t \geq 0 \end{aligned}, \tag{4.2}$$

before convolution with the Gaussian instrument function. The additional cosine term in $g(t)$ describes the damped oscillation associated with a periodic coherent motion, where A_2 is the amplitude of oscillation, ω is its angular frequency (in rads s^{-1}), ϕ is the initial phase and τ_d is its damping lifetime. In equation (4.2), the constant C_0 accounts for the fact that the spectrum in the 0.2 eV region is composed of detachment contributions from both the D_1 and D_0 states, while C_1 accounts for the offset of the exponential at long time (t = 5 ps). The fit shows that $C_1 \approx C_0$, indicating that the excited state population has *almost* fully decayed by 5 ps. The resultant fit is shown in Figure 4.10b (solid blue line) and reproduces the experimental data very well, particularly the deviation from exponential decay observed over the first few picoseconds. However, a correlated beat in the ground state is not observed, which we suggest is because of the significantly lower signal levels measured for this feature as evidenced in Figures 4.8a and 4.8b.

The extracted lifetime for the excited state decay is τ = 650 ± 70 fs, which correlates exceptionally well with the ground state recovery (640 ± 50 fs) and verifies that the excited state population is directly transferred to the ground state through IC. This highlights the utility of measuring the excited and ground state dynamics simultaneously in time-resolved photoelectron spectroscopy. Immediately following IC, the portion of the excited state population transferred back to D_0 state is vibrationally highly excited. In order to generate photoelectrons contributing to the high kinetic energy feature (2.0 eV), $TCNQ^-$ must absorb two probe photons, the first of which must be resonant with the D_2 state. One may expect there to be differences in the potential energy surfaces of the D_0 and D_2 states and hence, there to be a less favourable Franck-Condon overlap between these two states when the D_0 state is vibrationally highly excited. Although, the photoelectron spectrum at 3.1 eV (Figure 4.4a) indicates

that the geometries of $TCNQ^-$ in its D_0 and D_2 states are in fact quite similar, small differences in the potential energy surfaces provide an explanation for why the ground state feature does not appear to recover to its initial population. As internal vibrational relaxation (IVR) occurs and energy is redistributed throughout the available vibrational modes of the molecule, the Franck-Condon overlap between the D_0 and D_2 states becomes more favourable again. As a result, a slow recovery of the ground state signal at longer times (>5 ps) may be expected.

4.4.3 Excited State Wave Packet Dynamics

The fit to equation (4.2) also provides insight into the nuclear dynamics of the wave packet on the D_1 state. The wave packet motion may be isolated from the average decay by subtracting the exponential fit component in equation (4.2) from both the experimental (open circles) and fit data (solid blue line) in Figure 4.10b. The resultant wave packet dynamics are shown in Figure 4.12, where the open circles and red line correspond to the experimental and fit data, respectively. Positive signal indicates that there is more population in the excited state relative to the population of the D_1 state if it was decaying purely exponentially. Conversely, negative signal correlates to a depletion of population relative to the exponential decay. In addition to the relative

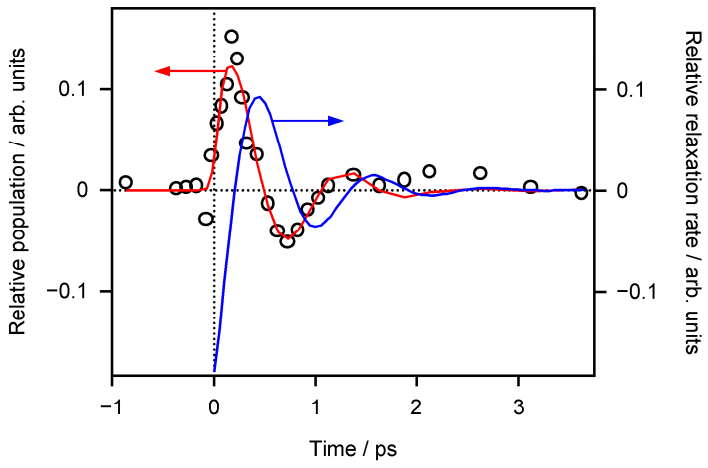

Figure 4.12: Isolated oscillatory component of the D_1 excited state population dynamics relative to the average exponential population decay. The experimental and fit oscillations have been obtained from Figure 4.10b by subtracting the exponential component of equation (4.2) from both the experimental and fit data, respectively. Open circles represent experimental data and the solid red line (left axis) the corresponding fit. Also shown is the relaxation rate relative to the average relaxation rate (exponential decay only) of the D_1 excited state population back to the D_0 ground state (solid blue line, right axis).

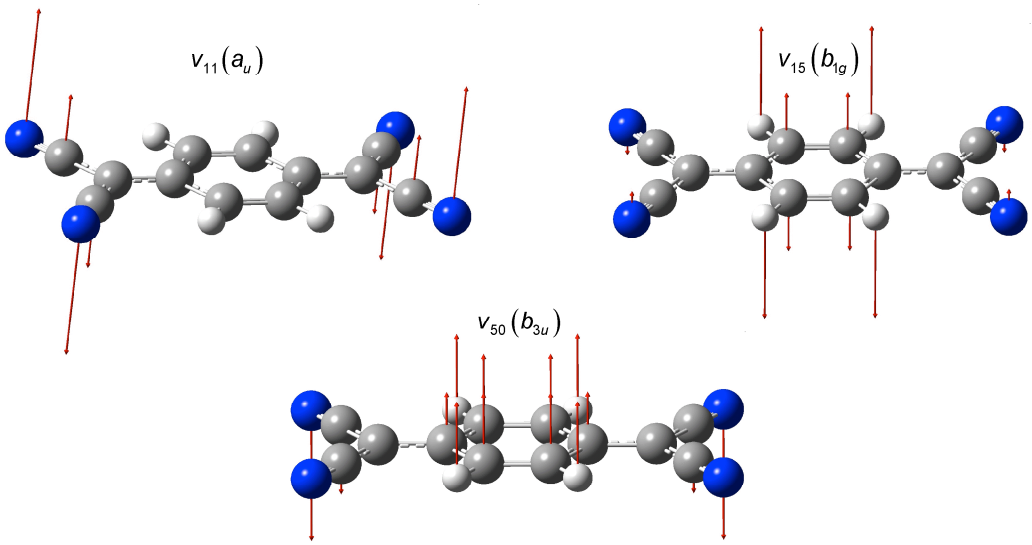

Figure 4.13: Candidate vibrational modes for the observed coherent oscillation on the D_1 excited state of $TCNQ^-$. The vibrational modes presented here correspond to vibrations of the anion ground state. Density functional theory calculations have been performed using the B3LYP functional and a 6-31G* basis set (B3LYP/6-31G*) with the Gaussian ′03 package.

populations, we may also gain insight into the decay rate relative to the average rate. This is shown by the blue line in Figure 4.12, which corresponds to the negative gradient of the oscillatory cosine component in equation (4.2), where we have omitted the convolution with the Gaussian instrument function for visual clarity. Positive signal corresponds to an enhanced rate and negative signal to a reduced decay rate, relative to the average rate of $(1/650)$ fs^{-1}.

The dynamics are occurring on a multi-dimensional potential energy surface. The period of the oscillation is 1.1 ps, corresponding to an average vibrational energy spacing, $\Delta\bar{\nu}$, of ~30 cm^{-1}. In principle, it is possible to assign the oscillation frequency to specific vibrational modes of $TCNQ^-$ in the D_1 state. $TCNQ^-$ is a non-linear polyatomic species with 20 atoms and 54 unique modes of vibration. Based on their calculated frequencies [22], we have identified three feasible modes that may be responsible for the observed coherent motion, shown in Figure 4.13.[3] The first is a torsional mode (ν_{11}) with an associated a_u symmetry and a frequency of 38 cm^{-1}. The

[3] Density functional theory calculations have been performed using the Gaussian ′03 package. Geometry optimisations and harmonic vibrational frequency calculations were performed using B3LYP/6-31G* for the ground state only. Although the absolute energy of the modes will change in the D_1 excited state, relative to the D_0 state, the mode assignments (ν_n) and symmetries displayed in Figure 4.13 will remain the same.

two remaining modes are the v_{15} torsional mode (b_{1g}) and the v_{50} out-of-plane bending mode (b_{3u}), which have calculated frequencies of 30 cm^{-1} and 43 cm^{-1}, respectively. The excellent correlation between the observed beat frequency and the calculated frequency for the v_{15} mode make it the most notable candidate for the observed coherent oscillation. However, the v_{11} and v_{50} modes can not be ruled out, due to the accuracy of semi-empirical frequency calculations, which is commonly to within ~10 % of experimentally observed frequencies [22].

Based on the frequency bandwidth of the ultrashort pump pulse (~500 cm^{-1}), we may expect that a superposition purely consisting of the v_{15} mode will contain up to ~15 individual vibrational states. However, in practice the wave packet will be made of many more individual states as a result of contributions from additional modes, giving rise to an observed $\Delta\bar{\nu}$ of 30 cm^{-1}. To confirm whether the wave packet is primarily defined by a single mode (v_{15}) a number of approaches may be considered. (1) Firstly, calculations can be performed to ascertain the Franck-Condon excitation factors for vibrational modes of the D_1 excited state, when excited from the D_0 ground state. The modes with weak excitation strengths from these calculations may then be discounted. (2) The energy of the pump pulse may be tuned to a higher or lower energy by more than its associated 500 cm^{-1} bandwidth. If the wave packet possesses contributions from multiple vibrational modes, then one may expect to observe a distinct change in any observed beat dynamics (or absence thereof). Conversely, if the coherent motion is predominantly due to overtones of a single mode, then qualitatively similar dynamics should be observed, where $\Delta\bar{\nu}$ will become red shifted at shorter pump wavelengths due to anharmonicity, and *vice versa* at lower pump energies. Taking all of the above into consideration, we therefore only *tentatively* assign the observed coherent motion in the D_1 excited state to a vibrational superposition predominantly composed of overtones of the v_{15} torsional mode.

A schematic representation of the wave packet dynamics is presented in Figure 4.14. The initial phase of the wave packet dynamics, ϕ, provides some information about the relative geometry of $TCNQ^-$ at; (1) the point where it undergoes IC and (2) the ground state geometry in which the D_1 state is initially prepared. A phase of $\phi = -1.1$ radians is extracted from the fit to equation (4.2). In terms of the relative rate of relaxation, this corresponds to a reduced rate when the wave packet is formed, as shown

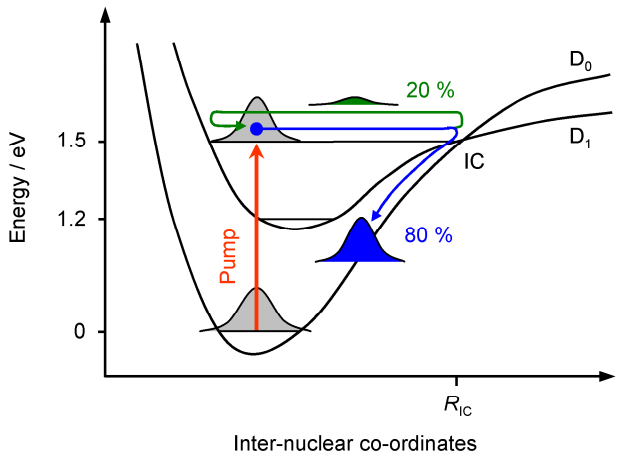

Figure 4.14: Schematic potential energy curves of the D_1 excited and D_0 ground states of $TCNQ^-$ showing the evolution of the excited state wave packet (green and blue arrows) following excitation at 1.5 eV (vertical red arrow). R_{IC} is the geometry at which internal conversion (IC) can occur.

by Figure 4.12, indicating that the Franck-Condon excitation region occurs at a geometry which differs from that required for IC to take place. However, the relative rate is also increasing (positive gradient) at t = 0, indicating that the Franck-Condon region is not precisely at the inner turning point. It also shows that the wave packet is initially moving towards the IC geometry (R_{IC}) on the D_1 state.

The relative relaxation rate reaches a maximum at ~430 fs, at which time the IC rate between the D_1 and D_0 states is maximised. A comparison of the relative populations at t = 150 fs and t = 1.3 ps suggests that approximately 80 % of the wave packet is transferred back to the D_0 ground state when the wave packet samples the IC geometry for the first time (blue wave packet in Figure 4.14), leaving only ~20 % in the D_1 excited state (green wave packet). This may indicate that the coupling between the D_1 and D_0 states is particularly strong, however, this is not definitive as it also depends on the momentum initially imparted to the wave packet on the D_1 excited state [31]. The remainder of the wave packet on the D_1 state then propagates away from R_{IC} and back towards the inner turning point, as indicated by the reduction in the relative rate of relaxation in Figure 4.12. The wave packet reaches the inner turning point at ~980 fs, before returning to R_{IC} at ~1.5 ps. After this time, the overall fit becomes poor. This could be due to more complicated dynamics occurring on the D_1 excited state or because of the much reduced signal levels as most of the D_1 population has decayed. Regardless, the coherent oscillation is mostly damped out after one period, indicating

that most of the population is transferred back to the D_0 state as the wave packet reaches the IC geometry for the first time.

It is worth noting that similar wave packet dynamics have been observed in time-resolved fluorescence up-conversion studies conducted on related tetracyanoethylene (TCNE) based CT complexes in the condensed phase [32,33]. In these studies the neutral CT complex is excited to the charge-separated state (donor$^+$-TCNE$^-$) and the subsequent relaxation dynamics are monitored. A single vibrational frequency is observed which is independent of the donor molecule used in the CT complexes. This observation led to the conclusion that an intramolecular mode in the TCNE species alone drives the relaxation dynamics of the complex. Clearly, the isolated dynamics of acceptor molecules in CT complexes is important, and it would be of interest if similar dynamics could be observed in the relaxation of TCNQ containing CT complexes.

4.4.4 Consideration of Negative Time Dynamics

For completeness, we also consider the reverse dynamics, which may be observed in these time-resolved experiments by changing the labels on pump and probe. In this case, we might expect to observe dynamics following excitation at 3.1 eV and probing at 1.5 eV, which should reflect the dynamics of the excited D_2 state. Recalling that the D_2 state is of mixed core and outer excited character, when probed at 1.5 eV, the outer excited $\pi^2 2\pi^{*1}$ configuration would correlate to the S_0 neutral state, leading to photoelectrons in the 1.8 eV range when $t < 0$. Additionally, we may expect to see depletion in the 0.2 eV region. However, we observe no such dynamics. If the core excited $\pi^1 1\pi^{*2}$ character of the D_2 state were probed, detachment would produce neutral TCNQ in the T_1 state yielding photoelectrons around 0.2 eV. We note that this character is likely to be long lived as it does not correlate with the S_0 ground state of the neutral and hence cannot readily autodetach. Alternatively, one may expect IC to the D_1 or D_0 states, however, we have observed no obvious dynamics in the reverse direction.

4.5 Summary and Conclusions

In summary, we have measured the photoelectron spectrum of TCNQ$^-$ at 3.1 eV, which corroborates the prediction that the D_2 state has mixed electronic character, provides

some insight into the relative potential energy surfaces of the excited states of the anion and neutral, and provides a measure of the optically forbidden $T_1 \leftarrow S_0$ transition energy of the neutral. Additionally, time-resolved photoelectron spectra show that the D_1 excited state undergoes IC back to the D_0 ground state with a lifetime of 650 fs. This is however an average value and a detailed analysis of the dynamics show that coherent nuclear motion can be observed on the excited state with a ~30 cm^{-1} frequency. At 430 fs, the wave packet reaches the geometry at which $TCNQ^-$ in the D_1 state internally converts to the D_0 state with an ~80 % efficiency.

The experiments described in the chapter also highlight the importance of considering multiple electronic configurations to individual states. The case of $TCNQ^-$ shows that by carefully deconstructing the different configurations to electronic states, it is possible to elegantly untangle and assign these different electronic contributions to observed photoelectron features with the aid of Koopmans' correlations. This method of analysing photoelectron spectra can provide information regarding the relative detachment cross-sections for individual electronic components of a state, and emphasises photoelectron spectroscopy as a powerful experimental technique for extracting detailed molecular level information, when results are approached with careful consideration. However, failure to take it account possible multiple state configurations can not only give rise to a misleading assignment of photoelectron features, but also an erroneous interpretation of any dynamics that may be occurring within these states in ultrafast TRPES experiments.

TCNQ and its derivatives remain a very active research area, and the results presented here provide a fundamental understanding of the electronic structure and energy flow in this important CT acceptor. Such detailed knowledge of the molecular building blocks on which a vast number of materials are based is a prerequisite to the design, development and understanding of materials with tailor-made properties, such as organic metals, non-linear optics and liquid crystal devices.

4.6 References

[1] L. R. Melby, W. Mahler, W. E. Mochel, R. J. Harder, W. R. Hertler, and R. E. Benson, *J. Am. Chem. Soc.*, **84**, 3374 (1962).

[2] W. J. Siemons, P. E. Biersted, and R. G. Kepler, *J. Chem. Phys.*, **39**, 3523 (1963).

[3] G. L. Closs and J. R. Miller, *Science*, **240**, 440 (1988).

[4] D. Jerome, *Chem. Rev.*, **104**, 5565 (2004).

[5] J. Ferraris, V. Walatka, D. O. Cowan, and J. H. Perlstein, *J. Am. Chem. Soc.*, **95**, 948 (1973).

[6] J. B. Torrance, *Acc. Chem. Res.*, **12**, 79 (1979).

[7] R. C. Wheland and J. L. Gillson, *J. Am. Chem. Soc.*, **98**, 3916 (1976).

[8] J. L. Segura and N. Martin, *Angew. Chem. Int. Ed.*, **40**, 1372 (2001).

[9] D. F. Perepichka, M. R. Bryce, C. Pearson, M. C. Petty, E. J. L. McInnes, and J. P. Zhao, *Angew. Chem. Int. Ed.*, **42**, 4636 (2003).

[10] H. Okamoto, K. Ikegami, T. Wakabayashi, Y. Ishige, J. Togo, H. Kishida, and H. Matsuzaki, *Phys. Rev. Lett.*, **96**, 037405 (2006).

[11] K. Ikegami, K. Ono, J. Togo, T. Wakabayashi, Y. Ishige, H. Matsuzaki, H. Kishida, and H. Okamoto, *Phys. Rev. B*, **76**, 085106 (2007).

[12] J. M. Cole, R. C. B. Copley, G. J. McIntyre, J. A. K. Howard, M. Szablewski, and G. H. Cross, *Phys. Rev. B*, **65**, 125107 (2002).

[13] L. O. Palsson *et al.*, *Mol. Cryst. Liq. Cryst.*, **402**, 279 (2003).

[14] D. Bloor *et al.*, *J. Mater. Chem.*, **11**, 3053 (2001).

[15] C. E. Klots, R. N. Compton, and V. F. Raaen, *J. Chem. Phys.*, **60**, 1177 (1974).

[16] R. N. Compton and C. D. Cooper, *J. Chem. Phys.*, **66**, 4325 (1977).

[17] E. A. Brinkman, E. Gunther, and J. I. Brauman, *J. Chem. Phys.*, **95**, 6185 (1991).

[18] E. A. Brinkman, E. Gunther, O. Schafer, and J. I. Brauman, *J. Chem. Phys.*, **100**, 1840 (1994).

[19] I. Haller and F. B. Kaufman, *J. Am. Chem. Soc.*, **98**, 1464 (1976).

[20] I. Zanon and C. Pecile, *J. Phys. Chem.*, **87**, 3657 (1983).

[21] V. G. Zakrzewski, O. Dolgounitcheva, and J. V. Ortiz, *J. Chem. Phys.*, **105**, 5872 (1996).

[22] P. Skurski and M. Gutowski, *J. Mol. Struct. (THEOCHEM)*, **531**, 339 (2000).

[23] M. Sobczyk, P. Skurski, and J. Simons, *J. Phys. Chem. A*, **107**, 7084 (2003).

[24] B. Milian, R. Pou-Amerigo, R. Viruela, and E. Orti, *Chem. Phys. Lett.*, **391**, 148

(2004).

[25] M. Makowski and M. T. Pawlikowski, *Chem. Phys. Lett.*, **388**, 367 (2004).

[26] M. Makowski and M. T. Pawlikowski, *Int. J. Quantum Chem.*, **106**, 1736 (2006).

[27] K. L. Reid, *Annu. Rev. Phys. Chem.*, **54**, 397 (2003).

[28] V. Blanchet, M. Z. Zgierski, T. Seideman, and A. Stolow, *Nature*, **401**, 52 (1999).

[29] A. Stolow, A. E. Bragg, and D. M. Neumark, *Chem. Rev.*, **104**, 1719 (2004).

[30] D. L. Jeanmaire and R. P. Vanduyne, *J. Am. Chem. Soc.*, **98**, 4029 (1976).

[31] C. Wittig, *J. Phys. Chem. B*, **109**, 8428 (2005).

[32] I. V. Rubtsov and K. Yoshihara, *J. Phys. Chem. A*, **101**, 6138 (1997).

[33] I. V. Rubtsov and K. Yoshihara, *J. Phys. Chem. A*, **103**, 10202 (1999).

Chapter 5: Observation of Ultrafast Dynamics through Time-resolved Photoelectron Angular Distributions

Time-resolved photoelectron imaging of the 7,7,8,8-tetracyanoquinodimethane (TCNQ) radical anion is presented. Photoelectron angular distributions (PADs) are qualitatively analysed in terms of the simple s-p model which is based on symmetry arguments. The internal conversion dynamics from the first excited state (1^2B_{3u}) to the ground state ($^2B_{2g}$) may be observed through temporal changes in the PADs of the spectrally overlapping photoelectron features, arising from photodetachment of the ground state and the excited state. A formulism for extracting the population dynamics from the β_2 anisotropy parameter of overlapping spectroscopic features is presented. This is used to extract the lifetime of the first excited state which is in good agreement with that observed in the time-resolved photoelectron spectra.

5.1 Using Photoelectron Angular Distributions to Study Ultrafast Dynamics

5.1.1 Isoenergetic Photoelectron Features

Arguably the most successful application of time-resolved photoelectron spectroscopy (TRPES) has been in the study of anions [1,2]. As the energy required to remove an electron is generally lower than for neutrals (or cations), both the ground and excited states may be monitored simultaneously [3,4], and is exemplified by the experiments conducted on the 7,7,8,8-tetracyanoquinodimethane (TCNQ) radical anion in Chapter 4. Consequently, population decay may be tracked from the initially prepared excited state to the final state *via* any intermediate states. There is currently an ongoing effort in using laser sources based on high harmonic generation to perform similar experiments in neutrals [5,6]. Despite the advantages of performing TRPES on anions, the method does require that Koopmans' correlations are favourable [7]. As both the ground and

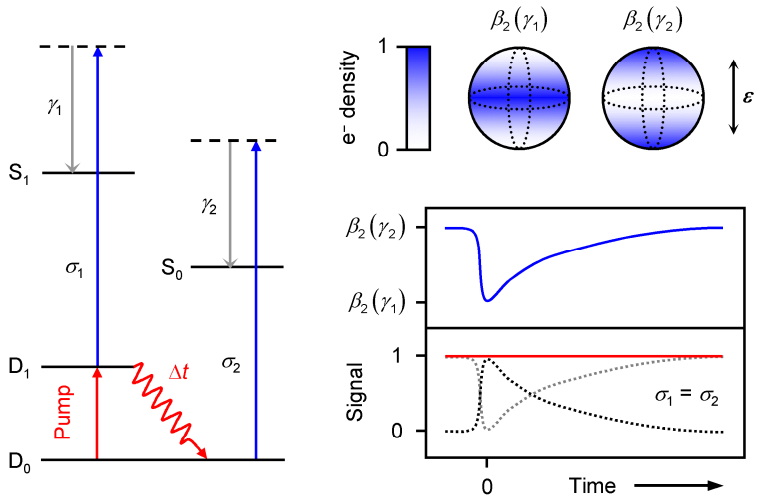

Figure 5.1: Example of a temporally evolving anion system, following excitation with a laser pump pulse (red arrow), which gives rises to two isoenergetic photoelectron features, γ_1 and γ_2 (grey arrows), after photodetachment (blue arrows), with associated detachment cross-sections σ_1 and σ_2, respectively. D_0 and D_1 are the doublet ground and excited states of the anion, respectively, and S_0 and S_1 are the singlet ground and excited states of the neutral. Shown inset are the photoelectron anisotropies associated with the two detachment features, $\beta_2(\gamma_1)$ and $\beta_2(\gamma_2)$ ($\boldsymbol{\varepsilon}$ is the laser polarisation vector). The temporal evolution of the measured anisotropy (upper panel, solid blue line) and the observed signal for the isoenergetic features (bottom panel, solid red line) are shown when $\sigma_1 = \sigma_2$. The evolution of the D_0 and D_1 state populations are also shown on the bottom panel (grey and black dotted lines, respectively).

excited state photoelectron features are varying with time, there is a requirement that these can be spectrally resolved. However, as shown in Chapter 4 accidental isoenergetic photoelectron features may arise. As an example, depicted in Figure 5.1, this may occur when: the anion excited state (D_1) correlates with an excited state in the neutral (S_1); the anion ground state (D_0) correlates with the neutral ground state (S_0); and the energy separation between the ground and excited states in the anion and neutral are similar, $E(D_1 \leftarrow D_0) \approx E(S_1 \leftarrow S_0)$. In this case, the internal conversion (IC) from the D_1 state to the D_0 state would lead to isoenergetic photoelectron features γ_1 and γ_2. Spectrally overlapping features present a particular problem in larger molecular systems for which photoelectron peaks are typically very broad, such as those observed in the TRPES of benzene following excitation to the S_1 state [8,9]. In the worst case, if the two features are isoenergetic and their respective electron detachment cross-sections are similar $(\sigma_1 = \sigma_2)$, then the relaxation dynamics cannot be observed through the photoelectron signal. As TRPES effectively measures state populations, when the excited state decays (black dotted line in Figure 5.1) and the ground state concomitantly recovers (grey dotted line), the total observed photoelectron signal will not change (solid red line) and hence, additional information is required to extract the timescales of the dynamics.

5.1.2 Time Dependent Photoelectron Angular Distributions

Time-resolved photoelectron imaging (TRPEI) yields photoelectron velocity spectra [10,11]. These provide not only the electron kinetic energy (*eKE*) but also angular information concerning the ejection angle of the electron relative to the photoionisation field polarisation, $\boldsymbol{\varepsilon}$. For atoms and small molecular systems it is relatively trivial to use the resultant photoelectron angular distributions (PADs) to extract information about the orbitals from which the electrons are removed [10-12]. As the ground and excited state orbitals in TRPEI experiments typically differ, it may be anticipated that the respective PADs of the isoenergetic features also differ, as depicted by $\beta(\gamma_1)$ and $\beta(\gamma_2)$ in Figure 5.1. In such a case, the relaxation dynamics may in principle be monitored using the time dependant changes in photoelectron anisotropy (blue line, Figure 5.1) as population is transferred from one electronic state to another.

In recent years the temporal evolution of PADs obtained from TRPEI

experiments, in collusion with complementary theoretical studies [12], have elegantly begun to be used as a tool for gleaming additional insights into ultrafast molecular processes. For example, TRPEI has been successfully applied to the study of rotational dynamics of molecules such as pyrazine [13] and C_2^- [14], which reveals that PADs are particularly sensitive to molecular alignment. More recently, TRPEI has been used to gain insight into the adiabatic dissociation dynamics of pre-aligned CS_2 molecules, providing molecular frame (MF) dynamics in which the temporally evolving PADs show the changing electronic character of the molecule as it evolves on the excited state [15]. Such experiments aptly demonstrate the use of the additional information provided by PADs. Furthermore, full three dimensional (3D) alignment of polyatomic molecules has been demonstrated [16], suggesting that there is scope for extending such methodologies to large polyatomic molecules. However, as molecular systems become larger, the contributions to the partial photoelectron waves that constitute the PADs rapidly increase in complexity and it is generally only practical to predict qualitative PADs, using methods such as the *s-p* model which is founded on symmetry arguments [10,11]; we discuss this methodology in greater detail in Section 5.3.2. Here, we show that subtle changes in the time-resolved PADs may be used to extract relaxation lifetimes for large molecular systems.

In Section 5.3 we present time-resolved PADs of near isoenergetic features obtained from pump-probe experiments on the TCNQ radical anion, which are interpreted using the *s-p* model, developed by Sanov and co-workers [10,11]. For the first time, a formulism for extracting population dynamics from time-evolving PADs is presented Section 5.3.4, and we utilise this to extract a lifetime for the first doublet excited state of the TCNQ radical, from the observed near isoenergetic feature.

5.2 Experiment Details

The experiment details used to perform TRPEI on $TCNQ^-$ have previously been described in Section 4.2 of Chapter 4.

PADs are obtained directly from the polar onion-peeling routine described in Chapter 3, in which they are extracted from fits to an angular distribution functionality, which may be described as [17]

$$\frac{d\sigma}{d\Omega} = \frac{\sigma}{4\pi}\sum_n \beta_n P_n(\cos\theta), \tag{5.1}$$

where σ is the total photodetachment cross-section, $P_n(\cos\theta)$ are n^{th} order Legendre polynomials, β_n are the anisotropy parameters and the factor 4π accounts for normalisation over the solid angle, Ω. For a one-photon process, only even terms up to $n = 2$ need to be considered, while for a two-photon transition, the additional alignment induced by the first photon requires even terms up to $n = 4$. β_2 values range from +2 to –1, which correlates to photoelectron emission that is predominantly parallel $(\|)$ or perpendicular $(\perp)$ to the laser polarisation axis, $\boldsymbol{\varepsilon}$, respectively.

5.3 Photoelectron Angular Distributions of the TCNQ Radical Anion

5.3.1 Interpretation of the Photoelectron Angular Distributions

TRPEI has been performed on the TCNQ radical anion (structure shown inset in Figure 5.2) by utilising pump and probe photon energies of 1.5 eV (800 nm) and 3.1 eV (400 nm), respectively. A schematic energy level diagram of the anionic and neutral states of TCNQ together with the pump-probe scheme is shown in Figure 5.2. D_0, D_1 and D_2 are the anion doublet ground state, $^2B_{2g}$, and excited states, 1^2B_{3u} and 2^2B_{3u}, respectively. S_0 and T_1 are the ground, ^1A_g, and first excited, $^3B_{1u}$, states of the neutral. Also shown inset in Figure 5.2 is the energy ordering of the valence molecular orbitals (MOs) of TCNQ with their respective orbital symmetries shown in parentheses. The 1.5 eV pump excites $TCNQ^-$ from the D_0 ground state to the first excited D_1 state, by promoting a core electron from the π $(3b_{3u})$ orbital into the $1\pi^*$ $(3b_{2g})$ orbital. The probe pulse at 3.1 eV subsequently detaches an electron from either the excited or ground anion states.

Figure 5.3a shows deconvoluted photoelectron images acquired over 1.75×10^5 laser shots at 500 Hz and obtained at two different pump-probe delays: $t = -1$ ps and $t = 0$ ps. The corresponding photoelectron spectra are shown in Figure 5.3b. When the probe pulse arrives before the pump pulse ($t = -1$ ps), the recorded photoelectron image shows two distinct features: an intense sharp feature at small radii and a broader feature at larger radii. Both of these processes exhibit anisotropy with photoelectrons detached

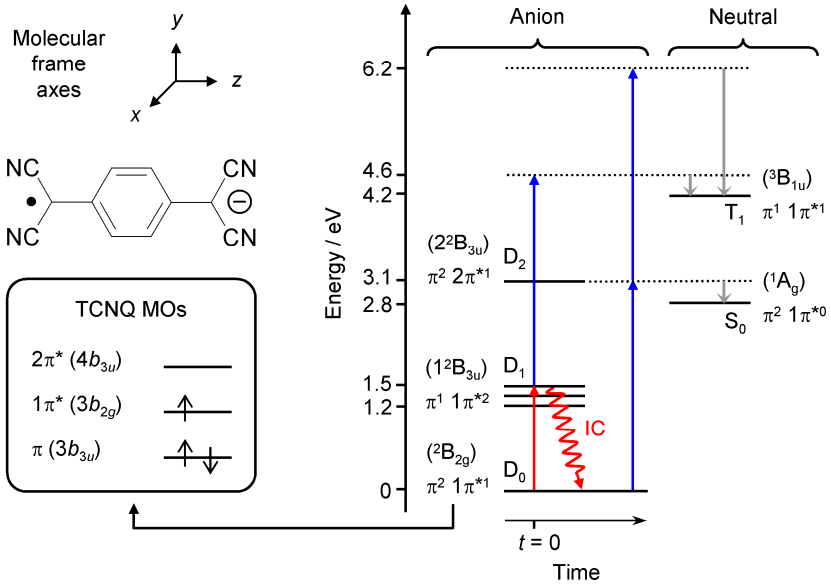

Figure 5.2: Energy level diagram for the 7,7,8,8-tetracyanoquinodimethane (TCNQ) radical anion (molecular structure shown inset) showing the temporal evolution of the D_1 excited state *via* internal conversion (IC) back to the D_0 ground state, following excitation at 1.5 eV (pump = red arrow, probe = blue arrow, electron kinetic energies = grey arrows). D_0, D_1, and D_2 correspond to the doublet states of the anion and S_0 and T_1 are the ground and first excited states of the neutral. Corresponding term symbols are show in parentheses with the state electron configurations below. Also presented inset are the valence molecular orbitals (MOs) of TCNQ with the D_0 state configuration shown (orbital symmetries are given in parentheses). The molecular frame (MF) Cartesian axes assigned to $TCNQ^-$ are shown above its molecular structure.

predominantly perpendicular to the laser polarisation axis, $\boldsymbol{\varepsilon}$ ($\beta_2 < 0$). The low energy feature corresponds to the peak at 0.2 eV in the photoelectron spectrum and arises when the 3.1 eV probe photon, which is resonant with the $D_2 \leftarrow D_0$ transition, excites $TCNQ^-$ to the higher lying D_2 state. As the excited D_2 state is unbound with respect to the neutral ground state, the electron promptly undergoes autodetachment to form neutral TCNQ in the correlated S_0 ground state. The second feature, corresponding to the broad peak at ~2.0 eV in the photoelectron spectrum, arises from a resonance enhanced two-photon detachment process from the D_0 ground state, *via* the D_2 state. Although the D_2 state has a dominant $\pi^2 2\pi^{*1}$ electron configuration, which correlates to the neutral S_0 state following electron detachment from the $2\pi^*$ $(4b_{3u})$ orbital, we have confirmed in Chapter 4 that this state possesses a significant contribution from the $\pi^1 1\pi^{*2}$ configuration. Detachment of an electron from the $1\pi^*$ orbital of the $\pi^1 1\pi^{*2}$ configuration of the D_2 state correlates to the T_1 state of the neutral, and it is this detachment process which gives rise to the photoelectron feature observed at 2.0 eV.

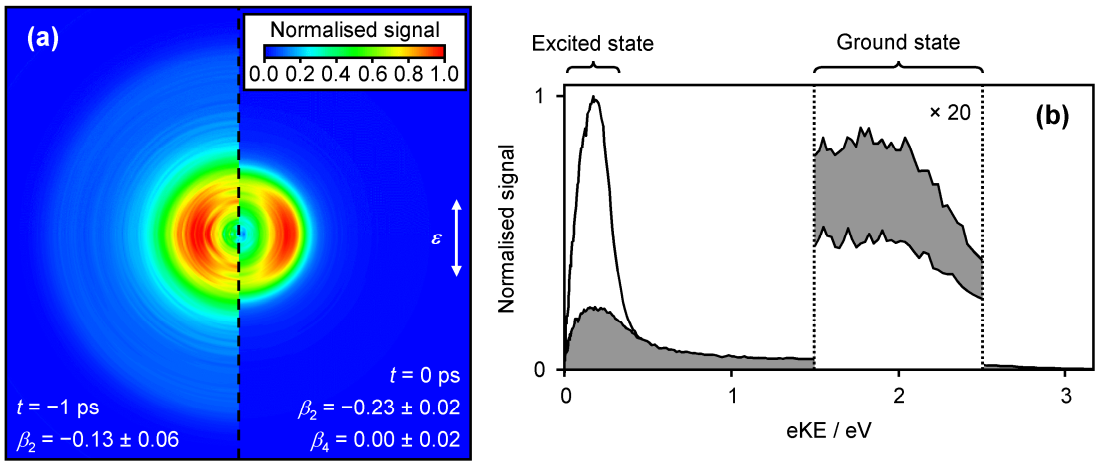

Figure 5.3: (a) Deconvoluted photoelectron images obtained from the time-resolved experiments performed on $TCNQ^-$, using pump and probe energies of 1.5 eV (800 nm) and 3.1 eV (400 nm), respectively. The left half corresponds to an image recorded at t = –1 ps and the right half to an image recorded at t = 0 ps (laser polarisation direction, $\boldsymbol{\varepsilon}$, is shown by the white arrow). Both raw images were acquired over 1.75 × 10^5 laser shots at 500 Hz. Also shown are the measured anisotropy parameters, β_n, for the low energy feature (0.2 eV) in both images. (b) Corresponding photoelectron spectra obtained from the images at t = –1 ps (grey) and t = 0 ps (white).

When the pump and probe are temporally overlapped (t = 0 ps) the pump pulse excites $TCNQ^-$ into the D_1 state, concomitantly depleting population in the D_0 ground state. The recorded photoelectron image shows a large increase in signal around 0.2 eV and depletion in the high energy 2.0 eV feature. The signal reduction in the latter peak is more clearly observed in the associated photoelectron spectra shown in Figure 5.3b and this feature is a direct measure of the D_0 state population. The increase in signal around 0.2 eV results from a new detachment process, which in Chapter 4 we assigned to the detachment of an electron from the 1π* orbital in the D_1 excited state. This process generates neutral TCNQ in its electronically correlated T_1 state. However, at this energy, there is also a feature arising from the D_0 ground state which is expected to decrease in intensity as some population has been transferred from the ground state into the excited state. These two features are spectrally overlapping and therefore *nearly* isoenergetic.

The isoenergetic nature of the two features arises from the fact that the $D_1 \leftarrow D_0$ transition is similar in energy to the $T_1 \leftarrow S_0$ energy separation, $E(D_1 \leftarrow D_0) \approx E(T_1 \leftarrow S_0)$ = 1.4 eV. In the case of $TCNQ^-$, these two features have very different detachment cross-sections. The cross-section for detachment from the D_1 excited state,

σ^e, is much greater than the detachment cross-section from the D_0 ground state, σ^g. As a result, changes in signal at 0.2 eV predominantly reflect excited state dynamics, hence the excited state label on the photoelectron spectra in Figure 5.3b, and we recall that an internal conversion (IC) lifetime of $\tau = 650$ fs has been measured in Chapter 4. This is a rather fortunate case and if the excited state and ground state detachment processes were to have similar detachment cross-sections, $\sigma^g \approx \sigma^e$, the time-resolved photoelectron spectra would not show temporal changes and the additional information concerning the PADs may be used to monitor the dynamics.

Comparison of the images obtained at $t = -1$ ps and $t = 0$ ps indicates that the PADs around the isoenergetic features at 0.2 eV change due to the change in relative contributions from the two detachment processes. Before $t = 0$, the detachment involves only a single photon and the anisotropy may be quantified by β_2 only. The average anisotropy parameter over the spectral range from 0.15 eV to 0.25 eV is $\beta_2 = -0.13 \pm 0.06$. At $t = 0$, the excited state feature involves two photons and requires the additional β_4 term to describe the PAD. Measured anisotropy parameters for the isoenergetic feature at $t = 0$ are $\beta_2 = -0.23 \pm 0.02$ and $\beta_4 = 0.00 \pm 0.02$.

5.3.2 Symmetry Analysis: The s-p Model

A distinct advantage of photoelectron imaging is that it provides direct access to PADs, which can be analysed to yield information about the symmetries of the orbitals from which the electrons are removed [18]. Although for large molecular systems, such as TCNQ, it is generally difficult to extract quantitatively meaningful information, Sanov and co-workers have demonstrated an elegant qualitative method to gain insight into the detachment process from anions for relatively slow photoelectrons [11]. At low kinetic energies, the Wigner threshold law (see equation (2.24) in Chapter 2) dictates that the outgoing photoelectron wave is dominated by low angular momentum (l) partial waves, specifically, *s*- and *p*-waves ($l = 0$ and 1, respectively) [19]. The so-called *s-p* model considers which symmetry components of these partial waves, $\Gamma(e^-)$, contribute to the total photoelectron wave, given the symmetry of the orbital from which the electron is detached, $\Gamma(\psi)$, and the *molecular frame* (MF) components of the transition dipole moment, $\Gamma(\mu_i)$, where i represents the Cartesian co-ordinate (see Figure 5.2 for a definition of the MF Cartesian axes):

$$\Gamma(\psi) \otimes \Gamma(\mu_i) \otimes \Gamma(\mathrm{e}^-) \supseteq \Gamma_{\mathrm{TS}}, \tag{5.2}$$

where Γ_{TS} is the totally symmetric irreducible representation of the point group the system belongs to. For the symmetry product in equation (5.2) to contain Γ_{TS}, the symmetry of the outgoing wave must be equal to $\Gamma(\psi) \otimes \Gamma(\mu_i)$:

$$\Gamma(\mathrm{e}^-) \equiv \Gamma(\psi) \otimes \Gamma(\mu_i). \tag{5.3}$$

As an example, we consider the detachment of an electron from a b_{2g} symmetry orbital in $TCNQ^-$, which belongs to the D_{2h} point group $(\Gamma_{\mathrm{TS}} = a_g)$. From the D_{2h} character table (provided in Appendix D) the transition dipole moment components have symmetries of $\Gamma(\mu_x) = b_{3u}$, $\Gamma(\mu_y) = b_{2u}$, and $\Gamma(\mu_z) = b_{1u}$. Based on equation (5.3), the *x*, *y*, and *z* Cartesian components of μ_i will therefore give rise to partial photoelectron waves with symmetries of $\Gamma(\mathrm{e}^-) = b_{1u}$, a_u, and b_{3u} in the MF, respectively. Inspection of the D_{2h} point group table subsequently shows that b_{1u} and b_{3u} symmetries correlate to p_z and p_x waves, respectively, while a symmetry of a_u corresponds to a photoelectron wave with an orbital angular momentum of $l > 2$. Table 5.1 presents an overview of the allowed photoelectron symmetry contributions in the MF upon detachment from the valence MOs of $TCNQ^-$ (see Figure 5.2).

Table 5.1: Predicted outgoing photoelectron wave symmetries, $\Gamma(\mathrm{e}^-)$, for detachment from the valence molecular orbitals (MOs) of $TCNQ^-$. The symmetry components of the transition dipole moment, $\Gamma(\mu_i)$, are shown on the left and $\Gamma(\mathrm{e}^-)$, displayed in the columns labelled MF, are determined using equation (5.3). The expected distributions in the lab frame (LF) relative to the laser polarisation vector, $\boldsymbol{\varepsilon}$ (defined as the LF *z*-axis), are provided in the columns labelled LF, where $\perp$ and $\bigcirc$ denote perpendicular and isotropic distributions, respectively.

D_{2h}	$\Gamma(\psi) = b_{2g}$		$\Gamma(\psi) = b_{3u}$	
	MF	LF	MF	LF
$\Gamma(\mu_x) = b_{3u}$	$b_{1u} \equiv p_z$	$\perp$	$a_g \equiv s$	$\bigcirc$
$\Gamma(\mu_y) = b_{2u}$	$a_u \equiv l \geq 2$	-	$b_{1g} \equiv l \geq 2$	-
$\Gamma(\mu_z) = b_{1u}$	$b_{3u} \equiv p_x$	$\perp$	$b_{1g} \equiv l \geq 2$	-

However, the observed PAD is measured in the *lab frame* (LF) and it is hypothetically possible for any of the components associated with detachment along individual μ_i in the MF to contribute to the measured PAD. Each individual μ_i component makes its largest contribution when it is aligned parallel to the laser polarisation vector, $\boldsymbol{\varepsilon}$, which is defined as the *z*-axis in the LF. We now consider how an outgoing photoelectron wave in the MF translates to an expected angular distribution relative to $\boldsymbol{\varepsilon}$ in the LF. To do this, we consider electron detachment from a b_{2g} orbital when μ_x is aligned parallel to $\boldsymbol{\varepsilon}$. With reference to Table 5.1, this process gives rise to p_z electron waves. As the outgoing waves are polarised along a different MF Cartesian axis to μ_x, we therefore qualitatively predict a perpendicular PAD $(\beta_2 < 0)$. Conversely, for a parallel distribution $(\beta_2 > 0)$ to arise the outgoing photoelectron wave must be polarised along the same MF axis as μ_i: $\Gamma(\mu_i) = \Gamma(\mathrm{e}^-)$. This is only possible when $\Gamma(\psi) = \Gamma_{\mathrm{TS}}$. The LF columns in Table 5.1 show the predicted LF PADs for detachment from the valence MOs of $TCNQ^-$, based on the associated MF photoelectron waves and μ_i components. We now go on to compare these *s*-*p* model PAD predictions with the experimentally observed PADs of $TCNQ^-$.

In the photoelectron image at $t = 0$, the PAD of the 0.2 eV feature is quantified by $\beta_2 = -0.23$, indicating that the photoelectron waves are predominantly emitted perpendicular to the laser polarisation axis, defined as the *z*-axis in the lab frame (LF). This feature is dominated by detachment from the D_1 state to the T_1 state of the neutral. However, the D_1 state is prepared by excitation from the D_0 state. The allowed components of the transition dipole moment, μ_i, in the excitation step, are defined by the symmetries of the singly occupied MOs of the D_0 and D_1 states. Specifically, $b_{3u} \otimes \Gamma(\mu_i) \otimes b_{2g}$ must contain the totally symmetric irreducible representation of the D_{2h} point group (a_g) that $TCNQ^-$ belongs to. This is only true for the *z*-component of the transition dipole moment $(\Gamma(\mu_z) = b_{1u})$. Hence, $TCNQ^-$ molecules that are excited in the D_1 state have their MF *z*-axis preferentially aligned parallel to the LF *z*-axis (polarisation axis). Within the *s*-*p* model, detachment from $1\pi^*$ (b_{2g}) orbital of the D_1 state, while the $\boldsymbol{\varepsilon}$ is preferentially aligned parallel to μ_z, is expected to yield photoelectron waves perpendicular to the LF *z*-axis. This is shown in Table 5.1 and yields a negative anisotropy, in qualitative agreement with Figure 5.3a.

In the photoelectron spectrum at $t = -1$ ps, the feature at 0.2 eV is generated by

one-photon detachment from the D_0 state to the S_0 ground state of the neutral. The detachment is either direct or occurs *via* the D_2 state, which promptly autodetaches to the electronically correlated S_0 state. For direct photodetachment, the *s-p* model predicts photoelectron waves with a negative anisotropy (see Table 5.1). However, the narrow feature at 3.1 eV (400 nm) in the gas phase photodetachment spectrum (see Figure 4.2 in Chapter 4) [20], suggests that autodetachment from the D_2 state is the dominant process. In this case, the transition dipole moment from D_0 to D_2, $\Gamma(\mu_z) = b_{1u}$, preferentially aligns the MF *z*-axis of the excited $TCNQ^-$ along the LF *z*-direction. As the autodetachment is fast (<100 fs),[1] one might expect to see anisotropy from this as the rotational period of $TCNQ^-$ is long ($\overline{T}_R \approx 4.1$ ns [21]).[2] Specifically, the overall symmetry of the initial state must be maintained in the final state (neutral and electron). Given the D_2 state symmetry is b_{3u} and the neutral S_0 state, a_g, the symmetry of the outgoing wave is expected to be b_{3u}, which requires that it is ejected perpendicular to the LF *z*-axis, as is observed in Figure 5.3a. However, the above analysis is of course an oversimplification because of a lack of detailed knowledge concerning the electron-neutral scattering dynamics and given that the direct detachment process may also interfere.

For the broad feature at 2.0 eV, which corresponds to detachment from the D_2 state to the T_1 state of the neutral, we extract anisotropy parameters $\beta_2 = 0.09 \pm 0.08$ and $\beta_4 = 0.00 \pm 0.07$. A similar analysis using the *s-p* model for this transition leads to an expected negative anisotropy, in contradiction to what is observed. This discrepancy highlights the main limitation of the model, in that it is only valid in the limit of low electron kinetic energies where the low-*l* partial waves have relatively high cross-sections [11,19].

---

[1] In Section 4.4.4 of Chapter 4 we discuss the dynamics of the D_2 state when pumped and probed at 3.1 eV and 1.5 eV, respectively. However, we observe no obvious dynamics associated with the outer excited $\pi^2 2\pi^{*1}$ character of the D_2 state within the temporal resolution of these time-resolved experiments (~100 fs), lending support to the hypothesis that autodetachment from the D_2 state to the S_0 neutral state is fast (<100 fs).

[2] The rotational constants for $TCNQ^-$ molecular rotation around all molecular frame Cartesian axes have been determined using the optimised geometry parameters calculated by Skurski and Gutowski [21]. Rotational constants are calculated using $\tilde{B} = \left(h/8\pi^2 c I_j\right)$, where h is Planck's constant (6.626×10^{-34} J s), c is the speed of light (2.99×10^8 m s^{-1}), and I_j is the moment of inertia (in kg m^2) about the relevant axis, *j*, in the MF. The molecular rotational period, T_R, is defined by $T_R = 1/\tilde{B}$, where $\tilde{B}$ is in Hz. Complete rotational constant calculations are presented in Appendix E.

5.3.3 Time-resolved Anisotropy Parameters of Isoenergetic Features

In Figure 5.4 the temporal evolution of the anisotropy parameters for the photoelectron features around 0.2 eV are shown. Figure 5.4a shows the time dependence of the β_2 parameter, which clearly indicates a change in the anisotropy when the D_1 excited state is populated at $t = 0$. The recovery of the β_2 parameter towards its value before $t = 0$ is indicative of a loss of population in the excited state through IC back to the D_0 ground state. Figure 5.4b indicates that the higher order β_4 parameter is approximately zero and displays no obvious time dependence. In both Figures 5.4a and 5.4b, the error bars represent a single standard deviation. The time variation of the β_2 anisotropy parameter, shown in Figure 5.4a for the isoenergetic features, suggests that it may be possible to extract the relaxation lifetime, τ, from the PADs alone.

5.3.4 Extracting Lifetimes from Temporally Evolving Angular Distributions

In Figure 5.4, the most prominent variation is observed in the temporal evolution of β_2, while β_4 is approximately zero and exhibits no significant time dependence. The β_4 parameter describes the alignment induced by the pump pulse and its evolution predominantly reflects the rotational dynamics of the system [14]. For $TCNQ^-$, the rotational motion is much longer than that of the electronic relaxation dynamics and so in the analysis that follows we assume that contributions from β_4 are negligible.

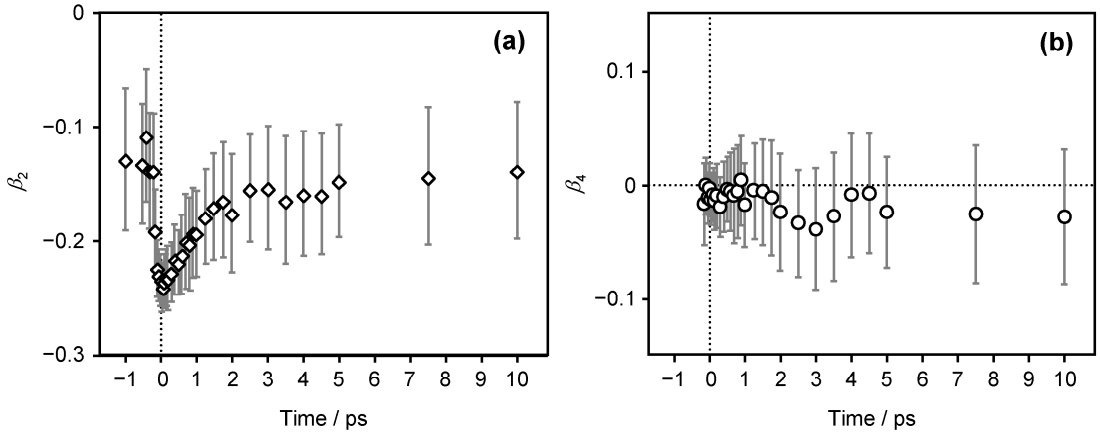

Figure 5.4: Temporal evolution of the measured β_2 (a) and β_4 (b) anisotropy parameters for the 0.2 eV photoelectron feature (see Figure 5.3). Error bars are shown in grey and correspond to a single standard deviation.

It is convenient to define the anisotropy parameter in terms of the components of the cross-section parallel, $\sigma_{\parallel}$, and perpendicular, $\sigma_{\perp}$, to the laser polarisation axis:

$$\begin{aligned}\sigma_{\parallel} &= \frac{\sigma}{4\pi}\left[\beta_2 + 1\right] \\ \sigma_{\perp} &= \frac{\sigma}{4\pi}\left[1 - \left(\beta_2/2\right)\right]\end{aligned} . \tag{5.4}$$

The expressions in equation (5.4) are obtained from equation (5.1) with the parallel $(\parallel)$ and perpendicular $(\perp)$ components corresponding to $\theta = 0$ and $\theta = \pi/2$, respectively. Using this definition in equation (5.4), we may express β_2 in terms of the ratio $R = \sigma_{\parallel} / \sigma_{\perp}$:

$$\beta_2 = \frac{R-1}{1+\left(R/2\right)} . \tag{5.5}$$

In order to extract β_2 from an image, the above definition is valid, although it is more accurate to fit the entire angular distribution using equation (5.1) as is done in the polar onion-peeling routine described in Chapter 3. However, by defining β_2 in terms of relative cross-sections, the effect of multiple contributions to the total observed signal may be considered in a more straightforward manner. For $TCNQ^-$, there are two features that are (near) isoenergetic. One originates from the photodetachment of the D_0 ground state and has an associated cross-section, σ^{g}, while the other from the photodetachment of the D_1 excited state with an associated cross-section, σ^{e}, as described in Section 5.3.1. The observed signal, S^k, from each of these processes can then be expressed in terms of their respective cross-sections:

$$\begin{aligned}S^{g} &\propto \sigma^{g} P^{g} \\ S^{e} &\propto \sigma^{e} P^{e}\end{aligned} , \tag{5.6}$$

where P^k represents the fractional population in state *k*. As the excited state is a transient with lifetime τ, we may introduce the first order time dependence associated with its decay and the concomitant recovery in the ground state:

$$\begin{aligned} S^{\mathrm{g}}(t) &\propto \sigma^{\mathrm{g}}\left[1-\alpha\cdot\exp\left(-t/\tau\right)\right] \\ S^{\mathrm{e}}(t) &\propto \sigma^{\mathrm{e}}\left[\alpha\cdot\exp\left(-t/\tau\right)\right] \end{aligned}, \tag{5.7}$$

where α is the fraction of molecules initially transferred to the excited state from the ground state by the pump pulse. The total signal, $S(t)$, is then simply the sum of the two components:

$$S(t) = S^{\mathrm{g}}(t) + S^{\mathrm{e}}(t). \tag{5.8}$$

When $\sigma^{\mathrm{e}} = \sigma^{\mathrm{g}}$, $S(t)$ becomes time independent and the dynamics cannot be observed *via* the signal in the photoelectron spectra alone. From equation (5.4), we may rewrite the observed signal in terms of the signal observed parallel and perpendicular to the laser polarisation axis:

$$\begin{aligned} S_{\parallel}(t) &= S_{\parallel}^{\mathrm{g}}(t) + S_{\parallel}^{\mathrm{e}}(t) = \frac{1}{4\pi}\left[S^{\mathrm{g}}(t)\left(\beta_2^{\mathrm{g}}+1\right) + S^{\mathrm{e}}(t)\left(\beta_2^{\mathrm{e}}+1\right)\right] \\ S_{\perp}(t) &= S_{\perp}^{\mathrm{g}}(t) + S_{\perp}^{\mathrm{e}}(t) = \frac{1}{4\pi}\left[S^{\mathrm{g}}(t)\left(1-\beta_2^{\mathrm{g}}/2\right) + S^{\mathrm{e}}(t)\left(1-\beta_2^{\mathrm{e}}/2\right)\right] \end{aligned}, \tag{5.9}$$

where β_2^k is the anisotropy associated with the photodetachment from state *k*. Substituting the relevant $S^k(t)$ from equation (5.7) into equation (5.9), the following expressions may be obtained:

$$\begin{aligned} S_{\parallel}(t) &\propto \alpha\left[\eta\beta_2^{\mathrm{e}} + \eta - \beta_2^{\mathrm{g}} - 1\right]\exp\left(-t/\tau\right) + \left[\beta_2^{\mathrm{g}}+1\right] \\ S_{\perp}(t) &\propto \alpha\left[\eta - \eta\left(\beta_2^{\mathrm{e}}/2\right) + \left(\beta_2^{\mathrm{g}}/2\right) - 1\right]\exp\left(-t/\tau\right) + \left[1-\left(\beta_2^{\mathrm{g}}/2\right)\right] \end{aligned}, \tag{5.10}$$

where $\eta = \sigma^{\mathrm{e}} / \sigma^{\mathrm{g}}$. For the specific case of $\sigma^{\mathrm{e}} = \sigma^{\mathrm{g}}$, equation (5.10) reduces to

$$\begin{aligned} S_{\parallel}(t) &\propto \alpha\left[\beta_2^{\mathrm{e}} - \beta_2^{\mathrm{g}}\right]\exp\left(-t/\tau\right) + \left[\beta_2^{\mathrm{g}}+1\right] \\ S_{\perp}(t) &\propto \frac{\alpha}{2}\left[\beta_2^{\mathrm{g}} - \beta_2^{\mathrm{e}}\right]\exp\left(-t/\tau\right) + \left[1-\left(\beta_2^{\mathrm{g}}/2\right)\right] \end{aligned}. \tag{5.11}$$

Analogous to equation (5.5), we may now define $\beta_2(t)$ as

$$\beta_2(t) = \frac{R(t)-1}{1+\left(R(t)/2\right)}, \tag{5.12}$$

with the ratio $R(t) = S_{\parallel}(t)/S_{\perp}(t)$.

The expression in equation (5.12) describes the temporal evolution of the β_2 anisotropy parameter for two isoenergetic photoelectron features arising from the photodetachment of an excited and ground state in a two-level system, when photodetachment is a one-photon process. It contains four unknown parameters: α, η, β_2^{e}, and τ. The ground state anisotropy, β_2^{g}, can be independently obtained as it corresponds to the measured value of β_2 when $t < 0$. In the limiting case when $\sigma^{e} = \sigma^{g}$, only three parameters are unknown because $\eta = 1$. It should also be noted that the parameter α may be extracted from pump power-dependence studies such that there would only be two remaining unknowns.

5.3.5 Temporal Anisotropy Fits: 1^2B_{3u} Excited State Lifetime of $TCNQ^-$

In the case of $TCNQ^-$ and the time dependent anisotropy presented in Figure 5.4a, the higher energy feature around 2.0 eV may be used to obtain information about the parameters α and $\eta = \sigma^{e}/\sigma^{g}$. This feature originates from two-photon detachment of the D_0 ground state. With reference to photoelectron spectra in Figure 5.3b, the parameter α, which is the fractional population transferred from the D_0 state to the D_1 state, is equal to the ratio of the integrated signal (taken between 1.7 eV and 2.3 eV) of the 2.0 eV feature at $t = 0$, to the integrated signal of this feature before $t = 0$. This ratio yields a value of $\alpha = 0.5$.

The parameter $\eta = \sigma^{e}/\sigma^{g}$ can also be determined using a similar methodology in which the photoelectron signal of the isoenergetic features at 0.2 eV is considered. Because the probe pulse for both components of this feature is the same, η is equivalent to the ratio of integrated intensities of the excited to ground state signals at $t = 0$:

$$\eta = \sigma^{e}/\sigma^{g} = S^{e}(t=0)/S^{g}(t=0). \tag{5.13}$$

With reference to Figure 5.3b, $S^{g}(t=0)$ is obtained from the integrated area (from 0.15 eV to 0.25 eV) of the 0.2 eV feature before $t = 0$, scaled by the fractional population ($\alpha = 0.5$) that is transferred to the D_1 state following excitation. $S^{e}(t=0)$ is then the integrated signal of the 0.2 eV feature at $t = 0$ with $S^{g}(t=0)$ subtracted from it. Their

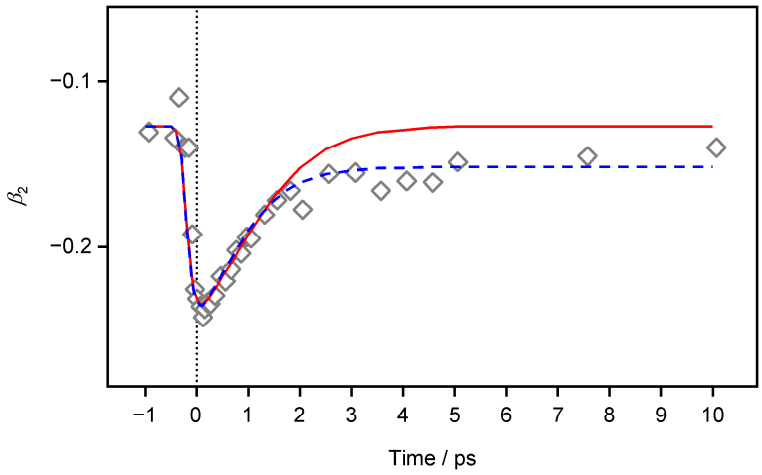

Figure 5.5: Results of the weighted least squares fitting procedure to the experimental β_2 data (Figure 5.4a) obtained from the isoenergetic features at 0.2 eV (grey diamonds). The red line shows the result of the fit to equation (5.12). The dashed blue line shows the resultant fit when an offset between the final anisotropy ($t \gg 0$) and the original ground state anisotropy is introduced ($t < 0$) into equation (5.7).

ratio yields an estimate for the relative cross-sections of $\eta = 7.4$. This value is in line with the observation that $\sigma^{e} > \sigma^{g}$ for $TCNQ^{-}$.

By extracting the parameters α, η, and β_2^{g} from the experimentally obtained time-resolved photoelectron spectra, the number of free parameters in equation (5.12) have been reduced to the excited state anisotropy, β_2^{e}, and the desired D_1 excited state lifetime, τ. As the excited state lifetime is short and the observed dynamics may be influenced by the temporal resolution of the laser pulses (~100 fs), a convolution with Gaussian instrument response functions has been included in equation (5.7) (see Appendix C). The data in Figure 5.4a is fitted to equation (5.12) using a weighted least squares fitting procedure, the result of which is shown as a solid red line in Figure 5.5. From this fit, an excited D_1 state lifetime of $\tau = 750 \pm 100$ fs is extracted, which is in reasonable agreement with the lifetime obtained from the temporally evolving signal in the time-resolved photoelectron spectra in Chapter 4 ($\tau = 650 \pm 50$ fs).

The overall fit is good, but becomes poorer at longer times ($t > 2$ ps). The data (see Figure 5.4a) suggest that the anisotropy does not recover completely to the ground state value of $\beta_2 = -0.13$. Given the experimental uncertainty, this offset may not necessarily be real. However, there is some evidence from the photoelectron signal at longer times that it may be real. Specifically, in Chapter 4 we show that the dominant relaxation pathway of the excited state is through IC, but at longer delays, there is

evidence that a small fraction of the population remains in the excited state, evidenced by the fact that the 0.2 eV feature does not completely recover to the expected $t < 0$ signal level (see Section 4.4.2). Such an offset may be included in the data analysis by assuming that not all the D_1 excited state population has decayed in equation (5.7). Fitting the data with this modification yields the dashed blue line in Figure 5.5, which accurately represents the observed anisotropy over the timescale monitored in this experiment. A value of $\tau = 600 \pm 100$ fs is extracted from this modified fit which is within the experimental errors of the lifetime extracted from the time-resolved photoelectron signal fits in Chapter 4. In reality, this small fraction of D_1 state population is also decaying, but on a different timescale. Although this could be included in the analysis, it would introduce additional parameters causing the fit to become ambiguous. An alternative explanation for the long time offset in anisotropy may be that the ground state is vibrationally highly excited following IC. As PADs are sensitive to the ro-vibrational state from which the electron was removed [22], the ground state anisotropy after IC is not necessarily the same as that observed before excitation.

5.3.6 Discussion and Limitations

Despite the unknowns described in Section 5.3.5 and the relatively large uncertainty in the measured anisotropy data (see error bars in Figure 5.4a), the main result from this study is that the lifetime extracted from a fit to the model provides strong support that population dynamics may be monitored through changes in photoelectron anisotropy. The error bars on the data represent a single standard deviation and highlight the difficulty in obtaining high quality anisotropy parameters. This is a serious drawback of TRPEI as in general it requires large amounts of data to produce high quality anisotropy measurements. On the other hand, signal stability is not an issue as this will only affect the relative error in obtaining an anisotropy parameter rather than the actual value. This is particularly emphasised by the results in Figure 5.4a, where we still observe dynamics for only a small change of $\Delta\beta_2 \approx 0.1$, even though this is comparable to the size of the error bars at $t < 0$ and $t \gg 0$. It should also be noted that $TCNQ^-$ is a particularly favourable case in which certain fit parameters could be determined experimentally, thus reducing the number of free parameters required for the fitting procedure and

ultimately making it more manageable. A least squares fitting procedure in which all parameters are allowed to vary is very sensitive to their initial values.

In addition to the excited state lifetime, the fit to equation (5.12) also provides a measure for the D_1 excited state anisotropy, which is determined to be $\beta_2^e = -0.26$ for both fits presented in Figure 5.5. This value is slightly lower than the measured anisotropy at $t = 0$ of the 0.2 eV feature ($\beta_2 = -0.23$), highlighting the remaining contribution of the D_0 ground state to this feature. In systems where the difference in anisotropies for the ground and excited states is more significant, the measured anisotropy may be very different from the actual anisotropy of the excited state.

The temporal evolution of the photoelectron anisotropy defined by equation (5.12) provides a reasonable qualitative and quantitative description of the dynamics. However, it does rely on a number of approximations. (1) As the photoelectrons emitted are isoenergetic, the two photoelectron waves will interfere with each other. This interference may manifest itself as a modulation on the energy spectrum [23] or may alter the observed PADs [18]. The latter will depend on the relative phases and amplitudes of outgoing partial waves formed. In the case of $TCNQ^-$, the amplitude of the excited state photoelectron wave is much larger than that of the ground state ($\sigma^e > \sigma^g$), such that this dominates. However, in a scenario where $\sigma^e \approx \sigma^g$, the observed anisotropy does not necessarily provide information about the excited state anisotropy as the two photoelectron waves can interfere. (2) There are no vibrational dynamics that lead to an energy shift in the photoelectron spectrum with time, or lead to changes in the symmetry of the orbital from which detachment occurs as the wave packet evolves. The latter is exemplified by the adiabatic dissociation dynamics of CS_2 [15]. If there are changes in photoelectron kinetic energy, the anisotropy may be modulated by the wave packet dynamics. In $TCNQ^-$, we have provided evidence for wave packet dynamics on the D_1 excited state in Chapter 4, however, the photoelectron energy shift associated with this coherent motion was very small (~10 meV, see Figure 4.11). (3) Only two states are involved in the relaxation and there is no internal vibrational relaxation (IVR) on the excited state. If any intermediate states are involved, the model presented would need to take into account the kinetics of the intermediate state, whether it contributed to the observed anisotropy or not. In the case of IVR on the excited state, this could change the photoelectron anisotropy of the excited state as this

is sensitive to ro-vibrational states [22]. Similarly, it is assumed that the ground state anisotropy is the same even though it will be highly vibrationally excited following IC. In principle, this may be accounted for and may be used to provide further insight into the dynamics of IVR in the ground state.

5.4 Summary and Conclusions

The dynamics of the TCNQ radical anion have been studied using time-resolved photoelectron imaging. The photoelectron images of $TCNQ^-$ reveal that the photodetachment for the ground D_0 state and the excited D_1 state exhibit a negative anisotropy, which is explained using the *s-p* model developed by Sanov and co-workers. To date, the *s-p* model has primarily been applied to small molecular anions (e.g. CS_2^-), and the symmetry analysis presented here emphasises that this model may be readily expanded to interpret PADs of more complex molecular anions, provided the system exhibits some degree of symmetry.

As the photoelectron features from the ground and excited states occur at nearly the same energy, the consequences of isoenergetic photoelectron features in time-resolved photoelectron spectroscopy are considered. In $TCNQ^-$, the ground and excited state features exhibit different anisotropy parameters and the relaxation dynamics may be observed from the temporally evolving anisotropy parameter of this isoenergetic feature. A simple model based on the relative population dynamics parallel and perpendicular to the laser polarisation axis is presented. The model allows the time dependent anisotropy to be calculated and is used to fit to the experimentally observed dynamics. The fit yields good quantitative agreement with the dynamics extracted from the time-resolved photoelectron spectra in Chapter 4 and indicates that, despite the relatively simplistic nature of the model, temporally evolving anisotropy parameters can provide detailed insights into the population dynamics of complex molecular systems.

5.5 References

[1] A. Stolow, A. E. Bragg, and D. M. Neumark, *Chem. Rev.*, **104**, 1719 (2004).

[2] J. R. R. Verlet, *Chem. Soc. Rev.*, **37**, 505 (2008).

[3] A. E. Bragg, J. R. R. Verlet, A. Kammrath, O. Cheshnovsky, and D. M. Neumark, *Science*, **306**, 669 (2004).

[4] A. E. Bragg, J. R. R. Verlet, A. Kammrath, O. Cheshnovsky, and D. M. Neumark, *J. Am. Chem. Soc.*, **127**, 15283 (2005).

[5] L. Nugent-Glandorf, M. Scheer, D. A. Samuels, A. M. Mulhisen, E. R. Grant, X. M. Yang, V. M. Bierbaum, and S. R. Leone, *Phys. Rev. Lett.*, **87**, 193002 (2001).

[6] L. Nugent-Glandorf, M. Scheer, D. A. Samuels, V. M. Bierbaum, and S. R. Leone, *J. Chem. Phys.*, **117**, 6108 (2002).

[7] V. Blanchet, M. Z. Zgierski, T. Seideman, and A. Stolow, *Nature*, **401**, 52 (1999).

[8] G. A. Worth, R. E. Carley, and H. H. Fielding, *Chem. Phys.*, **338**, 220 (2007).

[9] D. S. N. Parker, R. S. Minns, T. J. Penfold, G. A. Worth, and H. H. Fielding, *Chem. Phys. Lett.*, **469**, 43 (2009).

[10] A. Sanov and R. Mabbs, *Int. Rev. Phys. Chem.*, **27**, 53 (2008).

[11] R. Mabbs, E. R. Grumbling, K. Pichugin, and A. Sanov, *Chem. Soc. Rev.*, **38**, 2169 (2009).

[12] T. Seideman, *Annu. Rev. Phys. Chem.*, **53**, 41 (2002).

[13] M. Tsubouchi, B. J. Whitaker, L. Wang, H. Kohguchi, and T. Suzuki, *Phys. Rev. Lett.*, **86**, 4500 (2001).

[14] A. E. Bragg, R. Wester, A. V. Davis, A. Kammrath, and D. M. Neumark, *Chem. Phys. Lett.*, **376**, 767 (2003).

[15] C. Z. Bisgaard, O. J. Clarkin, G. R. Wu, A. M. D. Lee, O. Gessner, C. C. Hayden, and A. Stolow, *Science*, **323**, 1464 (2009).

[16] J. J. Larsen, K. Hald, N. Bjerre, H. Stapelfeldt, and T. Seideman, *Phys. Rev. Lett.*, **85**, 2470 (2000).

[17] R. N. Zare, *Angular Momentum: Understanding Spatial Aspects in Chemistry and Physics*. (Wiley, New York, 1988).

[18] J. Cooper and R. N. Zare, *J. Chem. Phys.*, **48**, 942 (1968).

[19] E. P. Wigner, *Phys. Rev.*, **73**, 1002 (1948).

[20] E. A. Brinkman, E. Gunther, O. Schafer, and J. I. Brauman, *J. Chem. Phys.*, **100**, 1840 (1994).

[21] P. Skurski and M. Gutowski, *J. Mol. Struct. (THEOCHEM)*, **531**, 339 (2000).

[22] P. Hockett, M. Staniforth, K. L. Reid, and D. Townsend, *Phys. Rev. Lett.*, **102**, 253002 (2009).

[23] M. Wollenhaupt *et al.*, *Phys. Rev. Lett.*, **89**, 173001 (2002).

Chapter 6: Concluding Remarks

The development and performance of the newly commissioned photoelectron imaging spectrometer is discussed. We subsequently propose a number of improvements to the spectrometer, in the form of a new ion trap and the development of more efficient laser baffles. We then move on to describe very recent work investigating the ultrafast dynamics of derivatives of the TCNQ radical anion. We also propose a research outlook for studying the solvation dynamics of a variety of multiply charged molecular anions. Finally, we conclude this thesis with brief closing remarks.

6.1 Overview of Main Results

In this thesis we have reported the development, construction, and commissioning of a new photoelectron imaging spectrometer for studying the spectroscopy and ultrafast dynamics of molecular anions. Importantly, this new instrument innovatively incorporates a soft electrospray ionisation source which has the capability of generating a vast class of large molecular anions, both as micro-solvated and isolated species.

One of the major issues of coupling electrospray ionisation sources and photoelectron imaging arrangements, is that electrospray must be performed at atmospheric pressure while the latter must be carried out under ultra-high vacuum conditions, commonly leading to a cumulative loss of ion current at successive differential pinholes. To alleviate this problem we have incorporated a compact ion guide/trap into the second differential region of the spectrometer. This device enables anions to be radially confined and accumulated in a trap at its terminus, before being injected into a Wiley-McLaren time-of-flight (TOF) spectrometer at a 1 kHz repetition rate, which is synchronous with the femtosecond laser system. When calibrated using the TOF spectrum of iodide, we have calculated that an individual ion packet contains approximately 200 ions at the detection region, which compares well with the predicted storage capacity of the ion trap, based on the trap volume (determined from Simion simulations) and space-charge limitations. The measured number of ions is approximately an order of magnitude smaller than previous experimental observations of ~10^3 anions per packet at 1 kHz [1]. Hence, at present the number of anions (per packet) which are able to reach the photoelectron imaging arrangement is restricted by the small dimensions on the trap.

The novel compact photoelectron imaging arrangement incorporated into the detection region of the spectrometer, described in Chapter 2, allows one to perform photoelectron imaging on anions without introducing the need for costly high voltage pulsers. Calibration of the arrangement *via* the well-known photoelectron images/spectra of iodide at 400 nm and 266 nm, reveals that the resolution ($\Delta E/E = 7.5\ \%$), although not as good as many other imaging arrangements, is acceptable for performing photoelectron imaging with broadband femtosecond laser

pulses. However, the imaging arrangement currently suffers from poor signal-to-noise levels when using ultra-violet (UV) laser pulses ($\leq$266 nm), due to stray laser photons producing undesired photoelectrons from the imaging electrodes. This is unfortunately due to the inefficiency of the laser baffles currently implemented in the detection region of the spectrometer.

The experiments performed on the 7,7,8,8-tetracyanoquinodimethane (TCNQ) radical anion, described in Chapters 4 and 5, are the first ultrafast time-resolved photoelectron imaging (TRPEI) experiments to be performed on anions generated through electrospray ionisation. Specifically in Chapter 4, we mapped the ultrafast dynamics of the first excited doublet state, 1^2B_{3u}, of $TCNQ^-$, in addition to recording and analysing its one-colour photoelectron spectrum at 400 nm (3.1 eV). We observed that: (1) following excitation at 800 nm (1.5 eV), the population transferred from the $^2B_{2g}$ anion ground state into the 1^2B_{3u} state, internal converts back to the ground state of the anion on a timescale of 650 fs; and (2) at this excitation energy, the 1^2B_{3u} state exhibits a coherent nuclear motion with an associated frequency of 30 cm^{-1}, which we tentatively assigned to a predominant superposition of overtones of the v_{15} $\left(b_{1g}\right)$ torsional mode.

In Chapter 5 we investigated how one may extract ultrafast dynamical information from the temporally-evolving photoelectron angular distributions (PADs), and specifically investigated the consequences of spectrally convoluted, but temporally evolving, photoelectron features (isoenergetic signals), which may commonly arise when probing large molecular species with photoelectron spectroscopy. Importantly, we showed that timescales for ultrafast dynamics may be extracted from isoenergetic features, using the PADs of isoenergetic features from $TCNQ^-$ as an example framework. The lifetime of the 1^2B_{3u} state extracted from the model correlates very well with the 650 fs lifetime extracted from the temporally evolving photoelectron signal. This demonstrates that there is certainly scope from expanding this methodology to other molecular systems exhibiting isoenergetic features with temporally evolving PADs, which we discuss in Section 6.3.2.

6.2 Spectrometer Improvements

6.2.1 Development of a New Ion Trap

One of the primary restrictions to performing time-resolved photoelectron imaging with the new spectrometer is the small number of ions which may be stored in the current ion trap, as a result of its small size (~0.2 mm^3). In Chapter 2 (see page 78) we calculated that for one-photon and time-resolved experiments, conservative estimates of ~10 and ~0.1 electrons per shot, respectively, may be expected for an ion packet containing 10^3 ions. We also recall from Colburn *et al*. [1] that it should indeed be possible to accumulate at least 10^3 ions per trap cycle at a rate of 1 kHz, provided the spatial dimensions of the trap are large enough. At present the trap capacity is limited to ~10^2 ions, hence, to attain the aforementioned signal levels we propose to replace the ion guide and trap with a newly developed radio frequency (RF) ion trap, which possesses a significantly larger trap volume.

The design, simulation, and construction of the new ion trap are currently underway. This trap is based on the principles of a cylindrical RF Paul Trap [2], and simulations performed using Simion 8.0 indicate that the trap may accommodate approximately ~10^5 ions, based on a simulated trap size of 500 mm^3 and a space-charge limit of 10^3 charges per mm^3 [3,4]. Additionally, these simulations also suggest that it may be operated in a mass selective mode by tuning the frequency and amplitude of the RF voltage, enabling the species of interest to primarily be accumulated in the trap volume. Simulations of injecting anions from the trap into the collinear Wiley-McLaren TOF spectrometer also show that ~50 % of the ions accumulated within the trap are successfully collimated into the TOF optics and through the spectrometer to the detection region.

Based on these early Simion simulations, the construction and implementation of this new ion trap should prove vital to optimising the photoelectron signal levels we can achieve when performing TRPEI experiments with the new spectrometer.

6.2.2 Development of New Laser Baffles

To improve the signal-to-noise levels when recording photoelectron images at 266 nm,

a new set of laser baffles are currently under construction. The conical baffles themselves are made from electro-formed copper. This electro-formed design will ensure that the edge of the aperture at the centre of the baffles will be produced to a 'knife-edge' finish, and will help to reduce any additional undesired light scattering. The new copper conical baffles will be spaced apart using tubular copper spacers, which will be oxidised according the method described by Richharia [5]. The copper oxide surface produced *via* this methodology is known to exhibit an exceptionally low net reflectance at 266 nm and below (<0.05) as a result of its porous structure [5], helping to reduce any scattered laser light from reaching the interaction region of the imaging arrangement. Similar baffles designs have been shown to be effective at improving the signal-to-noise in photoelectron images recorded with UV laser pulses [6].

The primary cause of the poor signal-to-noise levels is due to the work function of the μ-metal imaging electrodes ($\leq$4.5 eV) being less than the stray 4.66 eV laser photons. Hence, in addition to new laser baffles, consideration is also being given to coating the imaging electrodes with a high work function metal. An ideal metal for coating imaging electrodes is Gold, which has a work function of 5.1 eV (242 nm) [7] and gold sputtering sources are readily available. This approach should significantly reduce the number of undesired photoelectrons produced when stray UV laser photons collide with the imaging electrodes.

6.3 Research Outlook

6.3.1 Derivatives of the TCNQ Radical Anion

As an extension to the work on the TCNQ radical anion, presented in Chapter 4 of this thesis, we propose to investigate derivatives of TCNQ which are also pertinent to the field of charge transfer chemistry and organic metals. Initially, we aim to explore the electronic structure and dynamics of TCNQ's fluorinated derivative, 2,3,5,6-tetrafluoro-7,7,8,8-tetracyanoquinodimethane (F_4-TCNQ), the structure of which is shown inset in Figure 6.1a. Much like its parent molecule, there has only been a sparse amount of fundamental research conducted into understanding the electronic structure and spectroscopy of the isolated F_4-TCNQ radical anion, from both an experimental and

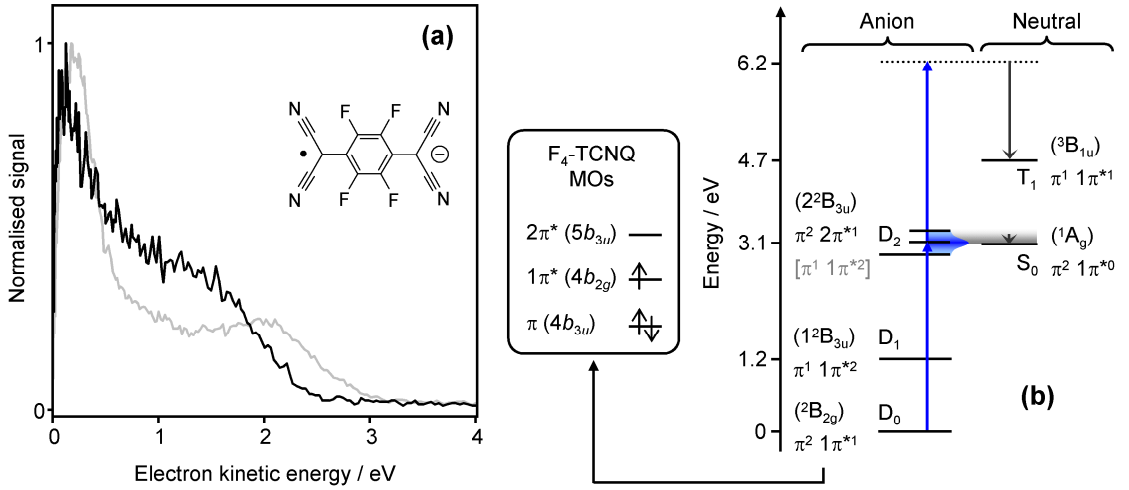

Figure 6.1: (a) Photoelectron spectrum of the 2,3,5,6-tetrafluoro-7,7,8,8-tetracyanoquinodimethane (F_4-TCNQ) radical anion at 3.1 eV (black line). Also shown is the photoelectron spectrum of $TCNQ^-$ at 3.1 eV (grey line). The molecular structure of F_4-TCNQ is shown inset. (b) Schematic energy level diagram of the photodetachment process at 3.1 eV (blue arrows), with respect to the doublet states of the anion (D_0, D_1, and D_2) and the resultant neutral states (S_0 and T_1). State term symbols are shown in parentheses with their tentatively assigned valence electron configurations shown below. The valence molecular orbitals (MOs) of F_4-TCNQ are shown on the left with their respective symmetries given in parentheses.

theoretical perspective [8,9]. Furthermore, no studies into the dynamics of this widely utilised electron acceptor have been performed to date. However, unlike $TCNQ^-$, modern theory calculations performed at the SCF/MP4 level of theory by Simons and co-workers [8], suggest that the second D_2 $\left(2^2B_{3u}\right)$ excited doublet state of F_4-$TCNQ^-$ is vertically bound with respect to the S_0 $\left(^1A_g\right)$ singlet ground state of the neutral, as schematically shown in Figure 6.1b. In principle this provides scope for also mapping the dynamics of the D_2 state, in addition to comparing the dynamics of the first excited D_1 $\left(1^2B_{3u}\right)$ state with those observed in $TCNQ^-$.

Currently, we have measured the one-colour photoelectron spectrum of F_4-$TCNQ^-$ at 3.1 eV (400 nm). Briefly, the one-colour photoelectron spectrum, shown in Figure 6.1, appears qualitatively similar to that of $TCNQ^-$ at the same detachment energy (shown in grey in Figure 6.1b). With respect to Figure 6.1b, early analysis suggests that the low energy feature around 0.1 eV corresponds to near threshold detachment of electrons from the D_2 state, with which the 3.1 eV detachment photons are resonant. At present, we tentatively interpret the broader feature centred around 1.5 eV as photoelectrons generated from resonance-enhanced two-photon detachment *via* the D_2

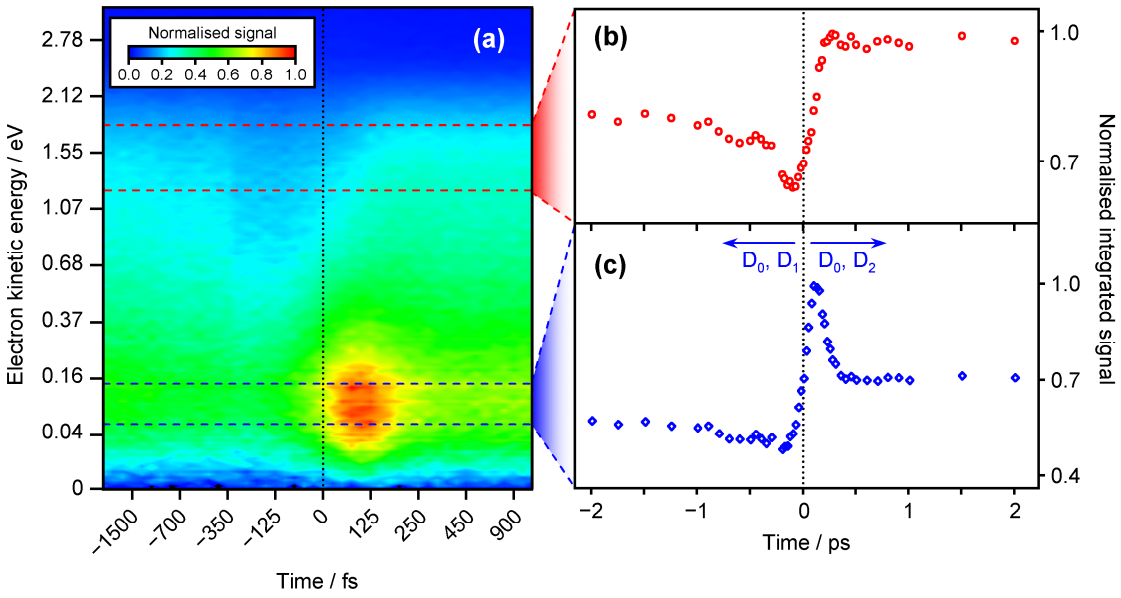

Figure 6.2: (a) Normalised false-colour intensity plot of the time-resolved photoelectron spectrum of F_4-$TCNQ^-$ as a function of pump-probe delay, *t*. These spectra were recorded at pump and probe energies of 3.1 eV and 1.5 eV, respectively. (b) Temporal plot of the normalised integrated photoelectron signal over an energy range of 1.25 eV to 1.75 eV. (c) Normalised integrated intensity over the energy range 0.05 eV to 0.15 eV as a function of pump-probe delay. In (c) negative delay dynamics correspond to signal from the D_0 and D_1 states, while positive delays represent signal from D_0 and D_2.

state. This assignment is based on the assumption that, like $TCNQ^-$, the D_2 state exhibits mixed outer and core excited electronic characteristics, which electronically correlate to the S_0 and the first excited T_1 $\left({}^3B_{1u}\right)$ triplet states of the neutral, respectively. To date, there are no published electronic structure calculations which have provided the electronic configuration contributions to any of the F_4-TCNQ states (both anion and neutral). Hence, to confirm the above interpretations of the photoelectron spectrum we are currently in the process of performing complimentary density functional theory calculations.

In conjunction to the aforementioned one-colour experiments, we have also performed preliminary TRPEI experiments with pump and probe energies of 3.1 eV and 1.5 eV (800 nm), respectively, to investigate the D_2 dynamics. The false-colour intensity plot in Figure 6.2a shows the results of these TRPEI experiments, where the individual photoelectron spectra are displayed as a function of pump-probe delay, *t*.

Figures 6.2b and 6.2c show the integrated signal intensities for the spectral ranges of 0.05 eV to 0.15 eV and 1.25 eV to 1.75 eV, respectively. When the pump and probe are temporally overlapped ($t = 0$), a rapid increases in signal around 1.5 eV and 0.1 eV

are observed. As time evolves ($t > 0$), Figure 6.2c shows how the feature around 0.1 eV rapidly decays on a timescale faster than the temporal resolution of the experiment (~100 fs), while the higher energy feature (Figure 6.2b) exhibits no further obvious signal dynamics over a duration of 2 ps. Conversely, the signal in these spectral regions at negative time delays (which should predominantly provide information regarding the D_1 state dynamics) displays a depletion relative to the signal at $t > 0$, which then go on to recover on two different timescales, respectively.

We are currently in the process of analysing these TRPEI results. Early interpretations indicate that there may be a number of competing features from the D_0, D_1 and D_2 states at $t = 0$, which are all isoenergetic (~0.1 eV). This scenario makes a definitive analysis of the D_1 and D_2 dynamics non-trivial at these pump and probe energies. In an attempt to eliminate this issue, we propose to carry out TRPEI experiments with a 400 nm pump and 500 nm (2.5 eV) probe, neither of which are resonant with the D_1 state.

6.3.2 Time-resolved Photoelectron Angular Distributions

Similar to the time-resolved studies on $TCNQ^-$ in Chapter 5, the TRPEI experiments performed on F_4-$TCNQ^-$ also exhibit time-resolved PADs, which we tentatively ascribe to the presence of isoenergetic photoelectron features in the 0.1 eV region of the

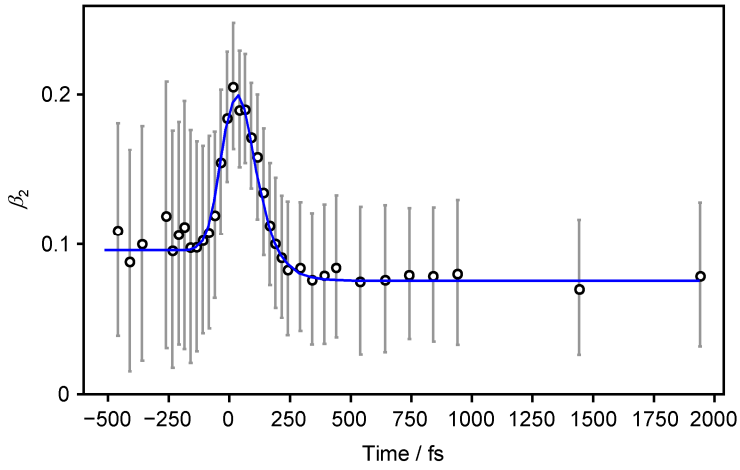

Figure 6.3: Time-resolved β_2 anisotropy parameters of the F_4-TCNQ radical anion over the energy range of 0.05 eV to 0.15 eV. Error bars (in grey) represent a single standard deviation. The solid blue line shows a fit to the model described in Chapter 5 of this thesis (equation (5.12)), and provides a relaxation time, τ, of <100 fs.

spectrum (0.05 eV to 0.15 eV). The average β_2 anisotropy parameters of these temporally evolving PADs in this energy region are shown in Figure 6.3, and have been extracted from fits to equation (5.1) in Chapter 5 using the polar onion-peeling algorithm described in Chapter 3. The solid blue line in Figure 6.3 corresponds to a fit to the model described in Chapter 5 (equation (5.12)), and provides a relaxation timescale, τ, of less than <100 fs. However, at $t = 0$ there is a possibility of more than two photoelectron contributions at ~0.1 eV: $D_2 \rightarrow S_0 + e^-$, $D_2 \rightarrow T_1 + e^-$, and $D_1 \rightarrow T_1 + e^-$. If this is indeed the case, then the formulism described in Chapter 5 would need to be modified to take this into account. None the less, the observation of such dynamics through PADs of isoenergetic features in a species other than the $TCNQ^-$, albeit being a direct derivative, provides additional scope for utilising the temporal evolution of PADs to gain insights into the ultrafast dynamics of large molecular species, particularly when photoelectron signals become broad and spectrally convoluted.

6.3.3 Micro-solvation Studies

At the beginning of this thesis we emphasised that one of the additional attributes of using electrospray ionisation to transfer large molecular anions into the gas phase, is that it also possesses the ability to generate micro-solvated species, provided the experimental conditions are optimised. Wang and co-workers have demonstrated on a number of occasions that this characteristic of electrospray sources can be exploited to extract detailed molecular level insights into solvation dynamics, through the discrete addition of solvent molecules to solute anions [10,11]. This is aptly exemplified by their work on the hydration dynamics of the SO_4^{2-} anion [10], a species which is not only pertinent to a vast range of inorganic chemistry but also plays a critical role in chemical processes within the Earths atmosphere, such as the nucleation of ice crystals [12].

In the gas phase, isolated SO_4^{2-} is unstable and undergoes rapid decay *via* electron loss, into its associated mono-anion and a free electron [13]. However, upon the addition of as little as 3 H_2O molecules, the ground state of SO_4^{2-} becomes sufficiently stabilised with respect to electron loss through the repulsive Coulomb barrier [10]. Wang and co-workers, subsequently performed a series of one-colour nanosecond photoelectron spectroscopy experiments, at both 193 nm (6.4 eV) and 157 nm (7.9 eV),

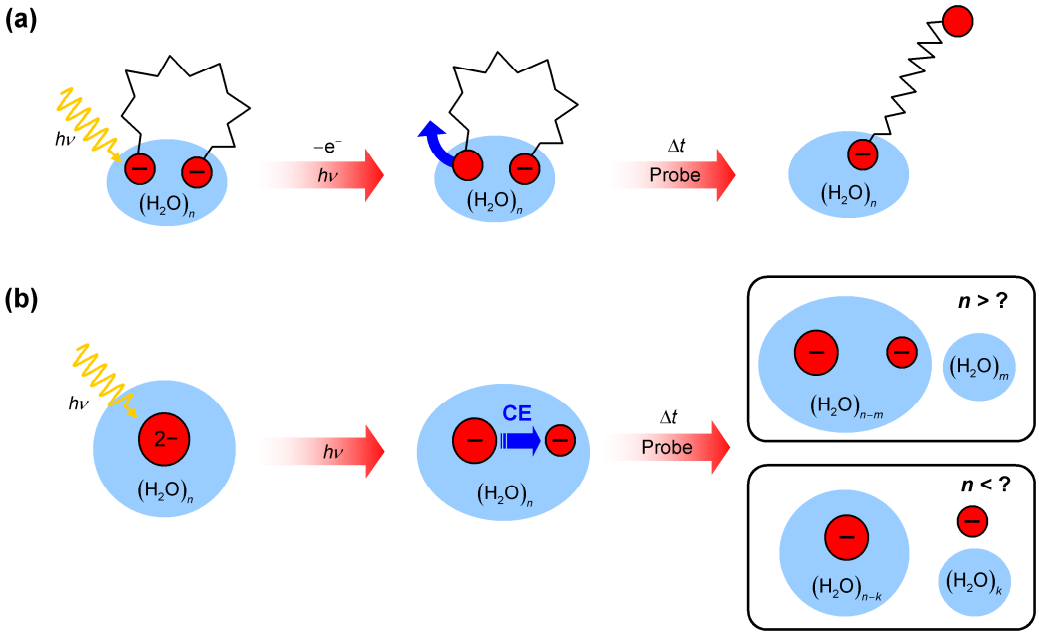

Figure 6.4: (a) Schematic illustration of a photo-initiated hydrophobic-hydrophilic interaction in a solvated dicarboxylate dianion, $\left({}^{-}O_2C(CH_2)_n CO_2^{-}\right)$. Red circles correspond to the CO_2 end groups connected by an aliphatic carbon chain. A pump photon, $h\nu$, detaches an electron from one CO_2 group while a time delayed probe photon of sufficient energy monitors any changes to the system. (b) A pump photon induces Coulomb explosion (CE) in a multiply charged anion, where a time delayed probe pulse is then used to monitor any subsequent caging dynamics as a function of solvation.

These experiments investigated the evolution of the electron detachment process from SO_4^{2-}, as the number of solvent species was incrementally increased up to 40 individual H_2O molecules [10]. After the addition of 18 solvent molecules, photoelectrons from SO_4^{2-} become unobservable, and only a feature corresponding the ionisation of the solvent cluster is detectable. This observation led Wang and co-workers to conclude that the photoelectron generated from the SO_4^{2-} solute anion is unable to escape the surrounding water cluster, resulting in its subsequent hydration: $SO_4^{-}(H_2O)_n^{-}$. However, since these experiments, no studies have been conducted into understanding the ultrafast dynamical processes which may take place following the solvation of the photoelectron into the solvent cluster. As such, may questions remain unanswered, which include: (1) can the electron solvation dynamics be observed?; (2) is recombination of either the initial geminate ion-electron pair $\left(SO_4^{-}\cdots e^{-}\right)$ or free SO_4^{-} mono-anion and hydrated electron possible?; and finally, (3) if the aforementioned processes are observed, what are their timescales and how are these dynamics perturbed by level of solvation? In the near future, we are ideally placed to investigate these unknown aspects of the

$SO_4^{2-}(H_2O)_n$ system.

From a broader perspective, we intend to interrogate a whole host of solvent mediated processes though micro-solvation studies. Some examples, shown in Figure 6.4, include photo-initiated hydrophobic-hydrophilic interactions in solvated dicarboxylate dianions $\left({}^{-}O_2C(CH_2)_n CO_2^{-}\right)$ and solvent caging dynamics in Coulomb explosion, respectively. The solvent plays a vital role in many chemical and biological phenomena, and by micro-solvating such species in the gas phase we can begin to gain a molecular level understanding of exactly how the solvent manipulates the chemical and bio-dynamics in question.

6.4 Closing Remarks

We have described the experimental design and commissioning of a new photoelectron imaging spectrometer, which has been developed to study the spectroscopy and ultrafast behaviour of molecular anions in the isolated environment of the gas phase. Using this new instrument we have reported the first time-resolved photoelectron imaging experiments to interrogate the ultrafast dynamics of large molecular anions generated *via* an electrospray ionisation source. Specifically, we have probed the ultrafast excited state dynamics of the 7,7,8,8-tetracyanoquinodimethane radical anion, which displays wave packet motion. Using this system we have also shown, for the first time, that, by using relatively intuitive arguments, it is possible to extract both a qualitative and quantitative description of ultrafast relaxation dynamics through temporally evolving photoelectron angular distributions.

6.5 References

[1] A. W. Colburn, A. E. Giannakopulos, and P. J. Derrick, *Eur. J. Mass Spectrom.*, **10**, 149 (2004).

[2] E. De Hoffmann, J. Charette, and V. Stroobant, *Mass Spectrometry: Principles and Applications*. (John Wiley & Sons, New York, 1999).

[3] E. Fischer, *Z. Phys.*, **156**, 1 (1959).

[4] S. H. Guan and A. G. Marshall, *J. Am. Soc. Mass Spectrom.*, **5**, 64 (1994).

[5] P. Richharia, *Sol. Energ. Mater.*, **20**, 199 (1990).

[6] I. Wilkinson and B. J. Whitaker, *Personal Communication* (2010).

[7] *CRC Handbook of Chemistry and Physics*, edited by D. R. Lide, (CRC Press, Boca Raton, FL, 2006) 87th ed.

[8] M. Sobczyk, P. Skurski, and J. Simons, *J. Phys. Chem. A*, **107**, 7084 (2003).

[9] S. Panja *et al.*, *J. Chem. Phys.*, **127**, 124301 (2007).

[10] X. B. Wang, X. Yang, J. B. Nicholas, and L. S. Wang, *Science*, **294**, 1322 (2001).

[11] X. B. Wang, X. Yang, and L. S. Wang, *Int. Rev. Phys. Chem.*, **21**, 473 (2002).

[12] R. Pincus and M. B. Baker, *Nature*, **372**, 250 (1994).

[13] A. T. Blades and P. Kebarle, *J. Am. Chem. Soc.*, **116**, 10761 (1994).

Appendices

Appendix A: Ion Trap Simulation Code

The ion trap simulations described in Chapter 2 have been simulated using the Simion 8.0 package. The trap conditions described for each of the relevant simulations in Chapter 2 have been controlled using the Lua script code provided below. This code has been modified from the code provided with Simion 8.0 for simulating pressure conditions within simulations.

```
-- RF Trap simulation

simion.workbench_program()

-- IMPORTANT INFORMATION REGARDING SCALING OF THE TRAP SIMULATION:
-- This simulation has been designed so that the geometry file has a
-- 10:1 scaling (i.e. 10mm = 1mm)
-- This has been taken into account in this user program regarding the
-- velocities and pressure calculations.
-- Scaling of electrode voltages: Input voltages need to be scaled by
-- a factor of 10, i.e. for 10V enter 100.
-- Scaling of Ion K.E. input: Scales by a factor of 100, i.e. for 1eV
-- ions, enter 100eV.

-- FUNNEL VOLTAGE INPUTS

adjustable ACamp = 500            -- AC Voltage amplitude
adjustable freq = 1               -- AC Voltage Frequency (MHz)
adjustable Vstart = -300          -- Start of DC ramp
adjustable Vend= -200             -- End of DC ramp
adjustable Lens = 0               -- Focal Lens Voltage

adjustable Trap_Open = 400        -- Trap Open Voltage
adjustable Trap_Closed = -400     -- Trap Closed Voltage
```

```
-- PRESSURE CONTROL INPUTS

adjustable BKmass = 28.0          -- Mass of background gas(amu)
adjustable Temp = 298.0           -- Gas temperature (K)
adjustable Press = 5.0            -- Gas pressure (0.1Pa ~ 1mTorr)
adjustable sigma = 5.0E-19        -- Collision-cross section (m^2)
adjustable MFPstep = 20.0         -- Mean number of time steps per MFP
local max_timestep                --  Maximum  time  step  (usec)  that
                                  fast_adjust should permit

-- CONSTANTS

local k = 1.3806505e-23           -- Boltzmann constant (J/K)
local R = 8.3145                  -- Ideal gas constant (J/(mol*K))
local kg_amu = 1.6605402e-27      -- (kg/amu) conversion factor
local pi = math.pi                -- PI constant

-- GENERATE A NORMALISED GAUSSIAN DISTRIBUTION USING A BOX-MULLER
-- ALGORITHM FOR PRESSURE CALCULATIONS

function gaussian_random()
     local s = 1
     local v1, v2
        while s >= 1 do
        v1 = 2*rand() - 1
        v2 = 2*rand() - 1
        s = v1*v1 + v2*v2
     end

     local rand1 = v1*sqrt(-2*ln(s) / s)      -- (assume divide by zero
                                              -- improbable?)
     return rand1
```

```
end

-- INITIALISE DC VOLTAGES OF ELECTRODES

function segment.init_p_values()
     adj_elect07 = Trap_Closed
     n = 31                                  -- Number of electrodes
     Vstep = (Vstart - Vend) / (n - 1)       -- Voltage step between
                                             -- electrodes
     for m=1,6 do
        adj_elect[m] = Vend + (Vstep * (m - 1))
     end
end

-- ADJUST TO SENSIBLE TIME STEPS FOR PRESSURE CALCULATIONS

function segment.tstep_adjust()
     if max_timestep and ion_time_step > max_timestep then
        ion_time_step = max_timestep
     end
end

-- ADJUST AC VOLTAGES OF ELECTRODES

function segment.fast_adjust()
     omega = (pi * 2) * freq       -- Angular freqeucny (rad usec-1)
     AC1 = ACamp * sin(omega * ion_time_of_flight)    -- AC (phi = 0)
     AC2 = ACamp * sin(omega * ion_time_of_flight + pi)-- AC (phi = pi)
     for p=0,2 do                            -- ODD ELECTRODE ADJUST LOOP
        local x = (p * 2) + 1
        adj_elect[x] = AC1 + Vend + (Vstep * 2 * p)
     end
```

```
     for q=1,3 do                              -- EVEN ELECTRODE ADJUST LOOP
        local y = (q * 2)
        adj_elect[y] = AC2 + Vend + Vstep + (Vstep * 2 * (q - 1))
     end
end

-- CALCULATE PRESSURE EFFECTS

function segment.other_actions()
     if Press == 0 then
        return
     end

-- CALCULATE ION SPEED

     local speed_ion = sqrt(ion_vx_mm^2 + ion_vy_mm^2 + ion_vz_mm^2)

-- Prevent divide by zero later in the code

     if speed_ion < 1E-7 then
        speed_ion = 1E-7
     end

-- (1) CALCULATE MEAN FREE PATH (MFP)
-- (A) Compute mean gas speed (mm/us)

     local c_bar_gas = sqrt(8 * k * Temp / pi / (BKmass * kg_amu)) /
     10000

-- (B) Compute median gas speed (mm/us)

     local c_star_gas = sqrt(2 * k * Temp / (BKmass * kg_amu)) / 10000
```

```
-- (C) Compute mean relative speed (mm/us) between gas and ion

     local c_bar_rel = sqrt(speed_ion^2 + c_bar_gas^2)

-- (D) Compute mean free path (mm)

     MFP = 100 * k * Temp * (speed_ion / c_bar_rel) / (Press * sigma)

-- (2) LIMIT TIME STEP SIZE TO FRACTION OF CALCULATED MFP

     max_timestep = MFP / speed_ion / MFPstep

-- (3) CALCULATE PROBABILITY OF COLLISION
-- For an infinitesimal distance (dx) travelled, the increase in the
-- fraction (f) of collided particles relative to the number
-- of yet uncollided particles (1-f) is equal to the distance
-- travelled (dx) over the mean-free-path (lambda):
-- df/(1-f) = dx / lambda
-- Solving this differential equation gives:
-- f = 1 - exp(- dx / lambda) = 1 - exp(- v dt / lambda)
-- This f can be interpreted as the probability that a single
-- particle collides in the distance traveled.

     local collision_prob = 1 - exp(- speed_ion * ion_time_step / MFP)

-- (4) DETERMINE COLLISION: if rand() > collision_prob then there is
-- no collision

     if rand() > collision_prob then
        return
     end
```

```
-- (5) CALCULATE VELOCITY CHANGE OF ION
-- (A) Calculate standard deviation of background gas velocity in one
-- dimension (mm/us).

-- From kinetic gas theory (Maxwell-Boltzmann), velocity in one
-- dimension is normally distributed with standard deviation
-- sqrt(kT/m).

    local SDvel = sqrt(k * Temp / (BKmass * kg_amu)) / 10000

-- (B) Calculate velocity of colliding background gas particle using a
-- simple Maxwell distribution

    local vx_gas = gaussian_random() * SDvel
    local vy_gas = gaussian_random() * SDvel
    local vz_gas = gaussian_random() * SDvel

-- (C) Translate velocity reference frame so that colliding background
-- gas particle is stationary.

    local vx = ion_vx_mm - vx_gas
    local vy = ion_vy_mm - vy_gas
    local vz = ion_vz_mm - vz_gas

-- (6) CALCULATE CHANGE IN ION ORIENTATION FROM COLLISION
-- ASIDES: Notes on collision orientation
-- A collision of the ion in 3D can now be reasoned in 2D since
-- the ion remains in some 2D plane before and after collision.
-- The ion collides with an gas particle initially at rest (in the
-- current velocity reference frame).
-- For convenience, we define a coordinate system (r, t) on the
-- collision plane. r is the radial axis through the centers of
```

```
-- the colliding particles, with the positive direction indicating
-- approaching particles. t is the tangential axis perpendicular to r.
-- An additional coordinate theta defines the the rotation of the
-- collision plane around the ion velocity axis.

-- (A) Compute randomized impact offset [0, 1] as a fraction of
-- collisional cross-section diameter.

-- 0 is a head-on collision; 1 would be a near miss.

-- You can imaging this as the gas particle being a stationary
-- dart board of radius 1 unit (representing twice the actual radius
-- of the gas particle) and the ion center is a dart
-- with velocity perpendicular to the dart board.
-- The dart has equal probability of hitting anywhere on the
-- dart board.  Since a radius "d" from the center represents
-- a ring with circumference proportional to "d", this implies
-- that the probability of hitting at a distance "d" from the
-- center is proportional to "d".

-- Formally, the normalized probability density function is
-- f(d) = 2*d for d in [0,1].  From the fundamental transformation
-- law of probabilities, we have:
-- integral[0..impact_offset] f(d) dd = impact_offset^2 = U,
-- where U is a uniform random variable.  That is,
-- impact_offset = sqrt(U).  Decrease it slightly
-- to prevent overflow in asin later.

    local impact_offset = sqrt(0.999999999 * rand())

-- (B) Convert impact offset to impact angle [0, +pi/2) (radians).
```

```
-- We Do this since the target is really a sphere (not flat
-- dartboard). This is the angle between the relative velocity
-- between the two colliding particles (i.e. the velocity of the dart
-- imagined perpendicular to the dart board) and the r axis
-- (i.e. a vector from the center of the gas particle to the location
-- on its surface where the ion hits).
-- 0 is a head-on collision; +pi/2 would be a near miss.

     local impact_angle = asin(impact_offset)

-- In other words, the effect of the above is that impact_angle has
-- a distribution of p(impact_angle) = sin(2 * impact_angle).

-- (C) Compute randomized angle [0, 2*pi] for rotation of collision

-- plane around radial axis.  The is the angle around the
-- center of the dart board.
-- Note: all angles are equally likely to hit.
-- The effect is that impact_theta has a distribution
-- of p(impact_theta) = 1/(2*pi).

     local impact_theta = 2*pi*rand()

-- (D) Compute polar coordinates in current velocity reference frame

     local speed_ion_r, az_ion_r, el_ion_r = rect3d_to_polar3d(vx, vy,
     vz)

-- (E) Compute ion velocity components (mm/us).

     local vr_ion = speed_ion_r * cos(impact_angle) -- radial velocity
     local vt_ion = speed_ion_r * sin(impact_angle) -- normal velocity
```

```
-- (F) Attenuate ion velocity due to elastic collision.
-- This is the standard equation for a one-dimensional
-- elastic collision, assuming the other particle is initially at rest
-- (in the current reference frame).
-- Note that the force acts only in the radial direction, which is
-- normal to the surfaces at the point of contact.

    local vr_ion2 = (vr_ion * (ion_mass - BKmass)) / (ion_mass +
    BKmass)

-- (G) Rotate velocity reference frame so that original ion velocity
-- vector is on the +y axis.

-- Note: The angle of the new velocity vector with respect to the
-- +y axis then represents the deflection angle.

    vx, vy, vz = elevation_rotate(90 - deg(impact_angle), vr_ion2,
    vt_ion, 0)

-- (H) Rotate velocity reference frame around +y axis.

-- This rotates the deflection angle and in effect selects the
-- randomized impact_theta.

    vx, vy, vz = azimuth_rotate(deg(impact_theta), vx, vy, vz)

-- (I) Rotate velocity reference frame back to the original.

-- For the incident ion velocity, this would have the effect
-- of restoring it.
```

```
     vx, vy, vz = elevation_rotate(-90 + el_ion_r, vx, vy, vz)
     vx, vy, vz = azimuth_rotate(az_ion_r, vx, vy, vz)
-- (J) Translate velocity reference frame back to original.

-- This undoes the prior translation that makes the velocity
-- relative to the colliding gas particle.

     vx = vx + vx_gas
     vy = vy + vy_gas
     vz = vz + vz_gas

-- (7) SET NEW VELOCITY VECTOR OF ION

     ion_vx_mm, ion_vy_mm, ion_vz_mm = vx, vy, vz

end
```

Appendix B: Polar Onion-peeling: C Syntax Code

The polar onion-peeling (POP) algorithm, described in detail Chapter 3, has been coded within a formula node in LabVIEW 8.5 using a C language syntax. The C code for POP is provided below.

```
/*
INPUT PARAMETERS AND DEFINITIONS
Note: The numbers in brackets represent the sections that each of the parameters are used in.
*/

int32 i; // For loop Increment (1,2,3,4)
int32 j; // For loop Increment (1,2,3,4)
int16 rp; // radius (2,3,4)
int16 qp; // polar pixel number (2,3,4)
int16 nainc; // number of angular increments for a radius rp (2,3,4)
float32 ainc; // angular increment of a radius rp (2,3,4)
float32 xp; // polar x coordinate for a given rp and alpha (2)
float32 yp; // polar y coordinate for a given rp and alpha (2)
int16 xc; // x coordinate of cartesian pixel for which the centre of the polar pixel (xp,yp) is in (2)
int16 yc; // y coordinate of cartesian pixel for which the centre of the polar pixel (xp,yp) is in (2)
float32 xd; // x percentage of cartesian pixel (xc,yc) that the polar pixel (xp,yp) occupies (2)
float32 yd; // y percentage of cartesian pixel (xc,yc) that the polar pixel (xp,yp) occupies (2)
float32 pint; // intensity of the polar pixel (rp,qp) (2)
float32 xa; // Calculation of the second order legendre polynomial (3)
float32 xb; // Calculation of the forth order legendre polynomial (3)
float32 y; // Intensity of the ira matrix at ira[rp][qp] (3)
```

```
float64 det; // Determinant of Matrix A (3)
float32 Na; // Absolute value of N (Beta[0]) (3)
int16 R; // radius of polar pixel extracted from LUT (3,4)
int16 pixels; // number of polar pixels (qp) at a given radius (rp)
(4)
float32 it; // intensity of pixel (qp) in expanded normalised LUT (4)
float32 alpha; // alpha (4)
float32 fact; // scaled angular distribution at pixel (R,qp) from LUT
(4)

/*
+--+--+--+--+--+--+--+--+--+--+--+--+--+--+--+--+--+--+--+--+--+--+--+--+--+--+--+--+--+--
PART I - RAW CARTESIAN IMAGE MANIPULATION

PART I folds the raw cartesian image (a) in four and centres the image
to generate a single quadrant (a4) . After this the folded Cartesian
image (a4) is then converted into an array of polar pixels (ira) so
that PART II of the code may be carried out using polar co-ordinates.

This involves step (1) and (2). A convoluted 1D radial spectrum is
generated at the end of PART I.
+--+--+--+--+--+--+--+--+--+--+--+--+--+--+--+--+--+--+--+--+--+--+--+--+--+--+--+--+--+--
*/

/*
+--+--+--+--+--+--+--+--+--+--+--+--+--+--+--+--+--+--+--+--+--+--+--+--+--+--+--+--+--+--
(1) CARTESIAN IMAGE CENTRING & 4 WAY FOLDING
(zzx,zzy) is defined as the centre of the image
The centre of a Cartesian pixel is defined as the centre of the pixel
(NOT the bottom left vertex)

Note: Only even dimension sizes can be used!
```

```
+--+--+--+--+--+--+--+--+--+--+--+--+--+--+--+--+--+--+--+--+--+--+--+--+--+--
*/

/*
INFO:
Background noise subtraction. Subtracts a specific background noise
intensity (Noise) from all pixels in the raw Cartesian image prior to
image centring and folding.
*/

for(i=0;i<=ix;i++) {
     for(j=0;j<=iy;j++) {
        a[i][j]=a[i][j]-Noise;
     }
}

/*
INFO:
Centring and folding of the of the raw Cartesian image
*/

a4[0][0]=a[zzx][zzy]*4;

for(i=1;i<=zz-1;i++) {
     a4[i][0]=(a[zzx+i][zzy]+a[zzx-i][zzy])*2;
     for(j=1;j<=zz-1;j++) {
        a4[i][j]=a[zzx+i][zzy+j]+a[zzx-i][zzy+j]+a[zzx+i][zzy-j]+a[zzx-
        i][zzy-j];
        a4[0][j]=(a[zzx][zzy+j]+a[zzx][zzy-j])*2;
     }
}
```

```
/*
+--+--+--+--+--+--+--+--+--+--+--+--+--+--+--+--+--+--+--+--+--+--+--+--+--+--+--+--+--+--+--+--
(2) CONVERSION FROM CARTESIAN TO POLAR COORDINATES: rp,alpha
alpha is the angle and qp is the pixel designation in alpha. qp=0 ->
alpha=0
This conversion takes into account that each of the Cartesian pixels
have a dimension 1x1
This is also true for the polar pixels generated.
+--+--+--+--+--+--+--+--+--+--+--+--+--+--+--+--+--+--+--+--+--+--+--+--+--+--+--+--+--+--+--+--
*/

ira[0][0]=a4[0][0];

for(rp=1;rp<=zz-1;rp++) {

/*
INFO:
For a given radius (rp) the angular increment (ainc) between each
polar pixel is calculated by first calculating the number of angular
increments for that radius (nainc). Nainc will be given by the number
of polar pixels (The number of polar pixels is calculated using
(rp+1)*(pi/2) which is then rounded down using floor) at that radius
minus one, as there are one less angular increments than there are
polar pixels.
*/

     nainc=PIXELS[rp][1];
     ainc=AINC[rp];

     for(qp=0;qp<=nainc;qp++) {
```

```
/*
INFO:
The angle at which a polar pixel lies (alpha) for a given radius (rp)
is calculated using ainc*qp. The x and y coordinates of the polar
pixel (xp and yp respectively) are then determined using
xp=rp*sin(alpha) and yp=rp*cos(alpha) from basic trigonometry.

The x and y coordinates of the Cartesian pixel (xc and yc
respectively) for which the centre of the polar pixel (xp,yp) lies in
is then determined by rounding xp and yp to the nearest integer (using
int) to give xc and yc respectively. (Note: xc and yc are integers but
xp and yp are floating point numbers).

The absolute value of the difference between the the polar and
Cartesian coordinates (i.e. abs(xc-xp) and abs(yc-yp)) is then
subtracted from 1 (1 because the size of the Cartesian pixels is 1x1).
This gives xd and yd respectively.
*/

        xp=rp*sin(ainc*qp);
        yp=rp*cos(ainc*qp);

        xc=int(xp);
        yc=int(yp);

        xd=1-abs(xc-xp);
        yd=1-abs(yc-yp);

/*
INFO:
xd and yd multiplied together (i.e. xd*yd) provides the percentage
overlap of the polar pixel (xp,yp) with the Cartesian pixel (xc,yc).
```

The intensity of the cartesian pixel (xc,yc) in the a4 array (i.e. a4[xc][yc]) is then multiplied by this percentage overlap. This provides the first of four values to be added together to determine the polar pixel intensity (pint).

If statements are used to determine which other three Cartesian pixels the polar pixel overlaps with. Firstly, the percentage of intensity that needs to be taken from each of these Cartesian pixels needs to be determined. Three moves in the Cartesian frame are possible and they each correspond to these percentages:

1. x coord=stay the same, y coord=change, percentage=xd*(1-yd)
2. x coord=change, y coord=stay the same, percentage=(1-xd)*yd
3. x coord=change, y coord= change, precentage=(1-xd)*(1-yd)

To determine the other three Cartesian pixels, a comparison between xp and xc and yp and yc is carried out. If polar>cartesian then +1 to the coordinate, if polar<cartesian then -1 from that coordinate.

All four intensity values are summed to give the intensity of the polar pixel (pint).
*/

```
        if(xp>=xc && yp>=yc) {
            pint=((xd*yd)*a4[xc][yc])+((xd*(1-yd))*a4[xc][yc+1])+(((1-
            xd)*yd)*a4[xc+1][yc])+(((1-xd)*(1-yd))*a4[xc+1][yc+1]);
        }
        if(xp>=xc && yp<=yc) {
            pint=((xd*yd)*a4[xc][yc])+((xd*(1-yd))*a4[xc][yc-1])+(((1-
            xd)*yd)*a4[xc+1][yc])+(((1-xd)*(1-yd))*a4[xc+1][yc-1]);
        }
        if(xp<=xc && yp>=yc) {
```

```
            pint=((xd*yd)*a4[xc][yc])+((xd*(1-yd))*a4[xc][yc+1])+(((1-
            xd)*yd)*a4[xc-1][yc])+(((1-xd)*(1-yd))*a4[xc-1][yc+1]);
        }
        if(xp<=xc && yp<=yc) {
            pint=((xd*yd)*a4[xc][yc])+((xd*(1-yd))*a4[xc][yc-1])+(((1-
            xd)*yd)*a4[xc-1][yc])+(((1-xd)*(1-yd))*a4[xc-1][yc-1]);
        }

/*
INFO: The polar pixel intensity is placed in the appropriate polar
pixel (i.e. ira[rp][qp]) in the polar matrix (ira).
*/

        ira[rp][qp]=ira[rp][qp]+pint;
     }
}

/*
INFO: Saving of the polar image ira into iraraw
*/

for(rp=0;rp<=zz-1;rp++) {
     nainc=PIXELS[rp][1];
     for(qp=0;qp<=nainc;qp++) {
        iraraw[rp][qp]=ira[rp][qp];
     }
}

/*
+--+--+--+--+--+--+--+--+--+--+--+--+--+--+--+--+--+--+--+--+--+--+--+--+--+--+--+--+--+--+--+--+
GENERATION OF THE CONVOLUTED PHOTOELECTRON SPECTRUM, PES I(R)
+--+--+--+--+--+--+--+--+--+--+--+--+--+--+--+--+--+--+--+--+--+--+--+--+--+--+--+--+--+--+--+--+
```

```
*/

for(i=0;i<=zz-1;i++) {
     nainc=PIXELS[i][1];
     PESR[i]=i;
     for(j=0;j<=nainc;j++) {
        PESI[i]=PESI[i]+ira[i][j];
     }
}

/*
+--+--+--+--+--+--+--+--+--+--+--+--+--+--+--+--+--+--+--+--+--+--+--+--+--+--+--+--+--+--
PART II - POLAR ONION PEELING ALGORITHM

PART II of the code carries out the deconvolution of the image via an
onion peeling method. This is carried out via removal of the phi (f)
contribution from the raw image (ira) at every radius (rp) to obtain a
"slice" through the centre of the original 3D distribution of
photofragments projected onto 2D detector surface i.e at f=0 only.

This involves repeating steps (3) and (4) for every radius (rp). This
is done by starting at the outermost radius (rp=zz-1) and
incrementally decreasing rp until rp=0 is reached.
+--+--+--+--+--+--+--+--+--+--+--+--+--+--+--+--+--+--+--+--+--+--+--+--+--+--+--+--+--+--
*/

/*
INFO:
The deconvolution is carried out using an overall rp "for loop" that
runs for every radius (rp) from zz-1 to 0.
*/
```

```
for(rp=zz-1;rp>=0;rp--) {

/*
+--+--+--+--+--+--+--+--+--+--+--+--+--+--+--+--+--+--+--+--+--+--+--+--+--+--+--+--+--+--+--+--
(3) OUTER RING FIT OF EXPERIMENTAL IMAGE (IRA) AT rp USING LINEAR REGRESSION

Note: theta=alpha, rp=R
Note: nainc+1 is the number of polar pixels at a given value of rp (i.e. for linear regression, the number of data points)

For information on how the linear regression technique works in more details see:

"Data Reduction and Error Analysis for Physical Sciences" 3rd Edition, by Philip R. Bevington & D. Keith Robinson

Chapter 7 - Least Squares Fit to a Polynomial
p122 - Matrix Solution(7.2)

(more specifically for Legendre Polynomials, p132)
+--+--+--+--+--+--+--+--+--+--+--+--+--+--+--+--+--+--+--+--+--+--+--+--+--+--+--+--+--+--+--+--
*/

/*
INFO: Zeroing of Matrices A and B before the outer ring fit begins for a given R
*/

B[0]=0;
B[1]=0;
B[2]=0;
```

```
for(i=0;i<=3;i++) {
     for(j=0;j<=3;j++) {
        A[i][j]=0;
     }
}

/*
INFO: Calculation of Matrices A and B
*/

nainc=PIXELS[rp][1];
for(qp=0;qp<=nainc;qp++) {
     y=ira[rp][qp];
     xa=0.5*((3*(cos(AINC[rp]*qp)**2))-1);
     xb=(1/8)*((35*(cos(AINC[rp]*qp)**4))-
     (30*(cos(AINC[rp]*qp)**2))+3);

     B[0]=B[0]+y;
     B[1]=B[1]+(y*xa);
     B[2]=B[2]+(y*xb);

     A[0][0]=A[0][0]+1;
     A[0][1]=A[0][1]+xa;
     A[0][2]=A[0][2]+xb;
     A[1][1]=A[1][1]+(xa**2);
     A[1][2]=A[1][2]+(xa*xb);
     A[2][2]=A[2][2]+(xb**2);
}

A[2][1]=A[1][2];
A[2][0]=A[0][2];
```

```
A[1][0]=A[0][1];

/*
INFO: Inversion of Matrix A
*/

Ain[0][0]=(A[1][1]*A[2][2])-(A[1][2]*A[2][1]);
Ain[0][1]=((A[1][0]*A[2][2])-(A[1][2]*A[2][0]))*-1;
Ain[0][2]=(A[1][0]*A[2][1])-(A[1][1]*A[2][0]);
Ain[1][1]=(A[0][0]*A[2][2])-(A[0][2]*A[2][0]);
Ain[1][2]=((A[0][0]*A[2][1])-(A[0][1]*A[2][0]))*-1;
Ain[2][2]=(A[0][0]*A[1][1])-(A[0][1]*A[1][0]);
Ain[1][0]=Ain[0][1];
Ain[2][0]=Ain[0][2];
Ain[2][1]=Ain[1][2];

/*
INFO: Calculation of the Determinant of Matrix A
*/

det=(A[0][0]*Ain[0][0])-(A[0][1]*(-Ain[0][1]))+(A[0][2]*Ain[0][2]);
for(i=0;i<=3;i++) {
     for(j=0;j<=3;j++) {
        Ain[i][j]=Ain[i][j]/det;
     }
}

/*
INFO: Calculation of the Beta co-efficient Matrix via mulitplication
of the Matrix Ain and Matrix B: Beta[0] = N (Intensity Factor),
Beta[1] = Beta2, Beta[2] = Beta4.
*/
```

```
Beta[0]=(B[0]*Ain[0][0])+(B[1]*Ain[1][0])+(B[2]*Ain[2][0]);
Beta[1]=((B[0]*Ain[0][1])+(B[1]*Ain[1][1])+(B[2]*Ain[2][1]))/Beta[0];
Beta[2]=((B[0]*Ain[0][2])+(B[1]*Ain[1][2])+(B[2]*Ain[2][2]))/Beta[0];

/*
INFO: Generation of Beta Spectra for Beta2 and Beta4
*/

Beta2[rp]=Beta[1];
Beta4[rp]=Beta[2];
Na=abs(Beta[0]);
if(Na==0) {
     PESId[rp]=0;
     PESRd[rp]=rp;
     continue;
}

/*
+--+--+--+--+--+--+--+--+--+--+--+--+--+--+--+--+--+--+--+--+--+--+--+--+--+--
(4) DECONVOLUTION

(a) EXPAND NORMALISED LUT TO OBTAIN SIMULATED IMAGE
(b) SELECT OUTER RING AT RP TO BE USED FOR IRADECON (EXPERIMENT OR
SIMULATED)
(c) SUBTRACT SIMULATED IMAGE FROM EXPERIMENTAL IMAGE FOR EACH PIXEL
(qp) AT EACH RADIUS (R)
(d) GENERATION OF DECONVOLUTED PES

Note: For this simulated image and fit the values of x and y
correspond to equivalent Cartesian coordinates
Note: Cos(q)**2 = (R/rp)**2 * Cos(a)**2, where q=theta & a=alpha. This
```

```
is due to alpha not being equal to theta at all values of phi (f).
+--+--+--+--+--+--+--+--+--+--+--+--+--+--+--+--+--+--+--+--+--+--+--+--+--+--
*/

PESRd[rp]=rp;
for(R=0;R<=rp;R++) {
     pixels=PIXELS[R][0];
     it=(LUT[rp][R]*((nainc+1)/pixels));
     for(qp=0;qp<=pixels-1;qp++) {
        alpha=AINC[R]*qp;
        fact=Beta[0]*it*(1+((Beta[1]*0.5)*(3*(R/rp)**2*(cos(alpha)**2)
        -1))+((Beta[2]*(1/8))*((35*(R/rp)**4*(cos(alpha)**4))-
        (30*(R/rp)**2*(cos(alpha)**2))+3)));
        if(Data==1 && R==rp) {
            PESId[R]=PESId[R]+fact*sqrt(R)*sin(alpha);
            iradecon[R][qp]=fact/sqrt(R);
        }
        else if(Data==0 && R==rp) {
            PESId[R]=PESId[R]+ira[R][qp]*sqrt(R)*sin(alpha);
            iradecon[R][qp]=ira[R][qp]/sqrt(R);
        }
        ira[R][qp]=ira[R][qp]-fact;
     }
}
}

/*
+--+--+--+--+--+--+--+--+--+--+--+--+--+--+--+--+--+--+--+--+--+--+--+--+--+--
END
+--+--+--+--+--+--+--+--+--+--+--+--+--+--+--+--+--+--+--+--+--+--+--+--+--+--
*/
```

Appendix C: Convolution with a Gaussian Instrument Function

The experimental data, $g(t)$, presented in Figure 4.10 in Chapter 4 of this thesis (see page 182) has been fitted to exponential decay functions, $e(t)$, convoluted with a Gaussian instrument function:

$$g_{\text{fit}}(t) = e(t) * E(z), \tag{7.1}$$

where $g_{\text{fit}}(t)$ is the resultant fit to the experimental data and $E(z)$ is the *complementary error function*, defined as

$$E(z) = \frac{2}{\sqrt{\pi}} \int_{z}^{\infty} \exp\left(t^2\right) dt\,. \tag{7.2}$$

For a convolution between an exponential decay and a Gaussian instrument function, z is evaluated as a function of time delay, t, using

$$z = \left(\frac{\sigma}{\sqrt{2}\tau}\right) - \left(\frac{t - t_0}{\sqrt{2}\sigma}\right), \tag{7.3}$$

where σ is the standard deviation of the Gaussian instrument function, τ is the characteristic relaxation time of the exponential decay, and t_0 is the true time zero offset. Here, we numerically evaluate $E(z)$ as

$$E(z) = 2N(z'), \tag{7.4}$$

where $N(z')$ is the *standard normal distribution*, expressed as

$$N(z') = \frac{1}{\sqrt{2\pi}} \exp\left(\frac{z'^2}{2}\right). \tag{7.5}$$

In equation (7.5) $z' = -\sqrt{2} \cdot z$, where the factor of $-\sqrt{2}$ is required to transform the standard normal distribution into the complimentary error function, formally defined in equation (7.2).

The experimental data, $g(t)$, is fitted to equation (7.1) through a linear least squares fitting method, using the solver macro function in Microsoft Excel 2003. Briefly, each data point of the experimental data set is compared to the corresponding value in the initial fit function, which contains the fit parameters σ, τ, and t_0, as well as the amplitude and offset contained in $e(t)$, defined as A_n and C_n, respectively, in equations (4.1) and (4.2) in Chapter 4. This comparison is formally defined as

$$r(t) = \left[g(t) - g_{\text{fit}}(t) \right]^2 . \tag{7.6}$$

A total relative error, *R*, associated with $g_{\text{fit}}(t)$ is subsequently obtained through

$$R = \sum r(t) . \tag{7.7}$$

The value of *R* is then minimised using the solver macro function, which iteratively optimises the fit variables (listed above). Here, the total number of iterations for the fit has been defined as 1000. Provided the initial values for the fit variables are reasonable, this results in a final scenario where $g_{\text{fit}}(t) \simeq g(t)$.

In Chapter 5, the approach described above is also used to convolute and fit equation (5.12) to the experimentally obtained β_2 anisotropy parameters (see Figures 5.4a and 5.5). Here however, the errors associated with each of the β_2 values, $\sigma(\beta_2)$, are used to perform a *weighted* linear least squares fit to the experimental data, where equation (7.6) is modified to become

$$r(t) = \sigma(\beta_2) \left[g(t) - g_{\text{fit}}(t) \right]^2 . \tag{7.8}$$

Appendix D: D_{2h} Character Table

Table 7.1: Character table for the D_{2h} point group. Orbitals (l) associated with the irreducible representations of the D_{2h} point group are shown in the end column for all orbital angular momentum up to $l = 1$.

D_{2h}	E	$C_2(z)$	$C_2(y)$	$C_2(x)$	i	$\sigma(xy)$	$\sigma(xz)$	$\sigma(yz)$	l
A_g	1	1	1	1	1	1	1	1	s
B_{1g}	1	1	–1	–1	1	1	–1	–1	
B_{2g}	1	–1	1	–1	1	–1	1	–1	
B_{3g}	1	–1	–1	1	1	–1	–1	1	
A_u	1	1	1	1	–1	–1	–1	–1	
B_{1u}	1	1	–1	–1	–1	–1	1	1	p_z
B_{2u}	1	–1	1	–1	–1	1	–1	1	p_y
B_{3u}	1	–1	–1	1	–1	1	1	–1	p_x

Appendix E: Rotational Constants of the TCNQ Radical Anion

With reference to Figure 7.1, the rotational constants, $\tilde{B}$, for the 7,7,8,8-tetracyanoquinodimethane (TCNQ) radical anion may be calculated using the relationship

$$\tilde{B} = \frac{\hbar}{4\pi c I_j}, \tag{7.9}$$

where $\hbar = h/2\pi$ ($h = 6.626 \times 10^{-34}$ J s), c is the speed of light ($c = 2.99 \times 10^{8}$ m s^{-1}) and I_j is the moment of inertia associated with rotation about the molecular frame (MF) Cartesian axis, j, in kg m^2 (see Figure 7.1 for the MF Cartesian axes of TCNQ). For a molecule containing n atoms, I_j is formally defined as

$$I_j = \sum_{i=1}^{n} m_i d_i^2, \tag{7.10}$$

where m_i are the atomic masses (in kg) of each atom, i, and d_i is the distance of the associated atom, i, from the relevant MF Cartesian axis, j, through the molecules centre of mass (blue dot in Figure 7.1 below). Here we define each of the individual rotational

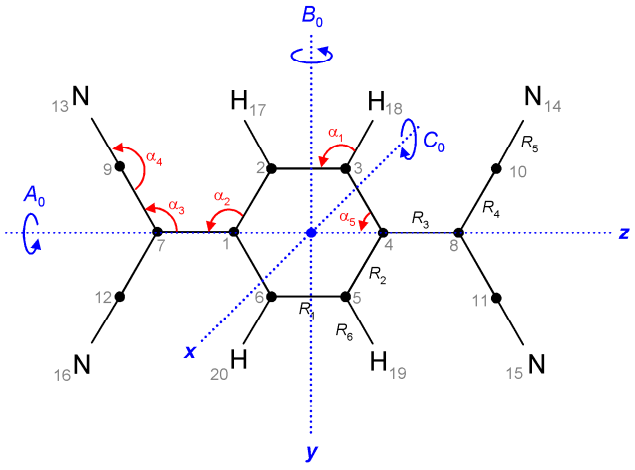

Figure 7.1: Internal co-ordinates, R_n and α_n, and atom labels (grey) used for calculating the rotational constant of TCNQ$^-$. The molecular frame (MF) Cartesian axes are labelled in blue with their associated rotational constants: A_0, B_0, and C_0. Carbon atoms are represented as black dots, and the centre of mass of TCNQ is shown as a blue dot.

constants, A_0, B_0, and C_0, to molecular rotation about the *z*, *y*, and *x* Cartesian axes, respectively, as shown in Figure 7.1.

Spectroscopically, $TCNQ^-$ is classed as an *asymmetric top*, defined as a molecule where $A_0 \neq B_0 \neq C_0$ (or $I_z \neq I_y \neq I_x$). This is confirmed through inspection of Figure 7.1. Here we calculate the rotational constants for $TCNQ^-$ in both its ground and first excited doublet states, $^2B_{2g}$ and 1^2B_{3u}, respectively, using the geometries calculated by Skurski and Gutowski at the SCF/PM3 level of theory (see reference [22] in Chapter 4). We also note that because the $^2B_{2g}$ state and second excited 2^2B_{3u} state geometries are similar, their rotational constants will be similar, hence, we do not present additional calculations for the 2^2B_{3u} state. The bond lengths, R_n (in Å), and bond angles, α_n (in degrees), obtained from these calculations are provided in Table 7.2 (see Figure 7.1 for bond length and angle labels).

The internal co-ordinates presented in Table 7.2 are used to calculate the absolute positions of each atom in $TCNQ^-$ in Cartesian co-ordinates, relative to the centre of mass, using simple trigonometry. These Cartesian positions, shown in Tables 7.3 and 7.4 for the ground and excited states, respectively, are then used to calculate the moments of inertia, using equation (7.10). Table 7.5 presents a summary of the rotational constants for $TCNQ^-$ calculated using equation (7.9).

Table 7.2: Equilibrium bond lengths, R_n, and angles, α_n, for $TCNQ^-$ in both its ground, $^2B_{2g}$, and first excited state, 1^2B_{3u}. All values have been obtained from the geometries calculated by Skurski and Gutowski at the SCF/PM3 level of theory (see reference [22] in Chapter 4). See Figure 7.1 for associated bond and angle labels.

n	Bond lengths, R_n / Å		Bond angles, α_n / degrees	
	$^2B_{2g}$	1^2B_{3u}	$^2B_{2g}$	1^2B_{3u}
1	1.366	1.392	119.75	119.33
2	1.425	1.398	121.40	120.63
3	1.403	1.458	122.25	121.45
4	1.411	1.399	179.14	179.23
5	1.165	1.169	58.60	59.37
6	1.096	1.096	-	-

Table 7.3: Masses, m_i, and Cartesian co-ordinate positions, $d_i(j)$, for the atoms, *i*, of $TCNQ^-$ in its $^2B_{2g}$ ground state. Positions are calculated using the equilibrium bond lengths and angles in Table 7.2.

Atom (*i*)	m_i / × 10^{-27} kg	$d_i(z)$ / Å	$d_i(y)$ / Å	$d_i(x)$ / Å
C (1, 4)	20.04	0	1.425	1.425
C (2, 3, 5, 6)	20.04	1.216	0.683	1.395
C (7, 8)	20.04	0	2.828	2.828
C (9, 10, 11, 12)	20.04	1.193	3.581	3.774
N (13, 14, 15, 16)	23.38	2.169	4.217	4.742
H (17, 18, 19, 20)	1.67	2.168	1.227	2.491

Table 7.4: Cartesian co-ordinate positions, $d_i(j)$, for the atoms, *i*, of $TCNQ^-$ in its first excited 1^2B_{3u} state. Positions are calculated using the equilibrium bond lengths and angles in Table 7.2 and the relevant masses, m_i, for the atoms, *i*, are given in Table 7.3.

Atom (*i*)	$d_i(z)$ / Å	$d_i(y)$ / Å	$d_i(x)$ / Å
C (1, 4)	0	1.408	1.408
C (2, 3, 5, 6)	1.203	0.696	1.389
C (7, 8)	0	2.866	2.866
C (9, 10, 11, 12)	1.193	3.596	3.788
N (13, 14, 15, 16)	2.183	4.218	4.749
H (17, 18, 19, 20)	2.159	1.233	2.486

Table 7.5: Rotational constants, A_0, B_0, and C_0, for $TCNQ^-$ in its ground $^2B_{2g}$ and first excited 1^2B_{3u} states. A_0, B_0, and C_0 have been calculated from the appropriate I_j values using equation (7.9).

Electronic State	A_0 / MHz	B_0 / MHz	C_0 / MHz
$^2B_{2g}$	1192	267	218
1^2B_{3u}	1187	265	217